University of Padova

Faculty of Arts and Philosophy
Faculty of Mathematical, Physical and Natural Science
Faculty of Engineering

Doctoral School in
Study and Preservation of Archeological and Architectural Heritage

Main Course in
Science and Technologies for Archeological and Architectural Heritage

Doctoral Thesis

FRP strengthening of masonry arches: analysis of local mechanisms and global behaviour

Candidate:
Matteo Panizza

Tutor:
Maria Rosa Valluzzi

XXII CYCLE

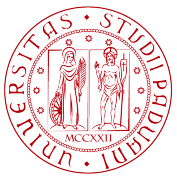

UNIVERSITÀ
DEGLI STUDI
DI PADOVA

Sede Amministrativa: Università degli Studi di Padova

Dipartimento di Archeologia
Dipartimento di Architettura, Urbanistica e Rilevamento

SCUOLA DI DOTTORATO DI RICERCA IN:
STUDIO E CONSERVAZIONE DEI BENI ARCHEOLOGICI E ARCHITETTONICI

INDIRIZZO:
SCIENZE E TECNOLOGIE PER I BENI ARCHEOLOGICI E ARCHITETTONICI

CICLO XXII

FRP STRENGTHENING OF MASONRY ARCHES: ANALYSIS OF LOCAL MECHANISMS AND GLOBAL BEHAVIOUR

Direttore della Scuola
Ch.mo Prof. Giovanni Leonardi

_____

Coordinatore di Indirizzo
Prof. Giuseppe Salemi

_____

Supervisore
Dr. Maria Rosa Valluzzi

_____

Dottorando
Ing. Matteo Panizza

_____

Rem tene, verba sequentur
Catone il Censore

Sommario

Negli ultimi due decenni, i materiali compositi FRP (*Fibre-Reinforced Polymers*) hanno trovato un crescente impiego nel rinforzo di costruzioni murarie sia moderne sia storiche (edifici, ponti, torri), nonché di vari elementi strutturali (pareti, archi e volte, pilastri e colonne). L'applicazione di FRP ad archi e volte in muratura può contribuire in modo significativo a migliorarne la capacità portante, attivando meccanismi locali a livello di materiali e interfaccia, ma comporta anche un cambiamento dei meccanismi di collasso della struttura originale, poiché il rinforzo impedisce la tipica rottura fragile causata dalla formazione di meccanismi a cerniera.

Evidenze sperimentali hanno messo in luce come il comportamento della sezione di un arco rinforzato sia assimilabile a quello del calcestruzzo o della muratura armati, mentre il collasso strutturale sia generalmente da imputare al distacco dell'FRP, nel caso di rinforzo intradossale, o allo scorrimento sul giunto murario, nel caso di rinforzo estradossale.

Nonostante un crescente numero di studi riguardanti il rinforzo di strutture murarie con FRP, le indagini sono tuttavia ancora limitate, se confrontate con applicazioni su calcestruzzo armato. Inoltre, anche a livello internazionale, pochi codici e raccomandazioni sono attualmente disponibili.

Muovendo dalle precedenti considerazioni, cinque temi sono stati indagati nel presente lavoro: il problema del reperimento e della condivisione di dati inerenti attività relative al rinforzo di strutture murarie; l'analisi di eventuali correlazioni fra la resistenza a pull-off e altre comuni proprietà meccaniche; l'indagine del comportamento di adesione nel caso di azioni tangenziali, mirato alla calibrazione di formule di progettazione, disponibili solo per questo meccanismo; l'indagine di un possibile contributo di resistenza del rinforzo soggetto ad azioni miste, come nel caso di scorrimento sul giunto; infine, la validazione di modelli predittivi, inerenti il comportamento globale della struttura rinforzata, mediante applicazione a numerosi casi studio sperimentali.

La prima parte della ricerca ha prodotto la struttura di un Database per la raccolta di dati relativi a lavori di sperimentazione, analisi e modellazione, interventi su edifici e altri temi, quali durabilità o tecniche non distruttive, riguardanti l'applicazione di materiali FRP alla muratura; tale prodotto è stato sviluppato nell'ambito dell'attività della Commissione Tecnica RILEM 223-MSC (Masonry Strengthening with Composite materials). Le più recenti *releases* del sistema, attualmente disponibile *on-line*, presentano significativi miglioramenti che hanno modificato il Database originario in un cosiddetto Data-Warehouse, il quale consente l'implementazione di funzionalità aggiuntive e offre a ricercatori esterni l'accesso e la possibilità di contribuire.

La parte centrale del lavoro ha indagato i tre summenzionati meccanismi locali collegati al collasso degli archi rinforzati, ossia il comportamento dell'interfaccia per azioni normali alla superficie (distacco dell'FRP osservato in strutture rinforzate all'intradosso), per azioni tangenziali (*plate-end* o *intermediate debonding*), e per azioni miste (relative allo scorrimento sul giunto murario osservato in strutture rinforzate all'estradosso).

Il primo meccanismo locale, comportamento dell'interfaccia nel caso di forze normali alla superficie, è stato indagato mediante l'esecuzioni di un ampio numero di prove combinate su mattoni pieni in laterizio (flessioni, compressioni e prove di pull-off). L'originalità del programma sperimentale risiede nell'aver condotto tre tipi diversi di prova sullo stesso elemento, in modo da lavorare non su valori medi delle proprietà in gioco, bensì su triplette di valori mutualmente legate (dati puntiformi). Sulla base dei risultati ottenuti, sono state

quindi calibrate appropriate relazioni fra la resistenza a pull-off e la resistenza a flessione, a compressione e a trazione indiretta, prendendo in considerazioni fattori quali il tipo di mattoni (estrusi o faccia a vista), il tipo di fibre e la presenza del primer. Inoltre, sono state tarate correlazioni empiriche fra la resistenza a flessione e quella a compressione o trazione indiretta.

Il comportamento di adesione per azioni tangenziali, secondo meccanismo locale, è stato indagato mediante l'esecuzione di *Double-lap Shear Tests* su mattoni pieni. Sono stati ricavati valori dell'energia di frattura per rinforzo in carbonio (CFRP) e in vetro (GFRP), ed è stata proposta una semplice legge di tipo esponenziale, mirata a ridurre le difficoltà del procedimento di taratura, per descrivere il comportamento sperimentale dell'interfaccia. Successivamente, tali prove sono state modellate mediante tecniche agli elementi finiti, al fine di condurre analisi sui principali parametri coinvolti nel fenomeno: due diversi approcci per la modellazione del rinforzo, fibre concentrate e fibre distribuite, sono stati messi a confronto, rivelandosi come sostanzialmente equivalenti; l'implementazione della legge di tipo esponenziale o di quella bilineare ha condotto a risultati assai simili; lo studio numerico ha inoltre fornito il valore di lunghezza efficace per CFRP e GFRP. Infine, la raccolta di dati disponibili riguardanti attività sperimentali simili ha consentito una taratura del coefficiente c_1 fornito dalle linee guida CNR DT-200.

Il terzo meccanismo locale, comportamento per azioni miste chiamato in causa quando avviene lo scorrimento sul giunto murario, è stato indagato adattando a supporti in laterizio il cosiddetto *V-shape Peel Test*, allo scopo di riprodurre a scala locale condizioni simili a quelle di rottura a taglio nel caso di archi con rinforzo estradossale. Nel corso della presente attività, per identificare gli aspetti principali del problema, sono stati sperimentati quattordici campioni. È stato messo in luce come il carico di *peeling*, durante il distacco, oscilli entro un intervallo limitato, nonostante uno *scattering* abbastanza elevato. Similmente, anche l'angolo di *peeling* si è mantenuto entro valori quasi costanti, con un ampio *scattering* anche in questo caso. L'applicazione di formulazioni disponibili, basate sulla meccanica della frattura, ha fornito una prima stima dei valori di energia di frattura in modo misto per i substrati impiegati nelle prove.

Infine, gli attuali modelli, interpretativi del comportamento globale delle strutture voltate, sono stati integrati, ove necessario, con i risultati ottenuti a scala locale nel corso del presente lavoro, al fine di applicarli a numerosi casi studio sperimentali, riguardanti modelli in scala, o a scala reale, di archi rinforzati, e di comparare i risultati analitici alle evidenze sperimentali. Riguardo il rinforzo estradossale, i modelli inerenti la crisi flessionale hanno condotto a carichi di rottura generalmente più alti di quelli sperimentali, poiché la resistenza della sezione non viene in genere attinta prima che la crisi a taglio provochi il collasso. Si è evidenziato, inoltre, che il rapporto spessore/luce potrebbe accentuare il comportamento flessionale. I modelli inerenti il distacco del rinforzo per azioni tangenziali, mai osservato nel corso delle campagne considerate, hanno portato a stime fortemente dipendenti dai valori scelti per il coefficiente c_1, e comunque distanti dalla realtà sperimentale. Il criterio di rottura a taglio non sembra sufficientemente adeguato a fornire una stima affidabile del carico di rottura, dal momento che esso dipende fortemente dal valore adottato per il coefficiente di attrito, dalla geometria della struttura e dallo schema statico prescelto, compresa la posizione delle cerniere. Riguardo il rinforzo intradossale, i modelli relativi al comportamento a flessione e al distacco per azioni tangenziali hanno condotto a considerazioni simili a quelle del rinforzo estradossale. Infine, il modello che descrive il distacco del rinforzo dovuto ad azioni normali, anche se in grado di interpretare correttamente il fenomeno, avendo pressoché in ogni caso sovrastimato il carico di rottura, sembra richiedere una taratura che possa meglio collegarlo alle grandezze in gioco.

Abstract

In the last two decades, FRP (Fibre-Reinforced Polymers) composite materials have been adopted for strengthening and repair of both modern and historic masonry constructions (buildings, bridges, towers) and structural components (walls, arches and vaults, pillars and columns).

Strengthening of brick masonry arches and vaults with FRP laminates can contribute significantly in the improvement of their structural capacity at a limit state, by activating local mechanisms both at material and interface levels, but also modifies the collapse mechanisms of the original structures, as the reinforcement prevents the typical brittle failure due to the formation of hinge-mechanisms.

Experimental evidences highlighted as the reinforced arch sections behave similarly to reinforced concrete or masonry, while structural failure is generally due to ripping of FRP, in the case of intrados reinforcement, or sliding on a mortar joint, in the case of extrados reinforcement.

Despite the increasing number of specific studies on FRP reinforcement of masonry structures, investigations are still limited if compared to reinforced concrete applications. Moreover, few codes and recommendations are currently available.

Starting from these points, five main topics have been evaluated as worthy to be investigated: the problem of collecting and sharing data concerning available activities based on strengthening of masonry structures; the analysis of possible correlations among pull-off strength and other more common mechanical properties of solid clay bricks; the investigation of bond behaviour in the case of tangential forces, targeted to the calibration of guidelines' provisions (available only for this mechanism); the investigation of a possible contribution of the reinforcement when subdued to mixed actions, as in the case of sliding of masonry on a mortar joint; finally, the validation of existing models, aimed at describing the collapse behaviour of reinforced masonry arches, through their application to several experimental case studies.

The first part of the research has produced the structure of a Database aimed at collecting data concerning available experimental, analytical, numerical works, as well as interventions on real structures or other topics as durability or Non-Destructive Techniques, related to the application of FRP materials to masonry, within the framework of the RILEM Technical Committee 223-MSC (Masonry Strengthening with Composite materials). Latest releases of this system, currently available on-line, present significant upgrades that modified the original Database into a Data-Warehouse, which allows to implement additional functions and provide access and contributions coming from external researchers.

The central section of the work has investigated the three above mentioned local mechanisms involved by the collapse of FRP-reinforced masonry arches, namely the interface behaviour in the case of stresses normal to the surface (FRP detachment observed in structures with intrados reinforcement), of tangential stresses (plate-end or intermediate debonding) and of mixed actions (related to the shear sliding on a mortar joint observed in structures with extrados reinforcement).

The first local mechanism, interface behaviour in the case of stresses normal to the surface, has been investigated through the execution of a large number of combined tests on solid clay bricks (flexural, compressive, splitting and pull-off tests). The originality of the experimental program was to perform three different tests on the same clay element, so as to work not on average values but on triplets of mutually related values (punctiform data).

Appropriate empirical correlations, which relate pull-off strength to flexural, compressive and splitting tensile strength, have been calibrated, on the basis of the obtained data, taking into account parameters such as the brick type (facing or extruded)the fibres type and the presence of primer. Moreover, empirical relations between flexural and compressive or splitting tensile strength have been calibrated.

The bond behaviour, second local mechanism, has been investigated by performing Double-lap Shear Tests on solid clay bricks. Interface fracture energy values, for carbon (CFRP) and glass (GFRP) interface, have been obtained, while a simple exponential-based bond-slip law, aimed at reducing the difficulties of the calibration problem, has been proposed to depict the experimental behaviour of the interface. Moreover, these tests have been modelled by Finite Elements techniques in order to carry out analyses concerning the main parameters involved in the phenomenon: two approaches for modelling the reinforced have been compared, concentrated versus distributed fibres, revealed as rather equivalent; the implementation of the exponential-based or the bilinear law has given very closer results; the numerical study on bond length has provided the effective length values for CFRP and GFRP. Finally, the collection of available data on similar experimental activities has allowed to calibrate the $c\_textup1$ coefficient provided by CNR DT-200 guidelines.

The third local mechanism, mixed-mode behaviour involved when sliding on a mortar joint occurs, has been investigated by adapting to clay substrates the V-shape Peel Test, in order to reproduce on a local scale the conditions related to the shear failure of arches with extrados reinforcement. Fourteen samples have been tested during this activity, aimed at identifying the primary aspects of the problem. It has been highlighted that the peel load, during the detachment, oscillated within a limited range, though the scattering was in some cases very large. The peel angle, similarly to the peel load, oscillated around quasi-constant values, with high scattering also in this case. By applying current available fracture mechanics formulations, a first estimation of mixed-mode fracture energy values has been provided for the tested substrates.

Finally, the available models, interpretative of the global behaviour of arched structures, have been integrated, when needed, with the results obtained at a local level during the present work, in order to apply them to several experimental case studies, concerning real-scale or scaled reinforced brick masonry arches and vaults, collected from literature, and to compare analytical results to experimental evidences. Concerning the extrados reinforcement, models related to the flexural crisis have led to failure loads generally higher than the experimental ones, since the bending strength could not be reached before the shear crisis occurs at lower load levels. It has also been found as the thickness/span ratio could emphasize the flexural behaviour. Models related to the intermediate FRP debonding, never observed during the reported campaigns, have given predictions strongly dependent on the chosen values of the experimental coefficient c_1, however distant from the experimental actuality. The shear failure criterion does not seem to be sufficiently adequate to provide a reliable estimation of the failure load, since it is strongly dependent on the assumed friction coefficient, on the geometry of the structure and the adopted static schemes, including the position of the hinges. Concerning the intrados reinforcement, models related to flexure and intermediate debonding give to considerations similar to the extrados reinforcement. Lastly, the model that describes the fibres detachment due to normal stresses generated by the curved morphology of the intrados, while correctly interprets the phenomenon, seems to need a calibration to be better connected to the involved quantities, since failure loads have been overestimated in most cases.

Acknowledgements

I would express gratitude to Prof. Claudio Modena, who gave the opportunity to work with his group, to Dr. Maria Rosa Valluzzi, to have supervised my work, to Enrico Garbin, for his precious help in almost every aspect of this research. I would like also to thank all the people working within the research group, particularly Giulia Bettiol, Filippo Casarin, Massimo Dalla Benetta, Francesca da Porto, Giovanni Guidi, Nicola Mazzon, Marco Munari, Flavio Mosele, Luca Nicolini, Bruno Silva, Elena Simonato, Elena Stievanin. Finally, I express gratitude also to my family, for having supported me during this experience.

Index

List of Figures

List of Tables

Chapter 1

Introduction

1.1 Background

As a matter of fact, innovative materials are often rapidly proposed in the current practice, even for restoration of historical constructions, where preservation criteria have to be taken into account; on the other hand, variability and complexity of masonry structures and typologies make difficult to correctly deal with appropriate structural models and interventions, since they should be based on the knowledge of both existing and new materials, and their interaction under environmental and loading conditions.

In the last two decades, FRP (Fibre-Reinforced Polymers) composite materials have been adopted for strengthening and repair of both modern and historic masonry constructions (buildings, bridges, towers) and structural components (walls, arches and vaults, piers and columns). The choice of these techniques is mainly aimed to increase the ultimate capacity of masonry structures and components, often by modifying mechanisms at collapse, which can involve further resisting phenomena.

Strengthening of brick masonry arches and vaults with FRP laminates can contribute significantly in the improvement of their structural capacity at limit state, by activating local mechanisms both at material and interface levels. These interventions modify the collapse mechanisms of the original structures: the reinforcement prevents the typical brittle failure due to the formation of more hinges, and introduces additional strength, at a limit state, related to the local behaviour of materials and interfaces (Faccio and Foraboschi 2000, Briccoli Bati and Rovero 2000, Valluzzi *et al.* 2001, Barbieri *et al.* 2002, Foraboschi 2004, Briccoli Bati and Rovero 2008, Focacci 2008). Besides available formulations regarding the global behaviour of the strengthened structure, an interpretation of local phenomena, based on the calibration of analytical models through simple experimental tests, could be really significant.

Experimental studies carried out at the University of Padova allowed to characterize the behaviour of masonry barrel vaults, strengthened on their intrados or extrados by means of carbon (CFRP) and glass (GFRP) fibre-reinforced polymers (externally bonded textiles), subjected to loads applied to a quarter of the span. These studies identified the limit conditions that activate the collapse (Valluzzi *et al.* 2001).

In the case of intrados reinforcement, rupture is mainly related to the detachment of composite from masonry support. This mechanism is due to stresses perpendicular to the interface, produced by the combination of tension forces and the curved shape of the composite. A simplified model, that takes into account the structure geometry and the reinforcement properties, is commonly proposed (Valluzzi *et al.* 2001, Foraboschi 2004, Briccoli Bati and Rovero 2008) to estimate the collapse load. This model should be calibrated

on the results obtained by pull-off tests that could be performed on small samples, both in laboratory and on-site.

On the other hand, if the reinforcement is applied on the extrados, a really brittle collapse due to shear sliding on a mortar joint can happen; in particular, for asymmetrical load condition, it occurs at the joint closest to the springer opposite to the loading point (Valluzzi *et al.* 2001, Foraboschi 2004, Briccoli Bati and Rovero 2008). In this case, it is supposed that the sliding resistance is related to a first contribution due to friction on the brick-mortar interface and a second contribution that involves the laminate-masonry interface along the perpendicular direction (a sort of dowel action). As the first contribution is supposed to be described by a simplified model based on the Coulomb law that could be calibrated by means of the rather standard triplet test, the second one requires a more complex modeling and experimental procedures to identify and characterize its behaviour.

Despite the increasing number of specific studies on FRP reinforcement of masonry structures, investigations are still limited if compared to reinforced concrete applications. Moreover, few codes and recommendations are currently available: most existing guidelines refer only to strengthening of concrete structures (fib Bulletin 14 2001, ACI 440.2R-02 2002), with the only exceptions of CNR DT-200 (2004), which also provides a section devoted to masonry buildings, and the not yet promulgated ACI 440.7R-10, draft presently still under development.

Harmonization of test procedures and methods is still needed, in order to calibrate analytical and numerical models for design and assessment rules.

Moving from this framework, five main topics have been evaluated as worthy to be investigated: the problem of collecting and sharing data concerning available activities based on strengthening of masonry structures; the analysis of possible correlations among pull-off strength and other more common mechanical properties of solid clay bricks; the investigation of bond behaviour in the case of tangential forces, targeted to the calibration of guidelines' provisions (available only for this mechanism); the investigation of a possible contribution of the reinforcement when subdued to mixed actions, as in the case of sliding of masonry on a mortar joint; finally, the validation of existing models, aimed at describing the collapse behaviour of reinforced masonry arches, through their application to several experimental case studies.

1.2 Aims and method of the present research

Starting from the above exposed background, the first part of the research has been focused on the development of a Database aimed at collecting data concerning available experimental, analytical, numerical works, as well as interventions on real structures or other topics as durability or Non-Destructive Techniques, related to the application of FRP materials to masonry. The main goal was to create and structure a tool sufficiently flexible to be improved in order to follow the evolution of such subjects, moving within the framework of the RILEM Technical Committee 223-MSC (Masonry Strengthening with Composite materials).

The central section of the work deals with experimental investigations on three local mechanisms involved by the collapse of FRP-reinforced masonry arches, namely the interface behaviour in the case of stresses normal to the surface (FRP detachment observed in structures with intrados reinforcement), of tangential stresses (plate-end or intermediate debonding) and of mixed actions (related to the shear sliding on a mortar joint observed in structures with extrados reinforcement).

The first local mechanism has been investigated through the execution of a large number of combined tests on solid clay bricks (flexural, compressive, splitting and pull-off tests) aimed at experimentally calibrating possible correlations among the corresponding strength parameters. The main goal was to relate the pull-off strength to the other more commonly available properties, in order to provide its preliminary estimation, currently lacking. Moreover, the possible influence of the fibres type and the presence of primer on the pull-off behaviour have been included into the experimental program. The originality of the experimental program was to perform three different tests on the same clay element, so as to work not on average values but on triplets of mutually related values (punctiform data).

The bond behaviour, second local mechanism, has been investigated by performing ten Double-lap Shear Tests on solid clay bricks, aimed at calibrating fracture energy value and bond-slip law for both CFRP and GFRP reinforcement. The adopted test set-up was chosen since it was more frequent in literature, for clay and stone elements, and easier to be implemented on the available machine. Concerning data analysis, a simple exponential-based bond-slip law, aimed at reducing the difficulties of the calibration problem, has been proposed to depict the experimental behaviour of the interface. Moreover, these tests have been modelled by Finite Elements techniques in order to carry out analyses, based on the experimental evidences, concerning the main parameters involved in the phenomenon; a comparison between different modelling approach for the FRP reinforcement, between the exponential-based and the bilinear bond-slip laws and, finally, the influence of the bond length have been investigated.

The third local mechanism, concerning the mixed-mode behaviour assumed to be involved when sliding on a mortar joint occurs, has been investigated by adapting to clay substrates a test set-up developed for FRP applications on reinforced concrete, known as V-shape Peel Test, in order to reproduce on a local scale the conditions related to the shear failure of arches with extrados reinforcement. Fourteen samples have been tested during this activity, aimed at identifying the primary aspects of the problem, such as strength values and load paths, since no previous results related to clay supports are currently available.

Finally, the available models, interpretative of the global behaviour of arched structures, have been integrated, when needed, with the results obtained at a local level during the present work, in order to apply them to several experimental case studies, concerning real-scale or scaled reinforced brick masonry arches and vaults, collected from literature, and to compare analytical results to experimental evidences.

1.3 Thesis Organization

The thesis is organized into eight chapters that, starting from the present introduction, face the main aspects of the application of FRP externally bonded textiles to masonry arches and barrel vaults: chapter 2 presents a state-of-the art review from both a research and a practical point of view, centred on unreinforced and reinforced arched structures; chapter 3 introduces the Data-Warehouse designed during this study in order to collect data on various research activities concerning the strengthening of masonry with composites materials; chapters 4, 5 and 6 expose the experimental activities performed to investigate the three local mechanisms that involve the FRP-masonry ensemble subject to normal, tangential and mixed forces, respectively; chapter 7 deal with the currently available models developed to interpret the global structural behaviour, updated, when needed, with the results obtained at a local level; finally, chapter 8 summarize the main conclusions reached by the present work.

Chapter 2

State-of-the-Art

2.1 Masonry arches and vaults

The first structures that can be properly defined as arches were realized in Mesopotamia, probably since the 2nd-millenium B.C., adopted and improved by Sumerians and Assyrians. Although known, it was rarely used by Greeks. Arches and domes were widely diffused by Romans, which improving these technology were allowed to manage structures of great complexity (Fig. 2.1 on the following page) like infrastructures, such as bridges and aqueducts, or public spaces such as basilicas and thermae (Guglielmi 2002).

The Romans characteristic shapes, round arches and domes, were widely used by Byzantines (Fig. 2.2 on the next page) and during the Middle Ages, until crossed vaults and ogive arches were introduced (Fig. 2.3 on the following page). These structural systems, declined in a multitude of forms, had been through the centuries the unique alternative to timber for covering spaces, also for housing buildings (Fig. 2.4 on page 7), until metallic elements and reinforced concrete supplanted them (see Watkin 1990, Caleca 2000, Guglielmi 2002). Figure 2.5 on page 7 shows some modern examples.

2.2 Mechanical behaviour of masonry arches and vaults

From the Roman age to the Renaissance, the problem of stability and correct design of arches were mainly faced under a geometrical point of view (Fig. 2.6 on page 9), even though the presence of horizontal thrusts was already perceived at least in the 1st–century B.C., as reported by Vitruvius within *De Architectura* (Benvenuto 1981).

Wide reviews of the historical progress of studies on masonry arches and vaults can be found in Benvenuto (1981), Heyman (1982), Carbone *et al.* (2001).

Robert Hooke (1635-1703) in 1657 and David Gregory (1657-1708), who published the mathematical formulation of the catenary curve, in 1687 asserted the analogy between a hanging chain and an arch, the latter introducing the simile of a necklace made by smooth spheres that, overturned, could stand up by blocking the ends; these ideas were applied by Giovanni Poleni (1683-1761) when he was called to Rome to examine the dome of Saint Peter's Basilica (Fig. 2.8 on page 10). Philippe de la Hire (1640-1718) proposed a collapse mechanism based on the partition of the arched structure into three rigid blocks, moving without friction. Claude Couplet (1642-1722) introduced the concept of collapse due to mutual rotations among adjacent portions, and treated qualitatively the presence of friction. Charles Coulomb (1736-1806) took into account four collapse mechanisms, evaluating in each case the limit load that could assure the equilibrium of the arch. Lorenzo Mascheroni (1750-1800) brought the problem back to the equilibrium of systems of beams. Louis-Claude

(a) The aqueduct of Segovia

(b) Domus Aurea, the octagonal hall

Figure 2.1: Examples from Roman architectures (Watkin 1990)

(a) Hagia Sophia, Istambul

(b) San Marco, Venice

Figure 2.2: Byzantine churches

(a) Chartes Cathedral

(b) Sainte Chapelle, Paris

Figure 2.3: Gothic cathedrals

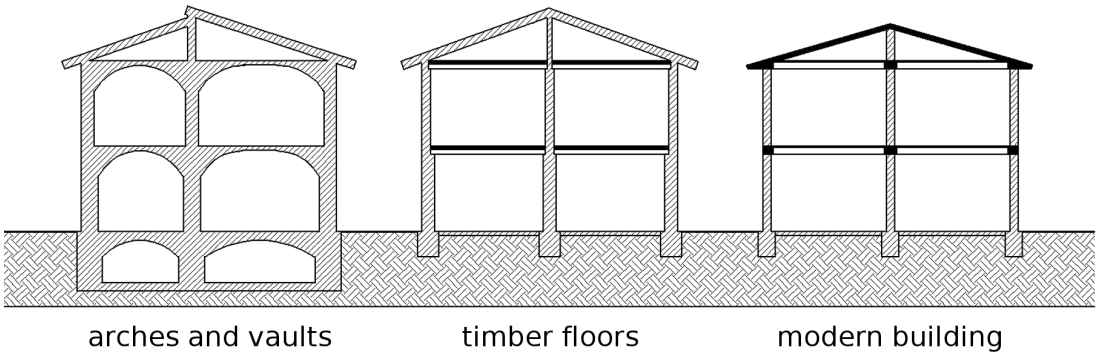

Figure 2.4: Traditional structural schemes for housing buildings (Preite 1987)

(a) Anton Gaudì, Milà House

(b) Eero Saarinen, Gateway Arch

Figure 2.5: Modern examples of arched structures

Boistard (1763-1823) highlighted the four-hinge mechanism of collapse by testing numerous 5-meter scaled models. František Josef Gerstner (1756-1832) introduced the concept of thrust line, and recognized that they are infinite, as William Henry Barlow (1812–1902) in 1846 observably demonstrated it (Fig. 2.7 on the next page). Louis Navier (1785-1836) applied the theory of elasticity to the arch, including in the analysis the strength of materials (Fig. 2.9 on page 11). Henry Moseley (1801-1872) in 1843 tried to solve the statically indeterminate problem imposing that the real thrust line is the one tangent to the extrados at the middle section and tangent to the intrados at the haunches, corresponding to the minimum horizontal force. Eugene Mery (1805-1866) identified the limit thrust line under the stricter condition of being contained by the central third of each section (Fig. 2.10 on page 11).

Therefore, it can be observed that as the theory of elasticity evolved, the rigid body hypothesis was abandoned, and the study of equilibrium was managed assuming the material as homogeneous, isotropic and with no tensile strength. As a matter of fact (Carbone *et al.* 2001), nowadays the elastic approach is not considered sufficiently appropriate, and the thrust line found on the basis of the minimum horizontal force could be closer to the actuality.

However, it is commonly accepted (Heyman 1982) that the collapse of a masonry arch occurs when the thrust line comes excessively near to the edges of the masonry section in a number of points sufficient to make the structure labile, since each of those points is a potential hinge.

The main problem consists in evaluating the safety of the arch. The commonly adopted hypotheses, necessary to surpass the indetermination, were formalized by Heyman (1982): sliding failure cannot occur, as friction along the joints is sufficient to prevent, in most cases, sliding due to shear forces; masonry has no tensile strength, since the joints could have no mortar, or could be deteriorated; masonry has an infinite tensile strength, assumption due to the fact that stresses are in general sufficiently lower than the strength, therefore compressive failure is not likely to occur.

There are infinite thrust lines, satisfying the equilibrium conditions, that can be drawn within the thickness of a certain arch; two of them represent the limit conditions related to the maximum and the minimum value of the abutment thrusts. Reducing incrementally the arch thickness, the extreme values of the thrust tend to coincide until the thickness reaches a limit that imply an incipient collapse (Fig. 2.11 on page 11).

The safe theorem, as stated by Heyman (1982), asserts that the arch cannot collapse if any satisfactory thrust line (i.e. equilibrating the external loads and lying within the arch thickness) can be found. The ratio between the actual thickness and the above mentioned limit value can be considered as a sort of geometrical factor of safety.

Figure 2.12 on page 12 shows a scheme that can be adopted (Focacci 2008) to perform a limit analysis of a semicircular arch with fixed springers. Provided that such a structure presents three hyperstatic conditions, four hinges are needed to allow a kinematic mechanism. For each set of possible hinges, the critical load can be found imposing the equivalence of virtual works; therefore, the collapse load is given by the minimum value of all the critical loads.

Figures 2.13 on page 12 and 2.14 on page 13 show possible mechanisms, due to the formation of hinges that let the corresponding masonry sections mutually rotate. These mechanisms could be due to asymmetric or excessive vertical loads, or to a relative displacement of the abutments.

Seismic mechanisms that involved arched elements, related to the earthquake that stroke the city of L'Aquila on April the 6$^{\text{th}}$ 2009, are shown from Figure 2.15 on page 13 to 2.18

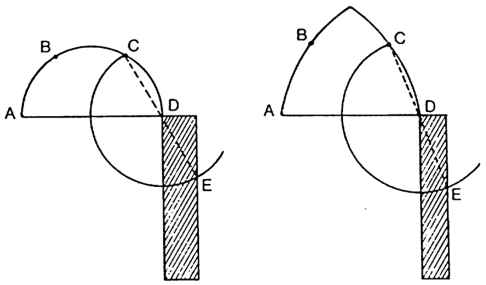

Figure 2.6: Geometrical design rule still used during the 18th–century (Benvenuto 1981)

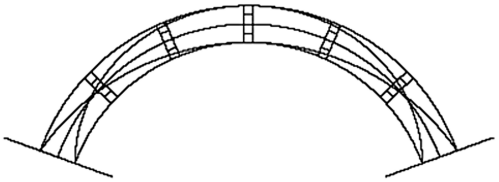

Figure 2.7: Scheme of Barlow's experiment on the thrust lines (Heyman 1982)

on page 15, compared to the basic mechanisms proposed by the form for the assessment of damage of churches developed by the Italian Civil Protection.

2.3 FRP composite materials

The expression "composite material" refers to a combination of two or more constituent materials (Fig. 2.19 on page 17) that, retaining their identities while differing in form, composition or macroscale (ACI 440.2R-02 2002), contribute to obtain particular physical properties and mechanical performances (Minguzzi 1998). Fibre Reinforced Polymers, FRP (formerly Fiber Reinforced Plastics, ACI 440.2R-02 2002), usually refer to composites made by continuous fibres.

FRP were initially developed in the military and aerospace fields near after the Second World War; during the sixties, they were adopted also by the motor and mechanical industries. As the research went on, their cost progressively diminished and their performances increased. During the eighties, the civil engineering began to use them for buildings and infrastructures, starting to develop applications related both on new constructions and strengthening of existing members, mainly concerning reinforced concrete and steel structures (Collepardi *et al.* 2005). During the nineties, composite materials were involved also in the strengthening and restoration of masonry structures (Triantafillou 1998a). Nowadays, FRP are considered as a significant solution for masonry rehabilitation and strengthening (Shrive 2006, Valluzzi 2008), since their high strength-to-weight ratio allows interventions with low load increments and, consequently, low transport and storage costs and reduced impact on the structures.

A wide information concerning FRP materials can be found in different guidelines such as ACI 440R-96 (1996), fib Bulletin 14 (2001), ACI 440.2R-02 (2002), CNR DT-200 (2004).

FRP for strengthening of civil structures are defined as a matrix of polymeric material reinforced by fibers or other reinforcement with a discernible aspect ratio of length to thickness (ACI 440R-96 1996).

The available systems can be classified as follows (CNR DT-200 2004): *pre-cured systems*, manufactured by pultrusion or lamination, directly bonded to the structural member; *wet lay-up systems*, manufactured with fibres lying in one or more directions and impregnated on-site; *prepreg systems*, manufactured with unidirectional or multidirectional fibre sheets pre-impregnated with partially polymerized resin.

Based on their application, FRP are usually classified as Externally Bonded Reinforcement (EBR), commonly textiles (Fig. 2.20 on page 17), laminates and grids, or Near Surface Mounted Reinforcement (NSMR), mainly bars and rods.

The most common fibres used to produce the composite's resisting elements are carbon

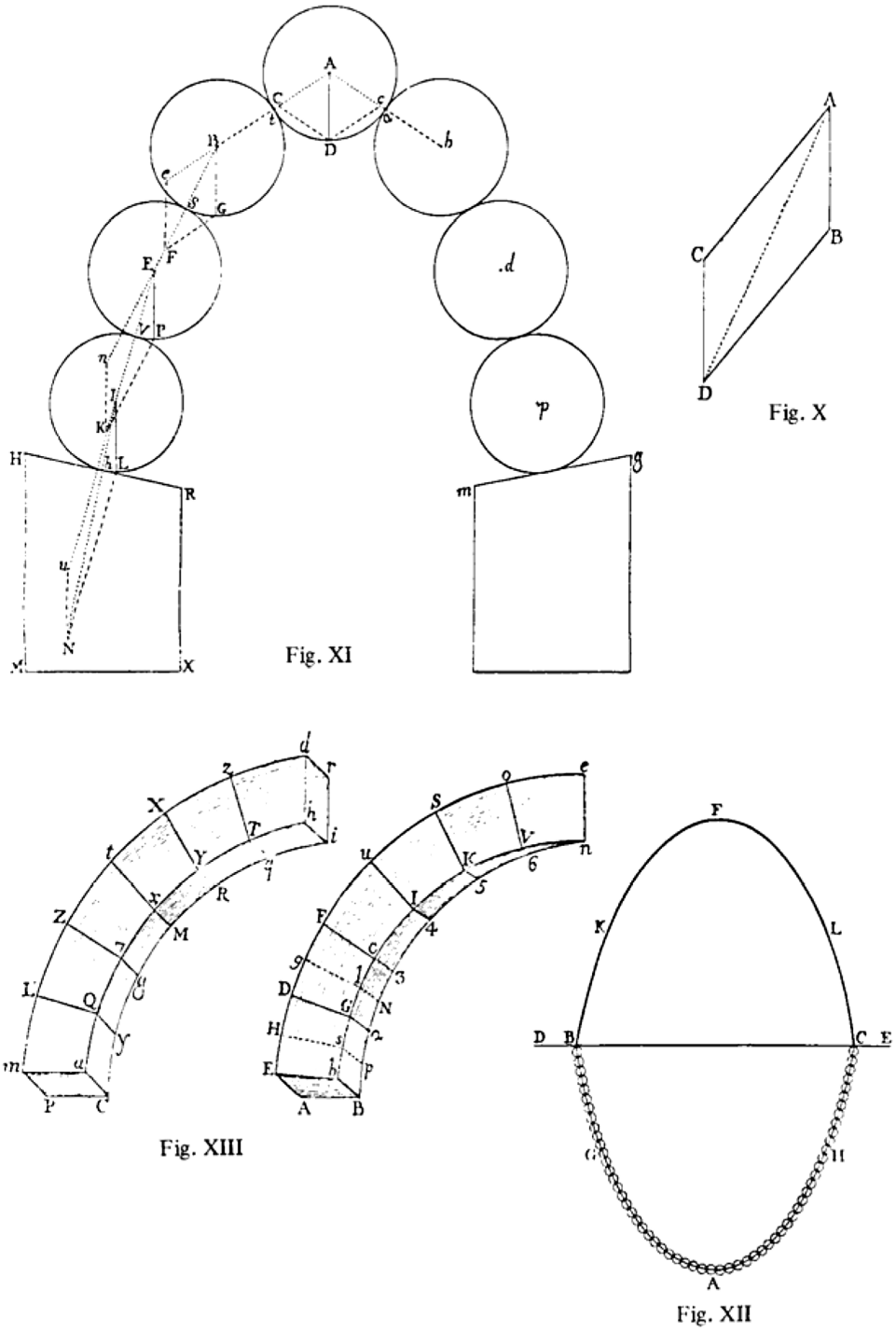

Figure 2.8: Poleni's studies for Saint Peter's dome (Heyman 1982)

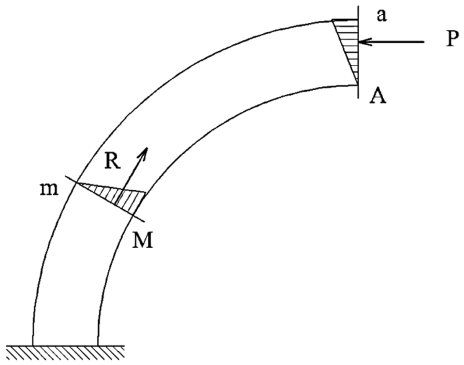

Figure 2.9: Limit stress distribution on the section, according to Navier (Benvenuto 1981)

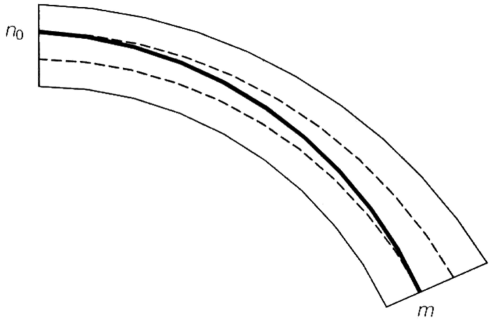

Figure 2.10: Limit thrust line identified by Mery (Carbone *et al.* 2001)

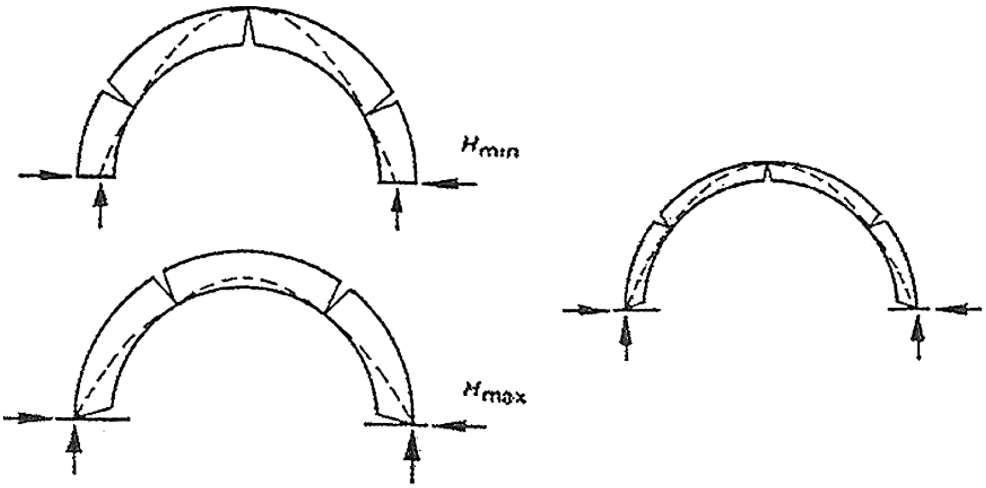

Figure 2.11: Limit configurations of the thrust line (Heyman 1982)

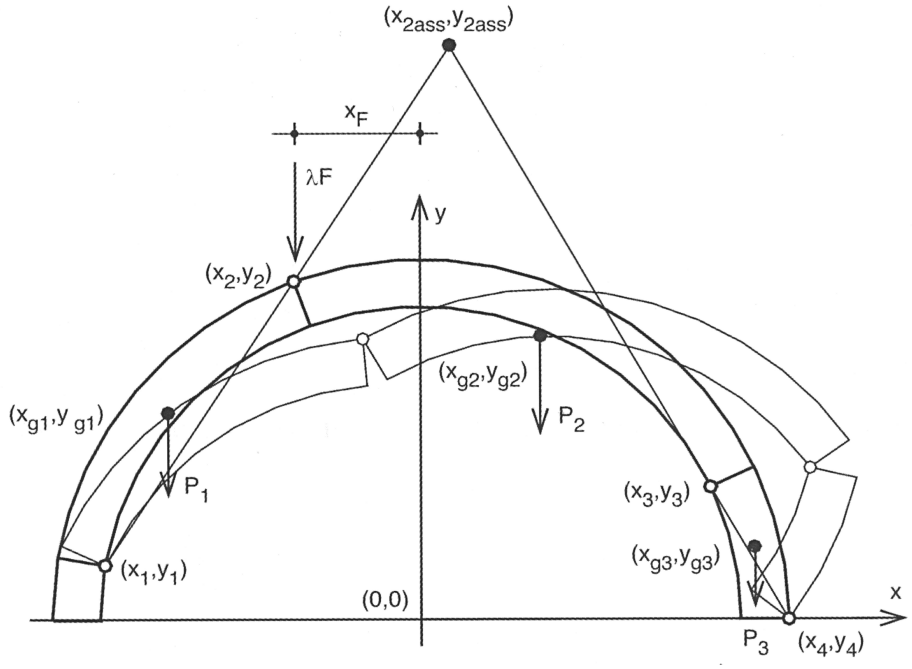

Figure 2.12: Limit analysis of a semicircular arch with fixed springers (Focacci 2008)

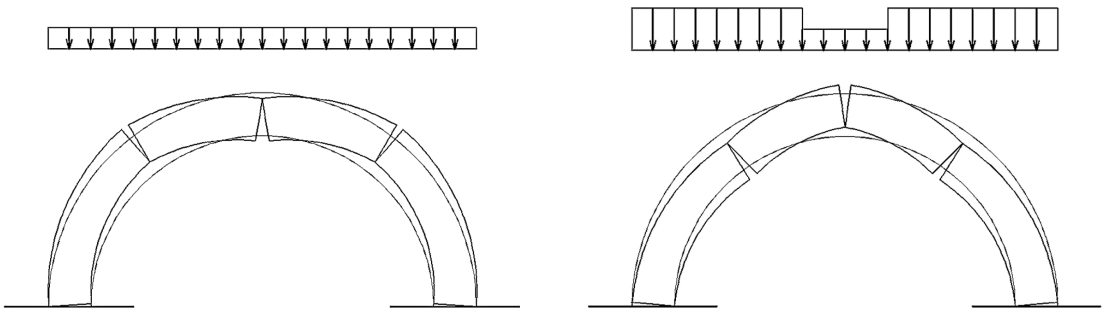

(a) Due to vertical loads

(b) Due to excessive load at the haunches

Figure 2.13: Possible collapse mechanisms for masonry arches (Carbone *et al.* 2001)

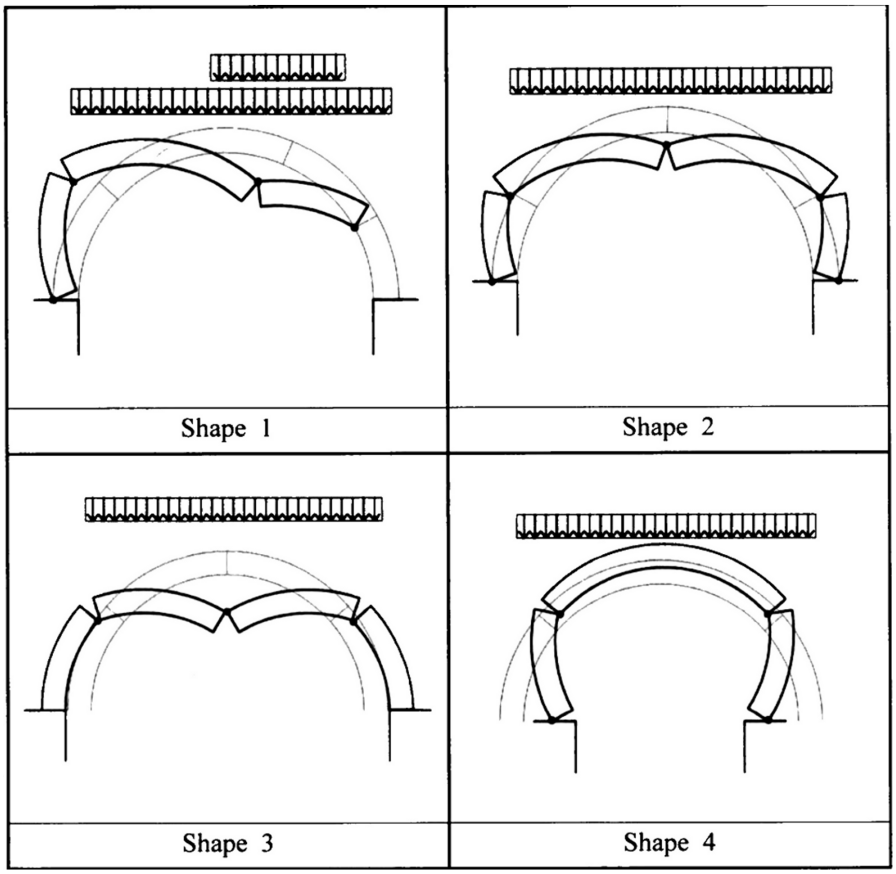

Figure 2.14: Possible collapse mechanisms for masonry arches (Foraboschi 2004)

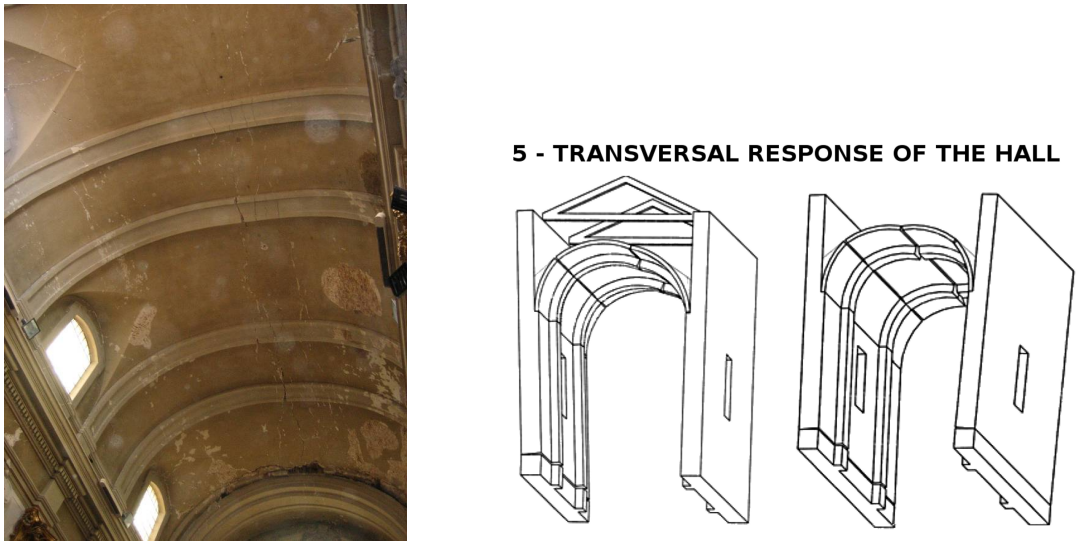

(a) **(b)**

Figure 2.15: Seismic actions: transversal response of the hall (Santa Margherita dei Gesuiti, L'Aquila – internal archive)

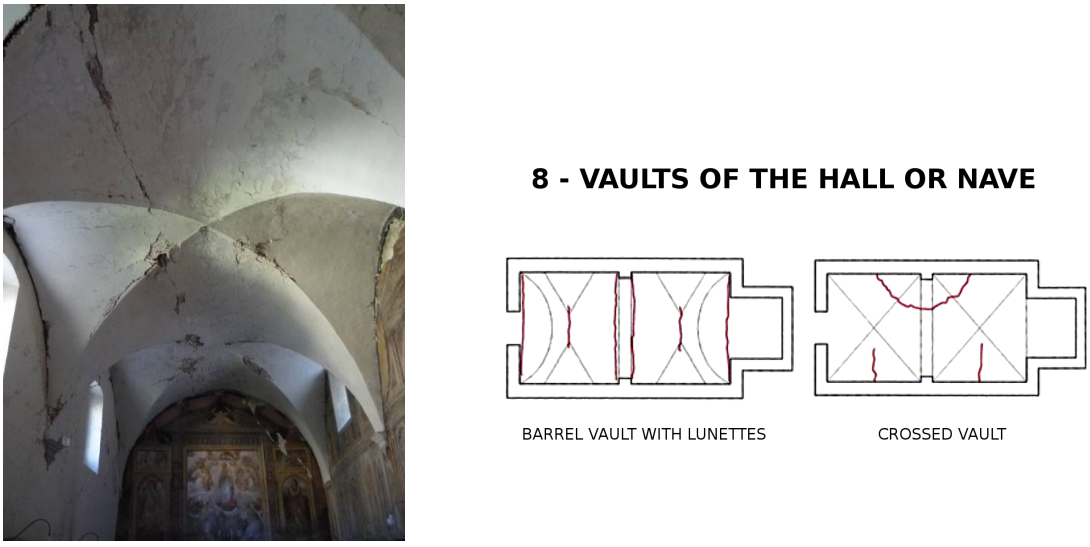

(a) **(b)**

Figure 2.16: Seismic actions: damaged vaults in the hall (Beata Antonia, L'Aquila – internal archive)

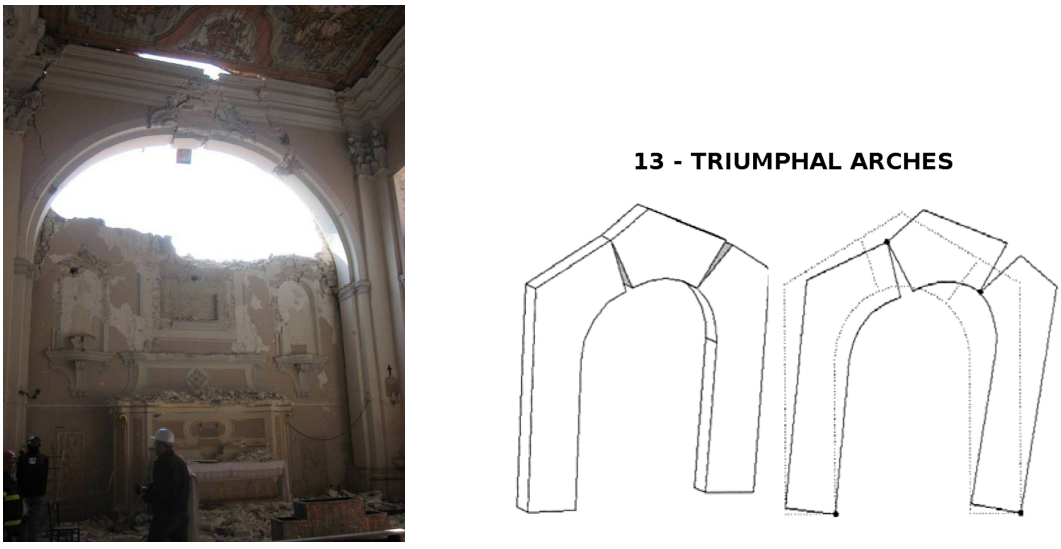

(a) **(b)**

Figure 2.17: Seismic actions: mechanism of the triumphal arch (Santi Marciano e Nicandro, L'Aquila – internal archive)

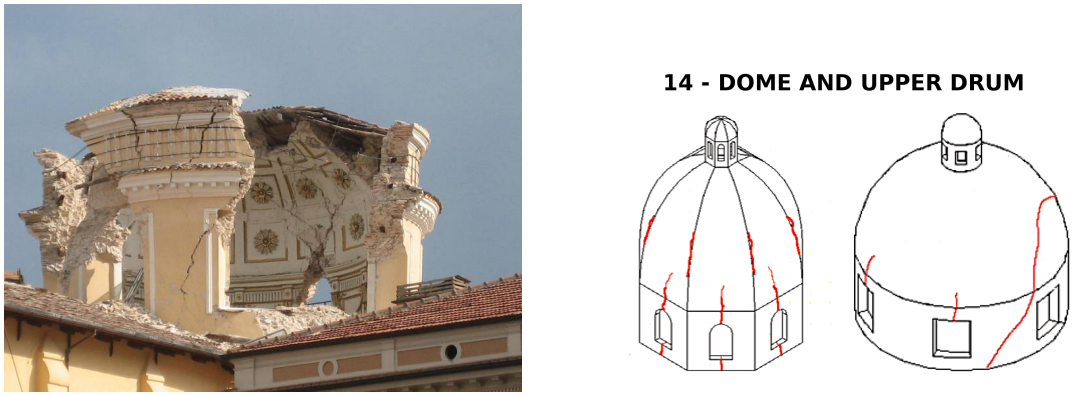

(a) (b)

Figure 2.18: Seismic actions: collapse of a dome (Anime Sante, L'Aquila – internal archive)

(CFRP), glass (GFRP), aramid (AFRP) and, recently proposed, basalt (BFRP). Figure 2.21 on page 17 shows typical stress-strain relationships for some types of fibres, which are practically linear up to failure.

There are two main types of carbon fibres, high strength and high modulus, whose different properties are due to a dissimilar fiber microstructure (ACI 440R-96 1996), although their values are both high (tensile strength from 1900 to 3500 N/mm^2, elastic modulus from 230000 to 640000 N/mm^2) if compared to glass or aramid; their behaviour is anisotropic, as the properties in the transverse directions are lower (CNR DT-200 2004).

Glass fibres are mainly made of tetrahedral structures (SiO4) of silicon (SiO2), while aluminium oxides and other metallic ions are added to modify certain properties or to ease the working operations (CNR DT-200 2004); their modulus of elasticity (70000 N/mm^2 for E-glass) is lower than carbon or aramid fibres; currently seven types of glass fibres are available on the market, signed by letters A, C, D, E, L, R, S (Collepardi *et al.* 2005).

Aramid fibres, introduced at the beginning of the seventies, are made of aromatic polyamides in an extremely oriented form and are characterized by high toughness. Their modulus of elasticity and their tensile strength are intermediate between glass and carbon fibres (CNR DT-200 2004). Their high strength and impact resistance make them suitable for military applications, such as bulletproof vests and aeronautic or armoured components (Collepardi *et al.* 2005).

The mechanical properties of polymer matrix materials depend strongly on ambient temperature, since over the Glass Transition Temperature (Tg) they change from a hard and often brittle solid to a soft solid, while the elastic modulus can be even reduced by five orders of magnitude. As the temperature increases, the polymer changes into a rubber-like solid capable of large elastic deformations under external loads. Compared to most common engineering thermoplastics polymers, thermosetting ones exhibit increased high-temperature and load-bearing performance (ACI 440R-96 1996).

Thermoplastic matrix polymers have high impact strength, high fracture resistance and higher strain-to-failure than thermosetting polymers; on the other hand, they are more viscous and difficult to combine with continuous fibres. Thermosetting matrix polymers are low molecular-weight liquids with very low viscosities, and provide good thermal stability and chemical resistance. They also shows reduced stress relaxation and creep, compared to thermoplastic polymers. Thermosetting polymers (epoxies, polyesters and vinyl esters) are the most diffused as FRP matrices (ACI 440R-96 1996).

Epoxy resins are characterized by resistance to moisture and chemical agents, and have

good adhesive properties; their main component consists of organic fluids with a low molecular weight, containing epoxy groups that are rings composed by an oxygen and two carbon atoms. The pre-polymer is usually a viscous fluid that has to be mixed to a reticulating agent, commonly called hardener, before the application; the reaction is exothermic and does not produce secondary products (CNR DT-200 2004). Figure 2.22 on the next page show some typical stress-strain curves or epoxy resins.

Polyester resins are versatile and highly reactive; in comparison to epoxy, they have a lower viscosity but also mechanical strength and adhesive properties generally lower. They have to be dissolved into a solvent before the application, as they are solid at room temperature (CNR DT-200 2004).

Vinylester resins can be considered as a compromise between traditional polyester resins and epoxy one, suitable for applications at high temperatures or chemically aggressive environment (CNR DT-200 2004).

The use of inorganic matrices, mainly cement-based or lime-based, for fibre-reinforced composites for construction is currently growing (De Lorenzis *et al.* 2004, Prota *et al.* 2006, Papanicolaou *et al.* 2008a,b), as well as the use of steel fibres with either organic or inorganic matrices, which have been named Steel Reinforced Polymers/Grout (SRP/G), as strengthening technique for concrete and masonry structures (Huang *et al.* 2005, Barton *et al.* 2005, Borri *et al.* 2006).

In most cases, the strength and stiffness of fibres is higher than those of resin, whereas the ultimate strain is usually lower and represents a limit for the whole composite material. Clearly (Fig. 2.23 on page 18), the resulting composite has mechanical properties intermediate between fibres and resin but, in the case of EBR applied through the wet lay-up system, it is usual (see ACI 440R-96 1996, ACI 440.2R-02 2002, fib Bulletin 14 2001, CNR DT-200 2004) to refer to dry fibres' properties.

A simple analysis of the composite's behaviour assumes hypotheses such as the isodeformation of fibres and matrix when subjected to axial forces and each fibre' length higher than the critical value that assure a bond strength to the matrix at least equal to the tensile strength (this is supposed to discriminate the continuous fibres reinforcements from other types). Therefore, it is possible to estimate the composite longitudinal elastic modulus E_c and the stress distribution between fibres and matrix (Eq. 2.1), being E_f, E_m the elastic moduli, V_f and V_m the volume fractions, σ_f and σ_m the stress of fibres and matrix, respectively. Replacing the isodeformation with the isotension hypothesis, the transversal elastic modulus $E_\mathrm{f,t}$, related to the direction at 90 degrees with respect to the reinforcement axis, can be evaluated (Eq. 2.1). As it can be noticed in Figure 2.24 on page 18, a slight variation, 5-10 degrees, of the stress direction implies a strong decrease of the elastic modulus (Scarinci 2002).

$$E_\mathrm{c} = E_\mathrm{f} V_\mathrm{f} + E_\mathrm{m} V_\mathrm{m} \tag{2.1a}$$

$$\frac{\sigma_\mathrm{f}}{\sigma_\mathrm{m}} = \frac{E_\mathrm{f}}{E_\mathrm{m}} \tag{2.1b}$$

$$E_\mathrm{c,t} = \frac{E_\mathrm{f} E_\mathrm{m}}{E_\mathrm{f} V_\mathrm{m} + E_\mathrm{m} V_\mathrm{f}} \tag{2.1c}$$

2.4 Mechanical behaviour of strengthened arches and vaults

It is known that stability and safety of curved masonry structures depend on their geometry, materials' properties and load conditions (Heyman 1982, Carbone *et al.* 2001,

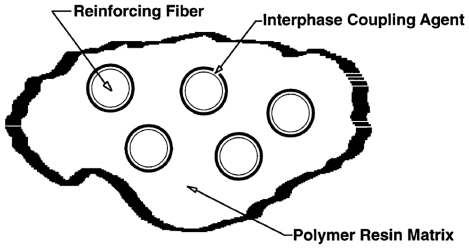

Figure 2.19: Micro-mechanical structure of a composite (ACI 440R-96 1996)

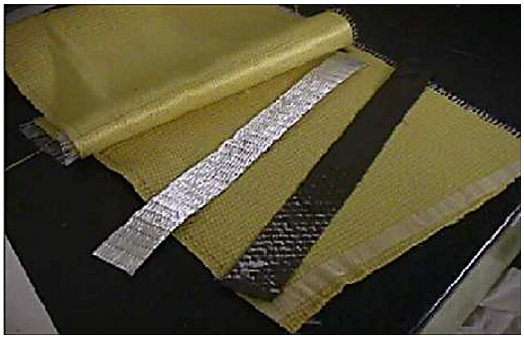

Figure 2.20: Samples of fibres textiles

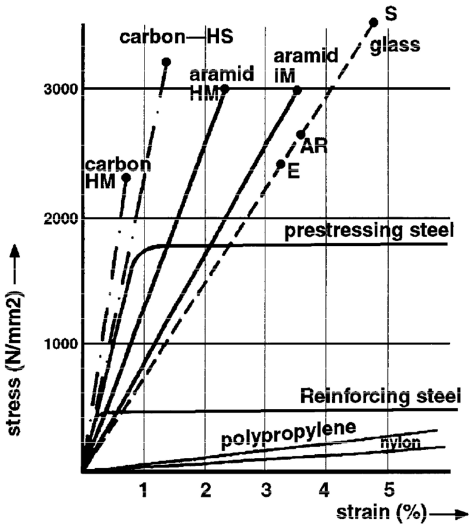

Figure 2.21: Typical stress-strain curves for common fibres (ACI 440R-96 1996)

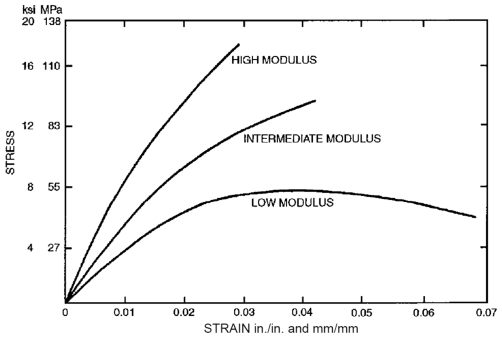

Figure 2.22: Typical stress-strain curves for epoxy resins (ACI 440R-96 1996)

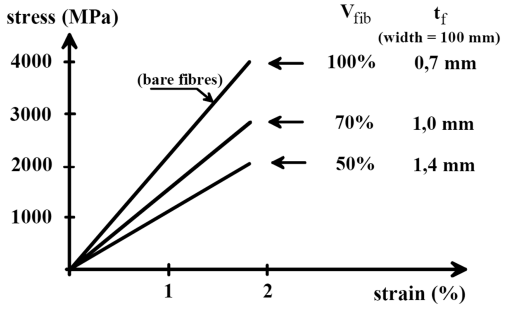

Figure 2.23: Variation of the composite properties in relation to the components fraction (fib Bulletin 14 2001)

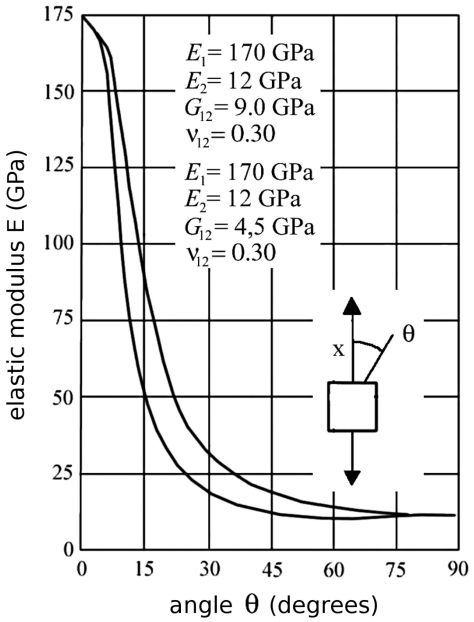

Figure 2.24: Variation of the composite properties in relation to the stress angle (Scarinci 2002)

Focacci 2008).

The mechanical behaviour of the unstrengthened structures is well described on the basis of the Heyman's hypotheses: masonry does not resist to tension stresses (within the joints, the mortar could be absent, poor or deteriorated), masonry has indefinite compressive strength (stresses are usually lower than materials' strength and, although local crushing could be observed, it does not affect the overall equilibrium) and, finally, the low shear stresses assure that friction prevents sliding on mortar joints. On the basis of these assumptions, crisis is ruled by the formation of plastic hinges, which number and position could make the structure labile and activate collapse (Fig. 2.25 on the facing page). When the resultant of the internal forces shifts from the internal core to the edge of the cross section, the section partialises and a local masonry crushing (hinge's centre) with mutual rotation of the adjacent faces could appear.

The application of a reinforcement, resisting to tensile stress, alters the brittle collapse mechanism of the unreinforced structure, preventing the formation of some hinges, because the edge of two adjacent faces are constrained not to split by the reinforcement's presence on that surface.

Externally bonded reinforcement, mostly used on curved structure for their morphological adaptability, can be applied to the extrados or the intrados, rarely on both the surfaces. Referring to common load conditions, it can be noticed (Fig. 2.26 on the next page) as the intrados application generally requires lower thrust values at the springers, therefore it could be preferred where supports are not able to offer sufficient resistance to horizontal forces (Focacci 2008).

The reinforced structure, namely the two parts between the hinges, can undergo flexural performance, similarly to reinforced concrete beams (Triantafillou 1998a,b), as the line of thrust is allowed to be external to the arch thickness (Fig. 2.27 on the facing page).

Therefore, crisis moves to a local level (Fig. 2.28 on page 20) and could be due to: (a)

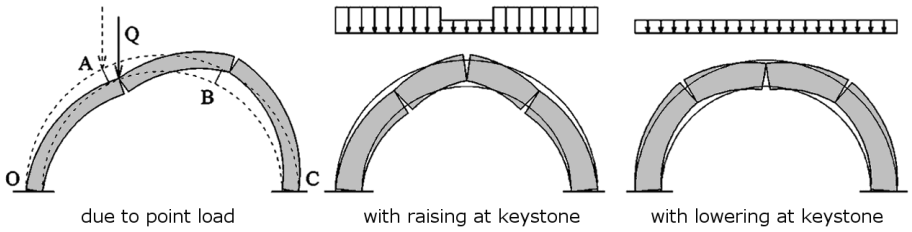

Figure 2.25: Various collapse mechanisms of unreinforced arches

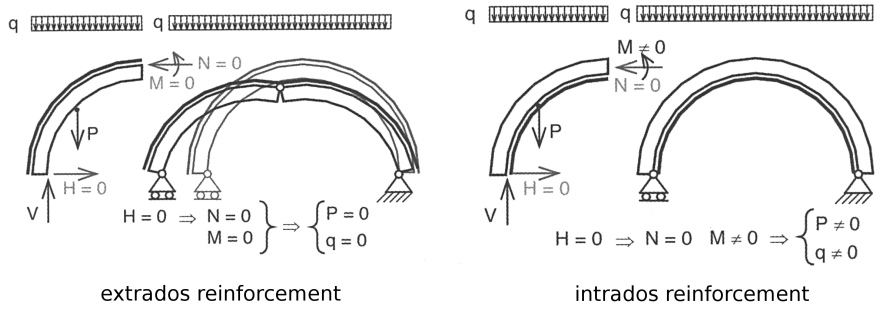

Figure 2.26: Reinforcement application on extrados or intrados (Focacci 2008)

masonry crushing or fiber rupture (combined compressive and bending stresses on the cross section), (b) detachment of the adhesion system on the composite-masonry interface, (c) shear failure of joints, with sliding on the bricks-mortar interface.

Several experimental researches on brick masonry arches and barrel vaults (Valluzzi *et al.* 2001, Foraboschi 2004, Basilio 2007, Castori 2006, Briccoli Bati and Rovero 2008) pointed out that ultimate collapse is most likely due to the composite detachment (b) in case of intrados reinforcement, and to the shear sliding on a joint (c) close to the springer opposite to the loading point in case of extrados reinforcement. The shear disconnection provokes a particularly brittle failure in comparison with the reinforcement detachment, since it does not preserve the integrity of the loaded structure.

2.4.1 Modelling of masonry crushing

As regards reinforced arches, it is possible to evaluate a quite good estimation of the ultimate strength of a masonry cross section, subject to combined compressive and

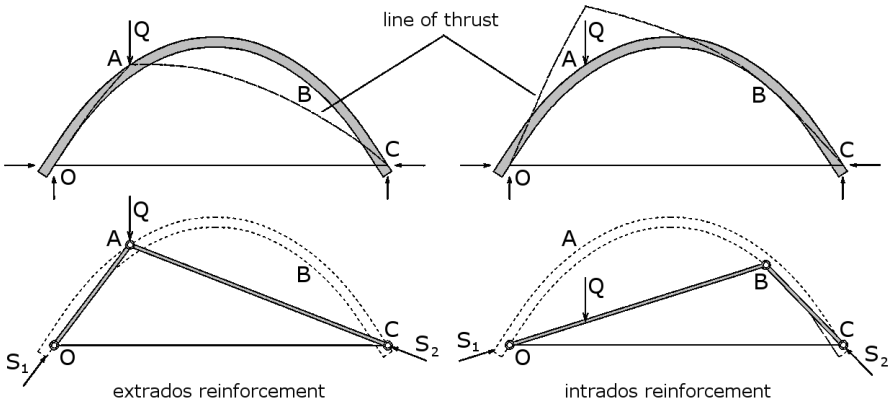

Figure 2.27: Mechanical behaviour of strengthened arches (Valluzzi *et al.* 2001)

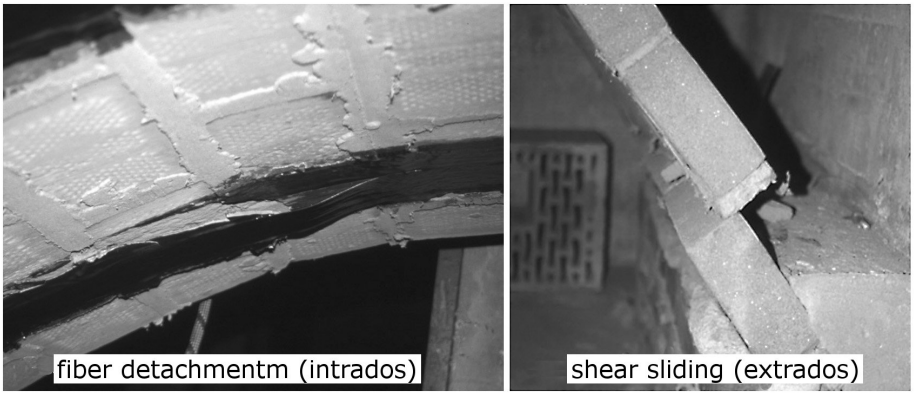

Figure 2.28: Collapse mechanisms for reinforced arches (Valluzzi *et al.* 2001)

bending stresses, by assuming a model based on the constitutive laws and stress and strain distributions shown in Figure 2.29 on the facing page. The maximum bending moment that the section could withstand, when masonry crushing occurs, can be evaluated on the basis of flexural tests performed on small-sized plain specimens (see Valluzzi *et al.* 2001). The resulting design formulas are given in Equation (2.2), where M_{Rd} and N_{Rd} are resisting design bending moment and normal force, b and t are width and thickness of the masonry section, respectively, x is the neutral axis depth, f_{k} and $\varepsilon_{\mathrm{M,u}}$ are design compressive strength and ultimate strain of masonry, E_{f}, $\varepsilon_{\mathrm{frp,u}}$ and A_{f} are elastic modulus, ultimate strain and area of the reinforcement, and ω is the normalized area fraction, while ω_{lim} is the limit value that accounts for the maximum fibres elongation.

A more simplified approach has been proposed by Foraboschi (2004), who affirmed to be adequate, on the basis of experimental evidences, the adoption, as stress-block, of a fixed compressed masonry area of one third of the arch thickness (Eq. 2.3, where $M_{\mathrm{Rd,f}}$ denotes the resisting bending moment evaluated with respect to the position of the reinforcement, extrados or intrados, and C_{max} stands for the maximum allowed compression on the masonry, which is given by the compressed area, one third of the section, multiplied by the design masonry compressive strength); moreover, this approach allows to estimate the compressive force C and the tensile force T respectively acting on masonry and reinforcement (Fig. 2.30 on the facing page), for any value of external load, and to identify the collapse as the compressive force uniformly distributed on that area equals the masonry compressive strength.

$$\frac{M_{\mathrm{Rd}}}{bt^2 f_{\mathrm{k}}} = \begin{cases} \frac{1}{2}\omega\frac{\varepsilon_{\mathrm{frp,u}}}{\varepsilon_{\mathrm{M,u}}} + \frac{0.4}{\gamma_{\mathrm{M}}}\frac{x}{t}\left(1-0.8\frac{x}{t}\right) & \text{if} \quad \omega \le \omega_{\mathrm{lim}} \\ \frac{1}{2}\omega\frac{1-\frac{x}{t}}{\frac{x}{t}} + \frac{0.4}{\gamma_{\mathrm{M}}}\frac{x}{t}\left(1-0.8\frac{x}{t}\right) & \text{otherwise} \end{cases} \tag{2.2a}$$

$$\frac{x}{t} = \frac{\gamma_{\mathrm{M}}}{1.6}\left(\frac{N_{\mathrm{Rd}}}{btf_{\mathrm{k}}} - \omega + \sqrt{\left(\omega - \frac{N_{\mathrm{Rd}}}{btf_{\mathrm{k}}}\right)^2 + \frac{3.2}{\gamma_{\mathrm{M}}}\omega}\right) \tag{2.2b}$$

$$\omega = \frac{\varepsilon_{\mathrm{M,u}}E_{\mathrm{f}}}{f_{\mathrm{k}}}\frac{A_{\mathrm{f}}}{bt} \tag{2.2c}$$

$$\omega_{\mathrm{lim}} = \frac{\varepsilon_{\mathrm{M,u}}}{\varepsilon_{\mathrm{frp,u}}}\left(\frac{0.8}{1+\frac{\varepsilon_{\mathrm{frp,u}}}{\varepsilon_{\mathrm{M,u}}}} - \frac{N_{\mathrm{Rd}}}{btf_{\mathrm{k}}}\right) \tag{2.2d}$$

$$M_{\mathrm{Rd,f}} = \frac{5}{6}C_{\mathrm{max}} = \frac{5}{18}btf_{\mathrm{k}} \tag{2.3}$$

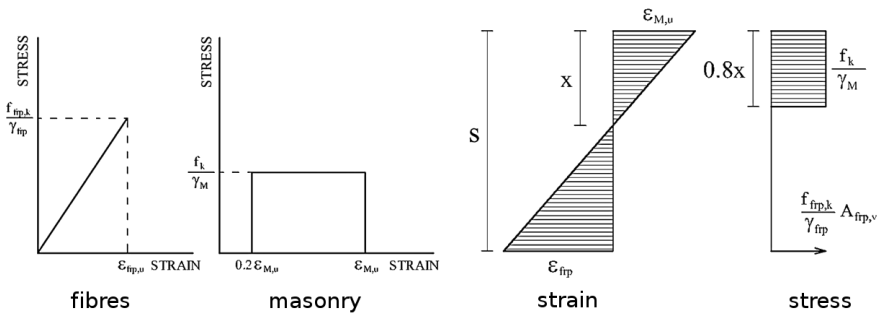

Figure 2.29: Constitutive laws and stress and strain distribution on the masonry cross section (Triantafillou 1998a)

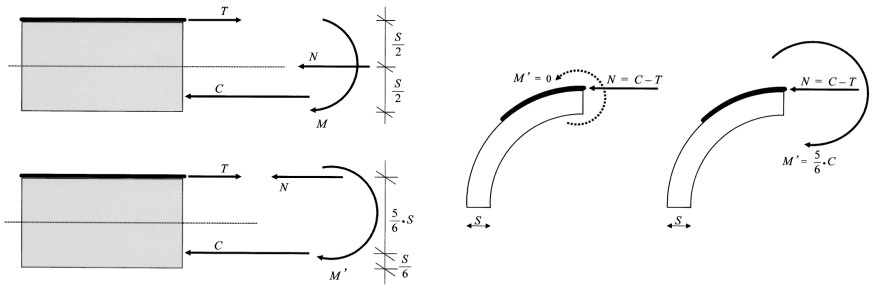

Figure 2.30: Equilibrium of the cross section (Foraboschi 2004)

2.4.2 Detachment of reinforcement at the composite-masonry interface

The application on a curved structure of a material designed to work in tension implies the presence of stresses perpendicular to the interface, produced by the spatial variation of the tensile force. In case of extrados reinforcement, these normal stresses are balanced by the underlying masonry, while in case of intrados reinforcement the equilibrium is ensured only by the adhesion properties of the interface (Fig. 2.31 on the next page). Equation (2.4) gives the relation among the normal stress σ_{n}, the tensile force on the reinforcement T, the intrados curvature radius R and the composite width bf. Therefore, the failure load can be defined as the load value that provokes a normal stress, on the critical section, comparable to the surface tensile strength measured by means of local pull-off tests (Valluzzi *et al.* 2001, Foraboschi 2004, Briccoli Bati and Rovero 2008).

$$\sigma_{\mathrm{n}} = \frac{T}{b_{\mathrm{f}} R} \tag{2.4}$$

2.4.3 Shear sliding on mortar joints

This mechanism is caused by the presence of shear stresses that are particularly high near the springers, in case of extrados reinforcement.

The modeling of strength usually considers only the contribution due to the friction on mutual surfaces (Valluzzi *et al.* 2001, Foraboschi 2004, Briccoli Bati and Rovero 2008, Focacci 2008); this quantity is commonly evaluated by adopting a Coulomb-like law (Eq. 2.6 on the following page) that assumes, during the post-critical phase, a proportionality between the shear strength V_{Rd} and the compressive force C controlled by the friction coefficient μ.

(a) Valluzzi *et al.* (2001) **(b)** Briccoli Bati and Rovero (2008)

Figure 2.31: Development of normal stresses at the intrados surface

A possible contribution to the resistance of the joint (Fig. 2.32 on the next page) offered by the reinforcement, $V_{\mathrm{Rd,frp}}$, was supposed by Valluzzi *et al.* (2001), as reported in Equation (2.5), then Briccoli Bati and Rovero (2008) proposed to estimate the additional strength due to the reinforcement, even though defined as scarce, by applying the formulation developed by Bikerman (1957). A first trial to experimentally characterize this contribution (Fig. 2.33 on the facing page) was carried out by the author (Panizza 2006), and the preliminary results confirmed that the strength, compared to plausible applied amount of reinforcement, could be significant in the case of thin vaults (Panizza *et al.* 2008b).

The coefficient μ, which should be properly intended as the ratio between the compressive stress and the ultimate tangential stress that a masonry section can withstand in the case of sliding on a joint, manly varies among 0.30 and 0.80, as stated by Tassios (1988); experimental results cited by Hendry (1986) varied from 0.3 to 1.05; Heyman (1982) reported 0.5, value defined conservative by Foraboschi (2004) that suggested 0.64, according to his experimental evaluations; the results of triplet tests carried out at the University of Padova (see Panizza 2006) fell into a range from 0.47 to 0.85, while 0.4 was adopted by Briccoli Bati and Rovero (2008) and 0.73 measured by Valluzzi *et al.* (2001).

$$V_{\mathrm{Rd}} = V_{\mathrm{Rd,m}} + V_{\mathrm{Rd,frp}} \tag{2.5}$$

$$V_{\mathrm{Rd,m}} = \mu C \tag{2.6}$$

2.5 Applications of FRP on masonry buildings

In the following, some examples of interventions that involved application of FRP composites on historical masonry structures are presented, in order to highlight the main advantages, particularly for bars and textiles, of not increasing the dead loads that burden a strengthened structure and having a high versatility.

The cross vaults of the church of S.ta Corona in Vicenza (Italy) have been reinforced at their extrados with 20 cm wide strips along their longitudinal direction, in combination

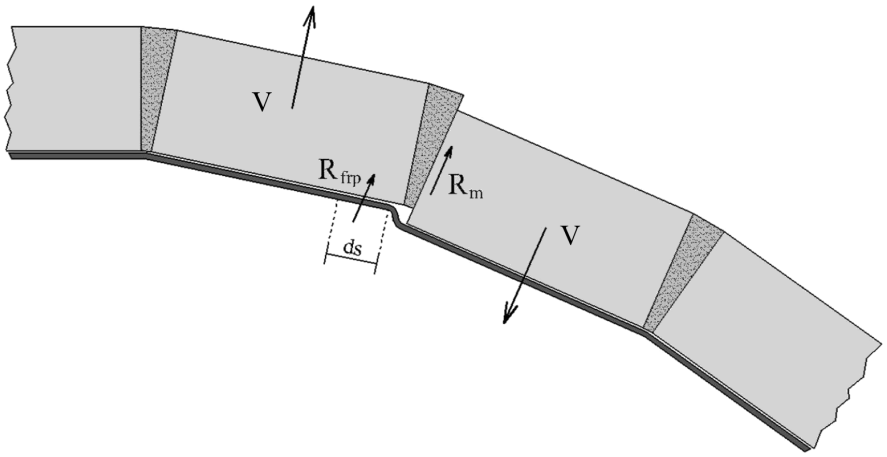

Figure 2.32: Contributions to the shear strength of the joint (Valluzzi *et al.* 2001)

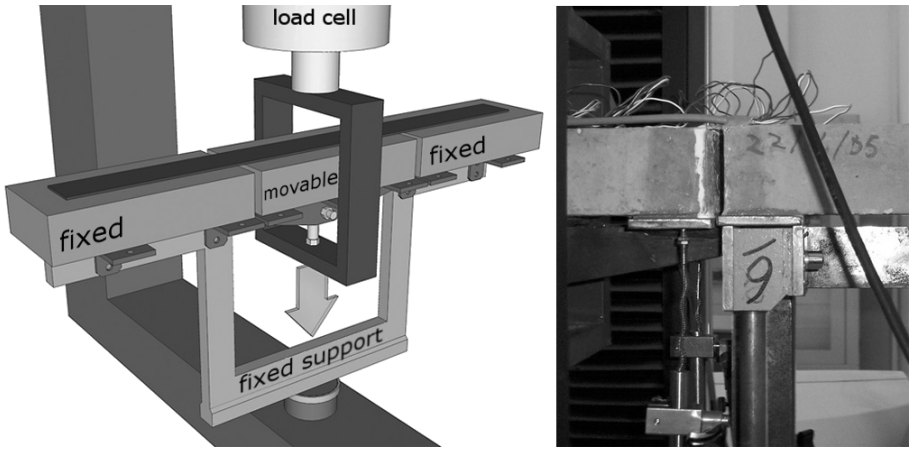

Figure 2.33: Experimental characterization of the reinforcement contribution (Panizza *et al.* 2008b)

Figure 2.34: Longitudinal stiffening of the vaults of Santa Corona in Vicenza (Valluzzi 2008)

Figure 2.35: Partial length reinforcement on the vaults of Villa Bruni in Padova (Valluzzi 2008)

with grout injections, to improve the global behaviour (Fig. 2.34). Figure 2.35 shows a partial length intervention to stitch severe cracks on a vault of Villa Bruni, in Padova, Italy (Valluzzi 2008).

In the Ducal Palace of Urbino (Italy), carbon strips have been applied not on the original surface of the vaults, but on new transversal stiffening masonry diaphragms (Modena *et al.* 2009), as shown in Figure 2.36 on the next page).

Figure 2.37 on the facing page shows the intervention on a bridge at the Lido of Venice, built in the XIX century, which involved a thickening of the masonry section and an extrados strengthening by means of FRP strips (Modena *et al.* 2004).

Finally, two peculiar interventions are shown in Figures 2.38 on the next page and 2.39 on the facing page: the first was the confinement of a capital by means of carbon strips, placed underneath the original metallic ring (Valluzzi 2008); the second one consisted in the restoration of deteriorated portions of the equestrian statue of Cansignorio della Scala, placed on the top of his stone tomb in Verona (Gaudini *et al.* 2008).

In order to depict the framework of FRP interventions on masonry buildings in Italy, around one hundred of case studies have been gathered, which data have been mainly collected from information made available by some companies, namely Fidia SrL, TEC.INN. SrL, FIBRE NET SrL, Ardea Progetti e Sistemi Srl, EDILSYSTEM SrL, E.C.T. Edil Composites Technology SrL. This collection is just partial, since it is affected by the limited investigation and by the location of the companies, mostly working in the central regions of Italy; however, some points can be pointed out: the major part of interventions involved ecclesiastic buildings and were mainly performed on vaults (Fig. 2.40 on page 26); the use of externally bonded textiles as reinforcement system and carbon as reinforcing fibres was predominant (Fig. 2.41 on page 26).

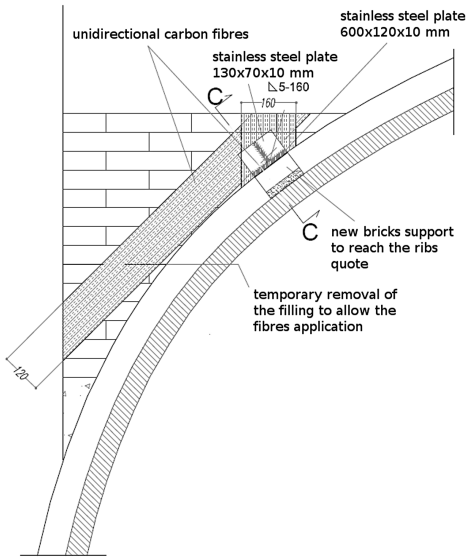

(a)

(b)

Figure 2.36: Reinforced transversal ribs on the vaults of the Ducal Palace in Urbino (Modena *et al.* 2009)

(a)

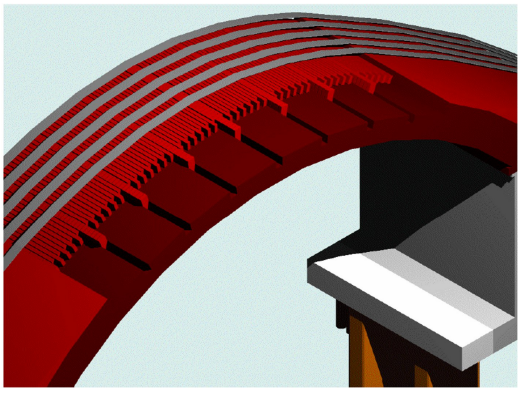

(b)

Figure 2.37: Intervention on a bridge at the Lido of Venice (Modena *et al.* 2004)

Figure 2.38: Integration of the original metallic confinement on a capital in Palazzo della Ragione, Padova (Valluzzi 2008)

Figure 2.39: Restoration of deteriorated portions of the equestrian statue of Cansignorio della Scala, Verona (Gaudini *et al.* 2008)

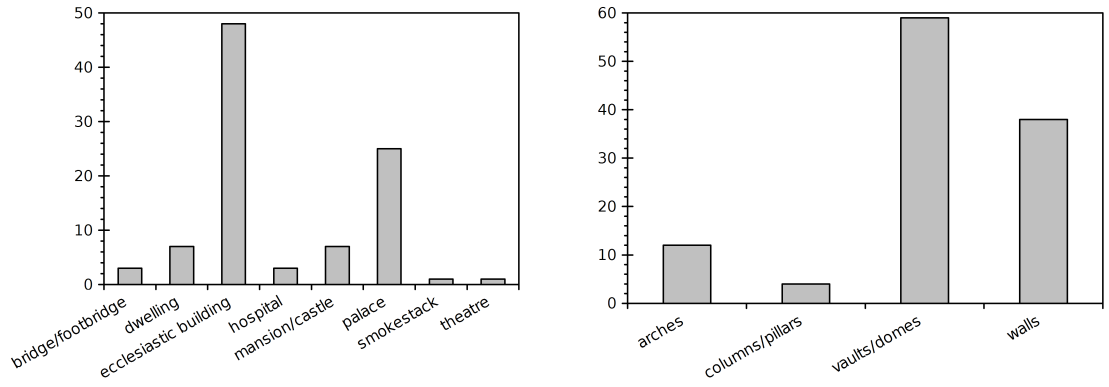

(a) **(b)**

Figure 2.40: Interventions with FRP classified by building typology (left) and by strengthened structural element (right)

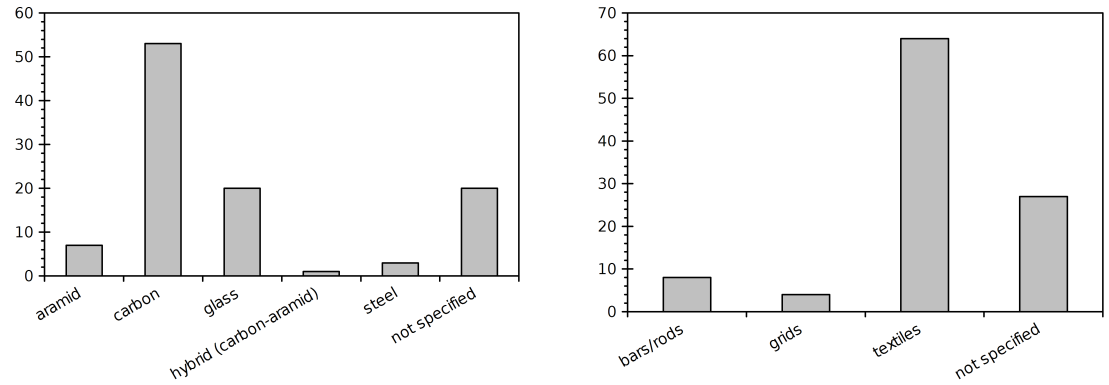

(a) **(b)**

Figure 2.41: Interventions with FRP classified by building type of fibres (left) and by type of reinforcement (right)

Chapter 3

Collection of FRP-masonry experiences: MSC Data-Warehouse

Within the framework of the RILEM Technical Committee 223-MSC (Masonry Strengthening with Composite Materials), an appropriate tool has been created in order to collect data on various research activities concerning the masonry strengthening with composites materials, as experimental work, analytical and numerical modelling, and cases study.

This system, whose structure (not the encoding) was designed during the present work, has arisen from the need of not only gathering detailed information but also exploiting the possibilities offered by modern technologies, which allow, for example, remote contributions, real-time updates, data analyses and exports, and more other features. Moreover, the Data-Warehouse has been configured in order to permit prospective upgrading related to possible evolutions of the treated topics.

3.1 Main characteristics of the on-line tool

The system is basically composed by two distinct sites, one reserved to the TC members and the other open for external contributions from registered members, available on-line (more information on the RILEM site, http://www.rilem.net), that allow to manage a shared database (Fig. 3.1 on the next page).

This tool was structured to receive data belonging to researches and works concerning single structural components, as arches and vaults, columns and pillars, walls and panels, as well as global behaviour, and some particular aspects like bond, or Non-destructive Test applications and durability problems.

The main scope was to systematize results related to experimental works concerning studies on the main categories available in literature. Therefore, consistently with the current progress on these topics, some sections were fully developed (e.g. the activity layout "Experimental Work" and categories such as "Arch/Vault", "Column/Pillar", "Wall/Panel" and "Bond"), whereas, concerning other activities and categories, the possibility to insert generic information and descriptions and to add links and attachments was included (Fig. 3.2 on the following page).

The Data Base Management System (DBMS) allows to define some elements (Materials, Publications and Activity Layout) independently from their utilization in a specific project and, moreover, they can be picked up or copied entirely to be used for different projects, also among different users, being provided some restrictions on editing and deleting other user's elements.

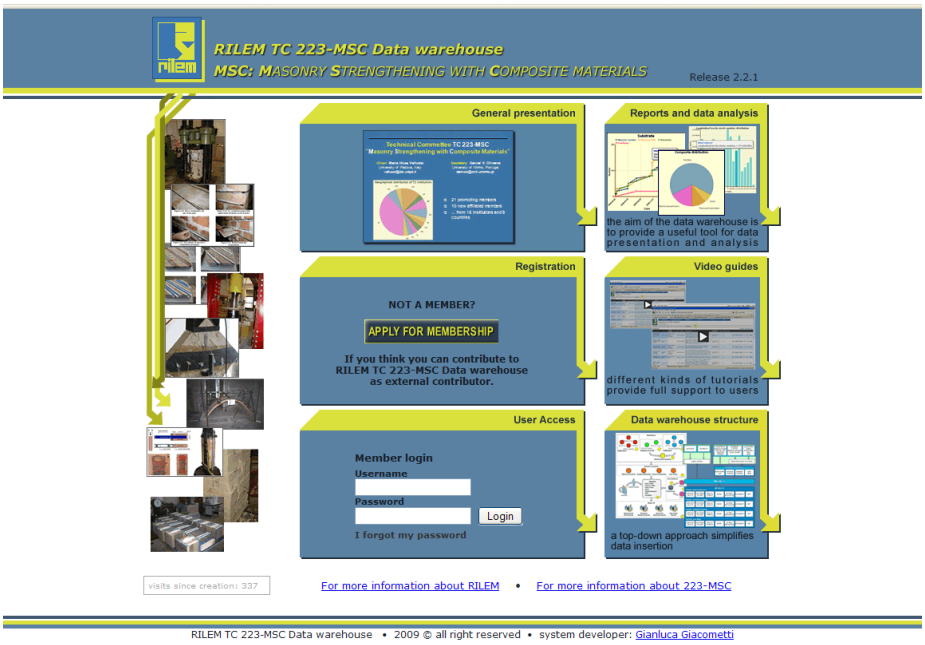

Figure 3.1: Access page of the DBMS for external contributors

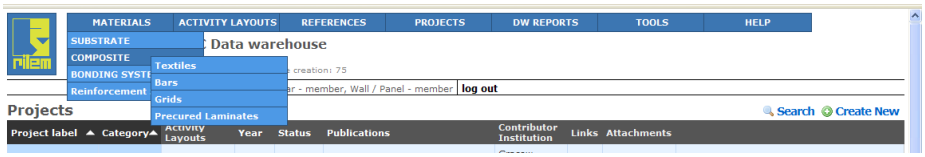

Figure 3.2: Menu bar on the upper side of the screen

The DBMS allows to create a pdf-format summary of inserted data for any single Material and an entire Project. Moreover, it is possible to insert Definitions, to view charts (Fig. 3.3 on the next page) based on the inserted data and to share topics for discussion. Finally a Frequently Asked Questions (FAQ) section is available in the HELP section.

Basically, the system that allows to interactively manipulate data is based on the nesting tables concept, which permits a quicker work and a higher control on the process (Fig. 3.4 on the facing page)

3.2 Structure of the Data-Warehouse

The Data-Warehouse, whose structure is shown in Figure 3.6 on page 31 and whose internal relationship are shown in Figure 3.6 on page 31, is basically divided into five main sections: Materials, Activity Layouts, References, Projects and Results (Fig. 3.5 on page 30).

materials they are divided into three main groups of tables: Substrate, Bonding System and Composite; each of the former group is composed by more tables that contain all the relevant data related to the basic materials belonging to the appropriate group, such as bars, textiles, grids for Composite.

activity layouts they are divided into four main kinds: Experimental Work, Analytical Modeling, Numerical Modeling and Case Study, and were designed in order to connect materials' data with specific details concerning each experience.

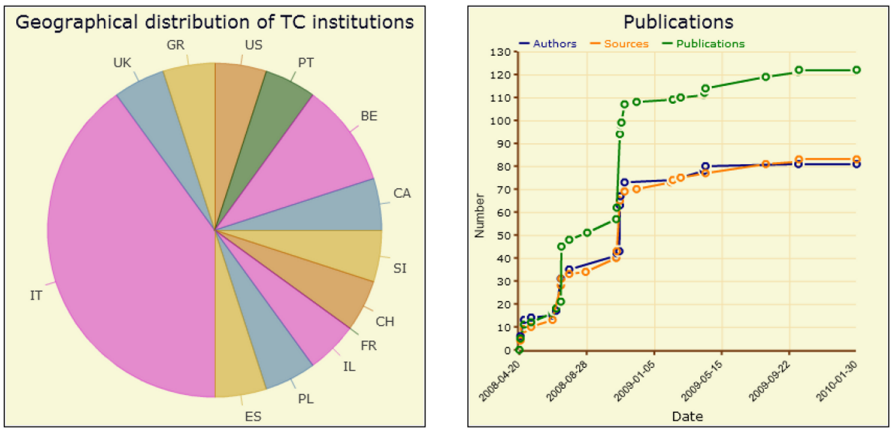

Figure 3.3: Examples of data charts

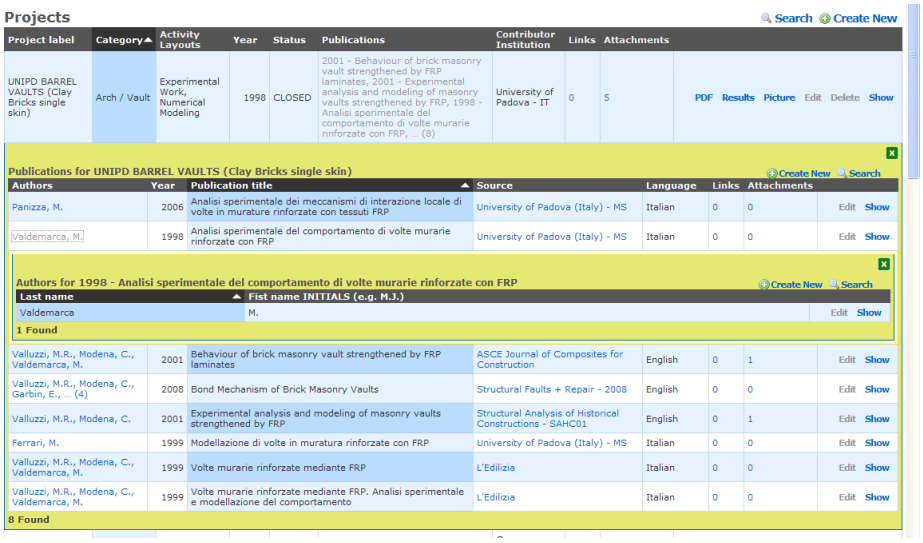

Figure 3.4: Example of nested tables

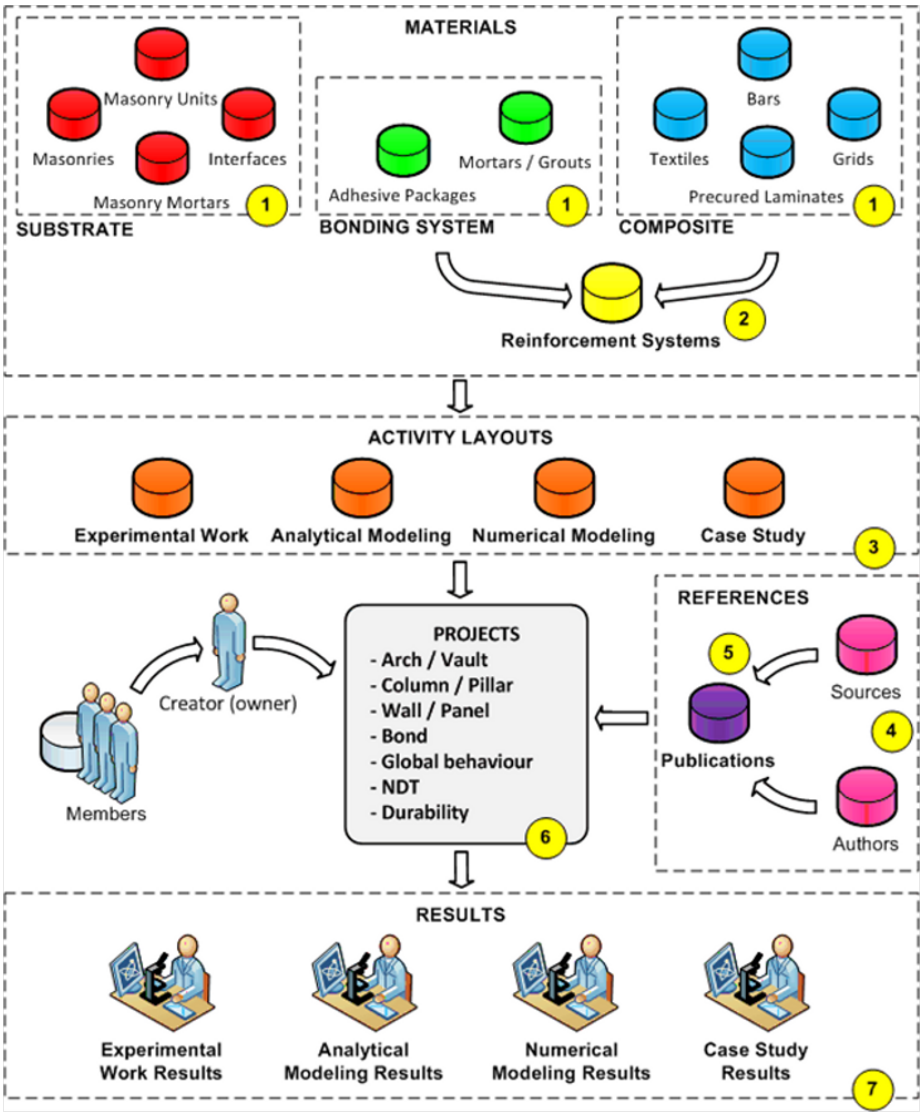

Figure 3.5: Structure of the Data-Warehouse

references this group contains three tables, one for publications and the others dedicated to collect authors and sources.

projects it is the main table, designed to gather previously defined Activity Layouts and References, and to define specific groups of Results. Each Project belongs to a specific Category, namely "Arches/Vaults", "Bond", "Columns/Pillars", "Walls/Panels", "Global behaviour", "NDT" and "Durability".

results this table collects data directly connected to Projects, and its records cannot be defined without a corresponding record on Projects. The record structure depends on the project Category and on the related Activity Layouts.

3.3 Current state of the Data-Warehouse

Since the system has been released, after the debugging period, up to present, ten international Institutions have contributed with their works (Fig. 3.8 on page 33), and thirty six projects have currently been inserted, mainly belonging to the following categories

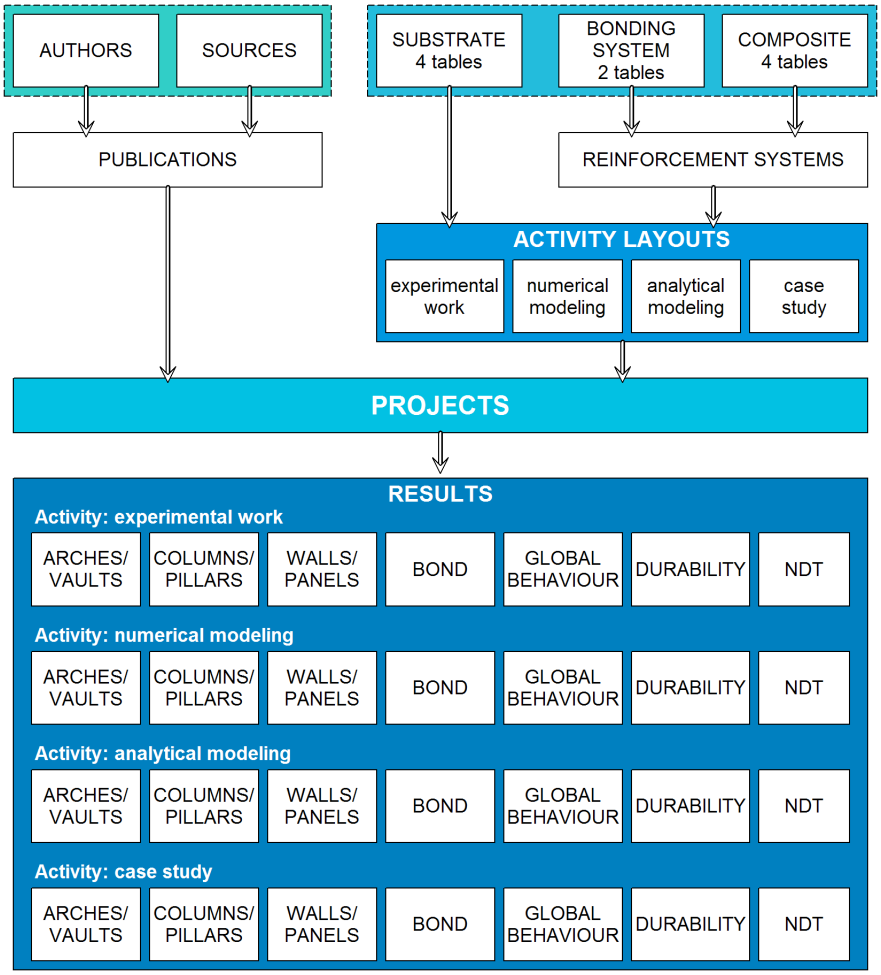

Figure 3.6: Structure of data tables

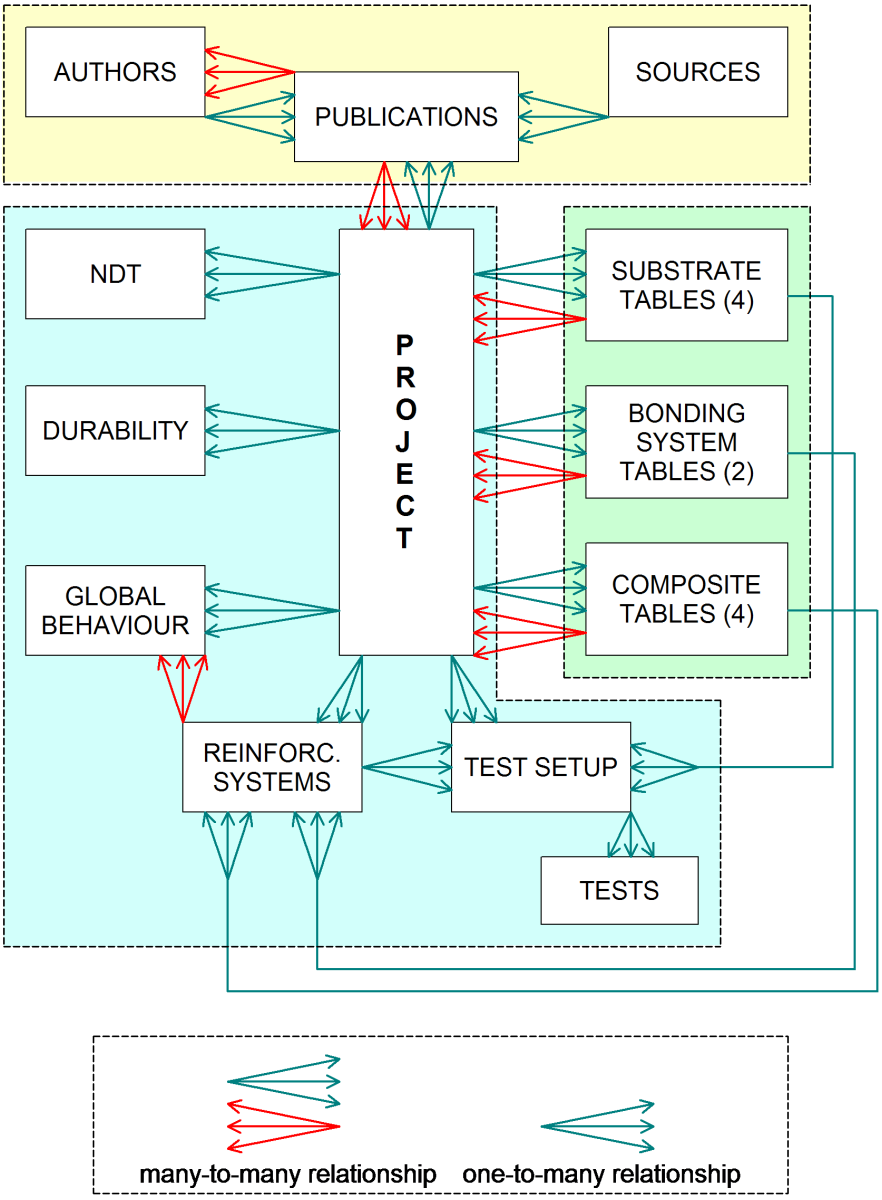

Figure 3.7: Relationships among tables

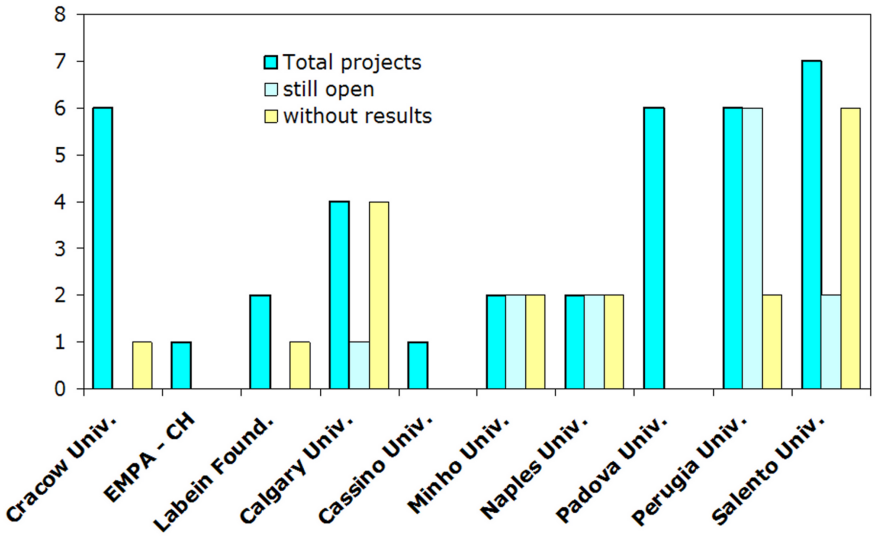

Figure 3.8: Presently contributing institutions

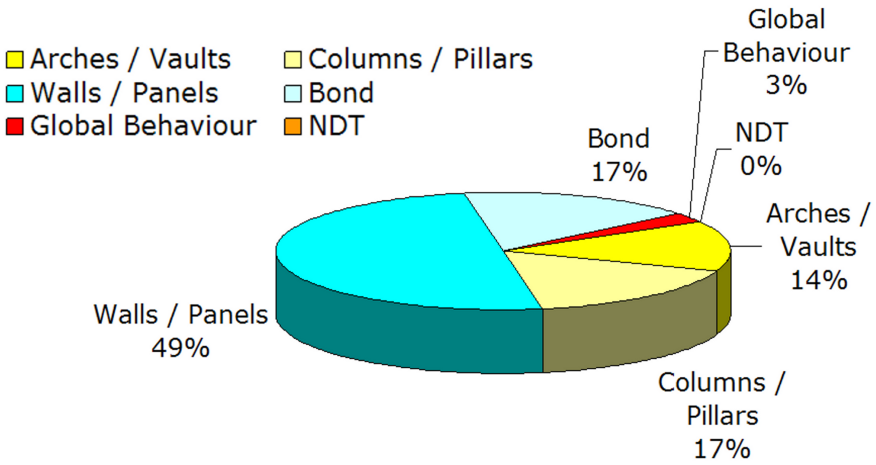

Figure 3.9: Collected projects

(Fig. 3.9): walls, arches/vaults, bond and columns. Around 66% of these projects have been denoted as "closed", which means that data insertion is completed, while the remaining are still in progress (Fig. 3.10 on the following page).

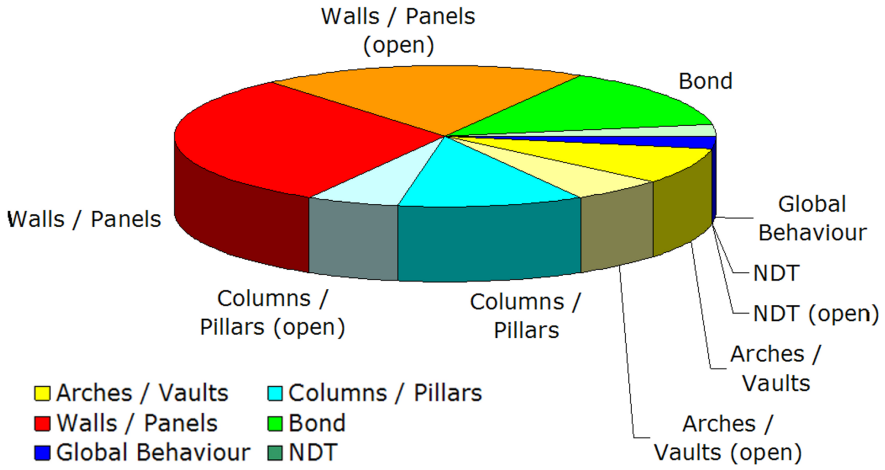

Figure 3.10: Current state of the inserted projects

Chapter 4

Interface behaviour in the case of normal actions

This chapter presents an experimental campaign focused on testing solid clay bricks, with externally applied FRP reinforcements. The adopted procedure, whose preliminary results have been reported in Panizza *et al.* (2009), consists in performing three types of mechanical test on the same clay element: more precisely, a three-points bending on the intact brick, a compressive test or a splitting tensile test on one of the two portion produced by the flexural failure, and two pull-off tests on the other clay portion, after the application of a layer of FRP textiles.

Pull-off tests, although quite common adopted for practical purposes (see ASTM C1583 2004, UNI-EN 1015-12 2002), are scarcely documented in literature; some trials were reported by Castori (2006), who tested solid concrete bricks, and by Basilio (2007), which performed some tests on masonry prisms, hence including a portion of mortar joint into the checked areas.

Two types of solid clay bricks have been used: extruded bricks and facing ones; four sets of extruded elements, three of which coming from the same manufacturer, and three sets of facing ones, two of which produced by the same factory, were used; carbon fibres (CFRP) and glass fibres (GFRP) have been applied by means of an epoxy matrix as reinforcement.

Therefore, three values of mechanical properties connected to the same masonry unit were obtained. On the basis of the first results, the possible relations between the pull-off strength and each of the other parameters (flexural, compressive and splitting tensile strength), were investigated, taking into account the variation of the clay substrate, the type of fibres (carbon or glass) and the presence, or not, of a layer of primer.

Moreover, the possible correlations among the average properties (flexural, compressive and splitting tensile strength) of the bricks tested during the present campaign and during previous experimental activities performed at the University of Padova, were investigated. The experimental matrix is reported in Table 4.1 on the next page.

4.1 Description of the experimental tests

4.1.1 Basic materials

Seven sets of solid clay bricks were used, namely four different sets of extruded bricks, three produced by Stabila Group and one by Solava SpA, and three sets of facing ones, two provided by Sant'Anselmo Furnace and one coming from San Marco Group (Tab. 4.2 on the following page).

Table 4.1: Combination of the experimental tests

Series	Brick type	Flexural tests	Compressive tests	Splitting tests	Pull-off tests
S1	extruded	⋆	⋆		CFRP w/o primer
		⋆	⋆		CFRP with primer
		⋆	⋆		GFRP with primer
S2	facing	⋆	⋆		CFRP with primer
		⋆	⋆		GFRP with primer
S3	extruded	⋆	⋆		CFRP with primer
		⋆	⋆		GFRP with primer
		⋆		⋆	CFRP with primer
S4	facing	⋆	⋆		CFRP with primer
		⋆		⋆	CFRP with primer
S5	extruded	⋆	⋆		CFRP with primer
		⋆		⋆	CFRP with primer
S6	facing	⋆	⋆		CFRP with primer
		⋆		⋆	CFRP with primer
S7	facing	⋆	⋆		CFRP with primer
					No fibres, with primer
		⋆		⋆	GFRP with primer
					No fibres, with primer

The main difference between these two types of elements consists in the manufacturing process, being the facing bricks moulded and sanded on the surface, as they get applied without any plaster, and the other ones extruded (Fig. 4.1 on the next page); on the other hand, extruded bricks are generally more compact and stronger.

The MBrace®Wet lay-up System was applied, as reinforcement, on the surfaces of one of the two pieces of brick generated by the flexural failure, in order to perform pull-off tests: high strength carbon fibres (CFRP) and alkali-resistant glass fibres (GFRP). The main properties of the reinforcement system, obtained from producers datasheets, are reported in Table 4.3 on the facing page.

Table 4.2: Solid clay bricks properties

Set code	Product name	Manufacturer	Type	Nom. dimensions
S1, S3, S5	11010R	Atesina Furnace (VR-IT)	extruded	240x115x60 mm
S2, S7	A001GL	Sant'Anselmo Furnace (VR-IT)	facing	250x120x55 mm
S4	"Vivo", rosa vivo	San Marco Group (VE-IT)	facing	250x120x55 mm
S6	A-005B	Solava SpA (AR-IT)	extruded	240x115x55 mm

4.1.2 Flexural tensile tests

According to UNI 8942/3 code, the flexural tests were performed adopting a three-point load scheme, by means of an apposite device. The distance between the support, l_s, was of 200 mm, fixed for all the samples. The flexural strength, f_f, was evaluated as conventional, assuming along the central cross section of the brick a triangular distribution for both the compressive (at the upper side) and the tensile stresses, as given in Equation (4.1), where

Table 4.3: Reinforcement components properties

Adhesive MBrace®Saturant		
Characteristic compressive strength	>80	N/mm^2
Characteristic direct tensile strength	>50	N/mm^2
Maximum tensile strain	2.5	%
Tensile elastic modulus	>3000	N/mm^2
High-strength Carbon MBrace®C1-30		
Equivalent thickness	0.165	mm
Characteristic direct tensile strength	3430	N/mm^2
Maximum tensile strain	1.5	%
Tensile elastic modulus	230000	N/mm^2
Alkali-resistant Glass MBrace®G60-AR		
Equivalent thickness	0.230	mm
Characteristic direct tensile strength	1700	N/mm^2
Maximum tensile strain	2.8	%
Tensile elastic modulus	65000	N/mm^2

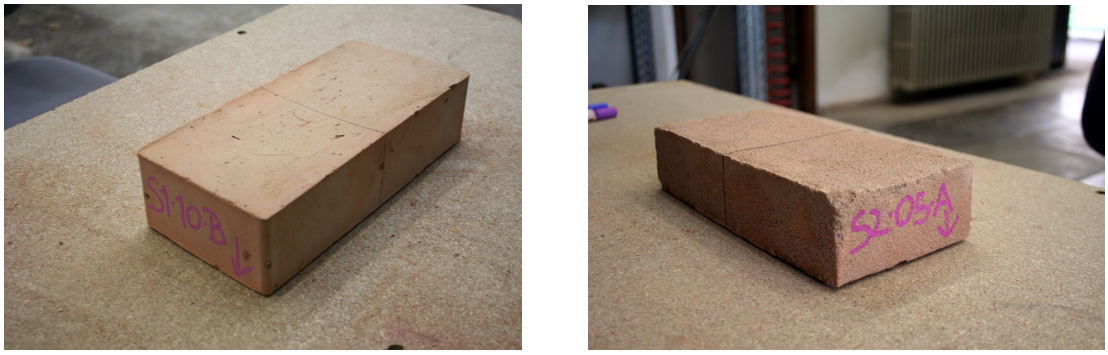

(a) Extruded brick **(b)** Facing brick

Figure 4.1: Types of solid clay brick used during the experimental campaign

Table 4.4: Results of flexural tests

Series	f_f N/mm^2	Stand. dev. N/mm^2	C. of V. %
S1	4.67	0.75	16.1
S2	5.29	0.61	11.4
S3	2.97	0.66	22.3
S4	5.42	0.47	8.6
S5	3.89	1.01	26.0
S6	5.64	0.27	4.8
S7	4.75	0.57	12.0

(a) Sample ready for testing **(b)** Typical brick failure

Figure 4.2: Performing of flexural tests

P_u denotes the failure load, b and h are the width and height of the specimen, respectively. The failure generally occurred near the central cross section, which is the most stressed, even if some irregular failure were observed, especially in the case of extruded bricks that revealed a slightly brittle behaviour (Fig. 4.2). Results, in terms of mean strength for each set of samples, are given in Table 4.4 and shown in Figure 4.3 on the next page. Facing bricks, compared to the extruded ones, generally presented a lower dispersion of the measured values, being the strength comparable to the others. The S3 set (extruded bricks), which showed the worst performances, presented a cooking not perfect to the core.

$$f_f = \frac{3P_u l_s}{2bh^2} \tag{4.1}$$

4.1.3 Compressive tests

Compressive tests were performed, by means of a hydraulic press commonly used to measure the strength of concrete specimens, on one of the two pieces of brick produced by the flexural failure of the intact element, being the other destined to pull-off tests; each sample was capped by a thin mortar layer in order to avoid uneven load distribution. According to EN 772-1 code, the compressive strength, f_c, was evaluated as conventional, assuming an uniform stress profile along each horizontal cross section, as shown in Equation (4.2), where P_u denotes the failure load, l and b are the length and the width of the specimen, respectively. All the tests presented a regular cubic failure (Fig. 4.4 on page 40). Results, in terms of mean strength for each set of samples, are given in Table 4.5 on the next page

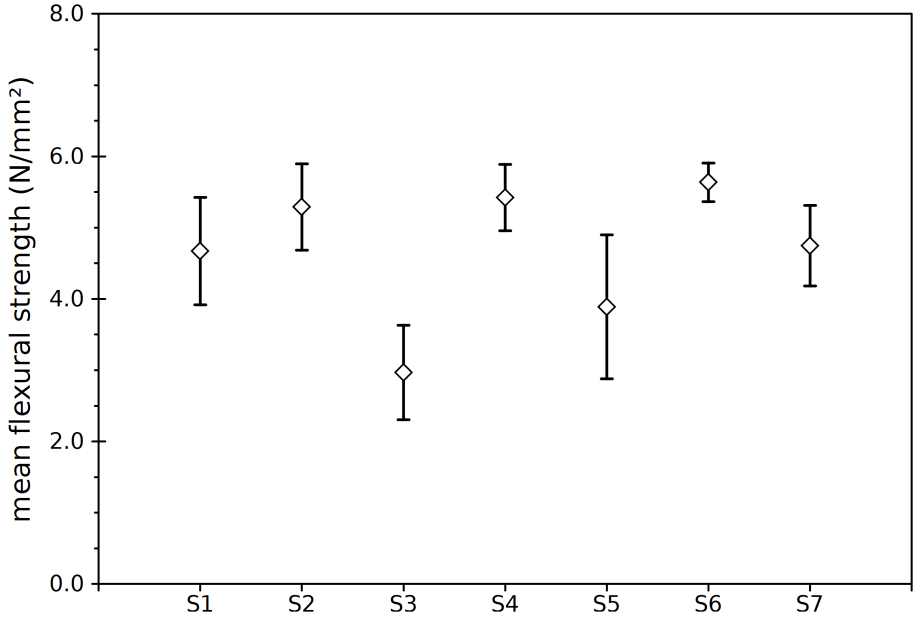

Figure 4.3: Results of flexural tests (mean values)

Table 4.5: Results of compressive tests

Series	f_c N/mm^2	Stand. dev. N/mm^2	C. of V. %
S1	35.36	3.19	9.0
S2	21.09	2.34	11.1
S3	33.29	2.39	7.2
S4	22.06	1.42	6.4
S5	38.39	3.18	8.3
S6	60.27	2.56	4.3
S7	16.51	1.22	7.4

and shown in Figure 4.5 on the following page. As expected, extruded bricks were stronger, their strengths covering a range from 30 to 60 N/mm^2, while facing bricks' values mostly varied from 15 to 25 N/mm^2. Two specimens of the S6 set, labelled as S1-01 and S1-02, were tested before a complete drying of the moisture absorbed during the application of the mortar caps, therefore those values were excluded by the subsequent calculations.

$$f_c = \frac{P_u}{bl} \tag{4.2}$$

4.1.4 Splitting tensile tests

Excluded S1 and S2 sets, some splitting tests were performed, according to UNI 8942/3 code, on one of the two pieces of brick (in place of compressive test) produced by the flexural failure of the intact element, being the other destined to pull-off tests; surfaces of each sample were accurately levelled in order to improve the contact with the test machine. Splitting tensile strength, f_s, was evaluated as conventional, as shown in Equation (4.3), where P_u denotes the failure load, b and h are the width and the height of the specimen, respectively. All the tests presented a regular failure localized on the loaded cross section

(a) Sample mounted on the press

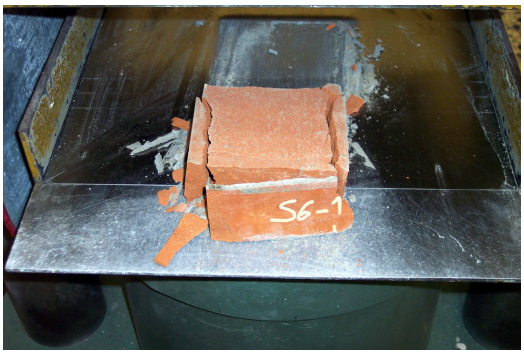

(b) Typical brick failure

Figure 4.4: Performing of compressive tests

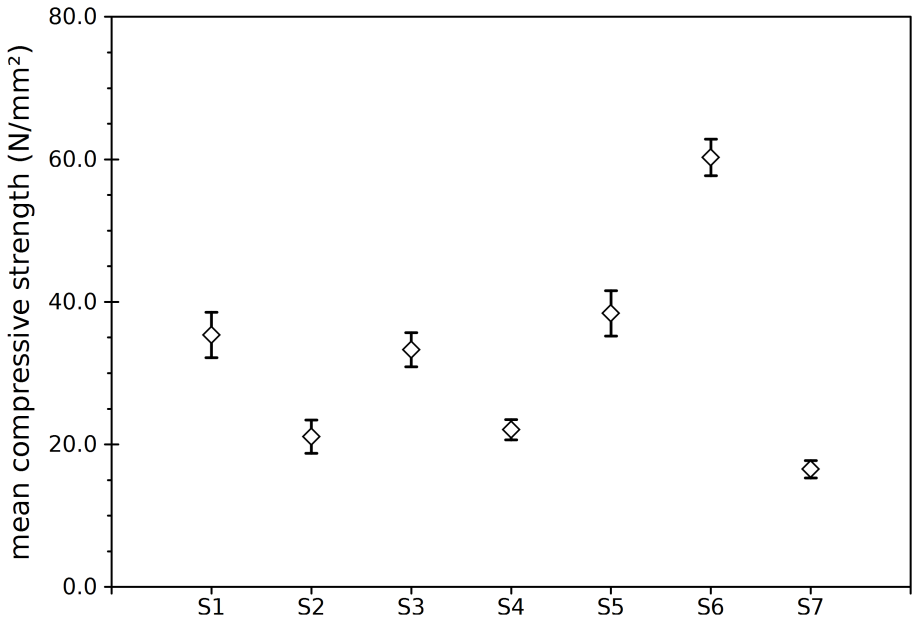

Figure 4.5: Results of compressive tests (mean values)

Table 4.6: Results of splitting tensile tests

Series	f_s N/mm^2	Stand. dev. N/mm^2	C. of V. %
S3	1.34	0.35	26.3
S4	4.02	0.23	5.8
S5	3.51	0.54	15.3
S6	5.89	0.38	6.5
S7	3.39	0.16	4.7

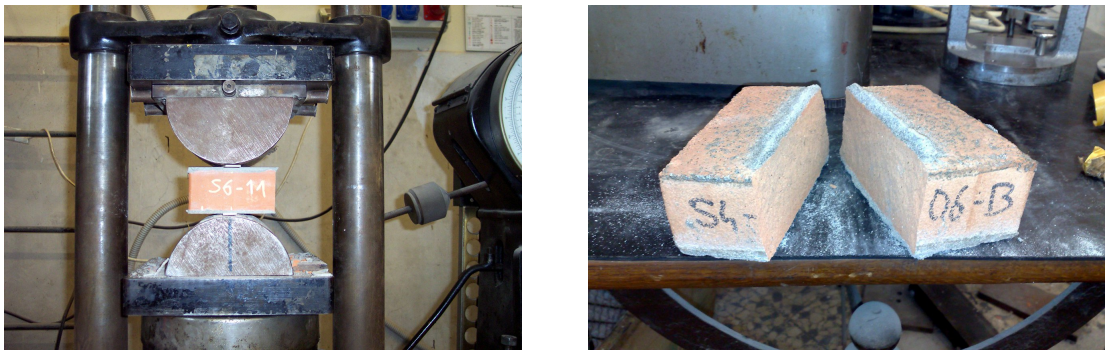

(a) Specimen on the test machine **(b)** Failure of a brick

Figure 4.6: Performing of splitting tensile tests

(Fig. 4.6), except two samples belonging to the S3 set, which values were excluded by the subsequent calculations; in these cases, the unexpected rupture was probably due to an imperfect regularization of the loaded surfaces. Results, in terms of mean strength for each set of samples, are given in Table 4.6 and shown in Figure 4.7 on the next page. Strength values were comparable for both extruded an facing bricks, excluding S3 set, which revealed an imperfect cooking, and S6 set, whose compressive strength (more than 60 N/mm^2) was unusual and similar to high-strength concrete.

$$f_s = \frac{2P_u}{\pi b h} \tag{4.3}$$

4.1.5 Pull-off tests

Pull-off tests were performed on the two wider surfaces, previously covered by composite reinforcement, of the second clay piece originated by the flexural failure of each intact brick, being the other portion destined to either a compressive or a splitting tensile test. This type of test, which is commonly used to verify the bond strength of overlay or repair materials applied on a different substrate (see UNI-EN 1015-12 2002, ASTM C1583 2004), consists in cutting a circular area on the surface, deep into the substrate, and pulling off that area, normally to the surface, after the glueing of an apposite aluminum plate able to accommodate a linking bolt. They were performed by means of a special portable tester, Matest E142, designed to work up to 16 kN (Fig. 4.8 on page 44).

The pull-off tensile strength, $f_{p\text{-}o}$, was evaluated as the average stress on the area, according to ASTM C1583 (2004), as given in Equation (4.4), where P_u denotes the failure load and r is the radius of the round cut. Two pull-off tests for each clay piece have been carried

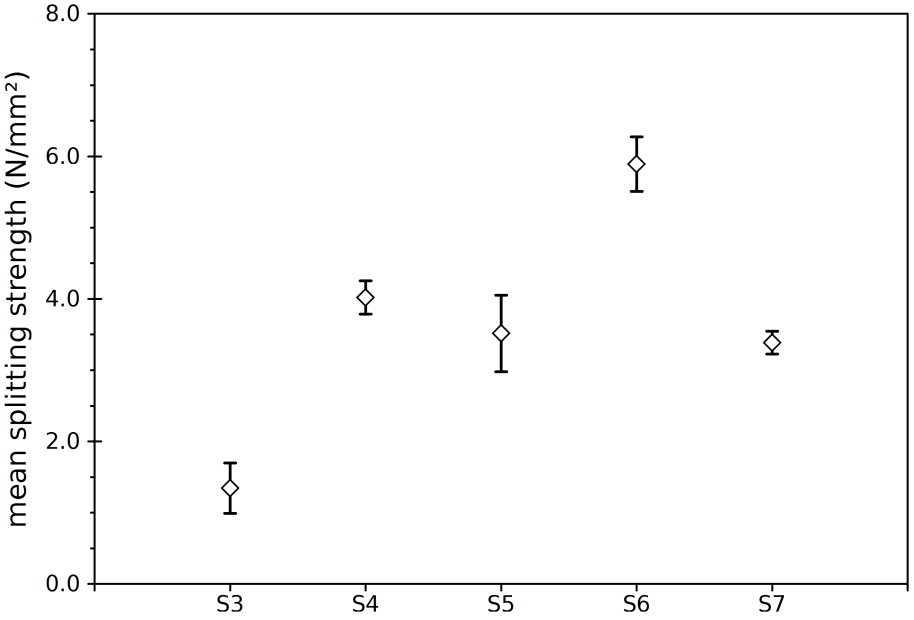

Figure 4.7: Results of splitting tensile tests (mean values)

out, and the pertinent failures have been labelled as type A (failure in substrate), type B (bond failure at the support/reinforcement interface) and type C (failure within the reinforcement) following ASTM C1583 (2004); failure type D (bond failure at reinforcement/epoxy interface) occurred only once, due to an incorrect application of the metallic plate.

The results of 166 pull-off tests are available: 14 concerning specimens reinforced with CFRP without applying any primer, 113 normally reinforced with CFRP, 25 with GFRP and, finally, only primer and adhesive were applied on 14 specimens, without inserting fibres. The common failure (Tab. 4.7 on page 45 and Fig. 4.10 on page 44), pertinent to 155 tests, was localized into the clay support (type "A"), although in some cases it occurred at the interface between substrate and adhesive (type "B") or within the reinforcement (type "C"): the latter event should be ascribed to an incorrect application, as it mainly affected samples reinforced with GFRP, while CFRP always broke as expected, except some samples without primer.

Results, in terms of mean strength for each set of samples, are given in Table 4.8 on page 45 and shown in Figure 4.11 on page 45. Extruded bricks showed better performances, in accordance with their compressive strength. It has to be underlined that only type "A" failures were involved in the calculations, since they refer to a property of the clay support, as well as the flexural, splitting and compressive strength; for this reason, no significant difference other than the failure mode was found related to the type of applied reinforcements.

A summary of all the tests results is reported in Table 4.9

$$f_{\text{p-o}} = \frac{P_{\text{u}}}{\pi r^2} \tag{4.4}$$

Table 4.9: Results of the combined tests on clay bricks

Spec.	ϱ	f_{f}	f_{c}	f_{s}	Fibres	Prim.	Side 1		Side 2	
							Fail.	$f_{\text{p-o}}$	Fail.	$f_{\text{p-o}}$
	kg/m^3	N/mm^2	N/mm^2	N/mm^2				N/mm^2		N/mm^2
S1-01	1690	3.97	34.58		CFRP	Y	A	1.76	n.a.	n.a.

Table 4.9 – from last page

	ϱ	f_f	f_c	f_s	Fibres	Prim.	Fail.(1)	$f_{p\text{-}o}$	Fail.(2)	$f_{p\text{-}o}$
S1-02	1755	3.93	42.11		CFRP	Y	A	3.72	A	3.49
S1-03	1686	4.63	33.46		CFRP	Y	A	3.04	A	4.52
S1-04	1710	6.18	36.47		CFRP	Y	A	2.90	A	2.90
S1-05	1677	5.05	38.16		CFRP	Y	A	2.07	A	2.40
S1-06	1697	4.47	34.72		CFRP	Y	A	2.88	A	2.89
S1-07	1763	5.30	33.30		GFRP	Y	C	1.85	A	3.68
S1-08	1697	5.03	33.53		GFRP	Y	C	0.61	A	3.47
S1-09	1722	4.08	40.78		GFRP	Y	C	1.29	A	3.32
S1-10	1669	3.67	31.29		GFRP	Y	n.a.	n.a.	n.a.	n.a.
S1-11	1719	4.29	32.87		CFRP	N	C	1.49	A	2.85
S1-12	1664	4.35	33.97		CFRP	N	A	3.78	A	3.10
S1-13	1673	5.77	34.40		CFRP	N	B	2.67	A	3.79
S2-01	1478	5.07	21.34		CFRP	Y	A	1.68	A	1.89
S2-02	1463	6.04	23.32		CFRP	Y	A	1.36	A	2.12
S2-03	1471	5.01	21.29		CFRP	Y	A	1.66	A	1.96
S2-04	1477	5.44	20.77		CFRP	Y	A	1.66	A	2.27
S2-05	1483	5.69	15.87		CFRP	Y	A	1.56	A	1.99
S2-06	1453	4.39	21.79		CFRP	Y	A	1.71	A	1.70
S2-07	1471	4.68	23.37		GFRP	Y	B	1.59	A	1.96
S2-08	1471	6.01	20.96		GFRP	Y	A	1.58	A	1.94
S3-01	1849	1.98	31.11		GFRP	Y	B	1.83	A	3.13
S3-02	1807	3.60	31.40		GFRP	Y	A	2.60	A	2.86
S3-03	1837	2.91	33.28		GFRP	Y	B	1.56	A	2.76
S3-04	1788	4.40	33.15		GFRP	Y	C	1.30	A	2.67
S3-05	1831	3.30		2.44	CFRP	Y	A	3.54	A	3.41
S3-06	1770	3.02		2.85	CFRP	Y	A	2.37	A	2.72
S3-07	1780	2.66		1.24	CFRP	Y	A	2.44	A	2.46
S3-08	1777	2.76		1.30	CFRP	Y	A	3.01	A	2.39
S3-09	1771	2.46		1.00	CFRP	Y	A	2.46	A	2.62
S3-10	1799	2.52		1.84	CFRP	Y	A	2.87	A	2.94
S3-11	1795	2.42	32.98		CFRP	N	B	2.90	A	2.55
S3-12	1788	3.58	37.79		CFRP	N	A	2.82	A	2.36
S4-01	1510	5.79		3.99	CFRP	Y	A	1.85	A	2.31
S4-02	1502	4.72		3.71	CFRP	Y	A	1.30	A	1.40
S4-03	1495	5.24		3.93	CFRP	Y	A	1.33	A	1.44
S4-04	1503	4.99		4.41	CFRP	Y	A	1.46	A	1.76
S4-05	1519	5.06		4.14	CFRP	Y	A	1.44	A	1.78
S4-06	1523	4.77		3.93	CFRP	Y	n.a.	n.a.	A	1.36
S4-07	1548	5.54	23.46		CFRP	Y	A	1.77	A	1.80
S4-08	1534	6.06	23.25		CFRP	Y	A	1.65	A	1.82
S4-09	1526	5.50	22.08		CFRP	Y	A	1.48	A	1.64
S4-10	1513	5.51	19.93		CFRP	Y	A	1.24	A	1.44
S4-11	1543	6.00	20.80		CFRP	N	A	1.17	A	1.54
S4-12	1543	5.88	22.84		CFRP	N	A	2.22	A	1.88
S5-01	1772	3.02	36.92		CFRP	Y	A	1.88	A	2.57
S5-02	1798	4.49	34.75		CFRP	Y	A	2.77	A	2.74
S5-03	1783	3.15	35.61		CFRP	Y	A	3.22	A	2.73
S5-04	1764	5.27	40.24		CFRP	Y	A	2.68	A	3.24
S5-05	1791	3.11	43.11		CFRP	Y	A	3.15	A	3.39
S5-06	1807	4.94	39.71		CFRP	Y	A	3.55	A	3.09
S5-07	1776	2.74		3.39	CFRP	Y	A	2.96	A	3.22
S5-08	1774	5.52		3.56	CFRP	Y	A	3.20	A	3.46
S5-09	1757	4.26		2.58	CFRP	Y	A	3.22	A	2.95
S5-10	1814	3.08		3.64	CFRP	Y	A	3.89	A	2.68
S5-11	1765	4.24		4.22	CFRP	Y	A	3.62	A	2.84
S5-12	1761	2.86		3.70	CFRP	Y	A	3.37	A	2.16
S6-01	1972	5.76	53.19		CFRP	Y	A	4.11	A	3.55
S6-02	1970	5.06	51.78		CFRP	Y	A	4.07	A	3.25
S6-03	1953	5.76	59.69		CFRP	Y	A	3.81	A	3.46
S6-04	1975	5.98	61.22		CFRP	Y	A	4.07	A	3.22
S6-05	1944	5.42	57.69		CFRP	Y	A	3.77	A	3.60
S6-06	1973	5.75	64.21		CFRP	Y	A	3.99	A	3.42
S6-07	1964	5.39	58.55		CFRP	Y	A	4.15	A	3.52
S6-08	1963	5.70		5.48	CFRP	Y	A	3.92	A	3.51
S6-09	1960	5.29		6.24	CFRP	Y	A	3.99	A	3.59
S6-10	1957	5.66		6.05	CFRP	Y	A	4.13	A	3.44
S6-11	1964	5.47		6.11	CFRP	Y	A	3.47	A	3.66
S6-12	1963	5.86		6.35	CFRP	Y	A	4.12	A	3.48
S6-13	1956	5.98		5.49	CFRP	Y	A	3.70	A	3.54
S6-14	1961	5.82		5.51	CFRP	Y	A	3.79	A	4.01
S7-01	1423	4.55	19.11		C(1)/No(2)	Y	A	1.59	A	1.41
S7-02	1419	4.78	15.24		C(1)/No(2)	Y	A	1.33	A	1.36
S7-03	1431	4.75	16.60		C(1)/No(2)	Y	A	1.48	A	1.29
S7-04	1427	5.32	16.20		C(1)/No(2)	Y	A	1.84	A	1.30
S7-05	1409	4.71	16.04		C(1)/No(2)	Y	D	1.31	A	1.38
S7-06	1418	4.07	16.13		C(1)/No(2)	Y	A	1.35	A	1.81
S7-07	1412	4.65	16.28		C(1)/No(2)	Y	A	1.38	A	1.74
S7-08	1431	5.42		3.52	G(1)/No(2)	Y	A	1.47	A	1.24
S7-09	1413	5.08		3.24	G(1)/No(2)	Y	A	1.33	A	1.72
S7-10	1430	4.85		3.49	G(1)/No(2)	Y	A	1.65	A	1.80
S7-11	1422	3.17		3.11	G(1)/No(2)	Y	A	1.57	A	1.11
S7-12	1419	5.06		3.45	G(1)/No(2)	Y	A	1.81	A	1.64
S7-13	1418	5.06		3.55	G(1)/No(2)	Y	A	1.55	A	1.50
S7-14	1417	4.98		3.36	G(1)/No(2)	Y	A	1.81	A	1.09

(a) Sample ready to be tested

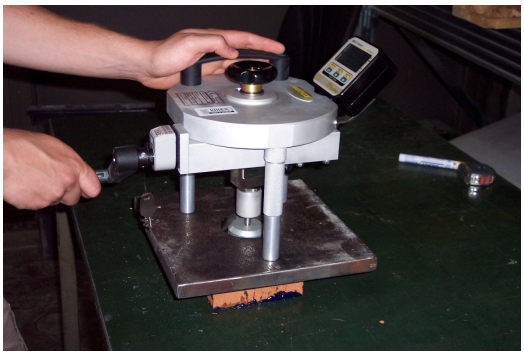

(b) Execution of a test

Figure 4.8: Performing of pull-off tests

(a) Failure in substrate (A)

(b) Bond failure at substrate and reinforcement interface (B)

(c) Failure within the reinforcement (C)

Figure 4.9: Observed failure of pull-off tests, labelled following ASTM C1583 (2004)

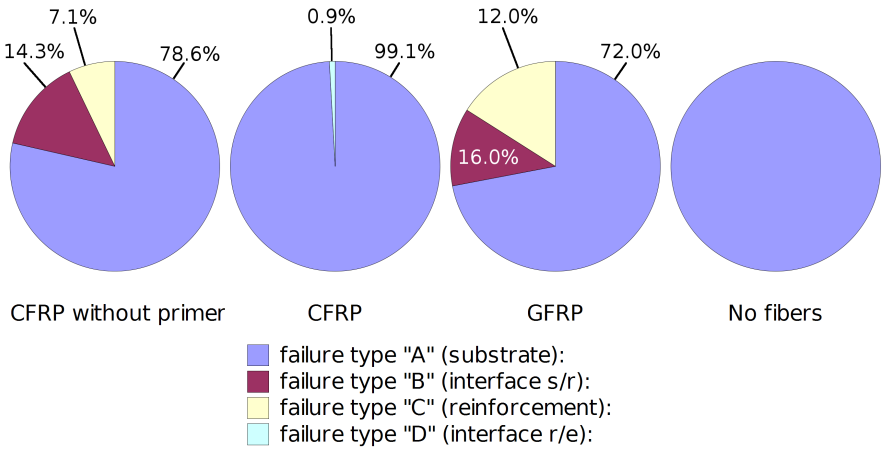

Figure 4.10: Occurrence of failure modes of pull-off tests

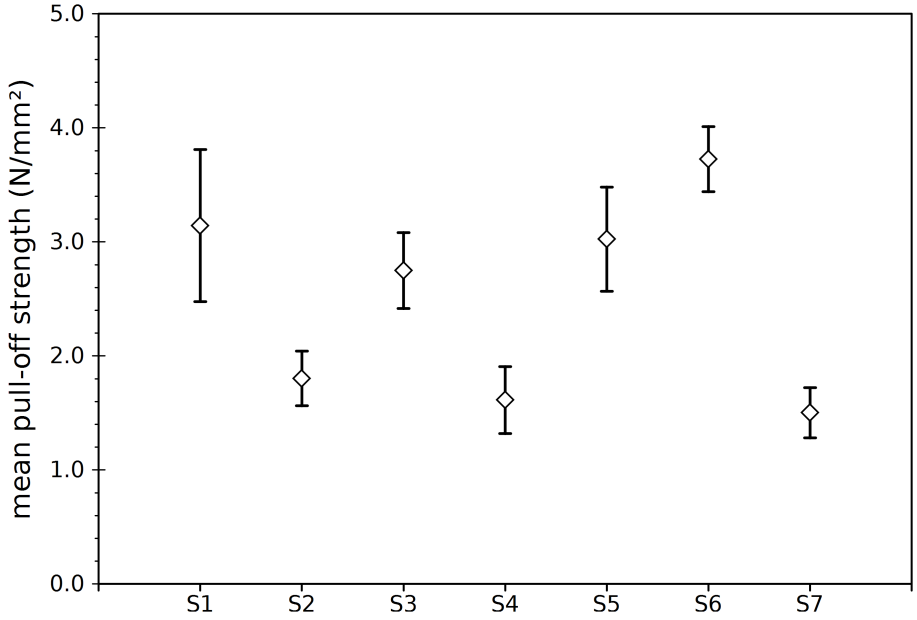

Figure 4.11: Results of pull-off tensile tests (mean values)

Table 4.7: Observed failures of the pull-off tests

	CFRP without primer		CFRP with primer		GFRP with primer		No fibres with primer	
available tests:	14		113		25		14	
"A" (substrate):	11	(78.6%)	112	(99.1%)	18	(72.0%)	14	(100.0%)
"B" (interface s/r):	2	(14.3%)	–		3	(12.0%)	–	
"C" (reinforcement):	1	(7.1%)	–		4	(16.0%)	–	
"D" (interface r/e):	–		1	(0.9%)	–		–	

Table 4.8: Results of pull-off tensile tests

Series	$f_{\text{p-o}}$ N/mm^2	Stand. dev. N/mm^2	C. of V. %
S1	3.14	0.67	21.2%
S2	1.80	0.24	13.3%
S3	2.75	0.33	12.1%
S4	1.61	0.29	18.2%
S5	3.02	0.46	15.1%
S6	3.73	0.29	7.7%
S7	1.50	0.22	14.7%

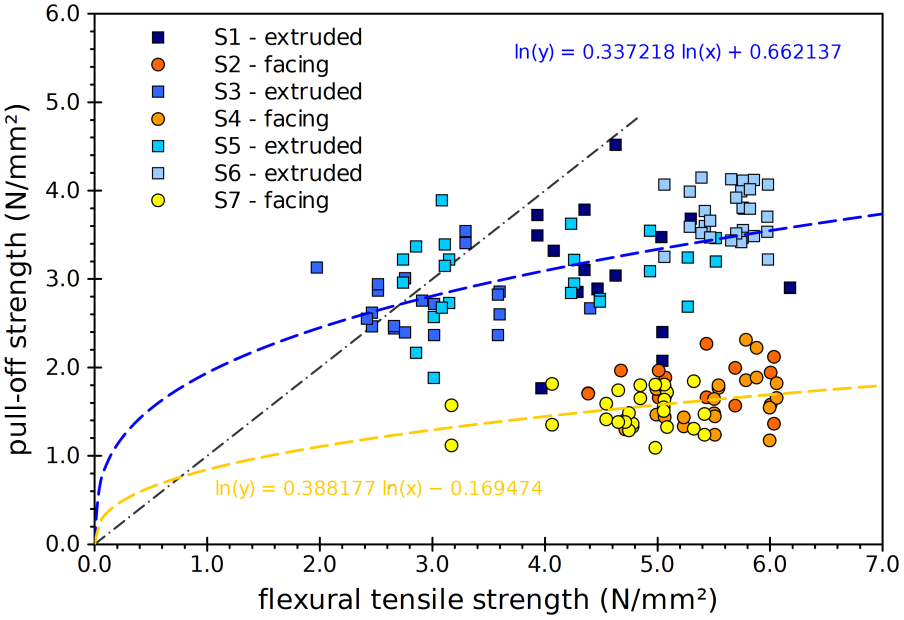

Figure 4.12: Pull-off plotted versus flexural strengths

4.2 Analysis of the results

4.2.1 Correlation between pull-off and flexural tensile strength

As previously highlighted, facing bricks showed good flexural performance, compared to extruded ones, despite their lower compressive strength; this fact could be imputed to their less brittle behaviour that permits a better stress distribution on the cross section, related to higher failure loads. On the other hand, the pull-off strength seems to be consistent with the compressive strength, since extruded bricks exhibited higher resistance. Plotting the pull-off versus the flexural tensile strengths, measured on the same clay element, extruded and facing bricks show similar trends, but higher values for the first ones (Fig. 4.12). These trends could be quite correctly described by a power-based regression, whose formulas are reported in Equation (4.5), where $f_{\text{p-o}}$ is the pull-off strength and f_{f} the flexural one.

$$f_{\text{p-o}} = 1.939 f_{\text{f}}^{0.337} \qquad \text{extruded bricks} \tag{4.5a}$$

$$f_{\text{p-o}} = 0.844 f_{\text{f}}^{0.388} \qquad \text{facing bricks} \tag{4.5b}$$

4.2.2 Correlation between pull-off and compressive strength

Pull-off strength seems to be consistent with the compressive one, since both the brick types show a similar trend. Plotting the pull-off versus the compressive strengths, measured on the same clay element, the behaviour of extruded and facing bricks could be depicted by the same curve (Fig. 4.13 on the next page), as the regression functions separately evaluated are just slightly different. These trends could be quite correctly described by a power-based regression, whose formulas are reported in Equation (4.6).

The next step was to calibrate two regression functions based on the shape provided by two codes, ACI 318-99 (2004) and DM 09-01-96 (1996), which correlate the splitting tensile strength, in the first case, and the direct tensile one, in the latter, to the compressive strength of concrete (cylindric in the first case, cubic in the other). Related formulas are reported in Eq. (4.7) and (4.8), respectively, where f_{s} and f_{t} denote splitting and direct

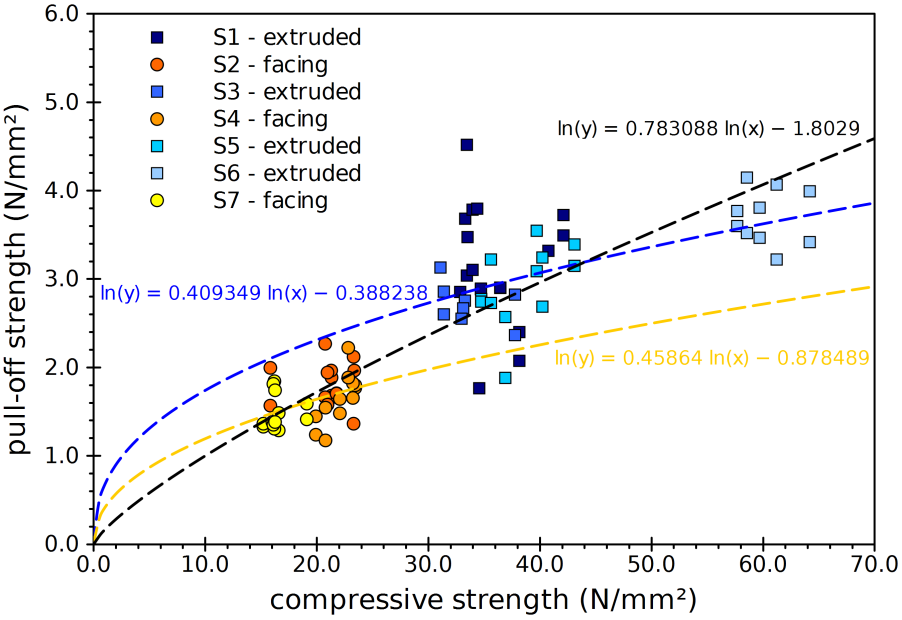

Figure 4.13: Pull-off plotted versus compressive strengths

tensile strength, R_{ck} and f'_c cubic and cylindric compressive strength; it has to be noted that the function provided by the ACI 318-99 (2004) is intended to be applied on values expressed in PSI and it will not work using SI units, therefore the correct coefficient is also reported in order to facilitate a comparison. Clearly, the pull-off tensile strength ($f_{p\text{-}o}$) and the cubic compressive one (f_c) where used in place of the parameters indicated by the codes, in order to preserve only the shape of the two functions. Each type of regression function was calibrate three times, first on data coming from extruded bricks, then on data related to facing ones and, finally, on all the joined data. Results (Fig. 4.14 on the following page, and Eq. 4.9 and 4.10 on page 49) show not great differences among these curves. Finally, Figure 4.15 on page 49 displays a comparison of the three regressions made on all the joined data (without distinguish among facing or extruded bricks).

$$f_{p\text{-}o} = 0.409 f_c^{0.678} \qquad \text{extruded bricks} \tag{4.6a}$$
$$f_{p\text{-}o} = 0.459 f_c^{0.415} \qquad \text{facing bricks} \tag{4.6b}$$
$$f_{p\text{-}o} = 0.165 f_c^{0.783} \qquad \text{all data} \tag{4.6c}$$

$$f_{ct} = 6.7\sqrt{f'_c} \qquad \text{ACI 318-99} \tag{4.7a}$$
$$f_{ct} = 0.56\sqrt{f'_c} \qquad \text{(SI units)} \tag{4.7b}$$

$$f_{ctm} = 0.27\sqrt[3]{R_{ck}^2} \qquad \text{DM 09-01-99} \tag{4.8}$$

$$f_{p\text{-}o} = 0.490\sqrt{f_c} \qquad \text{extruded} \tag{4.9a}$$
$$f_{p\text{-}o} = 0.371\sqrt{f_c} \qquad \text{facing} \tag{4.9b}$$
$$f_{p\text{-}o} = 0.456\sqrt{f_c} \qquad \text{all data} \tag{4.9c}$$

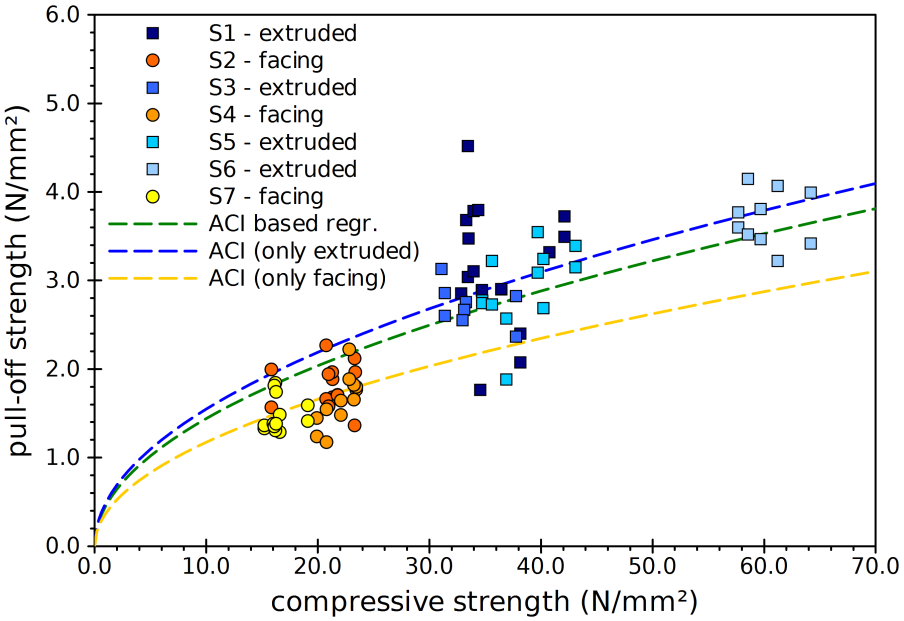

(a) ACI 318-99 (2004)

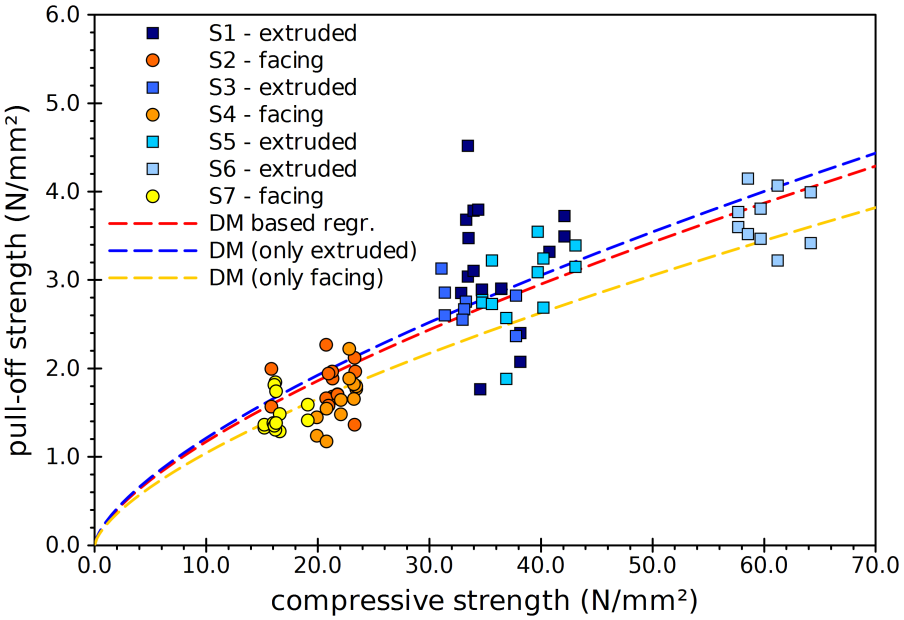

(b) DM 09-01-96 (1996)

Figure 4.14: Regressions based on code provisions

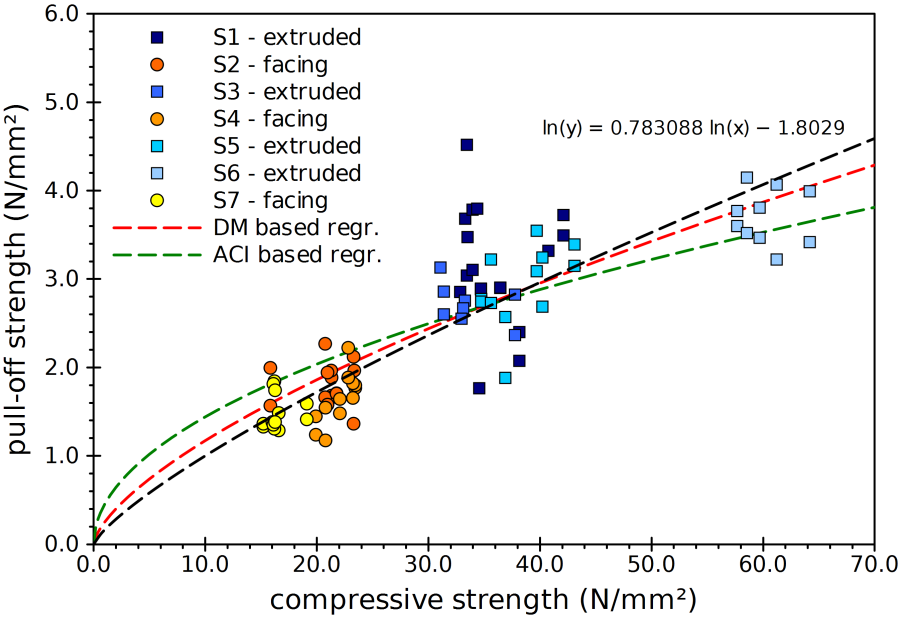

Figure 4.15: Comparison of regressions (all data)

$$f_{\text{p-o}} = 0.261 \sqrt[3]{f_{\text{c}}^2} \qquad \text{extruded} \tag{4.10a}$$

$$f_{\text{p-o}} = 0.371 \sqrt[3]{f_{\text{c}}^2} \qquad \text{facing} \tag{4.10b}$$

$$f_{\text{p-o}} = 0.253 \sqrt[3]{f_{\text{c}}^2} \qquad \text{all data} \tag{4.10c}$$

4.2.3 Correlation between pull-off and splitting tensile strength

As in the case of flexural tests, facing bricks showed good splitting performance, compared to the extruded ones, despite their lower compressive strength; again, this fact could be probably imputed to their less brittle behaviour that permits a better stress distribution on the cross section, related to higher failure loads. On the contrary, pull-off strength seems to be consistent with the compressive strength, since extruded bricks exhibited higher resistance. Extruded and facing bricks show similar trends, if pull-off versus splitting tensile strengths, measured on the same clay element, are plotted; but higher values for the first ones (Fig. 4.16 on the following page) were recorded. These trends could be quite correctly described by a power-based regression, whose formulas are reported in Equation (4.11), where $f_{\text{p-o}}$ is the pull-off strength and f_{s} the splitting one.

$$f_{\text{p-o}} = 2.441 f_{\text{s}}^{0.225} \qquad \text{extruded bricks} \tag{4.11a}$$

$$f_{\text{p-o}} = 0.881 f_{\text{s}}^{0.425} \qquad \text{facing bricks} \tag{4.11b}$$

4.2.4 Correlation between flexural tensile strength and compressive strength

In this case, the available range of values is not particularly wide, but the different behaviour of extruded and facing bricks can be noticed anyway: as previously observed, the latter elements exhibit better flexural performances in relation to their compressive

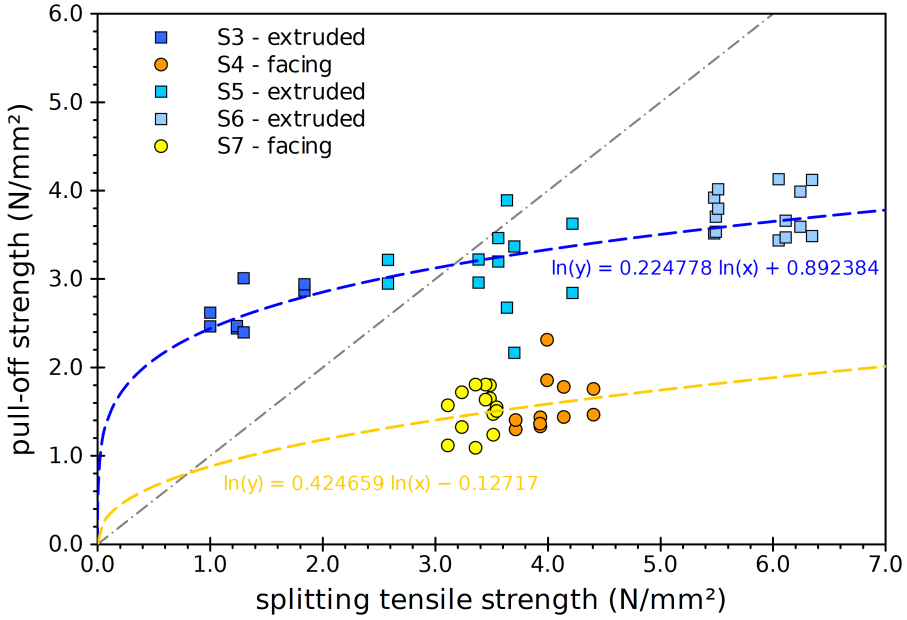

Figure 4.16: Pull-off strengths plotted versus splitting tensile strengths

strength. Therefore, the trend could be quite correctly described by two distinct power-based regression (Fig. 4.17 on the next page), whose formulas are reported in Equation (4.12), where f_f is the flexural tensile strength and f_c the compressive one.

$$f_f = 0.473 f_c^{0.602} \quad \text{extruded bricks} \tag{4.12a}$$
$$f_f = 1.647 f_c^{0.387} \quad \text{facing bricks} \tag{4.12b}$$

4.2.5 Correlation between flexural and splitting tensile strength

As both the parameters measure a tensile property of the material, the trend is almost proportional and no significant differences are noticeable between extruded and facing bricks. This trend could be quite correctly described by both a power-based regression or a linear one (Fig. 4.18 on page 52), whose formulas are reported in Equation (4.13) and Equation (4.14), power-based and linear regressions, respectively, where f_f is the flexural tensile strength and f_s the splitting tensile one.

$$f_f = 2.227 f_s^{0.484} \quad \text{extruded bricks} \tag{4.13a}$$
$$f_f = 2.037 f_s^{0.678} \quad \text{facing bricks} \tag{4.13b}$$
$$f_f = 2.340 f_s^{0.499} \quad \text{all data} \tag{4.13c}$$

$$f_f = 1.002 f_s \quad \text{extruded bricks} \tag{4.14a}$$
$$f_f = 1.342 f_s \quad \text{facing bricks} \tag{4.14b}$$
$$f_f = 1.118 f_s \quad \text{all data} \tag{4.14c}$$

4.2.6 Correlation among mean properties of solid clay bricks

Within this section, the possible relation among the mean mechanical properties of solid clay bricks (tested during the present experimental campaign and collected from previous

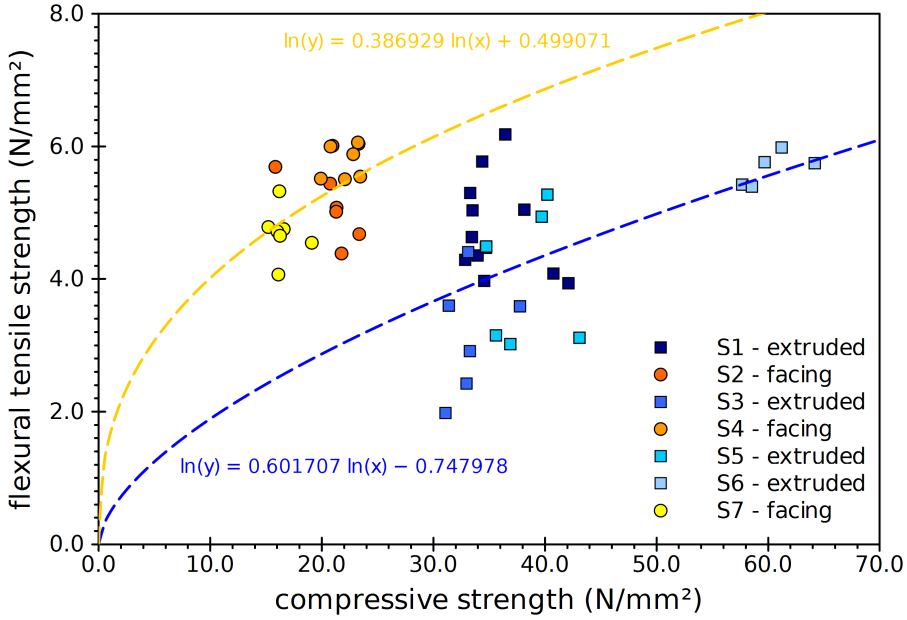

Figure 4.17: Pull-off strengths plotted versus splitting tensile strengths

works carried out at the University of Padova) have been investigated and compared, where possible, to the relations deduced by punctual data, that means properties measured on the same element. It has to be noticed that pull-off tensile strength values are available only for the seven sets of elements which results have been above presented, whereas the relation between compressive and splitting tensile strength cannot be investigated on punctual data, since only one portion for each brick was available to these types of test, being the other piece originated by the flexural failure destined to pull-off testing.

The available data are given in Table 4.10 on page 53, 4.11 on page 53 and 4.12 on page 54, where f_f, f_c and f_s indicate the flexural, compressive and splitting strength, respectively. Details concerning data collected from previous experiences, from UniPD 1999 to UniPD 2008, can be respectively found in Marchetti (1999), Disarò (2000), Bianculli (2002), Lucchin (2003), Cartolaro (2004), Garbin (2008).

The mean values of pull-off tensile strength plotted versus the flexural, compressive and splitting strength are compared to regression functions calibrated on the punctual data (Fig. 4.19 on page 54, 4.20 on page 55 and 4.21 on page 55, respectively); it can be observed that these values appear to be consistent with the previously evaluated regressions.

Concerning the relation between flexural and compressive strength, regressions based on mean values, whose coefficients are reported in Equation (4.15), do not substantially differ from the ones based on punctual data (two data, namely UniPD02 and UniPD03, have been excluded due to their peculiar behaviour, that could be imputed to problems during testing), as shown in Figure 4.22 on page 56, where dotted lines describe previous regressions. It has also been confirmed that a function based on all data cannot correctly depict any relation.

Regarding the relation between splitting and compressive strength, three power-based regression have been evaluated, whose coefficients are reported in Equation (4.16), but only the one based on all the values without distinguishing among facing or extruded bricks seems to lead to a significant relation, as shown in Figure 4.23 on page 56.

Finally, flexural and splitting tensile strength have been compared; also in this case, the regressions based on mean values, whose coefficients are reported in Equation (4.17) do not substantially differ from the ones based on punctual data (two data, namely UniPD02 and

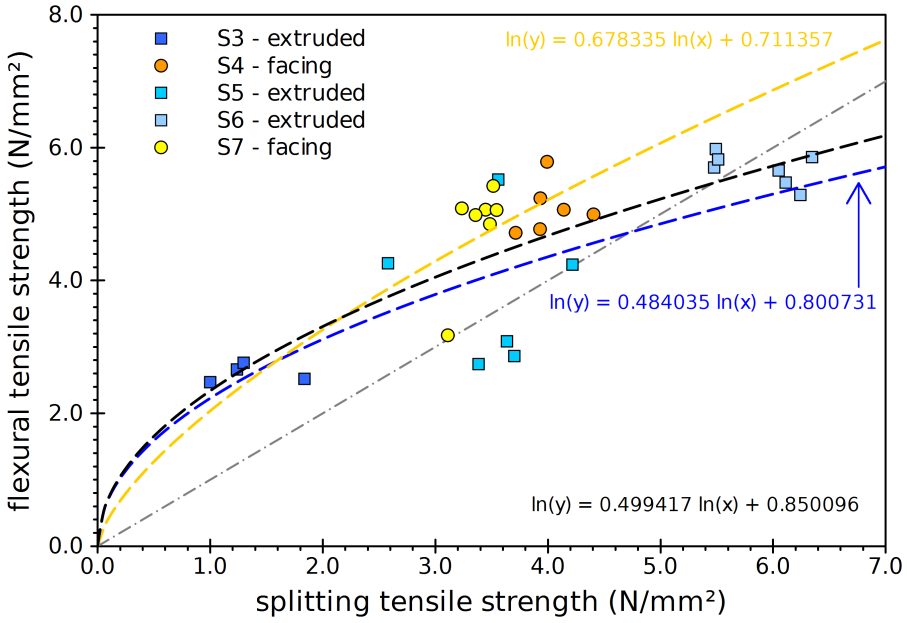

(a) Power-based regressions

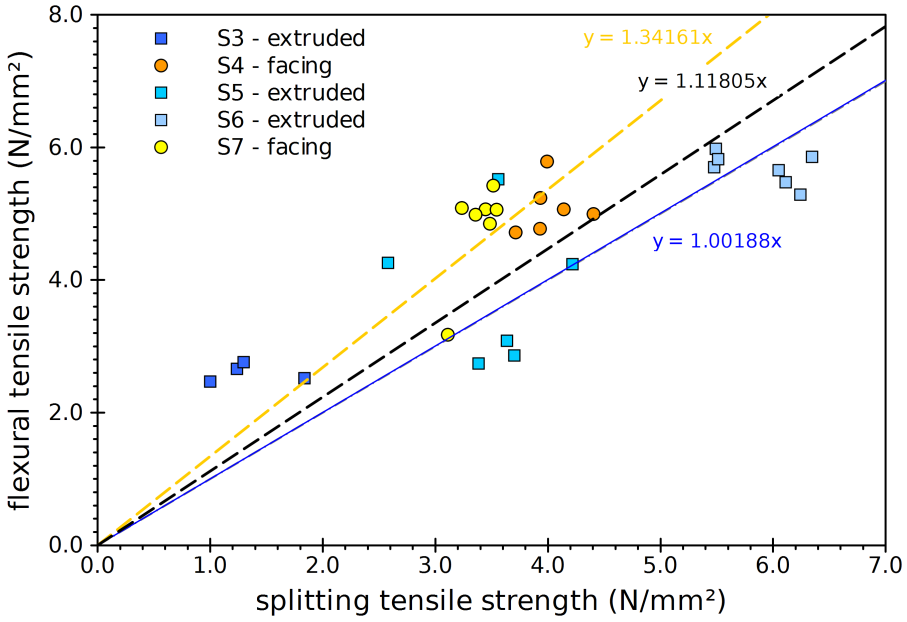

(b) Linear regressions

Figure 4.18: Flexural versus splitting tensile strength

Table 4.10: Mean values of flexural tensile strength

Series	f_f N/mm^2	Stand. dev. N/mm^2	C. of V. %
S1 ES_A	4.67	0.75	16.1%
S2 FaV	5.29	0.61	11.5%
S3 ES_B	2.97	0.66	22.3%
S4 FaV	5.42	0.47	8.6%
S5 ES_C	3.89	1.01	26.0%
S6 ES	5.64	0.27	4.8%
S7 FaV	4.75	0.57	11.9%
UniPD 1999			
UniPD 2000	4.74	0.73	15.4%
UniPD 2002	5.97	0.49	8.3%
UniPD 2003	6.40	0.47	7.3%
UniPD 2004	5.46	0.66	12.1%
UniPD 2008	5.98	0.80	13.4%

Table 4.11: Mean values of compressive strength

Series	f_c N/mm^2	Stand. dev. N/mm^2	C. of V. %
S1 ES_A	35.36	3.19	9.0%
S2 FaV	21.09	2.34	11.1%
S3 ES_B	33.29	2.39	7.2%
S4 FaV	22.06	1.42	6.4%
S5 ES_C	38.39	3.18	8.3%
S6 ES	60.27	2.56	4.3%
S7 FaV	16.51	1.22	7.4%
UniPD 1999	8.66	0.99	11.5%
UniPD 2000	16.53	2.77	16.8%
UniPD 2002	16.91	2.02	12.0%
UniPD 2003	43.03	2.41	5.6%
UniPD 2004	50.94	3.97	7.8%
UniPD 2008	25.74	1.85	7.2%

UniPD03, have been excluded due to their peculiar behaviour, as previously done), as shown in Figure 4.24 on page 57, where dotted lines describe previous regressions.

$$f_f = 0.173 f_c^{0.863} \quad \text{extruded bricks} \tag{4.15a}$$
$$f_f = 1.146 f_c^{0.505} \quad \text{facing bricks} \tag{4.15b}$$
$$f_f = 4.956 f_c^{-0.010} \quad \text{all data} \tag{4.15c}$$

$$f_s = 0.002 f_c^{2.032} \quad \text{extruded bricks} \tag{4.16a}$$
$$f_s = 0.135 f_c^{1.046} \quad \text{facing bricks} \tag{4.16b}$$
$$f_s = 0.455 f_c^{0.576} \quad \text{all data} \tag{4.16c}$$

Table 4.12: Mean values of splitting tensile strength

Series	f_s N/mm^2	Stand. dev. N/mm^2	C. of V. %
S1 ES_A			
S2 FaV			
S3 ES_B	1.34	0.35	26.3%
S4 FaV	4.02	0.23	5.8%
S5 ES_C	3.51	0.54	15.3%
S6 ES	5.89	0.38	6.5%
S7 FaV	3.39	0.16	4.7%
UniPD 1999	1.36	0.03	1.9%
UniPD 2000	2.28	0.29	12.8%
UniPD 2002	1.75	0.17	9.9%
UniPD 2003	4.94	0.82	16.6%
UniPD 2004	3.99	0.34	8.4%
UniPD 2008	4.02	0.45	11.3%

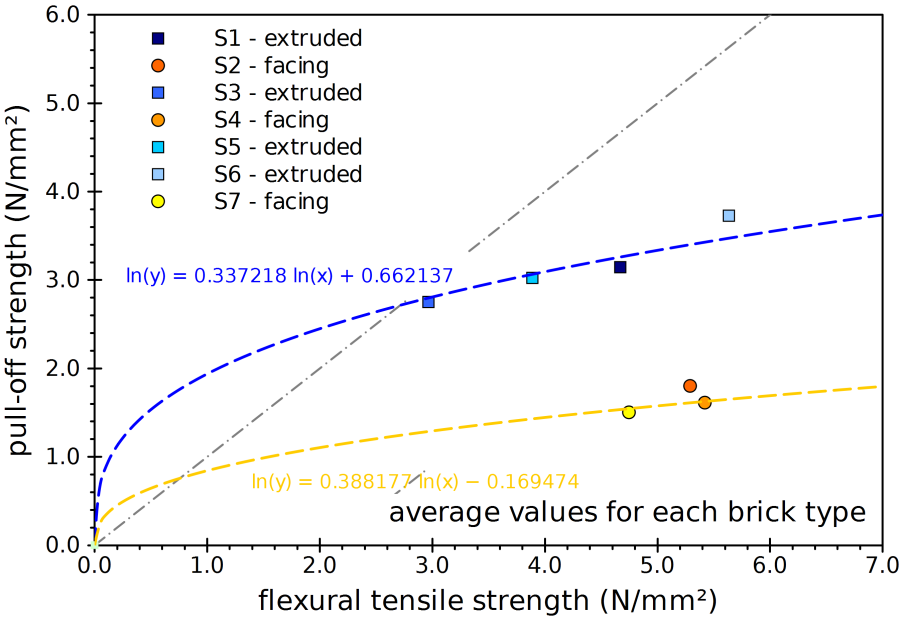

Figure 4.19: Mean pull-off plotted versus mean flexural tensile strengths

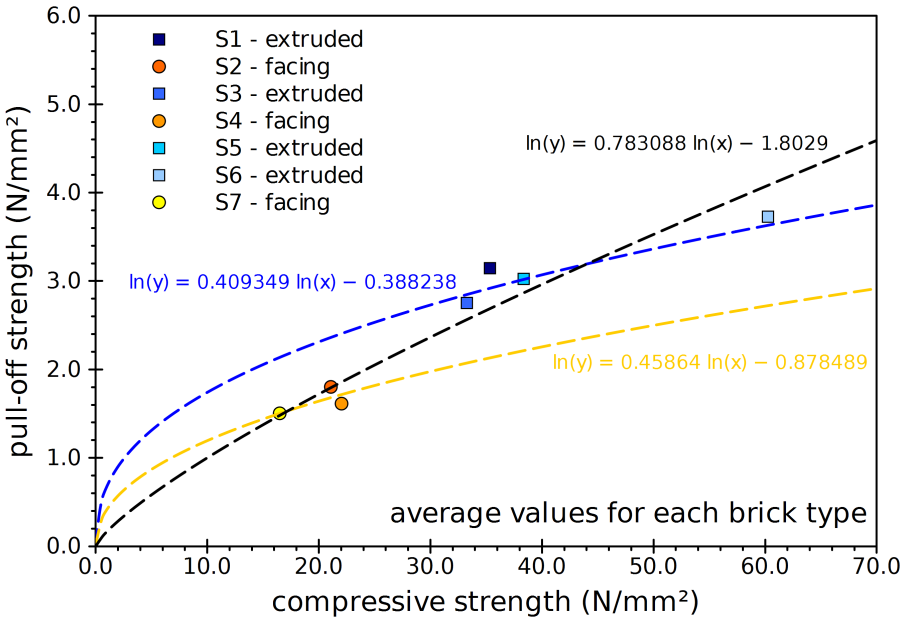

Figure 4.20: Mean pull-off tensile plotted versus mean compressive strengths

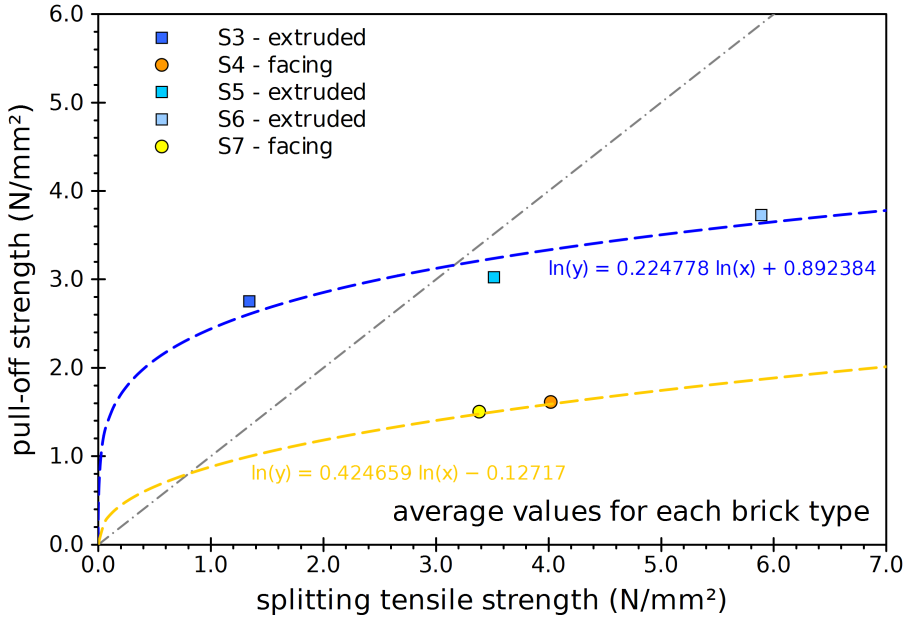

Figure 4.21: Mean pull-off plotted versus mean splitting tensile strengths

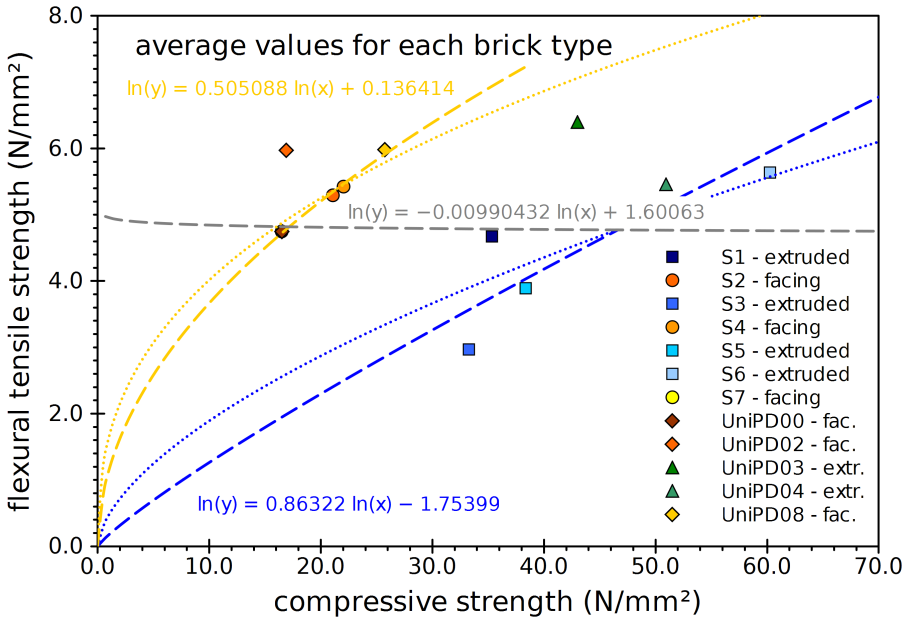

Figure 4.22: Mean flexural plotted versus mean compressive strengths

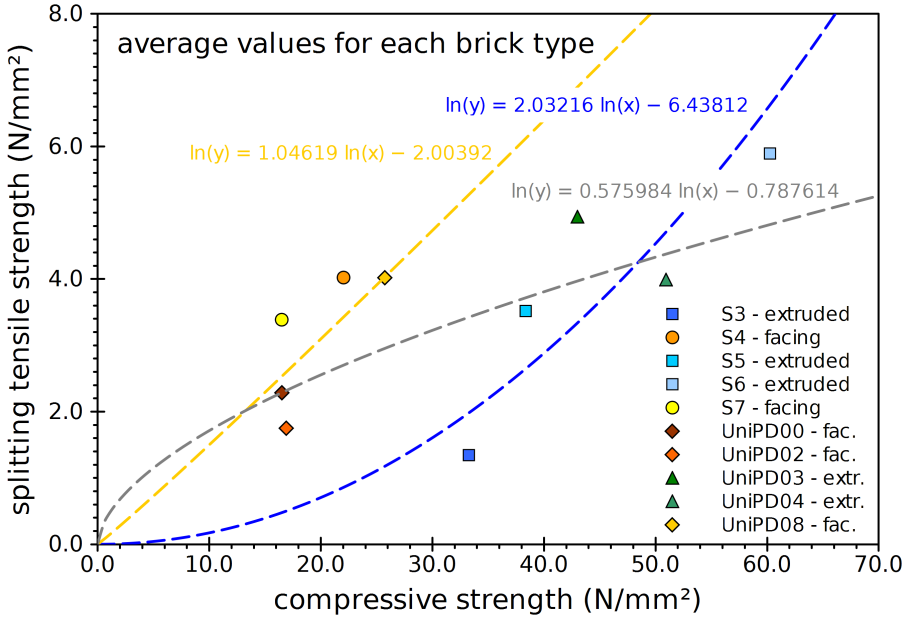

Figure 4.23: Mean splitting plotted versus mean compressive strengths

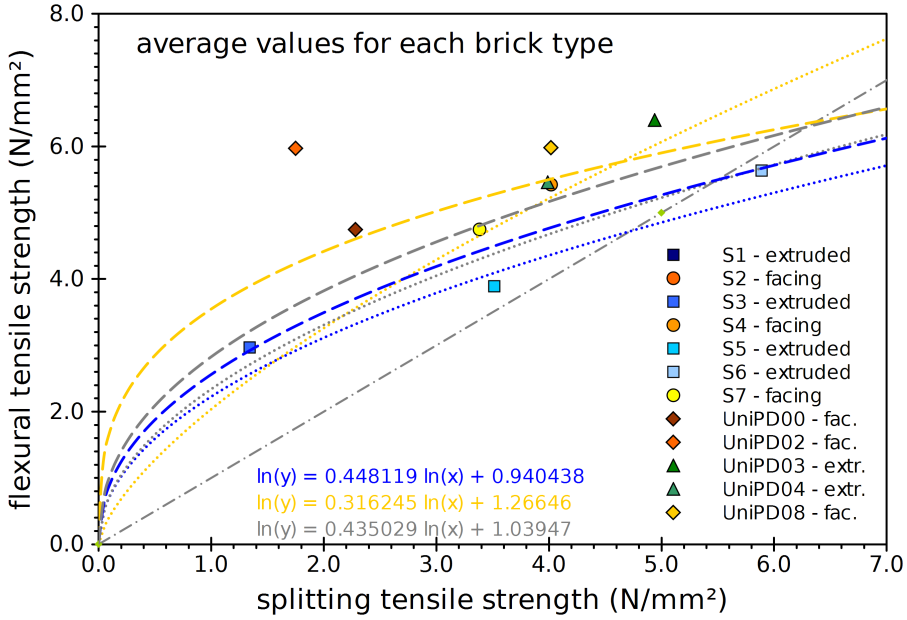

Figure 4.24: Mean flexural plotted versus mean splitting tensile strengths

$$f_f = 2.561 f_s^{0.448} \quad \text{extruded bricks} \tag{4.17a}$$

$$f_f = 3.548 f_s^{0.316} \quad \text{facing bricks} \tag{4.17b}$$

$$f_f = 2.828 f_s^{0.435} \quad \text{all data} \tag{4.17c}$$

4.3 Conclusive remarks

The results of the experimental campaign herein presented have led to the following conclusions:

- if the reinforcement is correctly applied, the type of fibres should not have any influence on the strength measured by the pull-off test; only the failure mode could be influenced, as glass fibres caused some unwanted failures that should however imputed to contingent factors related to that available portion of reinforcement, such as an incorrect conservation or cleaning. Moreover, the absence of primer could increase the likelihood of unwanted failures.

- Pull-off tensile strength could be correlated to flexural, splitting and compressive strength of the bricks by means of power-based regressions (Eq. 4.5, 4.6 and 4.11, respectively); except the relation with the compressive strength, of which a single function seems to correctly depict the tendency, in the other cases extruded and facing bricks showed a different behaviour, although the trends were similar.

- In addition, two code-based functions (see ACI 318-99 2004, DM 09-01-96 1996) have been calibrated to correlate pull-off and compressive strength of bricks, and it has been found that they could satisfactorily describe the trends.

- A different behaviour of extruded and facing elements was observed also in the correlation between flexural and compressive strength (Eq. 4.12), whereas a single

power-based regression (Eq. 4.13) or even linear regression (Eq. 4.14) could be sufficient to describe the trend that relates flexural and splitting tensile strength.

- Finally, the correlations among average values of the bricks properties, where sufficiently evident, substantially confirmed the previously calculated trends.

Chapter 5

Interface behaviour in the case of tangential actions

In this chapter, the main results of ten Double-lap Push-pull Shear Tests performed on CFRP and GFRP reinforcement (five samples for each type) externally bonded on solid clay bricks are presented. Based on the experimentally acquired data, the fracture energy value, Gf, has been calibrated for both the reinforcements, following the commonly adopted interpretation of these tests. An analytical function has been proposed as bond-slip law, and fitted on the experimental results as well as a bilinear relation. A bi-dimensional FE model has been developed, by means of a commercial software, in order to compare its results to the experimental evidences, and carry out analyses of the test specimens aimed at investigating the influence of the following parameters: different modelling approaches, shape of the local bond-slip law, bonded length. Finally, an extensive collection of experimental tests available in literature, concerning stones, clay bricks and masonry prisms used as substrate for the reinforcement, has been made in order to calibrate the c_1 coefficient provided by the CNR DT-200 (2004) Guidelines, which correlates the predicted value of fracture energy to the square root of the product of compressive and tensile strength of the masonry substrate.

5.1 Literature review

5.1.1 Experimental testing of bond between FRP and substrate

In the last decade, the bond of composite laminates, applied on concrete substrate and affected by axial loading, has been deeply investigated. The characterization of the behaviour has been performed by means of different test set-ups, all aimed at generating a state of stress that could be assimilated to pure shear.

Among various possibilities (Fig. 5.1 on page 62 and 5.2 on page 62), three main types of test can be identified as the most commonly used: Single-lap Shear Test (Chajes *et al.* 1996, Täljsten 1997, Bizindavyi and Neale 1999, Mazzotti *et al.* 2009), Double-lap Pull-pull Shear Test (Lee *et al.* 1999, Nakaba *et al.* 2001), Double-lap Push-pull Shear Test (Camli and Binici 2007) and Beam-type Test (De Lorenzis *et al.* 2001).

On the other hand, few investigations concerning debonding on masonry-like substrate are available, such as Aiello and Sciolti (2006) that investigated bond on natural stones, Faella *et al.* (2009) that compared natural stones and clay bricks, Briccoli Bati *et al.* (2007), Grande *et al.* (2008) and Panizza *et al.* (2008a) that tested bond on solid clay bricks, Camli and Binici (2007) that used hollow clay blocks, Casareto *et al.* (2003) that studied bond on clay blocks and block masonry prisms, Basilio (2007), Subramanian *et al.* (2009) that

tested bond on brick masonry prisms, Capozucca (2010) that chose historic clay bricks as support. They adopted either Single-lap Shear Test or Double-lap Push-pull Shear Tests, where the last is also known in literature by different names, such as Double-shear Push Test or Near-end Supported Double-shear Test (Yao *et al.* 2005). It consists in loading in tension two reinforcement strips, symmetrically connected to the support, in order to create mainly shear stresses at the interface, while the brittle support is subjected to compressive stresses.

The Double-lap Push-pull Shear Test set-up is based on the assumption that the applied load is equally distributed on the two strips, but it is also particularly simple and suitable for the usual common available test machines.

Concerning the concrete substrate, the main aspects of the phenomenon are currently supposed to be clarified, and can be summarized as follows (Fig. 5.4 on page 63 and 5.3 on page 63):

- increasing the bonded length of the reinforcement, L_b, the failure axial load, P_u, will increase until a certain value of L_b is reached; if the bonded length exceeds that value, usually defined as effective bond length, L_e, this fact will not affect the ultimate load.

- The failure load is directly proportional to the reinforcement width, b_f.

- The fracture energy G_f and the reinforcement axial stiffness per unit width $E_\mathrm{f}t_\mathrm{f}$, given by the product of the Young's modulus E_f and the thickness of the reinforcement, show a positive correlation with the failure load.

- If the substrate axial stiffness, $b_\mathrm{c}E_\mathrm{c}t_\mathrm{c}$, is sufficiently higher than the reinforcement one, it has no significant influence on the failure load.

5.1.2 Prediction of strength

During the last years, many predictive models have been developed to estimate the failure load of the composite-to-concrete bonded joint. Wide reviews of available strength or bond-slip models were given by Chen and Teng (2001), Lu *et al.* (2005), Karbhari *et al.* (2006), Ferracuti *et al.* (2007b).

Among them, the models of Tanaka (Eq. 5.1), Hiroyuki & Wu (Eq. 5.2), Maeda (Eq. 5.3), Khalifa (Eq. 5.4), reported in Chen and Teng (2001), Yang (Eq. 5.5), Sato (Eq. 5.6), Iso (Eq. 5.7), reported in Lu *et al.* (2005), express the failure load as the product of an area and a nominal average tangential stress, τ_u, different from model to model.

The models of Izumo (Eq. 5.8), Lu *et al.* (2005, see), Neubauer & Rostàsy (1) (Eq. 5.9), Chen & Teng (Eq. 5.10), both reported in Chen and Teng (2001), give other expressions for the failure load.

Finally, eleven ones provide an estimation of the fracture energy value G_f, which is correlated to the failure load (Eq. 5.11). In particular, the models of Monti (Lu *et al.* 2005), Lu et al. (2005), herein Lu Bilinear, Brosens & Van Gemert (Karbhari *et al.* 2006) and Italian Research Council (CNR DT-200 2004) utilize a bilinear bond-slip law (5.12); the models of Nakaba et al. (2001) and Savoia et al. (2003a) adopt a Popovics curve as bond-slip law (5.17); the models of Neubauer & Rostàsy (2) (Lu *et al.* 2005), Dai & Ueda (1) (2003), Dai & Ueda (2) (2005) and Lu et al. (2004), Precise and Simplified models, assume other types of bond-slip function. The corresponding formulas are reported from Equation (5.13) to (5.24).

Moreover, four models are reported, although not applied since they need, differently from the others, the knowledge of some parameters such as the value of the fracture energy

or the maximum bond stress: Täljsten (Täljsten 1996), Niedermaier, Yuan & Wu, Yuan et al. (Chen and Teng 2001). The related formulations are reported from (5.25) to (5.28).

In some cases, symbols have been changed, with respect to the source, in order to make them consistent; in other cases, some coefficients have been adapted to express lengths in mm, forces in N, stresses in N/mm^2.

The main parameters included in the above mentioned models, referring to the reinforcement, fibres and adhesive, and the support, are shown in Table 5.1 on page 64

5.1.3 Correlation of interface fracture energy to failure load

The interface fracture energy mode II, G_f, is defined as the definite integral of the tangential stress on the interface, τ, expressed as function of the mutual slip of composite and substrate, s (Eq. 5.29 on page 70).

One of the first analytical models of the concrete-composite bond strength was derived by Täljsten (1996), starting both from a linear approach, based on the beam theory, and from a non-linear approach, related to fracture mechanics. In the case of most of the epoxy adhesives commonly used, a simplified formulation, reported in Equation (5.25), was obtained.

Yuan (Chen and Teng 2001) proposed a modified constant value (Eq. 5.5 on page 65) that takes into account the width (b_f and b_c) ratio of the bonded materials.

In most cases, the constant value α_T, or α_Y, has a slight influence on the calculation. Many authors, such as Savoia et al. (2003a) and Dai et al. (2005), report the relation between ultimate load and fracture energy without any constant (see Eq. 5.11 on page 66).

It has also to be noticed that Equation (5.11), demonstrated in some cases (Wu *et al.* 2002, Dai *et al.* 2005), can be assumed in every case of regular interface law, as reported by Savoia (2003b).

5.1.4 Relation between local bond stress and mutual slip

Figure 5.5 on page 64 shows possible shapes of the bond-slip function: (a) cut-off, adopted by Neubauer and Rostàsy (Chen and Teng 2001); (b) bilinear, assumed by some guidelines like fib Bulletin 14 (2001), CNR DT-200 (2004), and by Monti (Lu *et al.* 2005), Brosens and Van Gemert (Karbhari *et al.* 2006) and Lu (Lu *et al.* 2004); (c) rigid with linear softening, by Chen and Teng (2001); (d) a single function, as the Popovics curve chosen by Savoia *et al.* (2003a) and Nakaba *et al.* (2001), or an exponential curve obtained by Dai *et al.* (2005); (e) two different non-linear functions for ascending and descending branch, for instance the expressions adopted by Lu *et al.* (2004) or dai:2003.

Therefore, it is commonly assumed that bond of composite laminates exhibits a softening behaviour, with an ascending branch followed by a descending one, and presenting no residual stress for wider slip. In the following, τ_max indicates the maximum bond stress reached by the interface, s_0 the corresponding mutual slip between substrate and reinforcement, and s_f the ultimate slip, where accounted.

The commonly adopted analyses of the interface behaviour is based on simple equilibrium and compatibility equations among bond stress τ, mutual slip s, strain ε and distance from the loaded end, x, reported in (5.30) (Fig. 5.6 on page 64); as usual, strain and slip refer only to the reinforcement, since the substrate is considered sufficiently stiffer to disregard its deformation (Täljsten 1997, Bizindavyi and Neale 1999, Yuan *et al.* 2004, Dai *et al.* 2005).

$$\tau_u = 6.13 - \ln(L_b) \tag{5.1a}$$

$$P_u = b_f L_b \tau_u \tag{5.1b}$$

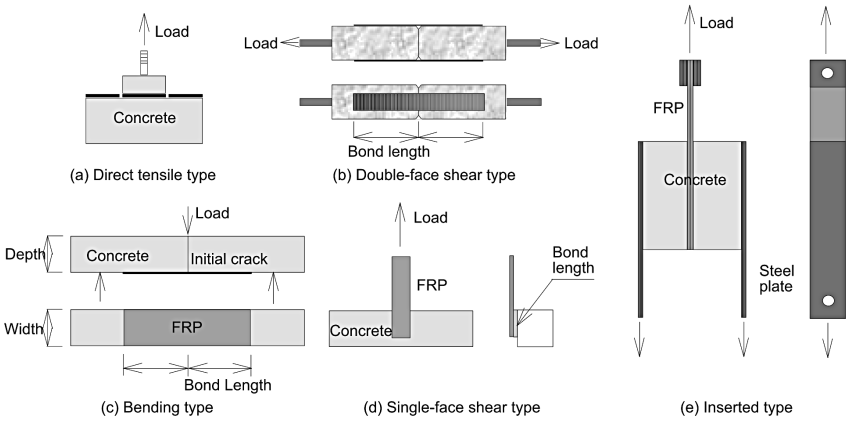

Figure 5.1: Different bond specimens (Nakaba *et al.* 2001)

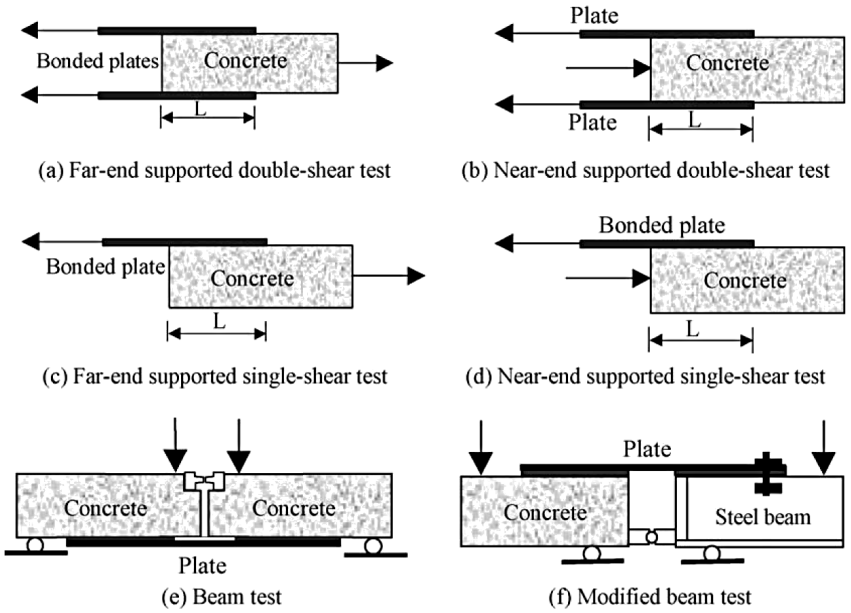

Figure 5.2: Classification of bond tests (Yao *et al.* 2005)

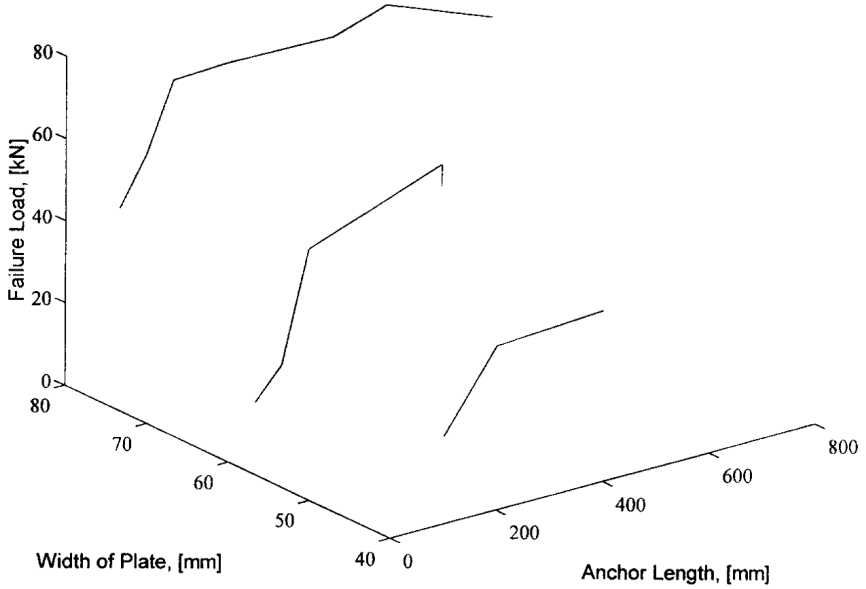

Figure 5.3: Failure load as a function of plate width and anchor length (Täljsten 1997)

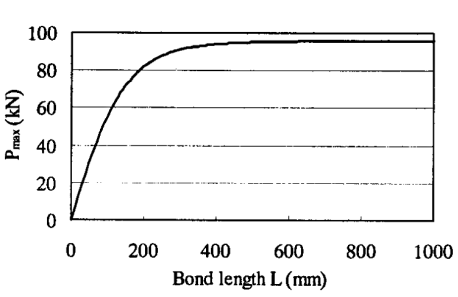

(a) Bonded length

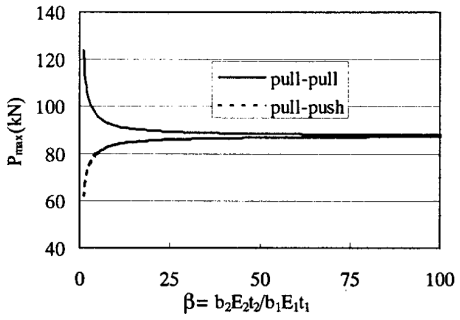

(b) Support/reinforcement axial stiffness ratio

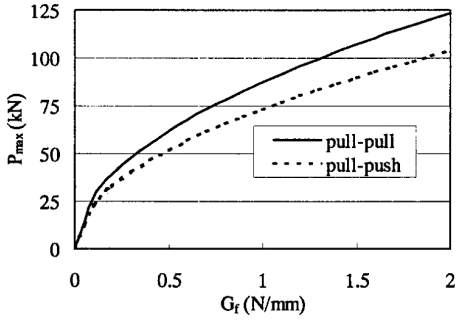

(c) Fracture energy

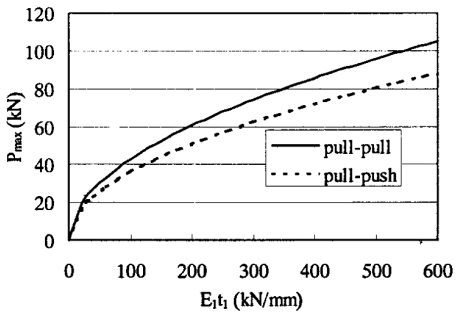

(d) Reinforcement axial stiffness per unit width

Figure 5.4: Influence of the main parameters on the ultimate failure load (Wu *et al.* 2002)

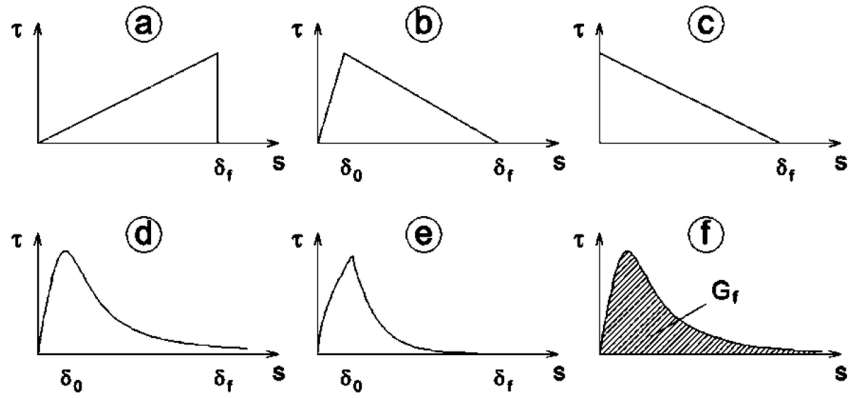

Figure 5.5: Different shapes for the bond-slip law

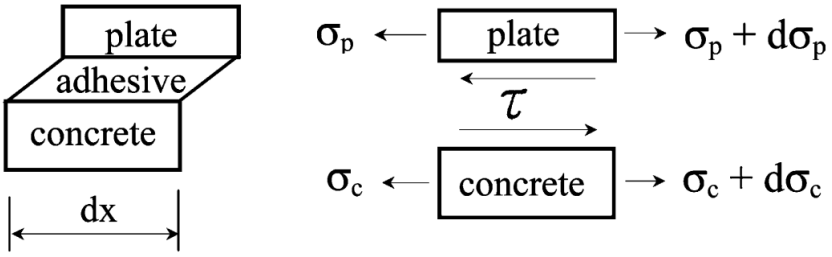

Figure 5.6: Simple model of reinforcement and concrete (Yuan *et al.* 2004)

Table 5.1: Parameters directly used by the predictive models

Model	b_f	L_b	t_f	E_f	t_a	E_a	G_a	b_c	t_{ref}	f'_c	f_t	E_c	G_c
Tanaka	⋆	⋆											
Hiroyuki	⋆	⋆											
Maeda	⋆		⋆	⋆									
Khalifa	⋆		⋆	⋆						⋆			
Yang	⋆		⋆	⋆							⋆		
Sato	⋆		⋆	⋆						⋆			
Iso	⋆		⋆	⋆						⋆			
Izumo	⋆	⋆	⋆	⋆						⋆			
Neubauer & Rostàsy (1)	⋆		⋆	⋆				⋆			⋆		
Chen & Teng	⋆		⋆	⋆				⋆		⋆			
Monti	⋆		⋆	⋆	⋆	⋆		⋆			⋆	⋆	
Lu et al. bilinear	⋆		⋆	⋆				⋆			⋆		
Brosens & Van Gemert	⋆		⋆	⋆	⋆	⋆		⋆	⋆	⋆	⋆	⋆	
CNR	⋆		⋆	⋆	⋆		⋆	⋆	⋆	⋆	⋆		⋆
Nakaba	⋆		⋆	⋆						⋆			
Savoia	⋆		⋆	⋆						⋆			
Neubauer & Rostàsy (2)	⋆		⋆	⋆				⋆			⋆		
Dai & Ueda (1)	⋆		⋆	⋆	⋆		⋆			⋆			
Dai & Ueda (2)	⋆		⋆	⋆	⋆		⋆			⋆			
Lu et al. precise	⋆		⋆	⋆	⋆		⋆	⋆	⋆		⋆		⋆
Lu et al. simplified	⋆		⋆	⋆				⋆			⋆		

$$\tau_u = 5.88(0.1L_b)^{-0.669} \tag{5.2a}$$
$$P_u = b_f L_b \tau_u \tag{5.2b}$$

$$\tau_u = 110.6 \cdot 10^{-6} E_f t_f \tag{5.3a}$$
$$L_e = e^{6.13 - 0.580 \ln 10^{-3} E_f t_f} \tag{5.3b}$$
$$P_u = b_f L_e \tau_u \tag{5.3c}$$

$$\tau_u = 110.2 \cdot 10^{-6} \sqrt[3]{\left(\frac{f'_c}{42}\right)^2} E_f t_f \tag{5.4a}$$
$$L_e = e^{6.13 - 0.580 \ln 10^{-3} E_f t_f} \tag{5.4b}$$
$$P_u = b_f L_e \tau_u \tag{5.4c}$$

$$\tau_u = 0.5 f_t \tag{5.5a}$$
$$L_e = 100\text{mm} \tag{5.5b}$$
$$P_u = \left(0.5 + 0.8\sqrt{\frac{E_f t_f}{100 f_t}}\right) b_f L_e \tau_u \tag{5.5c}$$

$$\tau_u = 2.68 f_c'^{0.2} E_f t_f \cdot 10^{-5} \tag{5.6a}$$
$$L_e = 1.89 (E_f t_f)^{0.4} \tag{5.6b}$$
$$P_u = (b_f + 2\Delta b_f) L_e \tau_u \quad \text{where } \Delta b_f = 3.7 \text{ mm} \tag{5.6c}$$

$$\tau_u = 0.93 f_c'^{0.44} \tag{5.7a}$$
$$L_e = 0.125 (E_f t_f)^{0.57} \tag{5.7b}$$
$$P_u = \begin{cases} b_f L_e \tau_u & \text{if } L_b \geq L_e \\ b_f L_b \tau_u & \text{otherwise} \end{cases} \tag{5.7c}$$

$$P_u = \begin{cases} \left(3.8 f_c'^{2/3} + 15.2\right) b_f L_b E_f t_f \cdot 10^{-6} & \text{(carbon fibres)} \\ \left(3.4 f_c'^{2/3} + 69\right) b_f L_b E_f t_f \cdot 10^{-6} & \text{(aramidic fibres)} \end{cases} \tag{5.8}$$

$$L_e = \sqrt{\frac{E_f t_f}{2 f_t}} \tag{5.9a}$$
$$P_u = \begin{cases} 0.64 \beta_w b_f \sqrt{E_f t_f f_t} & \text{if } L_b \geq L_e \\ 0.64 \beta_w b_f \sqrt{E_f t_f f_t} \frac{L_b}{L_e} \left(2 - \frac{L_b}{L_e}\right) & \text{otherwise} \end{cases} \tag{5.9b}$$
$$G_f = c_f f_t \text{cf} = 0.204 \pm 0.053 \tag{5.9c}$$
$$\beta_w = 1.125 \sqrt{\frac{2 - b_f/b_c}{1 + b_f/400}} \tag{5.9d}$$

$$L_e = \sqrt{\frac{E_f t_f}{\sqrt{f'_c}}} \tag{5.10a}$$

$$P_u = 0.427 \beta_w \beta_l b_f L_e \sqrt{f'c} \tag{5.10b}$$

$$\beta_w = \sqrt{\frac{2 - b_f/b_c}{1 + b_f/b_c}} \tag{5.10c}$$

$$\beta_l = \begin{cases} 1 & \text{if } L_b > L_e \\ \sin \frac{\pi L_b}{2 L_e} & \text{otherwise} \end{cases} \tag{5.10d}$$

$$P_u = b_f \sqrt{2 E_f t_f G_f} \tag{5.11}$$

$$\text{Bilinear bond-slip curve:} \quad \tau(s) = \begin{cases} \tau_{\max} \left(\frac{s}{s_0} \right) & \text{if } s \leq s_0 \\ \tau_{\max} \left(\frac{s_f - s}{s_f - s_0} \right) & \text{if } s_0 < s \leq s_f \\ 0 & \text{otherwise} \end{cases} \tag{5.12}$$

$$\tau_{\max} = 1.8 \beta_w f_t \tag{5.13a}$$

$$s_0 = 2.5 \tau_{\max} \left(\frac{t_a}{E_a} + \frac{50}{E_c} \right) \tag{5.13b}$$

$$s_f = 0.33 \beta_w \tag{5.13c}$$

$$\beta_w = \sqrt{1.5 \frac{2 - b_f/b_c}{1 + b_f/100}} \tag{5.13d}$$

$$\tau_{\max} = 1.5 \beta_w f_t \tag{5.14a}$$

$$s_0 = 0.0195 \beta_w f_t \tag{5.14b}$$

$$s_f = \frac{2 G_f}{\tau_{\max}} \tag{5.14c}$$

$$\beta_w = \sqrt{\frac{2.25 - b_f/b_c}{1.25 + b_f/b_C}} \tag{5.14d}$$

$$G_f = 0.308 \beta_w^2 \sqrt{f_c} f(K_a); \quad f(K_a) = 1 \text{ if not defined} \tag{5.14e}$$

$$\tau_{\max} = \sqrt{\frac{1.47\,(2 - b_f/b_c)}{1 + b_f/85}}\frac{f'_c f_t}{f'_c + f_t} \tag{5.15a}$$

$$s_0 = \tau_{\max}\left(2.4\frac{t_{\text{ref}}}{E_c} + 2.5\frac{t_m}{E_m} + n\frac{t_a}{E_a}\right) \tag{5.15b}$$

$$s_f = \frac{2G_f}{\tau_{\max}} \tag{5.15c}$$

$$G_f = \frac{0.588\,(2 - b_f/b_c)}{1 + b_f/85} f_c \tag{5.15d}$$

$$L_e = \frac{2\lambda + a\tan\left(\tanh\left(2\right)/\lambda\right)}{\lambda\omega} \tag{5.15e}$$

$$\lambda = \sqrt{\frac{s_0}{s_f - s_0}} \tag{5.15f}$$

$$\omega = \sqrt{\frac{\tau_{\max}\left(1 + \left(\frac{E_f A_f}{E_c A_c}\right)\right)}{s_0 E_f t_f}} \tag{5.15g}$$

$$a \quad \text{not defined in Karbhari } \textit{et al.} \text{ (2006)} \tag{5.15h}$$

$$\tau_{\max} = 0.64\beta_w\sqrt{f_{\text{ck}} f_t} \tag{5.16a}$$

$$s_0 = \frac{\tau_{\max}}{\frac{c_1}{t_a/G_a + t_c/G_c}} \tag{5.16b}$$

$$s_f = \frac{2G_f}{\tau_{\max}} \tag{5.16c}$$

$$G_f = k_g\beta_w\sqrt{f_{\text{ck}} f_t} \tag{5.16d}$$

$$\beta_w = \sqrt{\frac{2 - b_f/b_c}{1 + b_f/400}} \tag{5.16e}$$

$$k_g = 0.064 \qquad \Rightarrow \qquad s_f = 0.2 \tag{5.16f}$$

$$\text{Popovics-like bond-slip curve:} \quad \tau(s) = \tau_{\max}\frac{s}{s_0}\frac{n}{n - 1 + \left(\frac{s}{s_0}\right)^n} \tag{5.17}$$

$$\tau_{\max} = 3.5 f_c'^0.19 s_0 = 0.065 n = 3 \tag{5.18}$$

$$\tau_{\max} = 3.5 f_c'^0.19 s_0 = 0.051 n = 2.86 \tag{5.19}$$

$$\tau(s) = \begin{cases} \tau_{\max}\left(\frac{s}{s_0}\right) & \text{if } s \le s_0 \\ 0 & \text{otherwise} \end{cases} \tag{5.20a}$$

$$\tau_{\max} = 1.8\beta_w f_t \tag{5.20b}$$

$$s_0 = 0.202\beta_w \tag{5.20c}$$

$$\beta_w = 1.125\sqrt{\frac{2 - b_f/b_C}{1 + b_f/400}} \tag{5.20d}$$

$$\tau(s) = \begin{cases} \tau_{\max} \left(\frac{s}{s_0}\right)^{0.575} & \text{if } s \leq s_0 \\ \tau_{\max} e^{-\beta(s-s_0)} & \text{otherwise} \end{cases} \tag{5.21a}$$

$$\tau_{\max} = \frac{-1.575\alpha K_a + \sqrt{2.481\alpha^2 K_a^2 + 6.3\alpha\beta^2 K_a G_f}}{2\beta} \tag{5.21b}$$

$$s_0 = \frac{\tau_{\max}}{\alpha K_a} \tag{5.21c}$$

$$K_a = \frac{G_a}{t_a} \tag{5.21d}$$

$$G_f = 7.554 {K_a}^{-0.449} {f'_c}^{0.343} \tag{5.21e}$$

$$\alpha = 0.028 \left(10^{-3} E_f t_f\right)^{0.254} \tag{5.21f}$$

$$\beta = 0.0035 K_a \left(10^{-3} E_f t_f\right)^{0.34} \tag{5.21g}$$

$$\tau(s) = 2UG_f \left(e^{-Us} - e^{-2Us}\right) \tag{5.22a}$$

$$\tau_{\max} = 0.5UG_f \tag{5.22b}$$

$$s_0 = \frac{\ln(2)}{U} \tag{5.22c}$$

$$U = 6.846 \left(10^{-3} E_f t_f\right)^{0.108} \left(10^{-3} \frac{G_a}{t_a}\right)^{0.833} \tag{5.22d}$$

$$G_f = 0.446 \left(10^{-3} E_f t_f\right)^{0.023} \left(10^{-3} \frac{G_a}{t_a}\right)^{-0.352} {f'_c}^{0.236} \tag{5.22e}$$

$$\tau(s) = \begin{cases} \tau_{\max}\left(\sqrt{\frac{s}{s_0 A}} - B\right) & \text{if } s \leq s_0 \\ \tau_{\max} e^{-\alpha\left(\frac{s}{s_0}-1\right)} & \text{otherwise} \end{cases} \tag{5.23a}$$

$$\tau_{\max} = 1.5\beta_w f_t \tag{5.23b}$$

$$s_0 = 0.0195\beta_w f_t + s_e \tag{5.23c}$$

$$\alpha = \frac{\tau_{\max} s_0}{G_f - {G_f}^a} \tag{5.23d}$$

$$\beta_w = \sqrt{\frac{2.25 - b_f/b_c}{1.25 + b_f/b_c}} \tag{5.23e}$$

$$A = \frac{s_0 - s_e}{s_0} \tag{5.23f}$$

$$B = \frac{s_e}{2\left(s_0 - s_e\right)} \tag{5.23g}$$

$$s_e = \frac{\tau_{\max}}{K_0} \tag{5.23h}$$

$$K_0 = \frac{K_a K_c}{K_a + K_c} \tag{5.23i}$$

$$K_a = \frac{G_a}{t_a} \tag{5.23j}$$

$$K_c = \frac{G_c}{t_c} \tag{5.23k}$$

$$G_f = 0.308{\beta_w}^2\sqrt{f_t} f\left((K_a)\right) \tag{5.23l}$$

$${G_f}^a = \int_0^{s_0} \tau ds = \tau_{\max} s_0 \left(\frac{2A}{3}\left(\frac{1 + B^2 A}{A}\right)^{\frac{2}{3}} - B - \frac{2}{3}B^3 A\right) \tag{5.23m}$$

$$\tau(s) = \begin{cases} \tau_{\max}\left(\sqrt{\frac{s}{s_0}}\right) & \text{if } s \leq s_0 \\ \tau_{\max} e^{-\alpha\left(\frac{s}{s_0}-1\right)} & \text{otherwise} \end{cases} \tag{5.24a}$$

$$\tau_{\max} = 1.5\beta_w f_t \tag{5.24b}$$

$$s_0 = 0.0195\beta_w f_t \tag{5.24c}$$

$$\alpha = \frac{1}{\frac{G_f}{\tau_{\max} s_0} - \frac{2}{3}} \tag{5.24d}$$

$$\beta_w = \sqrt{\frac{2.25 - b_f/b_c}{1.25 + b_f/b_c}} \tag{5.24e}$$

$$G_f = 0.308{\beta_w}^2\sqrt{f_t} f\left((K_a)\right) \tag{5.24f}$$

$$P_u = b\sqrt{\frac{2G_f E_f t_f}{1 + \alpha_T}} \tag{5.25a}$$

$$\alpha_T = \frac{E_f t_f}{E_c t_c} \tag{5.25b}$$

$$P_u = \begin{cases} 0.78 b_f \sqrt{2 G_f E_f t_f} = 0.78 \beta_w b_f \sqrt{2 c_f E_f t_f f_{\mathrm{ctm}}} & \text{if } L_b \geq L_e \\ 0.78 b_f \sqrt{2 G_f E_f t_f} \frac{L}{L_e} = 0.78 \beta_w b_f \sqrt{2 c_f E_f t_f f_{\mathrm{ctm}}} \frac{L_b}{L_e} & \text{otherwise} \end{cases} \tag{5.26a}$$

$$L_e = \sqrt{\frac{E_f t_f}{2 f_{\mathrm{ctm}}}} \tag{5.26b}$$

$$G_f = c_f \beta_w^2 f_c tm \tag{5.26c}$$

$$\beta_w = 1.125 \sqrt{\frac{2 - b_f / b_c}{1 + b / 400}} \tag{5.26d}$$

$$P_u = \begin{cases} \frac{\tau_{\max} b_f}{\lambda} & \text{if } L_b \geq L_e \\ \frac{\tau_{\max} b_f}{\lambda} \sin(\lambda L_b) & \text{otherwise} \end{cases} \tag{5.27a}$$

$$L_e = \frac{\pi}{2\lambda} \tag{5.27b}$$

$$\lambda^2 = \frac{\tau_{\max}}{s_f E_f t_f} (1 + \alpha_Y) \tag{5.27c}$$

$$\alpha_Y = \frac{b_f E_f t_f}{b_c E_c t_c} \tag{5.27d}$$

$$P_u = \frac{\tau_{\max} b_f}{\lambda_2} \frac{s_f}{s_f - s_0} \sin(\lambda_2) \tag{5.28a}$$

$$L_e = a_0 + \frac{1}{2\lambda_1} \ln \left(\frac{\lambda_1 + \lambda_2 \tan(\lambda_2 a_0)}{\lambda_1 - \lambda_2 \tan(\lambda_2 a_0)} \right) \tag{5.28b}$$

$$\lambda_1^2 = \frac{\tau_{\max}}{s_0 E_f t_f} (1 + \alpha_Y) \tag{5.28c}$$

$$\lambda_2^2 = \frac{\tau_{\max}}{(s_f - s_0) E_f t_f} (1 + \alpha_Y) \tag{5.28d}$$

$$a_0 = \frac{1}{\lambda_2} \sin^{-1} \left(0.97 \sqrt{\frac{s_f - s_0}{s_f}} \right) \tag{5.28e}$$

$$\tanh(\lambda_1 (L_b - a)) = \frac{\lambda_2}{\lambda_1} \tan(\lambda_2 a) \tag{5.28f}$$

$$G_{\mathrm{f}} = \int_0^\infty \tau(s) ds \tag{5.29}$$

$$\frac{d\varepsilon(x)}{dx} = \frac{1}{E_{\mathrm{f}} t_{\mathrm{f}}} \tau(x) \tag{5.30a}$$

$$\varepsilon(x) = \frac{ds(x)}{dx} \qquad \Rightarrow \qquad s(x) = \int_0^x \varepsilon(x) dx \tag{5.30b}$$

$$\frac{d^2 s(x)}{dx} - \frac{1}{E_{\mathrm{f}} t_{\mathrm{f}}} \tau(x) = 0 \tag{5.30c}$$

Table 5.2: Bricks properties

Mean cubic compressive strength	50.94	N/mm^2
Mean direct tensile strength	2.37	N/mm^2
Mean splitting tensile strength	3.99	N/mm^2
Mean flexural tensile strength	5.46	N/mm^2
Secant elastic modulus	16100	N/mm^2

Table 5.3: Reinforcement components properties

Adhesive MBrace®Saturant		
Characteristic compressive strength	>80	N/mm^2
Characteristic direct tensile strength	>50	N/mm^2
Maximum tensile strain	2.5	%
Tensile elastic modulus	>3000	N/mm^2
High-strength Carbon MBrace®C1-30		
Equivalent thickness	0.165	mm
Characteristic direct tensile strength	3430	N/mm^2
Maximum tensile strain	1.5	%
Tensile elastic modulus	230000	N/mm^2
Alkali-resistant Glass MBrace®G60-AR		
Equivalent thickness	0.230	mm
Characteristic direct tensile strength	1700	N/mm^2
Maximum tensile strain	2.8	%
Tensile elastic modulus	65000	N/mm^2

5.2 Description of the experimental tests

In the following, the main details concerning the execution of ten Double-lap Push-pull Shear Tests, also presented in Panizza *et al.* (2008a), are reported. This type of test consists in loading in tension two reinforcement strips, symmetrically connected to the support, in order to create shear stresses at the interface and to force the brittle support to be subjected to compressive stresses. Therefore, the adopted test set-up was chosen since it was more frequent in literature, for clay and stone elements, and easier to be implemented on the available machine. In order to perform the related data analyses, the applied load was assumed, as usual (see Nakaba *et al.* 2001, Casareto *et al.* 2003, Aiello and Sciolti 2006, Briccoli Bati *et al.* 2007, Camli and Binici 2007), to be equally distributed on the two strips.

Five samples for high-strength carbon reinforcement (CFRP) and five samples for alkali-resistant glass reinforcement (GFRP) were tested.

5.2.1 Materials characterization

Solid clay bricks (nominal dimension 250x120x55 mm), type 11010C produced by Fornaci Giuliane S.p.A. (Cormons–UD, Italy) were used as substrate, and the MBrace®Wet lay-up System as reinforcement. High strength carbon fibres (CFRP) on five specimens and alkali-resistant glass fibres (GFRP) on other five specimens were used. The main bricks properties (average values) are summarized in Table 5.2 (Cartolaro 2004), while the properties of the reinforcement system, obtained from producers datasheets, are reported in Table 5.3.

Table 5.4: Dimensions of the specimen

Brick nominal dimensions			
Length	L_{brick}	250	mm
Width	b_{brick}	120	mm
Thickness	t_{brick}	55	mm
Reinforcement dimensions (single strip)			
Bonded length	L_{b}	200	mm
Strip width	b'_{f}	50	mm
Unbonded length	L_{ub}	30	mm

Figure 5.7: Solid clay brick used

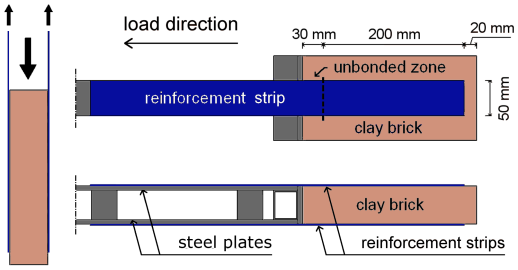

Figure 5.8: Specimen geometry (Panizza *et al.* 2008a)

5.2.2 Experimental test set-up

Each sample was made by a single clay brick (Fig. 5.7) with two strips of externally bonded reinforcement (wet lay-up system), symmetrically applied on the opposite wider surfaces. Each strip was 50 mm wide and was bonded to the brick for 200 mm. An unbonded length of 30 mm, from the limit of the brick next to the loaded end, was imposed in order to minimize edge effects. The geometry of the specimen, reported in Table 5.4, is shown in Figure 5.8.

An universal mechanical press, Galdabini SUN60 (maximum load 600 kN), was used as test machine. Each strip of reinforcement, made by a single layer of fibres and two layers of epoxy resin, was bonded at the loaded end to a steel support connected to the test machine. The brick was fixed to the machine through a steel frame, made by two plates linked by bolts (Fig. 5.9 on the next page).

The load was applied axially and tests were controlled by a displacement rate of 0.2 mm/minute.

On the outer side of one of the two reinforcement strip for each specimen, seven strain gauges were applied, distributed as follows: one on the unbonded zone, next to the loaded end of the reinforcement, and six on the bonded one. To optimize the number of instruments and to monitor the whole bonded region, the strain-gauges were not equally distributed, but less spaced near the loaded end (Fig. 5.10 on the facing page).

5.2.3 Test results

After test, all specimens revealed the complete detachment of the reinforcement from the support. The failure involved the brick surface, where curved cracks and ripping of clay pieces were observed (Fig. 5.11 on page 74).

It was assumed that strain is uniform on the composite cross section, and that is possible to refer mechanical properties to the dry woven: this approach is accepted by many authors

(a) (b)

Figure 5.9: Test machine, on the left, and a sample ready for testing (Panizza *et al.* 2008a)

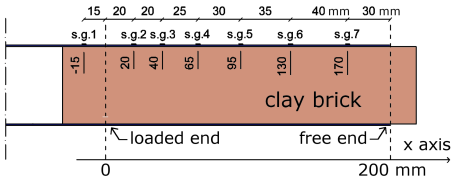

Figure 5.10: Distribution of the strain-gauges (Panizza *et al.* 2008a)

(Chen and Teng 2001, Lu *et al.* 2005) and by some guidelines, such as Italian CNR DT-200 (2004). Another possible approach, which can be found in older papers (e.g. Karbhari and Engineer (1996)), starts from the estimation of equivalent properties, such as tensile strength and elastic modulus, related to the actual area of the reinforcement that includes fibres and adhesive; however, on the basis of the common hypotheses, these two approaches could be considered equivalent (CNR DT-200 2004), on the condition that it is possible to measure the actual thickness of the composite.

Therefore, it was possible to calculate the nominal tensile stress on the textile, defined as the load and cross section area ratio. By coupling the strain measures (obtained from the strain-gauge glued the unbonded region) with the load values, and by assuming the linear elastic behaviour of the composite, it was also possible to evaluate Young's modulus of the reinforcement for each sample (Tab. 5.5 on the following page) through a best fitting involving the linear branch of the load-strain curve, as given in Equation (5.31), where E_f is the longitudinal elastic modulus of the reinforcement, σ and ε are nominal tensile stress on the cross section and the longitudinal strain measured on the unbonded area, P the applied load, b'_f and t_f stand for width and equivalent thickness of a single FRP strip.

Failure loads for both CFRP and GFRP, P_u, are given in Table 5.5 on the next page, along with the failure load per unit width ($P_u/2b'_f$) and the nominal tensile stress on the cross section at failure (σ_u), and plotted in Figure 5.12 on page 75. It is possible to note as specimens strengthened with CFRP showed better performances than GFRP one: the mean failure load in the first case was around 35% higher than the latter. On the other hand, the nominal tensile stresses, evaluated on the reinforcement at failure, were closer to the strength f_t in the case of GFRP (68% in average) than CFRP (64% in average). Concerning the elastic moduli, they showed a quite large scattering, resulting in a mean value higher than the ones reported in the producer's datasheet (22% for CFRP and 25% for GFRP).

$$E_\mathrm{f} = \frac{\sigma}{\varepsilon} = \left(\frac{P}{2b'_\mathrm{f}t_\mathrm{f}}\right) \tag{5.31}$$

(a) Surface of the reinforcement

(b) Ripping of clay pieces

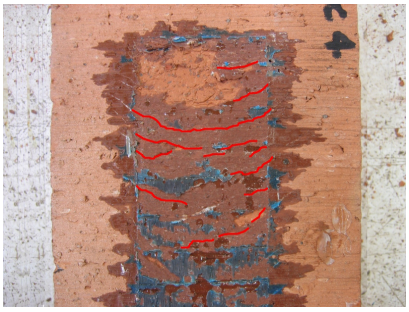

(c) Curved cracks on the brick's surface

Figure 5.11: Reinforcement and support after the test

Table 5.5: Experimental results for carbon and glass reinforcements

Specimen	P_u N	P_u/b_f N/mm	E_f N/mm^2	σ_u N/mm^2	σ_u/f_t
High-strength Carbon MBrace®C1-30					
ShC1	31884	318.8	164419	1932	56%
ShC2	34233	342.3	336439	2075	60%
ShC3	35325	353.3	284991	2141	62%
ShC4	39210	392.1	277511	2376	69%
ShC5	40301	403.0	338456	2442	61%
Average	36191	361.9	280363	2193	64%
Standard deviation	3505	35.1	70696	212	
Coefficient of variation	9.7%	9.7%	25.2%	9.7%	
Alkali-resistant Glass MBrace®G60-AR					
ShG1	23380	233.8	50934	1017	60%
ShG2	27940	279.4	87014	1215	71%
ShG3	27300	273.0	80545	1187	70%
ShG4	26400	264.0	102598	1148	68%
ShG5	28360	283.6	84082	1233	73%
Average	26676	266.8	81035	1160	68%
Standard deviation	1985	19.9	18817	86	
Coefficient of variation	7.4%	7.4%	23.2%	7.4%	

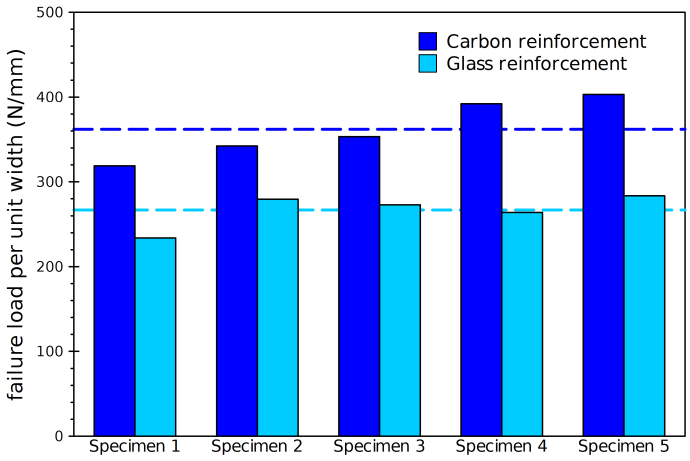

Figure 5.12: Recorded failure loads per unit width

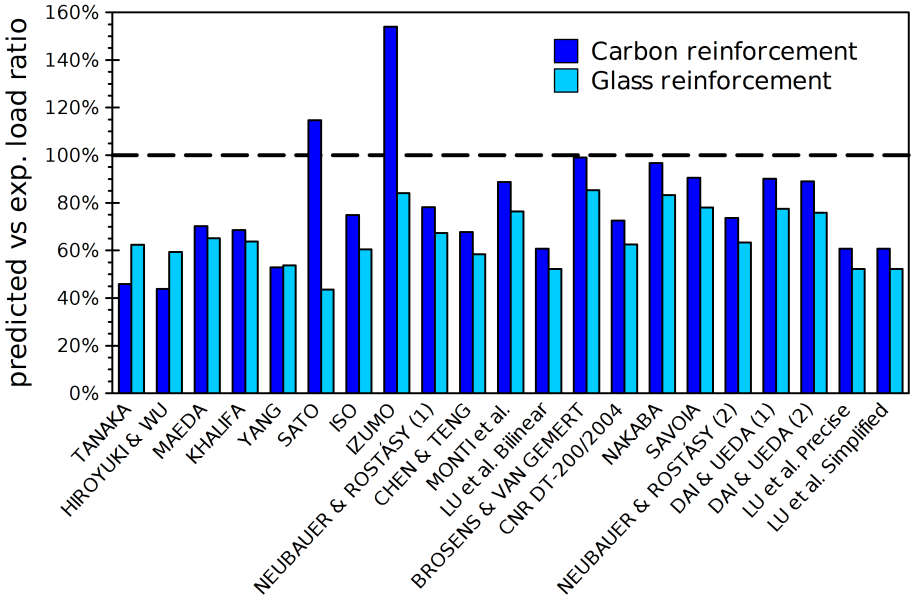

Figure 5.13: Predicted versus experimental load ratio

5.3 Tests analysis

5.3.1 Application of predictive models

Twenty one of the aforementioned models, which provide a prediction of the ultimate failure load P_u, were applied in this study, in order to make a comparison with the experimental data of tests on clay substrate. Results, given in Tables 5.6 on the next page and 5.7 on the following page, are shown in Figure 5.13.

It can be seen that all the predictions, except for the models of Sato and Izumo in the case of carbon reinforcement, underestimate the mean experimental failure load. Moreover, all formulations provide an estimation closer to test results in the case of CFRP than GFRP, except for the Tanaka and Hiroyuki models.

However, results show large differences from model to model: predictions varied between 44% and 154% of experimental mean failure load, for carbon reinforcement, and between 43% and 85%, for glass one, even though it has to be noticed how estimations of fracture energy based models are generally closer to the experimental values.

Table 5.6: Predictions provided by the applied models (CFRP)

Model	$P_{u,pred}$ N	P_u/b_f N/mm	L_e mm	$P_{u,pred}/P_{u,exp}$ %
Tanaka	16634	166		46.0%
Hiroyuki & Wu	15850	159		43.8%
Maeda	25432	254	50	70.3%
Khalifa	24836	248	50	68.6%
Yang	19170	192	100	53.0%
Sato	41490	415	139	114.6%
Iso	27106	271	57	74.9%
Izumo	55704	557		153.9%
Neubauer & Rostásy (1)	28284	283	99	78.2%
Chen & Teng	24532	245	85	67.8%
Monti et al.	32114	321		88.7%
Lu et al. bilinear	21968	220		60.7%
Brosens & van Gemert	35854	359		99.1%
CNR DT-200/2004	26276	263		72.6%
Nakaba	35014	350		96.7%
Savoia	32784	328		90.6%
Neubauer & Rostásy (2)	26648	266		73.6%
Dai & Ueda (1)	32594	326		90.1%
Dai & Ueda (2)	32194	322		89.0%
Lu et al. precise	21968	220		60.7%
Lu et al. simplified	21968	220		60.7%

Table 5.7: Predictions provided by the applied models (GFRP)

Model	$P_{u,pred}$ N	P_u/b_f N/mm	L_e mm	$P_{u,pred}/P_{u,exp}$ %
Tanaka	16634	166		62.4%
Hiroyuki & wu	15850	159		59.4%
Maeda	17356	174	84.2	65.1%
Khalifa	17012	170	84.2	63.8%
Yang	14330	143	100.0	53.7%
Sato	11610	116	96.5	43.5%
Iso	16140	161	34.0	60.5%
Izumo	22430	224		84.1%
Neubauer & Rostásy (1)	17948	179	62.7	67.3%
Chen & Teng	15568	156	54.0	58.4%
Monti et al.	20378	204		76.4%
Lu et al. bilinear	13940	139		52.3%
Brosens & van Gemert	22752	228		85.3%
CNR DT-200/2004	16674	167		62.5%
Nakaba	22218	222		83.3%
Savoia	20804	208		78.0%
Neubauer & Rostásy (2)	16910	169		63.4%
Dai & Ueda (1)	20684	207		77.5%
Dai & Ueda (2)	20216	202		75.8%
Lu et al. precise	13940	139		52.3%
Lu et al. simplified	13940	139		52.3%

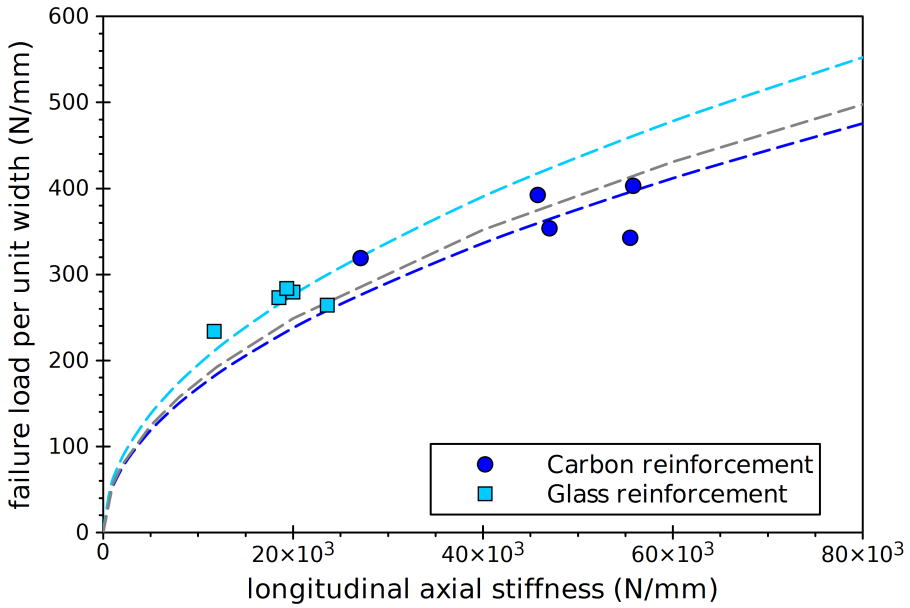

Figure 5.14: Fracture energy regressions based on the square root of the axial stiffness

Table 5.8: Evaluation of fracture energy

Reinforcement	G_f from mean values N/mm	G_f from s.r. fitting N/mm
Carbon	1.42	1.41
Glass	1.91	1.91
All data	1.72	1.55

5.3.2 Fracture energy calibration

Although the aforementioned relations have been developed concerning the bond between FRP and concrete, they are considered significant also for the clay substrate adopted in the present work, since it behaves as a quasi-brittle material as well.

As previously remarked, in most cases the constant value α_T, or α_Y, involved in some models that relate the ultimate load to the fracture energy, has a slight influence on the calculation, since many authors (Savoia *et al.* 2003a, Dai *et al.* 2005, see) report the relation without any constant.

By applying these formulas to the experimental data of this work, it emerges that taking or not into account the parameters α_T or α_Y leads to a difference lower than 2%.

Accordingly with Equation (5.11), it was possible to calibrate the fracture energy G_f through the mean values of failure load and elastic modulus. The estimated quantity, for glass reinforcement, is around 35% higher than carbon one. Moreover, the fracture energy was also calibrated using a regression based on the square root of the axial stiffness (Fig. 5.14); as the Equation (5.11) has been adopted, the regression coefficient is the square root of the doubled fracture energy. Results, reported in Table 5.8, show no significant difference from those directly obtained by mean values, provided that reinforcement types have been separated. Indeed, since the fracture energy should be related only to the substrate properties, there should not be evident reasons, except a better adherence to the experimental data, to separate the calibration process on the basis of the reinforcement type.

5.3.3 Calibration of the bond-slip law

To calibrate the bond-slip law on the experimental results, this combined approach was adopted: tangential stress and interface slip points (τ–s) were obtained from strain-gauges monitoring, while the fracture energy value, G_f, was calculated from failure loads trough Equation 5.11 on page 66. Fracture energy represents a restraint for the bond-slip function (Eq 5.29 on page 70) and allows to reduce the number of free parameters involved in the calibration process.

Assuming to disregard the slip component of the substrate, sufficiently stiffer than composite, the discrete formulas given in Equation (5.32), used before in Valluzzi *et al.* (2003), Panizza *et al.* (2008a) were applied; they allow to manipulate data from devices not uniformly spaced. Notation i-nth indicates the strain-gauge position; the orientation of the x axis makes i increasing from loaded end ($x = 0$) to free end ($x = 200$mm).

Hence, it was possible to couple slip values with the corresponding tangential stresses. As above explained, it is assumed that the bond-slip law should show an ascending segment and a softening behaviour. For the sake of simplicity, instead of using two different mathematical expressions for the ascending and the descending branch, a single function was chosen. Although there could be a slight loss of adherence to experimental data, it reduces the required parameters making easier the fitting process.

The proposed law, easy to integrate and derive, is given in Equation (5.33), where A and B are regression constants, τ is the interface tangential stress and s the composite slip. By applying the calibrated fracture energy value, it was possible to have a fitting function that depends on just one parameter, as shown in Equation (5.34). It is useful to rewrite the law, herein labeled UniPd curve (Panizza *et al.* 2008a), in a normalized form (Eq. 5.35 on the facing page), where $s_0 = 1/B$ and $\tau_\mathrm{max} = \tau(s_0)$ are the coordinates of the point of maximum tangential stress.

After the optimization of the UniPD curves, in the case of carbon reinforcement and glass one, it was possible to calibrate a bilinear law, whose analytical form is reported in Equation (5.12), where s_f is the ultimate strain, related to null stress. This shape is commonly proposed by some guidelines (fib Bulletin 14 2001, CNR DT-200 2004).

Since the bilinear function depends on more parameters, to reduce them the peak tangential stress value, obtained from the fitted Unipd curve, and the calibrated fracture energy were imposed. Figures 5.15 on the next page and 5.16 on page 80 show the optimized curves and the experimental stress-slip data. It can be noticed that carbon reinforcement interface seems to be slight stiffer than glass one.

Tables 5.9 on page 80 and 5.10 on page 81 report the significant values (fracture energy, peak tangential stress with related slip, and ultimate slip) calculated by the fitting process, in the case of CFRP and GFP, respectively; they have been compared with the values estimated through the eleven models based on the fracture energy prediction previously mentioned.

Estimated values vary into a quite wide range. It has to be noticed that not all models provide significant differences from carbon to glass reinforcement; in particular, the difference between the fracture energy values experimentally calibrated, in the case of CFRP and GFRP, is not in agreement with most predictions.

$$\tau_i = \tau(x_i) = \frac{1}{2} E_\mathrm{f} t_\mathrm{f} \left(\frac{\varepsilon_i - \varepsilon_{i+1}}{x_{i+1} - x_i} + \frac{\varepsilon_{i-1} - \varepsilon_i}{x_i - x_{i-1}} \right) \tag{5.32a}$$

$$s_i = s(x_i) = s_{i+1} + \frac{1}{2} \left(\varepsilon_i + \varepsilon_{i+1} \right) \left(x_{i+1} - x_i \right) \tag{5.32b}$$

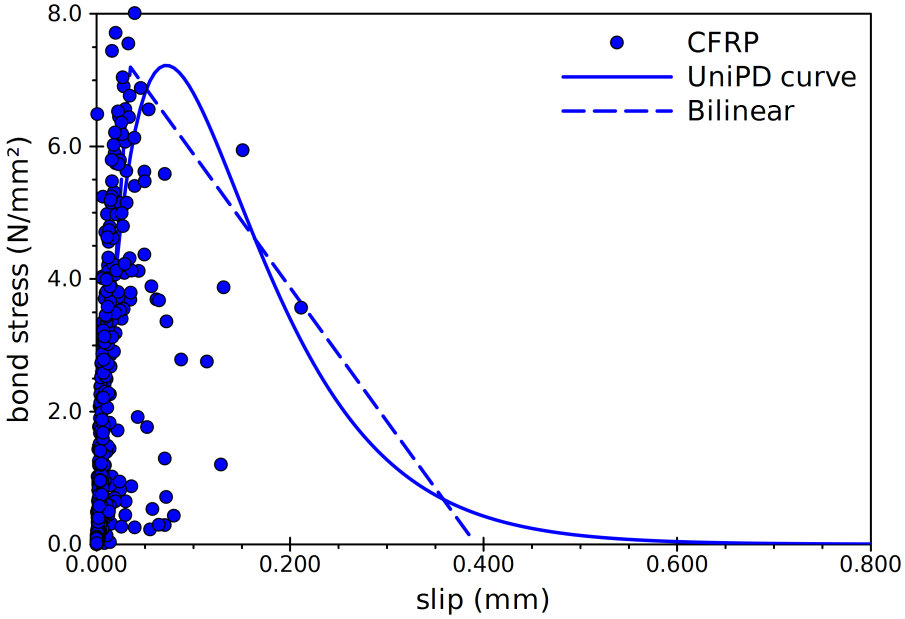

Figure 5.15: Calibrated bond-slip laws for CFRP

$$\tau(s) = Ase^{-Bs} \tag{5.33}$$

$$\int_0^\infty \tau(s) = \frac{A}{B^2} \qquad \Rightarrow \qquad A = B^2 G_{\mathrm{f}} \tag{5.34a}$$

$$\tau(s) = B^2 G_f s e^{-Bs} \tag{5.34b}$$

$$\tag{5.34c}$$

$$\tau(s) = \tau_{\max} \left(\frac{s}{s_0} \right) e^{1-\frac{s}{s_0}} \tag{5.35}$$

5.4 FE analyses of bond

The bond behaviour of CFRP and GFRP laminates on brick masonry concerning the test specimens was studied by means of the finite element method. Simulations were performed using a refined commercially available non-linear finite element code, DIANA 9.3 (TNO Diana BV. 2008).

In order to reduce the computational burden, the 3D FRP-to-brick specimen was modelled as a 2D plane stress problem by using eight-node quadrilateral isoparametric element for both FRP and brick materials. Due to symmetry, only half of the specimen was modelled. Therefore, suitable boundary conditions were assigned to the brick and the FRP (Fig. 5.17 on page 82).

The Wet lay-up System can be modelled according with three options (Lu *et al.* 2005): (a) a plate with its thickness being equal or similar to the actual thickness of the laminate including all adhesives, but with fibres concentrated in a thickness equal to the nominal thickness of the sheet laying in the middle of the plate, (b) a plate with its thickness being

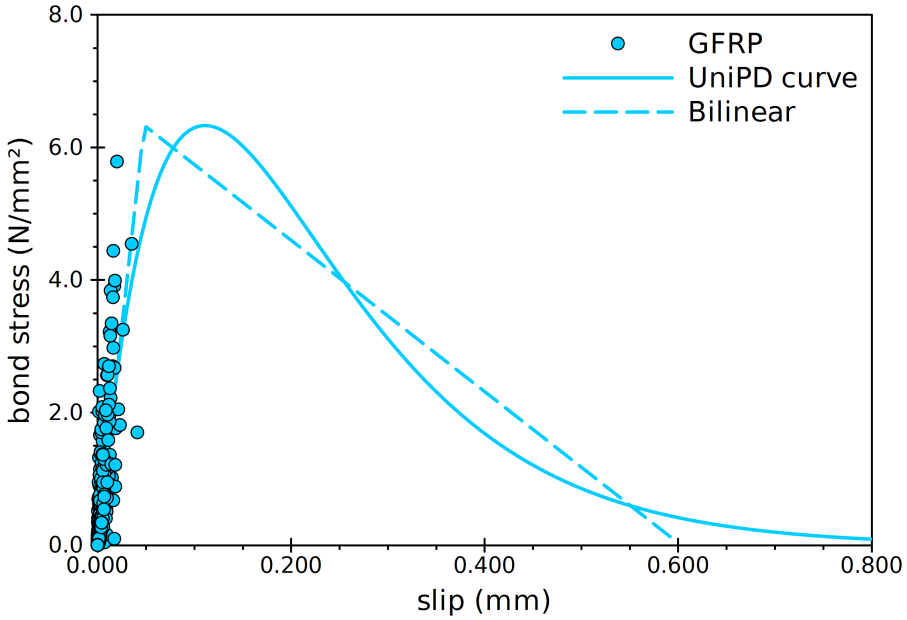

Figure 5.16: Calibrated bond-slip laws for GFRP

Table 5.9: Significant values for local bond of CFRP

CURVE	G_f N/mm	τ_{max} N/mm^2	s_0 mm	s_f mm
UniPd fitting	1.42	7.22	0.072	–
Bilinear fitting	1.42	7.22	0.034	0.392
Monti et al.	1.11	5.37	0.046	0.415
Lu et al. Bilinear	0.52	3.73	0.048	0.280
Brosens & V. G.	1.39	2.71	0.012	1.025
CNR	0.75	7.46	0.056	0.200
Nakaba et al.	1.32	7.08	0.065	–
Savoia et al.	1.16	7.08	0.051	–
Neubauer and R.	0.77	5.69	0.270	–
Dai and Ueda (1)	1.15	8.58	0.103	–
Dai and Ueda (2)	1.12	6.41	0.061	–
Lu et al. Precise	0.52	3.73	0.054	–
Lu et al. Simplif.	0.52	3.73	0.048	–

Table 5.10: Significant values for local bond of GFRP

Curve	G_f N/mm	τ_{max} N/mm^2	s_0 mm	s_f mm
UniPd fitting	1.91	6.33	0.111	–
Bilinear fitting	1.91	6.33	0.048	0.603
Monti et al.	1.11	5.37	0.046	0.415
Lu et al. Bilinear	0.52	3.73	0.048	0.280
Brosens and V. G.	1.39	2.71	0.012	1.025
CNR	0.75	7.46	0.056	0.200
Nakaba et al.	1.32	7.08	0.065	–
Savoia et al.	1.16	7.08	0.051	–
Neubauer and R.	0.77	5.69	0.270	–
Dai and Ueda (1)	1.15	7.10	0.107	–
Dai and Ueda (2)	1.10	5.69	0.067	–
Lu et al. Precise	0.52	3.73	0.054	–
Lu et al. Simplif.	0.52	3.73	0.048	–

equal or similar to the actual thickness of the laminate including all adhesives, with the fibres assumed to be evenly distributed across the plate thickness; and (c) a plate with a nominal thickness (generally the thickness of the fibre sheet) without considering the adhesive. In general, option (a) and (b) are more suitable for modelling FRP laminates since both material properties of fibre and matrix are explicitly considered. In order to examine the differences between options (a) and (b), a comparison of the finite element results was carried out. In the case of option (a), the fibres were modelled by using a full-bonded reinforcement element available in the finite element program, that was inserted in the centreline of the composite material. In the case of option (b), suitable homogenised mechanical properties for the FRP laminates were calculated from the experimental data.

The numerical models are completed by the introduction of six-node finite element interfaces between the FRP laminate and the brick. Therefore, the non-linear behaviour was condensed and modelled by the interface element. The calibrated exponential and bilinear bond stress-slip laws were assigned to the interface element according with the data obtained from Tables 5.9 on the facing page and 5.10 and Figures 5.15 on page 79 and 5.16 on the preceding page. In the finite element model, both FRP and brick are considered as isotropic elastic material.

Summaries of the material properties of brick and FRP used in the finite element analysis are reported in Tables 5.2 on page 71 and 5.3 on page 71, whereas Figure 5.18 on the following page shows the mesh used the for finite element models.

Non-linear analyses were performed by using an energy based convergence criterion together with arc-length control method. Monotonic incremental load steps were assigned to the loading end of the FRP laminate. The equilibrium of the system was calculated and the corresponding reactions, internal stresses/strains and deformations of the specimen were obtained.

5.4.1 Concentrated versus distributed fibres

The numerical results, obtained using the exponential bond stress – slip law herein labelled UniPD curve, of the maximum loaded end displacement of FRP (s) and the corresponding load (P) of models with concentrated fibre and distributed fibre are shown in Figures 5.19 on page 83 and 5.20 on page 83.

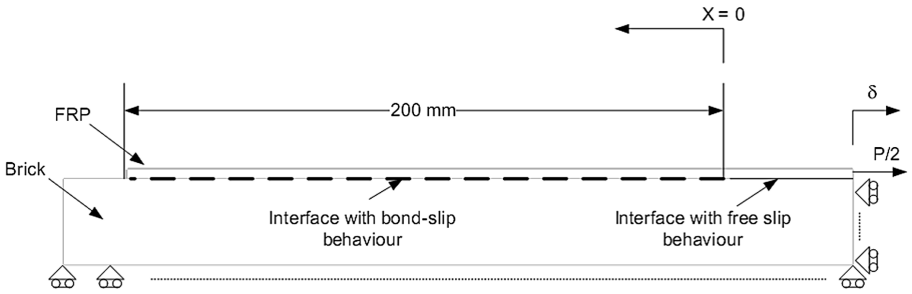

Figure 5.17: Boundary conditions of FE model

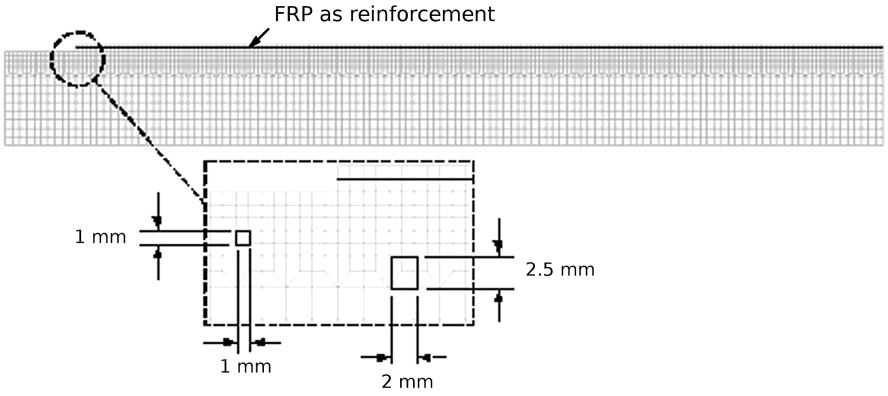

Figure 5.18: Typical fine mesh used in FE models

For the CFRP specimens, the maximum loaded end displacement and the maximum load for both models are almost the same. For the GFRP specimen, it is observed that the model with distributed fibre showed a slightly increase in maximum displacement and maximum load. Nevertheless, the results obtained in both models presented absolutely negligible differences in term of both maximum loaded end displacement and maximum load.

The finite element strain results for both CFRP and GFRP specimens, derived from the models with concentrated and distributed fibres, were compared to the experimental data at three different load levels, namely 30%, 90% and 100% of maximum loading level (Fig. 5.21 on page 84). The numerical results showed a very good agreement with the experimental ones in both cases of concentrated and distributed reinforcement fibres. Therefore, it can be concluded that the two numerical approaches lead almost to the same results, that match well with the experimental data, in the case of both CFRP and GFRP specimens (Lam 2009). Consequently, the distributed fibres approach might be preferred due to its slightly lower computational burden.

5.4.2 Exponential versus bilinear bond stress - slip law

The finite element results of the maximum loaded end displacement of FRP (s) and the corresponding load (P) obtained with the exponential-based (UniPD curve) and bilinear bond stress – slip laws are showed in Figures 5.22 on page 85 and 5.23 on page 86.

The maximum loaded end displacement and maximum load of GFRP and CFRP laminates are practically coincident for both exponential and bilinear bond stress – slip law. However, the model with the bilinear bond law showed a slightly increase in maximum displacement and maximum load. For CFRP laminates the average ultimate loads ($P_{\mathrm{u,ave}}$) predicted by the models with exponential and bilinear bond law were the 95% and 96% of the experimental

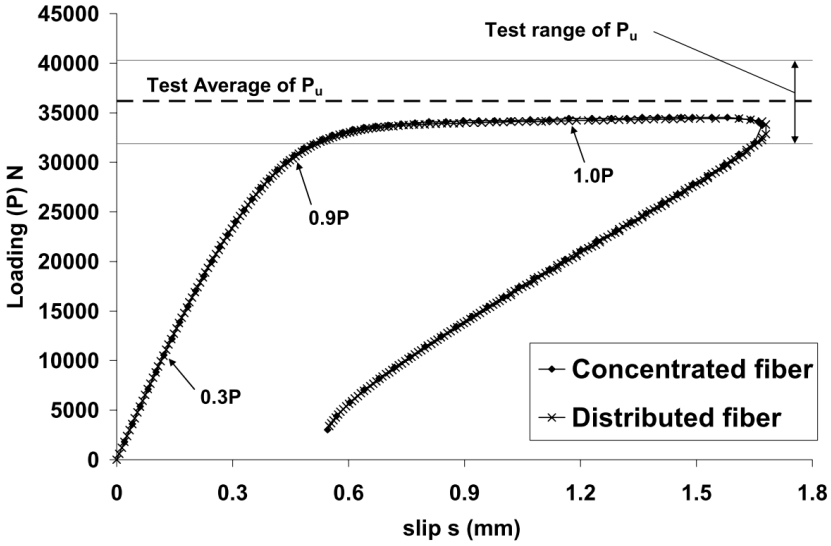

Figure 5.19: Comparison of the load versus loaded end displacement of CFRP specimens with exponential bond stress-slip law (concentrated versus distributed fibres)

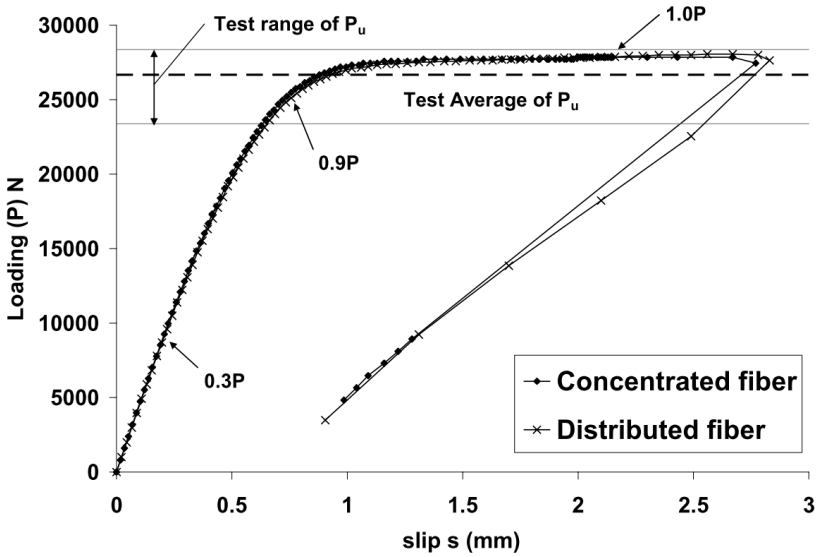

Figure 5.20: Comparison of the load versus loaded end displacement of GFRP specimens with exponential bond stress-slip law (concentrated versus distributed fibres)

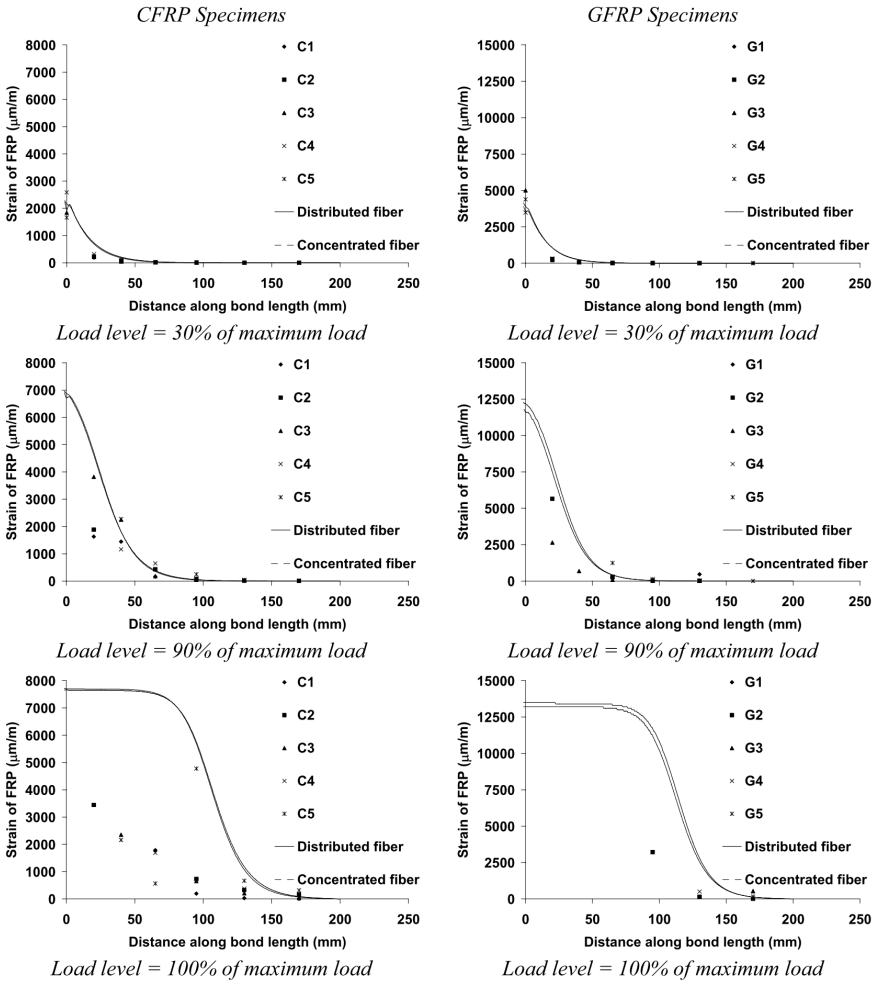

Figure 5.21: Comparison of numerical and experimental strain results for CFRP (left) and GFRP specimens (right) obtained with the exponential bond-slip law (concentrated versus distributed fibres)

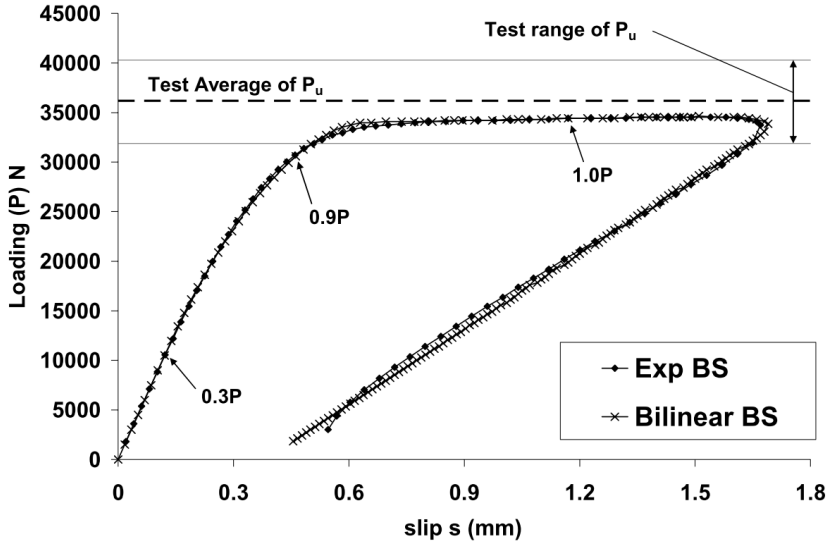

Figure 5.22: Comparison of load versus loaded end displacement of CFRP specimens (exponential versus bilinear bond-slip behaviour)

mean failure load, respectively, whereas for GFRP laminates the predicted average ultimate loads ($P_{\mathrm{u,ave}}$) with exponential and bilinear bond law were respectively the 104% and 106% of experimental one. Therefore, it can be concluded that both the bond laws lead to totally equivalent results in terms of maximum loaded end displacement and maximum load.

The finite element strain results of the models with exponential and bilinear bond law are showed in Figure 5.24 on the following page, compared to the experimental data, for both CFRP and GFRP specimens, at three different load levels (30Therefore, even a simple bilinear bond stress – slip law may be sufficient to properly describe the bond phenomenon between clay bricks (and likely any other quasi brittle material) and EB-FRP laminates, without resorting to more sophisticated local laws.

5.4.3 Comparison with the analytical solution

The finite element results were compared with the prediction obtained by the full-range analytical solution proposed by Yuan *et al.* (2001, 2004), that makes use of a bilinear bond-slip law which features a linear ascending branch followed by a linear descending one. The finite element results of load versus slip curves were compared with the analytical solution, in which the FRP is considered as a homogenous material with a homogenised elastic modulus. Thus, the results given by the FE model with distributed fibres were used for comparison. Moreover, in the analytical solution, the actual width of the FRP laminate and brick can be assigned; therefore, two results, one with the width ratio equals to 50/120 and the other with the width ratio equals to 1, are included for comparison.

Figures 5.25 on page 87 and 5.25 on page 87 show the results obtained from the finite element analysis and the analytical solution: it can be noticed as the analytical solution matches very well with the FE results, thus validating the use of the analytical model.

In general, for the maximum load, the results derived from the analytical solution are slightly lower than those obtained through the finite element analysis (about 3% lower for both specimens). For the maximum displacement, the results obtained from the analytical solution are equivalent to those given by the finite element analysis. Furthermore, it can be observed that the analytical maximum loads evaluated using the width ratio of 50/120 are

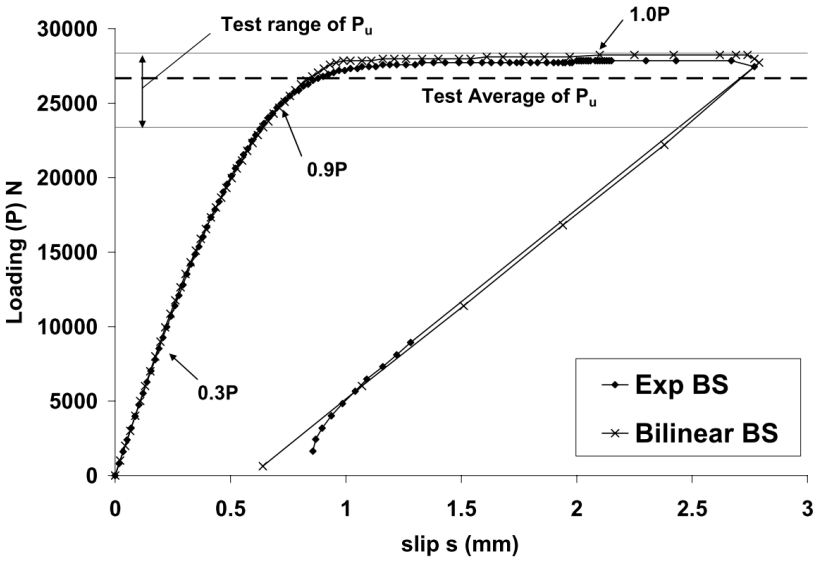

Figure 5.23: Comparison of load versus loaded end displacement of GFRP specimens (exponential versus bilinear bond-slip behaviour)

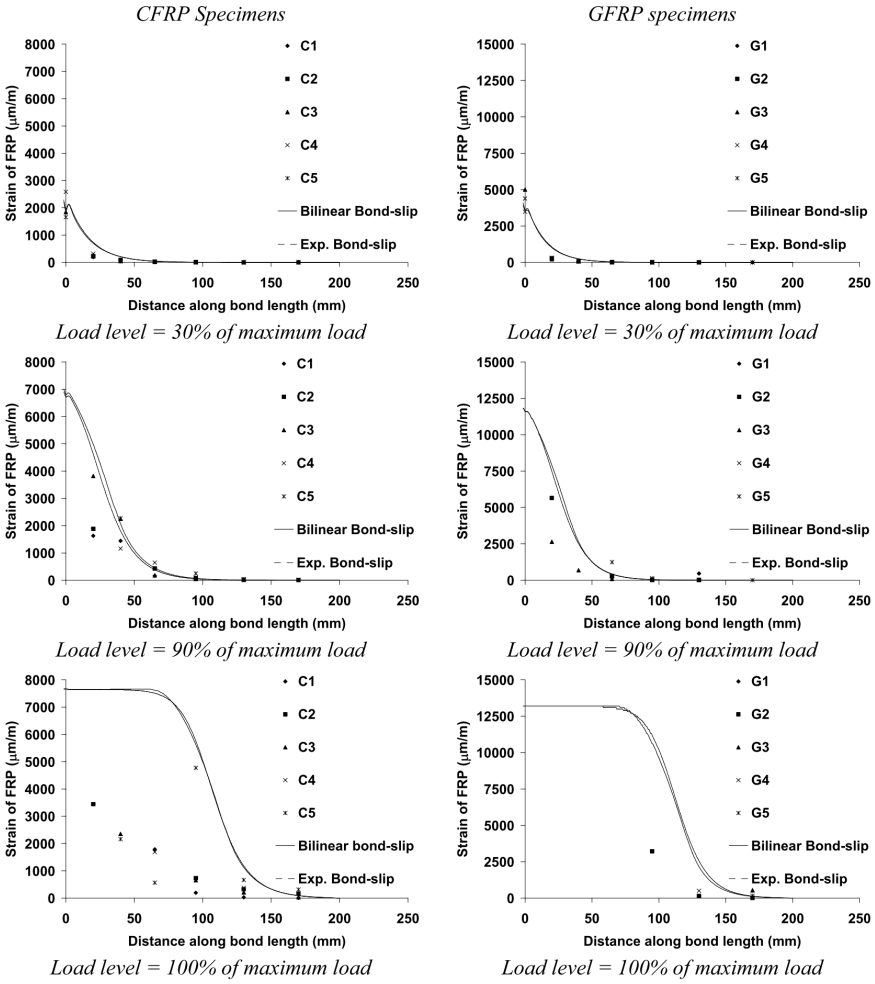

Figure 5.24: Comparison of numerical and experimental strain results for CFRP (left) and GFRP specimens (right) obtained (exponential versus bilinear bond-slip law)

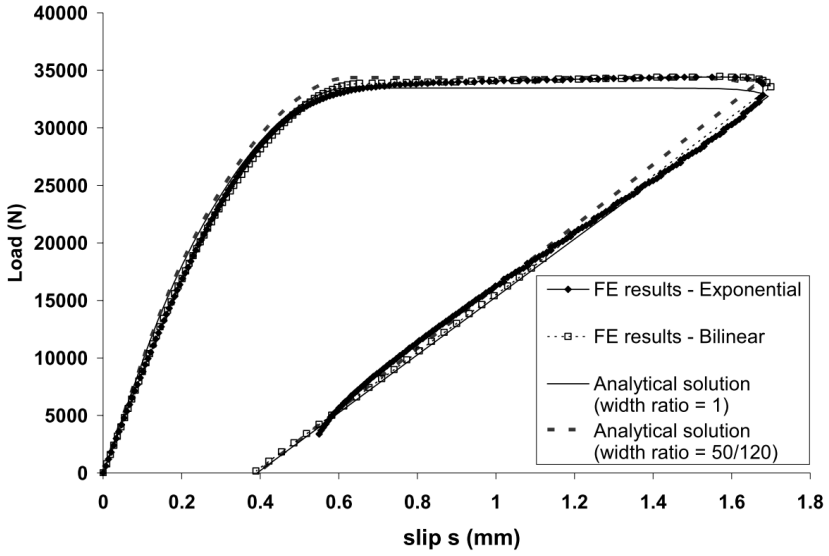

Figure 5.25: Comparison of FE results and analytical solution for CFRP specimens

slightly larger than those obtained with the width ratio of 1 (about 3% higher for CFRP specimens and 1% higher for GFRP specimens). The corresponding maximum displacement obtained from the analytical solutions that considered the width ratio of 50/120 are slightly lower than that obtained adopting the width ratio of 1 (about 2% lower for CFRP specimens and 1% lower for GFRP specimens).

5.4.4 FEA and analytical results: effect of the dimension of the bonded length

In this part of the work, several finite element models based on the distributed fibres concept were implemented with four different bond lengths, namely 80 mm, 120 mm, 160 mm and 200 mm. The bilinear bond-slip curve with the corresponding interfacial fracture energy was used, for both the FE model and the analytical solution proposed by Yuan *et al.* (2004).

The numerical and analytical results for CFRP and GFRP laminates are presented and compared in Figures 5.27 on page 89 and 5.28 on page 89, respectively.

The results obtained from the analytical solution were stiffer than those obtained from finite element analyses, as the predicted maximum loaded end displacements were slightly smaller in the first case than in the latter. For the CFRP models with short bond length a higher numerical load than the analytical one was obtained. As the bond length increases, the difference between the finite element and analytical solutions becomes negligible. Nevertheless, the results obtained from the analytical solution matched well with the finite element results, in terms of both load and loaded end displacement, particularly in the case of the GFRP models that showed a very close agreement.

As it can be observed (Fig. 5.27 on page 89 and 5.28 on page 89), bond lengths longer than 80 mm do not increase the maximum load, due to the fact that 80 mm was already longer than the minimum bond length requirement for both specimens, that can be calculated according to the model proposed by Yuan *et al.* (2001, 2004): the evaluation gives 70.13 mm and 59.41 mm for CFRP and GFRP specimens, respectively. When the bond length is smaller than the minimum required, the maximum load capacity of the joint can not be

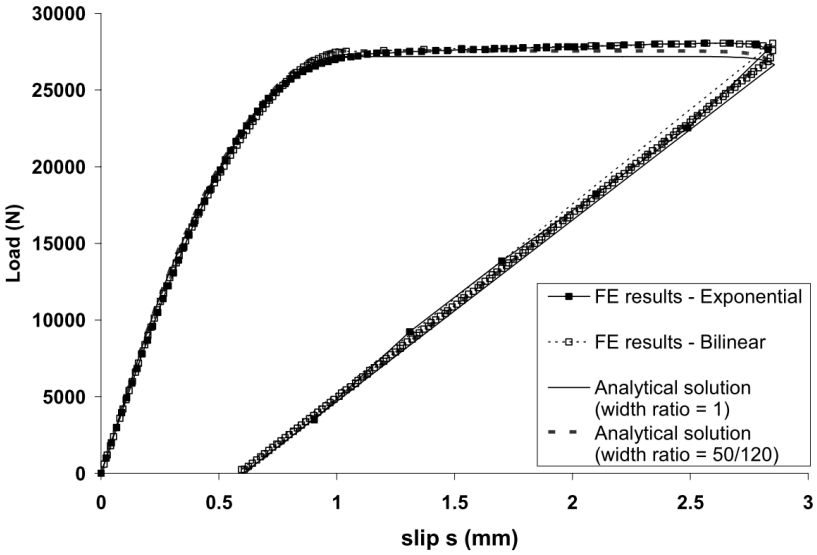

Figure 5.26: Comparison of FE results and analytical solution for GFRP specimens

achieved. However, increasing the bond length has a significant effect only on the maximum loaded end displacement of the joint.

5.5 Calibration of the CNR DT-200 provision for estimating the fracture energy

Concerning the problem of plate-end debonding, CNR DT-200 guidelines propose an approach derived from the current concrete-based formulations. An expression (Eq 5.36 on page 90) to evaluate the effective length L_e is provided, which is the same included in fib Bulletin 14 (2001) for CFRP reinforcement and derived by Neubauer and Rostásy modifying a proposal of Holzenkämpfer; E_f and t_f stand for elastic modulus and equivalent thickness of the fibres. The characteristic value of fracture energy, $\Gamma_{F,k}$, is also proposed as proportional to the square root of the product of characteristic compressive, f_{ck}, and tensile, f_{ctm}, strength of concrete (Eq. 5.37 on page 90), similarly to what fib Bulletin 14 (2001) proposes. The k_b factor takes into account the possible size effects, and it has been reported by many authors (see Eq. 5.39 on page 90, where b_f and b are the reinforcement and substrate width, respectively), whereas the k_G factor has been experimentally evaluated as 0.064 (mean value) $\pm$ 0.023 (standard deviation), with 0.026 as characteristic value and, therefore, 0.03 as design proposal (CNR DT-200 2004). Finally, the design parameter is given as a limit value of tensile stress for the reinforcement, substantially deduced by dividing the ultimate failure load evaluated through Eq. (5.11) by the equivalent fibres area (Eq. 5.38 on page 90, where $\gamma_{f,d}$ and γ_c are partial factors related to the failure mechanism and the concrete material).

The same approach is adopted in the case of masonry substrate, since the only difference, excluded the different partial factor γ_M related to masonry, is given by the expression of the characteristic fracture energy $\Gamma_{F,k}$ (Eq 5.37 on page 90). Instead of using the size-effect parameter k_b, only one coefficient, c_1, is proposed. This moves from the fact that, in the case of application on masonry walls, the width ratio between reinforcement and substrate is not clearly defined, and probably less significant, as in the case of reinforced concrete beams.

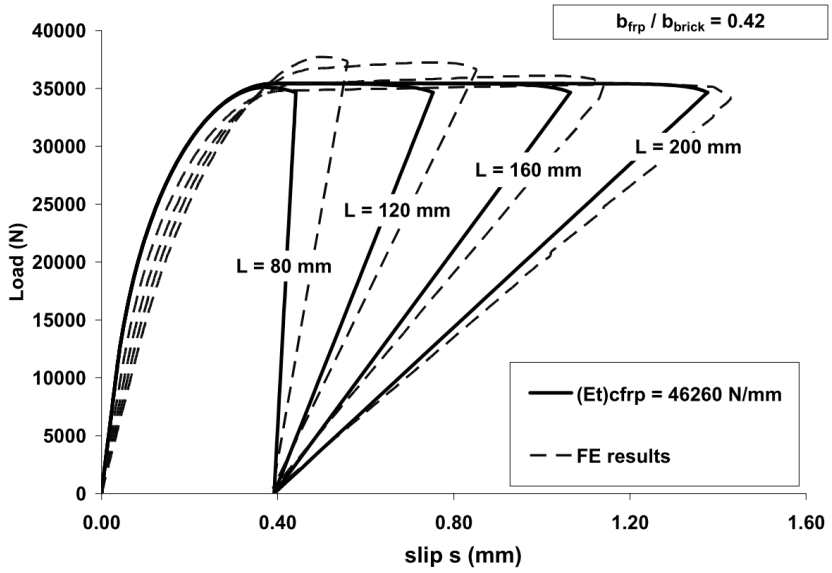

Figure 5.27: Load versus displacement curve of CFRP specimens with different bond lengths (Analytical versus finite element results)

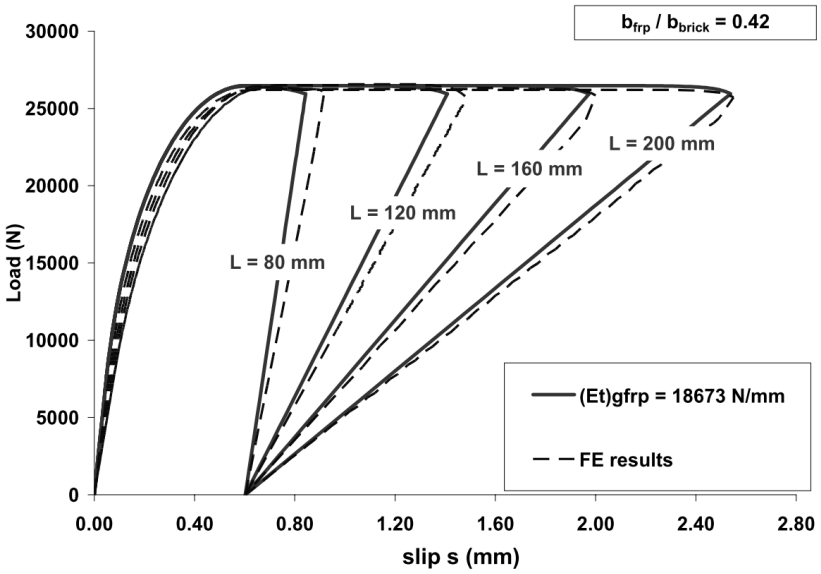

Figure 5.28: Load versus displacement curve of GFRP specimens with different bond lengths (Analytical versus finite element results)

Another remark is related to the substitution of f_{ctm}, mean tensile strength of concrete, with f_{mtm}, which is defined as the tensile strength of masonry, possibly equal to $0.1 f_{\mathrm{mk}}$, but, at the same time, as the mean tensile strength of the elements that compose the masonry, since they assure the development of the resisting mechanism.

$$L_{\mathrm{e}} = \sqrt{\frac{E_{\mathrm{f}} t_{\mathrm{f}}}{2 f_{\mathrm{ctm}}}} \qquad \text{concrete} \tag{5.36a}$$

$$L_{\mathrm{e}} = \sqrt{\frac{E_{\mathrm{f}} t_{\mathrm{f}}}{2 f_{\mathrm{mtm}}}} \qquad \text{masonry} \tag{5.36b}$$

$$\Gamma_{\mathrm{F,k}} = k_{\mathrm{G}} k_{\mathrm{b}} \sqrt{f_{\mathrm{ck}} f_{\mathrm{ctm}}} \qquad \text{concrete} \tag{5.37a}$$

$$\Gamma_{\mathrm{F,k}} = c_1 \sqrt{f_{\mathrm{mk}} f_{\mathrm{mtm}}} \qquad \text{masonry} \tag{5.37b}$$

$$f_{\mathrm{fdd}} = \frac{1}{\gamma_{\mathrm{f,d}} \sqrt{\gamma_{\mathrm{c}}}} \sqrt{\frac{2 E_{\mathrm{f}} \Gamma_{\mathrm{F,k}}}{t_{\mathrm{f}}}} \qquad \text{concrete} \tag{5.38a}$$

$$f_{\mathrm{fdd}} = \frac{1}{\gamma_{\mathrm{f,d}} \sqrt{\gamma_{\mathrm{M}}}} \sqrt{\frac{2 E_{\mathrm{f}} \Gamma_{\mathrm{F,k}}}{t_{\mathrm{f}}}} \qquad \text{masonry} \tag{5.38b}$$

$$k_{\mathrm{b}} = 1.125 \sqrt{\frac{2 - b_{\mathrm{f}}/b}{1 + b_{\mathrm{f}}/400}} \qquad \text{Neubauer \& Rostásy (Chen and Teng 2001)} \tag{5.39a}$$

$$k_{\mathrm{b}} = 1.06 \sqrt{\frac{2 - b_{\mathrm{f}}/b}{1 + b_{\mathrm{f}}/400}} \qquad \text{fib Bulletin 14 (2001)} \tag{5.39b}$$

$$k_{\mathrm{b}} = \sqrt{\frac{2 - b_{\mathrm{f}}/b}{1 + b_{\mathrm{f}}/b}} \qquad \text{Chen and Teng (2001)} \tag{5.39c}$$

$$k_{\mathrm{b}} = \sqrt{1.5 \frac{2 - b_{\mathrm{f}}/b}{1 + b_{\mathrm{f}}/100}} \qquad \text{Monti (Chen and Teng 2001)} \tag{5.39d}$$

$$k_{\mathrm{b}} = \sqrt{\frac{2.25 - b_{\mathrm{f}}/b}{1.25 + b_{\mathrm{f}}/b}} \qquad \text{Lu } \textit{et al.} \text{ (2004)} \tag{5.39e}$$

$$k_{\mathrm{b}} = \sqrt{\frac{2 - b_{\mathrm{f}}/b}{1 + b_{\mathrm{f}}/400}} \qquad \text{CNR DT-200 (2004)} \tag{5.39f}$$

Besides the ten samples tested at the University of Padova, which results have been above presented, data of other shear tests available in literature were collected to the aim of calibrating the fracture energy coefficient c_1 for masonry substrates.

Overall 78 tests were considered, 68 of which were taken into account for the calculations, since the unwanted failure modes, such as fibres breaking or support rupture, were excluded: 29 tests on solid clay bricks, but Briccoli Bati (2007, 2009) reports only average results, 20 reinforced with carbon and 9 with glass fibres (Briccoli Bati *et al.* 2007, Briccoli Bati and Rovero 2009, Capozucca 2010, Faella *et al.* 2009, Grande *et al.* 2008, Panizza *et al.* 2008a); 4 tests on hollow clay blocks (Camli and Binici 2007), reinforced with carbon fibres; 18 tests on natural stones (calcarenite, Naples tuff, leccese stone), 15 reinforced with carbon and 3

with glass fibres (Aiello and Sciolti 2006, Faella *et al.* 2009); finally, 17 tests on masonry prisms, 6 reinforced with aramidic, 5 carbon and 6 glass fibres (Basilio 2007, Casareto *et al.* 2003). Data are reported in details within the Appendix.

Three procedures were adopted to calibrate the c_1 coefficient: the first and the second are based on a regression of the experimental points depending on a single parameter (Eq. 5.40, obtained from 5.11 on page 66 modified by adopting a linear behaviour for the reinforcement, in order to express the ultimate load as a function of the strain at failure $\varepsilon_{\max}$), the third consists in the calculation of the average value, as previously done by other authors (Ferracuti *et al.* 2007a) in the case of concrete.

Where available, mean experimental values for the mechanical properties of substrate and reinforcement were used for the calibrations.

Figure 5.29 on the following page gives the experimental data in terms of strain at failure $\varepsilon_{\max}$ and abscissa ξ (see Eq. 5.40). It can be noticed that, rather unexpectedly, points related to masonry prisms show a slightly better behaviour.

The results of the calibration of the c_1 factor are reported in Table 5.11 on the following page, while Figures 5.30 on the next page and 5.31 on page 93 show the regression curves compared to the experimental points. The knowledge of the actual elastic modulus of the reinforcement, usually not reported by papers that generally provide only the manufacturer's value, could lead to a more refined calibration, as the trend of UniPadova samples clearly show.

As a matter of fact, it cannot be defined an unique method to calibrate the c_1 coefficient, as the results (Tab. 5.11 on the next page) are quite different: this could be imputed to the still limited database, compared to the wide variability of the materials properties, and to the lack of some experimental data that were replaced by average values taken from literature or datasheets or evaluated by means of common design formulas. However, it can be observed that tests on stone and clay elements show a similar behaviour, while masonry prisms seem to offer sligthly higher performances, evaluated on the basis of the previously presented procedure.

For comparison, data related to the shear tests on concrete specimens, reported by Lu *et al.* (2005), were treated using the same procedures previously applied, and superimposed to the masonry data (Fig. 5.32 on page 93).

Finally, the same methods have been applied to calibrate the k_{G} coefficient, adopting the formulations proposed for concrete substrate by CNR DT-200 (2004). Results are given in Table 5.12 on page 93 and shown in Figures 5.33 on page 94 and 5.34 on page 94.

$$\varepsilon_{\max} = \sqrt{c_1}\frac{1}{\xi} \qquad \text{where} \quad \xi = \sqrt{\frac{E_{\mathrm{f}} t_{\mathrm{f}}}{2\sqrt{f_{\mathrm{c}} f_{\mathrm{t}}}}} \tag{5.40a}$$

$$\varepsilon_{\max}^2 = c_1\frac{1}{\xi'} \qquad \text{where} \quad \xi' = \xi^2 \tag{5.40b}$$

5.6 Conclusive remarks

- Experimental failure loads have been compared with twenty-one predictive models developed for concrete substrate. All predictions, except two in the case of CFRP, underestimate the results of the tests; models, except two in the case of GFRP, seem to work better for carbon reinforcement. However, the strength predictions vary into an wide range (between 44% and 154% of experimental mean failure load for CFRP, 43%

Table 5.11: Calibrated values for the c_1 coefficient

Data set	First regr. $\varepsilon_{max} - \xi$	Second regr. $\varepsilon^2_{max} - \xi'$	Average values
UniPadova:	0.170	0.184	0.157 ± 0.036
Bricks + stones:	0.124	0.166	0.103 ± 0.057
Bricks only:	0.151	0.177	0.127 ± 0.054
Stones only:	0.039	0.035	0.059 ± 0.034
Prisms only:	0.359	0.395	0.353 ± 0.152
All data (prisms + elements):	0.171	0.204	0.165 ± 0.141

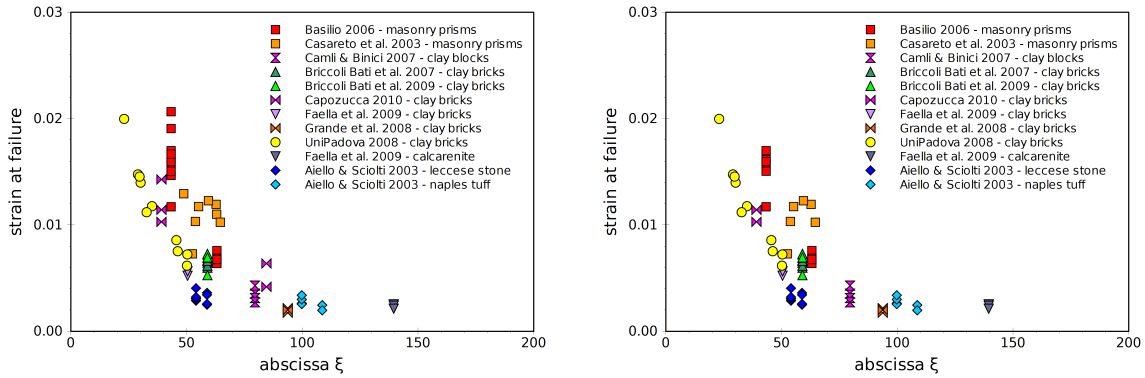

(a) All the collected data **(b)** Filtered data

Figure 5.29: Shear tests on masonry: experimental results

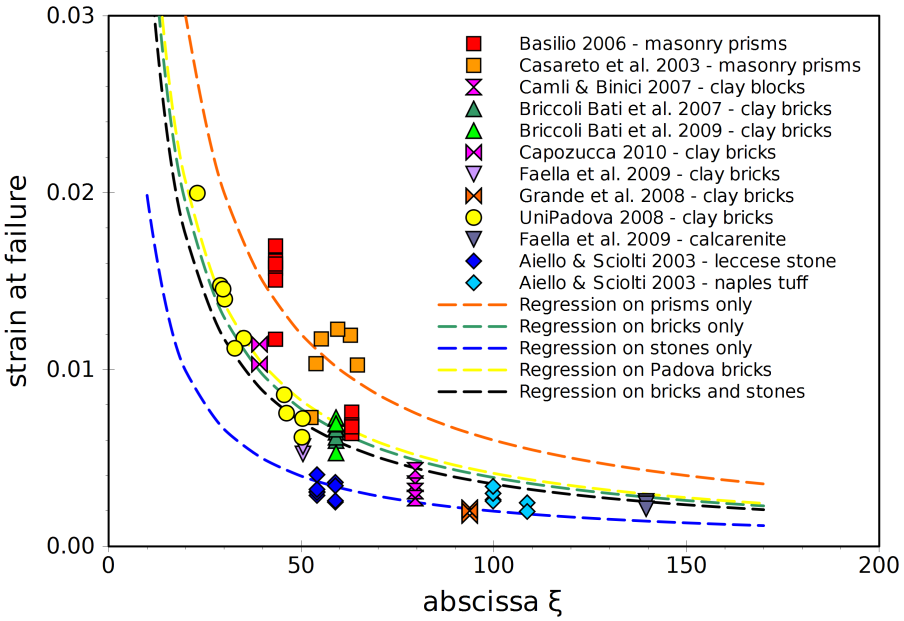

Figure 5.30: c_1 regressions (first type) on the experimental data

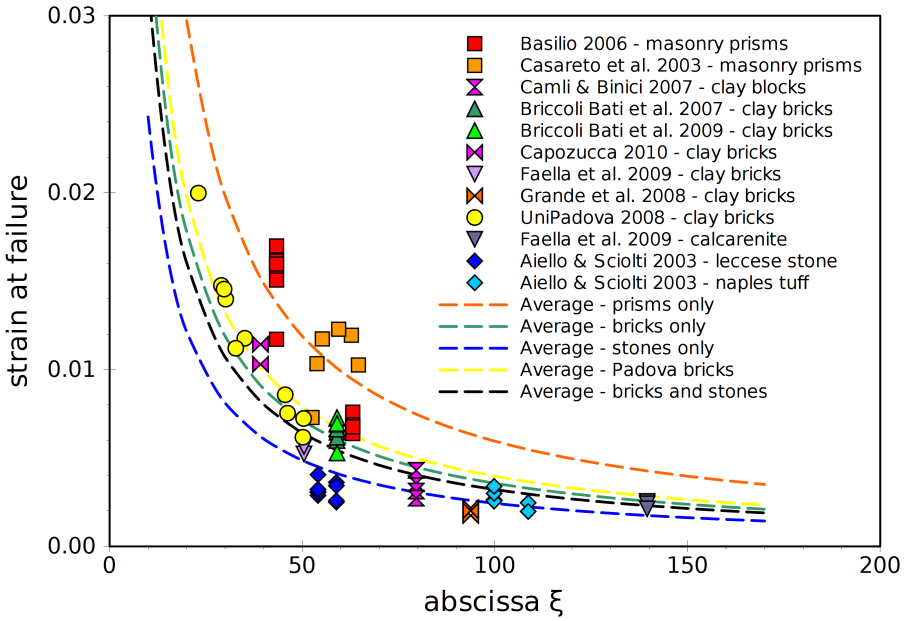

Figure 5.31: Hyperbola branches based on the average values of c_1

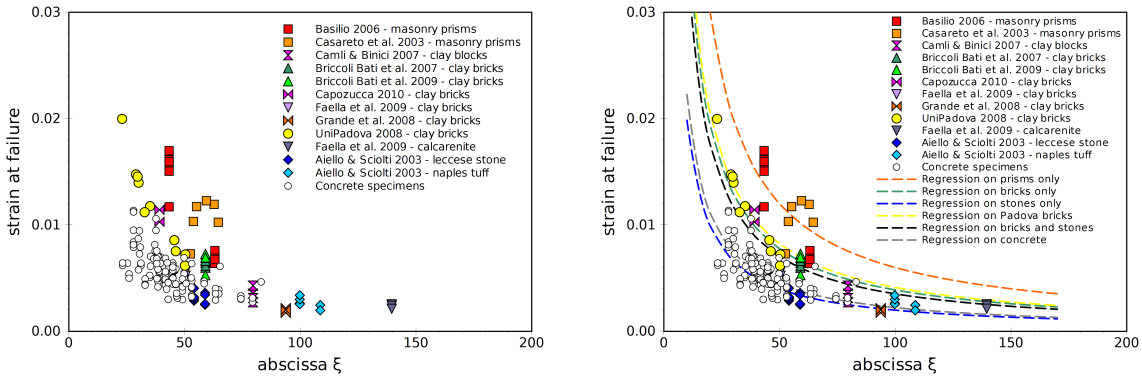

(a) Concrete and masonry data

(b) Comparison of the regression curves

Figure 5.32: Shear tests on masonry compared to concrete: calibration of c_1

Table 5.12: Calibrated values for the k_G coefficient

Data set	First regr. $\varepsilon_{max} - \xi$	Second regr. $\varepsilon_{max}^2 - \xi'$	Average values
UniPadova:	0.143	0.155	0.132 ± 0.030
Bricks + stones:	0.106	0.141	0.088 ± 0.047
Bricks only:	0.126	0.149	0.105 ± 0.044
Stones only:	0.036	0.031	0.059 ± 0.037
Prisms only:	0.287	0.312	0.289 ± 0.131
All data (prisms + elements):	0.145	0.173	0.139 ± 0.116

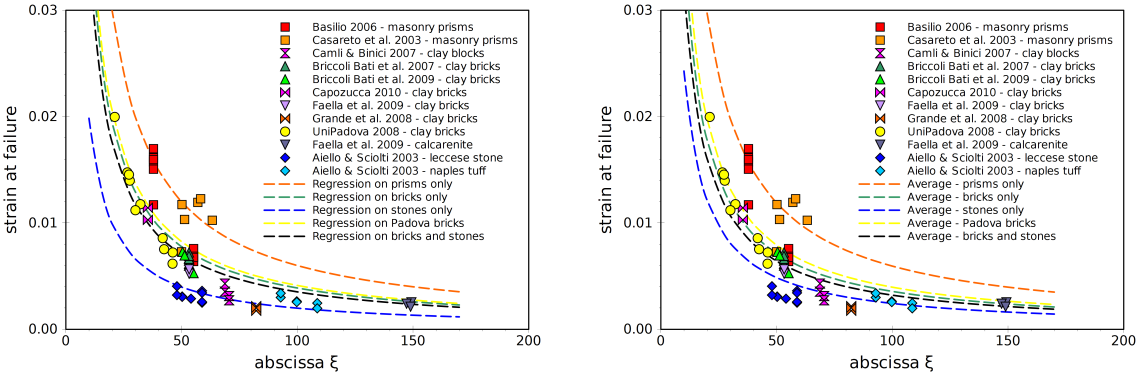

(a) k_G regressions (first type)

(b) Hyperbola branches based on the average values of k_G

Figure 5.33: Shear tests on masonry: calibration of k_G

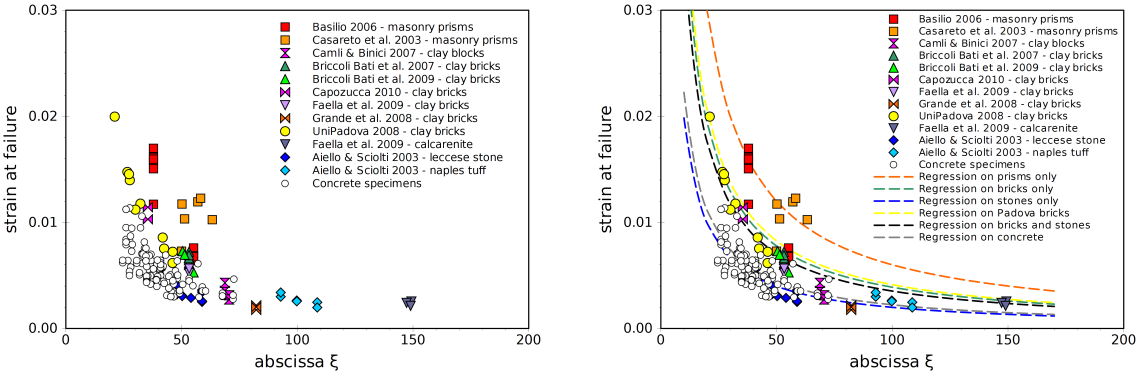

(a) Concrete and masonry data

(b) Comparison of the regression curves

Figure 5.34: Shear tests on masonry compared to concrete: calibration of k_G

and 85% for GFRP), although the fracture energy based models provide estimations closer to test results.

- From measured failure loads, different fracture energy values have been derived, around 35% higher in the case of glass reinforcement than carbon one. Actually, there should not be evident reasons to perform different calibrations other than an enhanced adherence to the experimental data, as the fracture energy should be related only to the substrate properties.

- To analyze stress and slip from strain-gauges measurement, when instruments are not uniformly spaced, discrete equations have been used, consistent with central finite difference methods. Moreover, a mathematical function easy to integrate and derive is proposed as bond-slip law. This function has been fitted in the case of both carbon and glass reinforcement; beside these fittings, two bilinear functions have been also calibrated. The optimized functions seem to show an interface local behaviour of CFRP slightly stiffer than GFRP.

- The reliability of the experimental set-up needs to be verified; despite of its simplicity, the actual distribution of the load should be more clarified, as it could cause undesired bending moments inside the test specimen.

- Finite element analyses of the test specimens were carried out implementing the calibrated bond stress – slip laws. Several comparison of numerical results obtained from different models were performed: (1) FRP modelled with the concentrated fibres approach versus FRP modelled with the distributed fibres, (2) exponential-based versus bilinear bond stress – slip law, (3) influence of the bond length. The finite element results were also compared with the results obtained from the analytical solution proposed by Yuan *et al.* (2001, 2004). As it has been shown, the analytical solution provides reasonable prediction of the maximum load and loaded end displacement. The results pointed out that the concentrated fibres approach is equivalent to the distributed one, although the last one might entail a slightly lower computational burden. FE results match quite well the experimental data, even though they slightly underestimate the failure load in the case of CFRP and overestimate the GFRP one; this could suggest that a single value for fracture energy could be properly considered, intermediate among the two estimated ones and independent from the reinforcement type. Moreover, the use of a simple bilinear bond stress – slip law can be sufficient to properly describe the bond phenomenon, without resorting to more sophisticated local laws. The combination of numerical modelling and analytical solution provided the minimum required bond length both for CFRP and GFRP applied on clay brick, which are of 70.13 mm and 59.41 mm, respectively.

- Concerning the calibration of the c_1 coefficient, related to the evaluation of the fracture energy proposed in CNR DT-200 (2004), the obtained results show a similar behaviour of stones and bricks, although a quite large scattering depending on the calibration method has been observed, whereas masonry prisms seem to offer higher performances. Reliability of these results, however, is strongly affected by the limited base of data currently available and by the lacking of some crucial data that are rarely given by the common sources.

Chapter 6

Interface behaviour in the case of mixed actions

This chapter reports the main results of a series of V-shape Peel Tests (herein somewhere labelled as V-peel for the sake of brevity), which experimental program is given in Table 6.1 on the following page, carried out on solid clay bricks (coming from the same sets used for performing the pull-off tests) reinforced with high-strength carbon fibers (CFRP) bonded with epoxy to their surface. The aim of this type of test was to investigate the behaviour of the FRP-clay interface when subdued to mixed forces acting normally and on a parallel plane with respect to the reinforcement, since this condition should be verified in the case of incipient sliding on a mortar joint near the springer of a masonry arch reinforced at its intrados.

6.1 Literature review

Peeling usually indicates the detachment between two materials connected by an adhesive layer; peel angle indicates the angle between the external force (peel force, generally a concentrated load positioned at the end) and the materials' plane. It is frequently supposed that the stiffness of one of the two elements is sufficiently higher than the other to let it be considered as a rigid material.

To analyze the peeling phenomenon, Bikerman (1957) moved from a peel angle of 90 degrees and identified the failure criterion as the maximum elongation of the adhesive, evaluated using the theory of beams on elastic soil (Fig. 6.1 on page 99), reported by Briccoli Bati and Rovero (2008) as a possible evaluation of the FRP contribution to the shear strength of masonry arches with extrados reinforcement.

Gent and Hamed (1975) compared the result of an energy-based approach to the one related to the evaluation of the tensile stress on the adhesive, and imputed the differences to the energy released by local plastic deformations.

Nicholson (1977) developed an analysis based on great deformations hypotheses and demonstrated the coincidence of this approach to the energy-based ones, in terms of peel force and peel angle relation.

Thouless and Jensen (1992) performed an analysis based on linear elastic fracture mechanics on the peel test, recently reported by De Lorenzis and Zavarise (2008) who compared analytical to numerical results based on the adoption of uncoupled cohesive interface laws for normal and tangential directions.

Yuan *et al.* (2003) proposed an analytical solution for normal and tangential stresses that affect the interface between adhesive and FRP laminates.

Table 6.1: Experimental program of V-Shape Peel Tests

Specimen	brick type	loading path
Vp01 (pilot test)	S4 - facing	monotonic (A)
Vp02 (pilot test)	S3 - extruded	cyclic (A)
Vp03	S3 - extruded	cyclic (A)
Vp04	S4 - facing	cyclic (A)
Vp05	S4 - facing	monotonic (A)
Vp06	S4 - facing	cyclic (A)
Vp07	S3 - extruded	cyclic (B)
Vp08	S3 - extruded	cyclic (B)
Vp09	S3 - extruded	monotonic (B)
Vp10	S3 - extruded	cyclic (B)
Vp11	S4 - facing	cyclic (B)
Vp12	S5 - extruded	monotonic (B)
Vp13	S2 - facing	monotonic (C)
Vp14	S2 - facing	cyclic (C)

Sun *et al.* (2004) treated analytically and numerically the peel tests, defined by them as pull-off test (Fig. 6.2 on the facing page).

Karbhari and Engineer (1996), Karbhari *et al.* (1997) performed various peel tests on concrete substrate, changing the imposed peel angle (Fig. 6.3 on the next page).

Both Kimpara *et al.* (1998) and Giurgiutiu *et al.* (1999, 2001) carried out peel tests on the FRP-concrete interface, the first adopting a symmetric set-up while the latter an asymmetric one, shown in Figures 6.4 on page 100 and 6.5 on page 100. Wan *et al.* (2002, 2004) adopted a set-up similar asymmetric set-up

Dai and Ueda (2003) carried out experiments to measure mode I, mode II and mixed-mode fracture energies of FRP bonded on concrete (Fig. 6.6 on page 100), reporting that the fracture energy mode II is not considerably influenced by fibres stiffness, depending first on the adhesive properties and, then, on the concrete strength, whereas the fracture energy mode I depends mainly on the substrate properties; concerning the mixed-mode fracture energy, the involved effective length was rather short and the strength against the peel load, defined as dowel force, was rather low.

Other studies (Wu *et al.* 2005a,b) on the mixed-mode load conditions (Fig. 6.7 on page 101) were performed in Japan in relation to the repair technique consisting on applying FRP fibres on the intrados of tunnels and bridges in order to prevent the spalling of deteriorated concrete (Ueda and Dai 2005).

Concerning the experiments on concrete substrate, it was pointed out that (Wu *et al.* 2005b, Ueda and Dai 2005) the peel force per unit width and the peel angle, during the detachment, remain almost constant; it was also observed that the peel strength is quite low, and that the presence of a peel force (e.g. beams subject to shear and flexure) may affect the global resistance causing a premature detachment of the FRP laminate (Ueda and Dai 2005). Figure 6.8 on page 101 compares experimental and idealized load-displacement curves (Dai *et al.* 2007).

The formulas afterwards adopted to analyze the fracture energy are reported in Equations (6.1) and (6.2), following Thouless and Jensen (1992), Karbhari and Engineer (1996), De Lorenzis and Zavarise (2008), and (6.3), following Wu *et al.* (2005b), whereas the reference schemes are shown in Figure 6.9 on page 101.

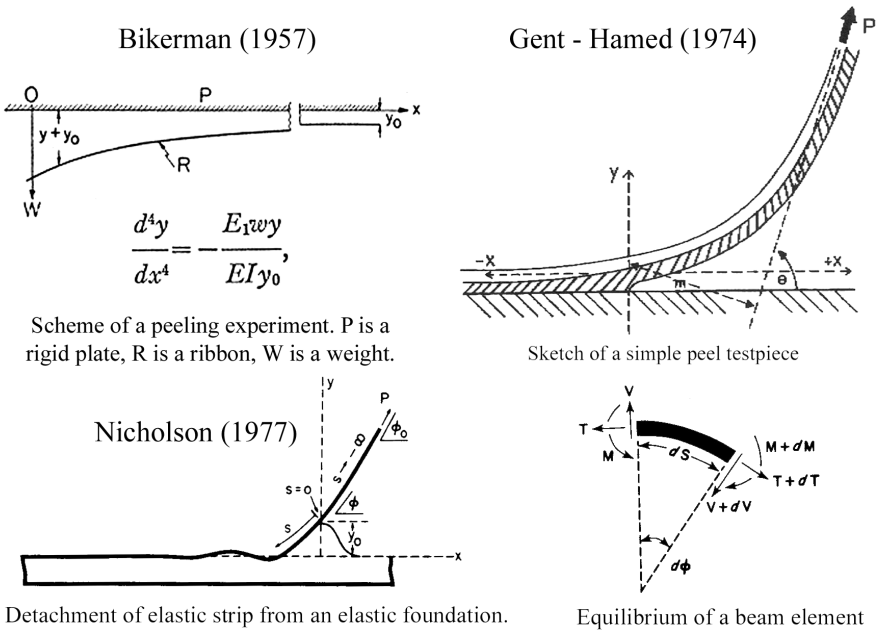

Figure 6.1: Schemes adopted for analysis (Bikerman 1957, Gent and Hamed 1975, Nicholson 1977)

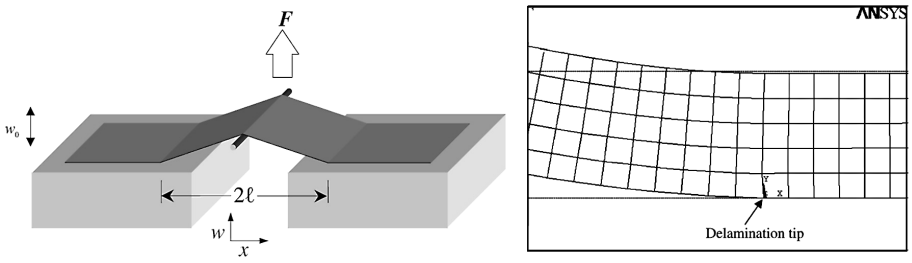

Figure 6.2: Peel analyses performed by Sun *et al.* (2004)

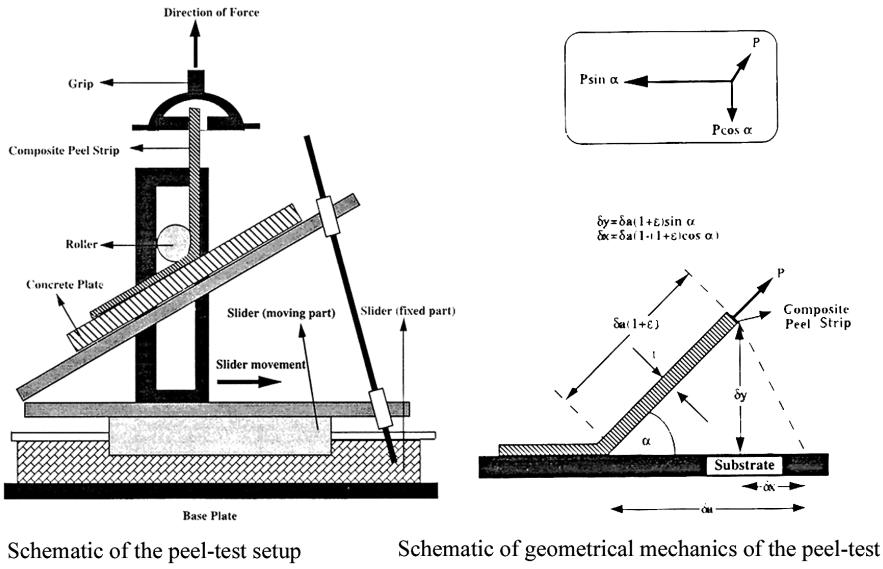

Figure 6.3: Peel test performed by Karbhari and Engineer (1996)

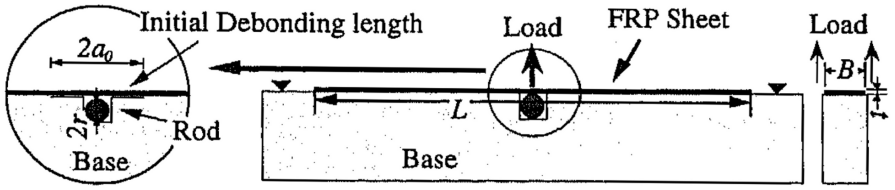

Figure 6.4: Peel test performed by Kimpara *et al.* (1998)

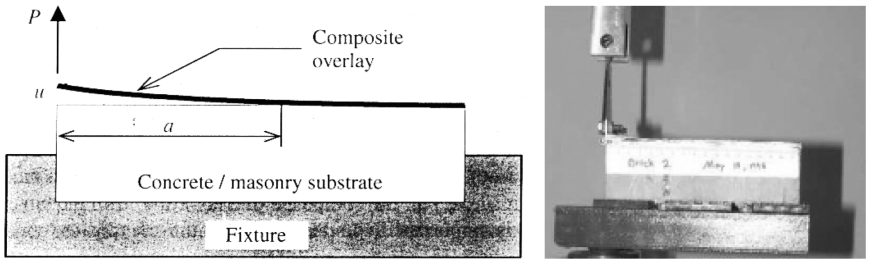

Figure 6.5: Peel test performed by Giurgiutiu *et al.* (1999, 2001)

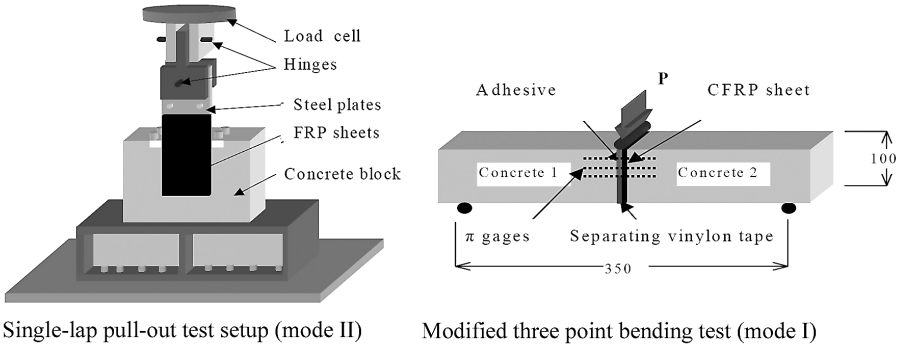

Figure 6.6: Peel test performed by Dai and Ueda (2003), Dai *et al.* (2007)

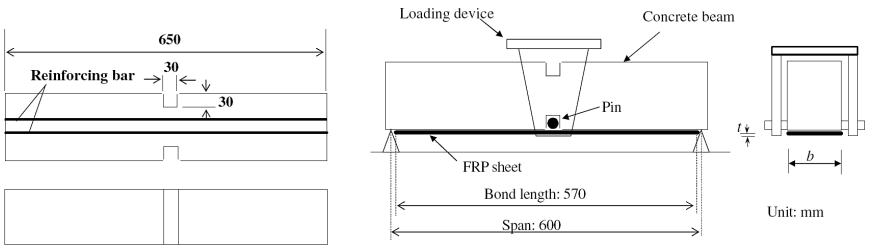

Figure 6.7: Peel test performed by Wu *et al.* (2005b)

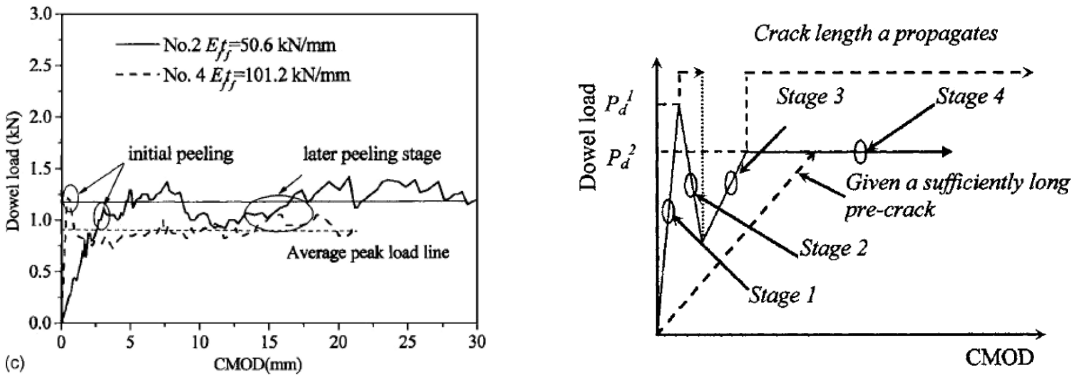

(a) **(b)**

Figure 6.8: Experimental (left) and idealized load-displacement curve (Dai *et al.* 2007).

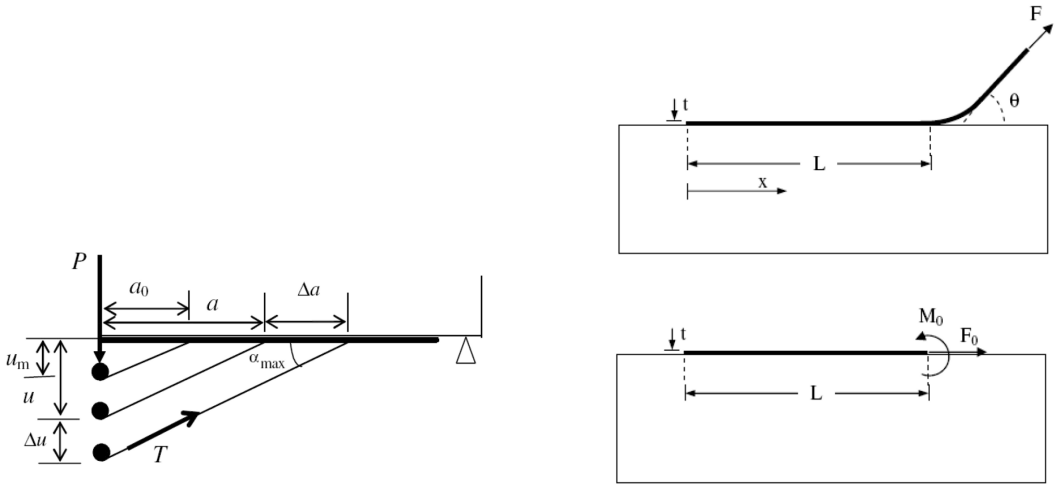

(a) Wu *et al.* (2005b) **(b)** De Lorenzis and Zavarise (2008)

Figure 6.9: Reference schemes for the adopted fracture energy analyses

$$F_0 = F cos(\alpha) \tag{6.1a}$$

$$M_0 = \sqrt{\frac{E_f t_f^3}{6}\left(\frac{F^2 sin^2\alpha}{2E_f t_f}\right) + F(1 - cos\alpha)} \tag{6.1b}$$

$$G_{II} = \frac{F_0^2}{2E_f t_f} \tag{6.2a}$$

$$G_I = \frac{6M_0^2}{E_f t_f^3} \tag{6.2b}$$

$$G = G_I + G_{II} \tag{6.2c}$$

$$\psi = \text{atan}\,\frac{t_f F_0}{\sqrt{12} M_0} \tag{6.2d}$$

$$P_{max} = 2.087 b_f G^{0.75} (E_f t_f)^{0.25} \tag{6.3}$$

6.2 Description of the experimental tests

In order to locally reproduce a state of stress, for the reinforcement, similar to that related to shear sliding on a mortar joint, a test set-up derived and adapted from the ones proposed by Wu *et al.* (2005b) and Dai *et al.* (2007) was adopted, since it was estimated more feasible, with respect to the available equipment, and less problematic if compared to the previous test method (Panizza 2006, Panizza *et al.* 2008b) that revealed some troubles during its execution.

6.2.1 Basic materials

As previously mentioned, solid clay bricks belonging to the same sets used to perform the pull-off tests, namely S3 and S5 (extruded elements) and S2 and S4 (facing ones), were used as substrate; therefore,the mechanical characterization is given in chapter 4 on page 35. One type of fibres was used as reinforcement, namely high-strength carbon MBrace® C1-30, which was the same used for Shear Tests and pull-off tests, hence its properties can be found in chapters 5 on page 59 and 4 on page 35.

6.2.2 Experimental test set-up

The test set-up, aimed at reproducing the detachment mechanism related to the sliding on a mortar joint of a masonry arch reinforced at the extrados, is shown in Figure 6.10 on the next page. Two solid clay bricks were disposed along their axis and bonded to a top steel beam; the beam was sufficiently longer to be provided of two lateral steel supports sustained by the roller support of an apposite device generally used to perform flexural tests (see chapter 4 on page 35. Therefore, the bricks were connected only to the top beam, being spaced of 30 mm one from the other, in order to accommodate the steel pin used to apply the peel force on the reinforcement, and sufficiently spaced from the lateral supports to avoid unwanted contact during the test. On the bottom surface of the bricks, a reinforcement strip 50 mm wide was applied, glued to the end of the bricks imposing an unbonded distance of 30 mm from each central edge of the brick. A detailed scheme is reported in Figure 6.11 on page 104.

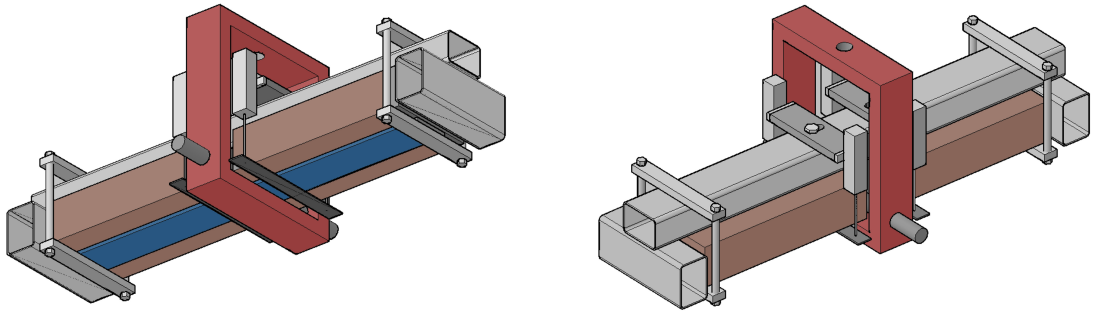

(a) **(b)**

Figure 6.10: Model of the V-shape Peel test (Giomo 2008)

Table 6.2: Adopted test procedures

Phase	Displ. rate	pin direct.	duration	Displ. rate	pin direct.	duration
	CYCLIC (A)			MONOTONIC (A)		
1	2 mm/min	down	180 s	2 mm/min	down	up to failure
2	2 mm/min	up	150 s			
3	2 mm/min	down	600 s			
4	back to phase (2)					
	CYCLIC (B)			MONOTONIC (B)		
1	1 mm/min	down	360 s	1 mm/min	down	up to failure
2	2 mm/min	up	150 s			
3	2 mm/min	down	600 s			
4	back to phase (2)					
	CYCLIC (C)			MONOTONIC (C)		
1	0.6 mm/min	down	600 s	0.6 mm/min	down	up to failure
2	1.2 mm/min	up	250 s			
3	1.2 mm/min	down	500 s			
4	back to phase 2					

Tests were performed on the universal test machine Galdabini SUN2500 (maximum load 2.5 kN), equipped with an additional load cell connected to the external acquisition system. The vertical load was transmitted by a solid steel ring surrounding the top beam and connected to a steel pin acting directly on the FRP strip. Each specimen was monitored by six coupled displacement devices (potentiometers) measuring the lowering in three positions: at the central point, corresponding to the pin, and the beginning of the bonded areas (points A, B, C and D). Three strain-gauges were applied to the FRP bottom surface of part of the samples. Figure 6.12 on the following page shows the positions of instruments.

The loading path, controlled by displacement rate, was monotonic for five specimens and cylic for nine, and a pre-loading force equal to 10 N was always applied in order to accommodate part of the deformations related to the test system. Being exploratory tests, some parameters were adjusted during the campaign. Table 6.2 reports the main properties of the adopted test procedures.

Figure 6.13 on page 105 shows images taken during the preparation of samples.

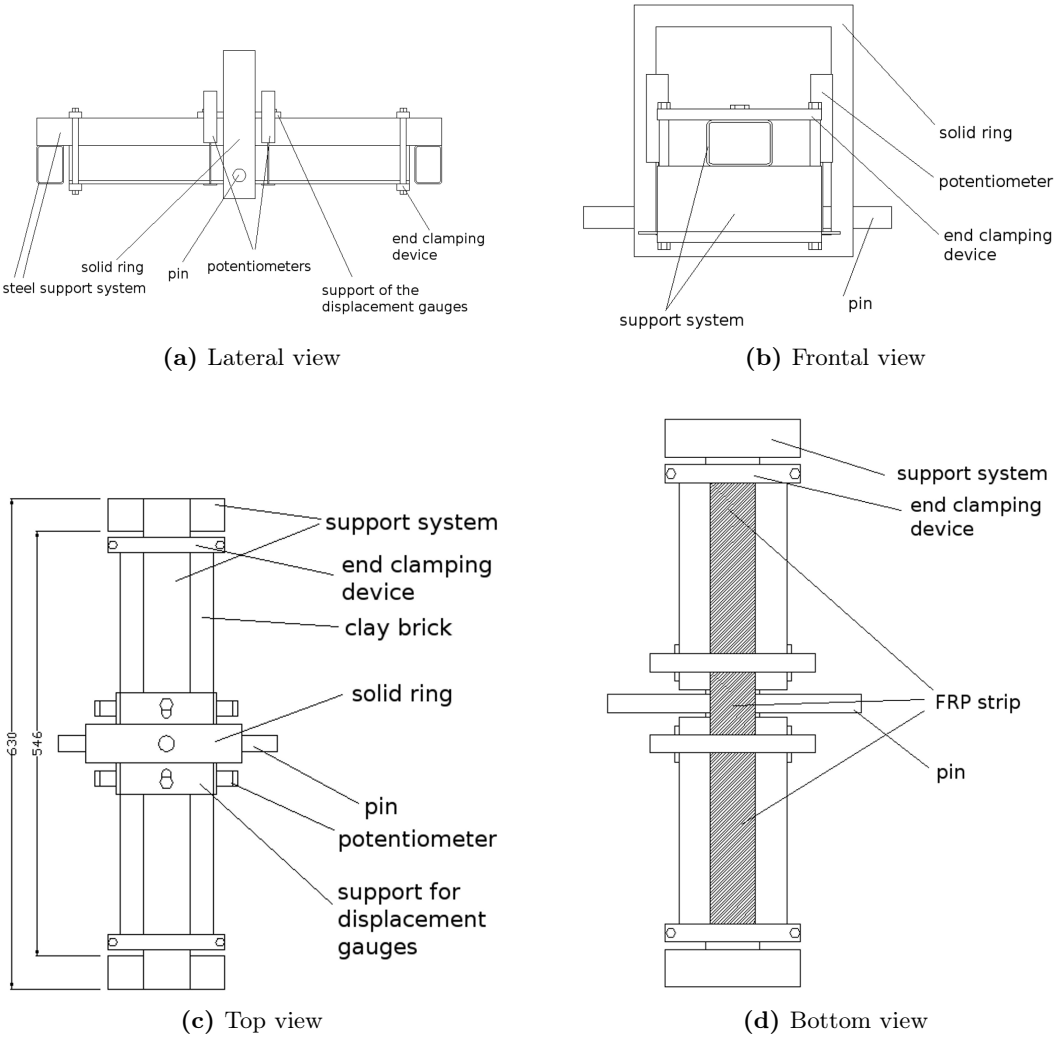

(a) Lateral view **(b)** Frontal view

(c) Top view **(d)** Bottom view

Figure 6.11: Scheme of the V-shape Peel test

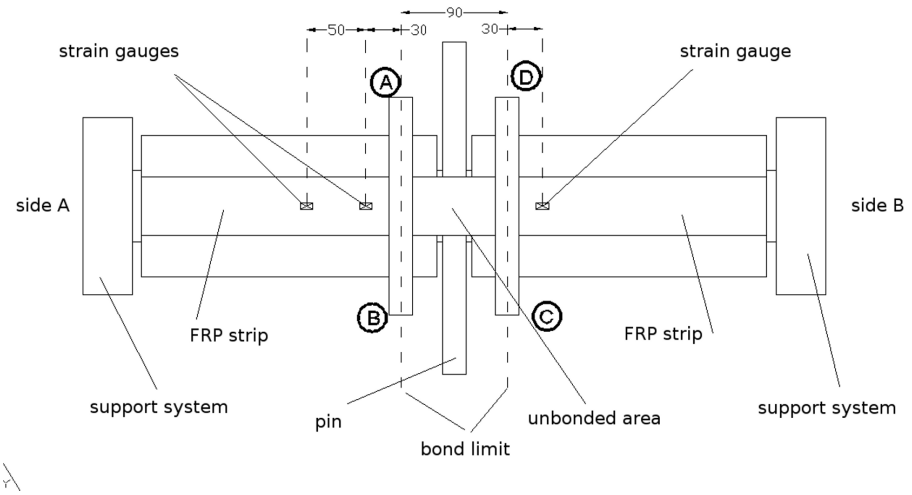

Figure 6.12: Position of the applied measurement devices

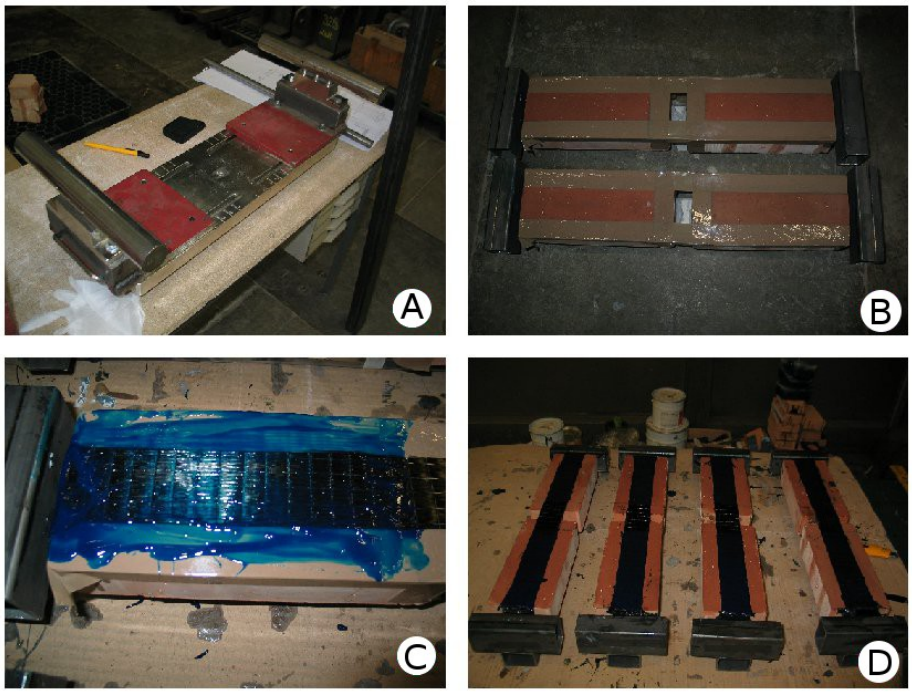

Figure 6.13: Images taken during the specimens preparation: device for flexural tests (A), two samples before the FRP application (B), bonding of fibres (C) and specimens ready for testing (D)

6.2.3 Test results

Images taken during the tests are reported in Figure 6.14 on the next page, while typical load-displacement curves for monotonic and cyclic tests are shown in Figures 6.16 on page 107 and 6.17 on page 107. Failure generally involved the detachment of a thin layer of brick, in the case of facing elements, whereas it was localized at the interface of extruded bricks, without ripping any clay portion (Fig. 6.15 on the following page). Results (Tab. 6.3 on page 108), in terms of maximum vertical load P_{u}, were rather variable (Tab. 6.4 on page 108), particularly for extruded bricks that showed the higher dispersion. Facing bricks generally offered larger values of strength, compared to extruded bricks. This fact could be correlated to the different failure mode observed: facing elements, whose surface is more scabrous and irregular, could had involved a stronger adhesion of the reinforcement, differently from the smoother and more compact extruded bricks, that affected the clay substrate.

6.3 Test analyses

6.3.1 Load-displacement

The maximum load value was recorded, for all the monotonic tests, when the reinforcement started to detach from the support; after that peak, the vertical load values oscillated within inferior limits (Tab. 6.5 on page 109 and Fig. 6.18 on page 109, which compare the first peak load to the average subsequent peaks), however showing a generally high scatter around an average, constant or slightly variable. This trend was lightly different to those observed during the cyclic tests, where the trend among the various peak loads were less recurrent.

Concerning the cyclic tests, as expected each cycle showed a lower stiffness on the loading/unloading phases, due to the progressive detachment of the reinforcement that

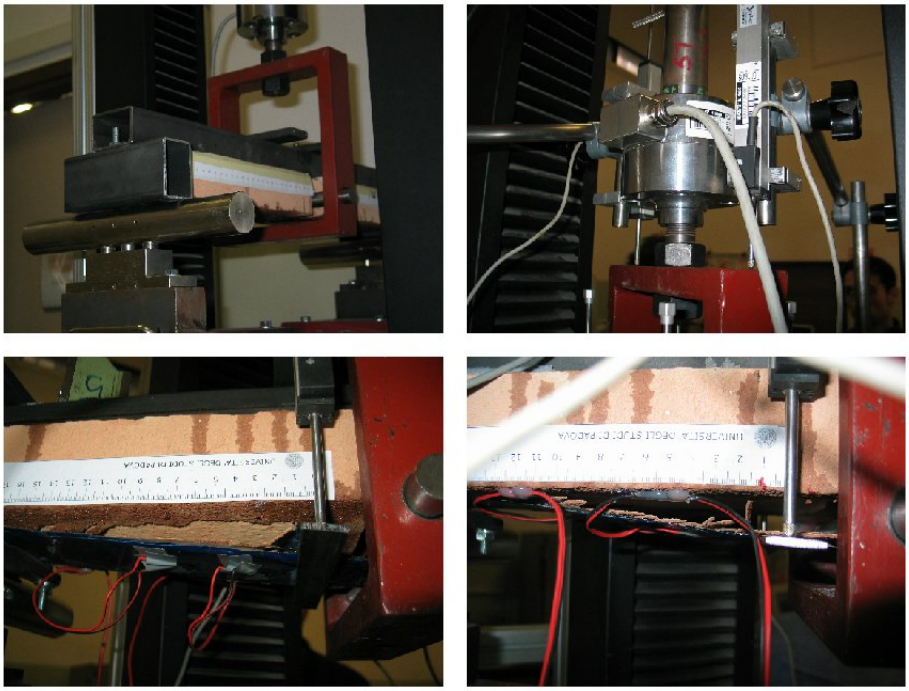

Figure 6.14: Images taken during the V-shape Peel Tests

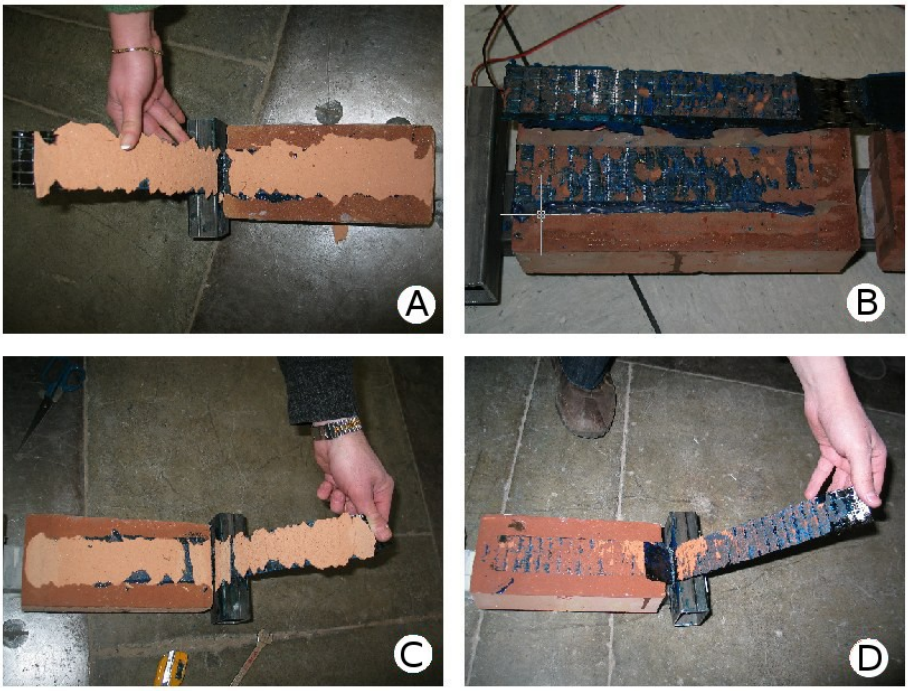

Figure 6.15: Typical failures: facing bricks S2 (A) and S4 (C), extruded bricks S3 (B) and S5 (D)

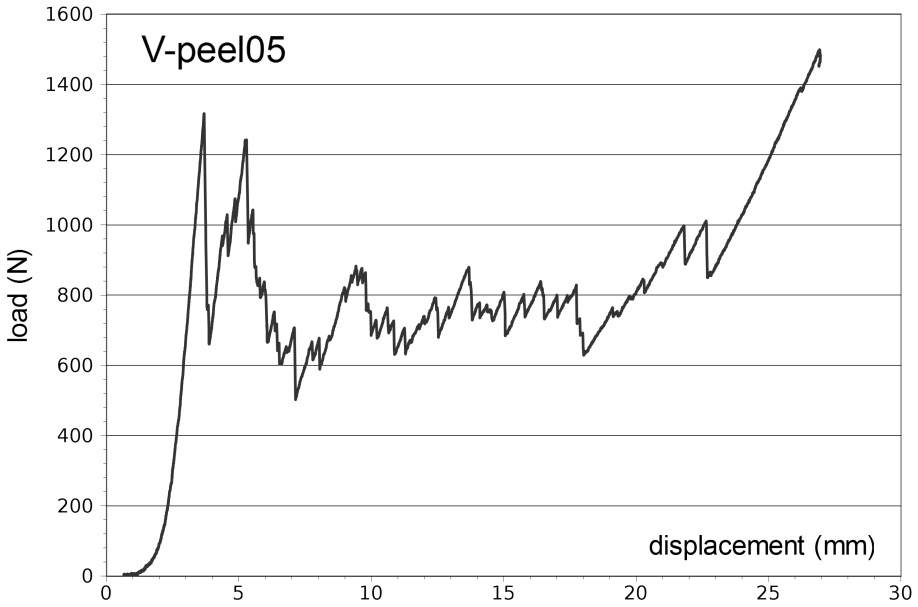

Figure 6.16: Typical monotonic function for load and vertical deflection of the central point

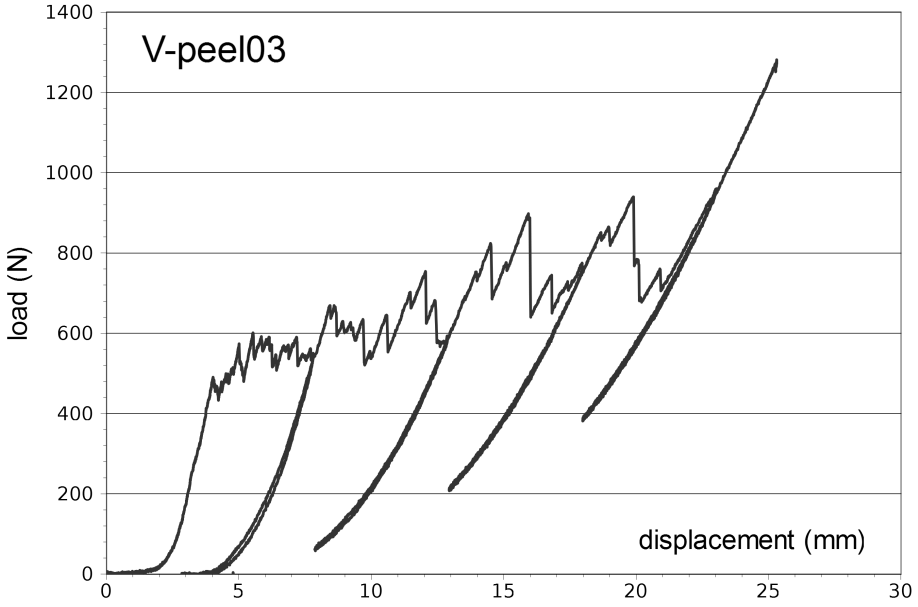

Figure 6.17: Typical cyclic function for load and vertical deflection of the central point

Table 6.3: Experimental results of the V-Shape Peel Tests

Specimen	brick type	P_u N	P_u/b_f N/mm	failure cycle	failure localization
Vp01	S4 - facing	1555	31.1	-	substrate
Vp02	S3 - extruded	1302	26.0	third	interface
Vp03	S3 - extruded	963	19.3	fourth	interf. and substrate
Vp04	S4 - facing	1280	25.6	second	substrate
Vp05	S4 - facing	1317	26.3	-	substrate
Vp06	S4 - facing	1795	35.9	first	interf. and substrate
Vp07	S3 - extruded	935	18.7	fourth	interface
Vp08	S3 - extruded	853	17.1	first	interface
Vp09	S3 - extruded	717	14.3	-	interface
Vp10	S3 - extruded	830	16.6	fourth	interface
Vp11	S4 - facing	1243	24.9	first	interf. and substrate
Vp12	S5 - extruded	937	18.7	-	interface
Vp13	S2 - facing	912	18.2	-	substrate
Vp14	S2 - facing	912	18.2	first	substrate

Table 6.4: Experimental maximum loads sorted by brick type

Brick type	Specimen	P_u N	P_u/b_f N/mm
S2 - facing	Vp13	912	18.2
S2 - facing	Vp14	912	18.2
	average	912	18.2
S3 - extruded	Vp02	1302	26.0
S3 - extruded	Vp03	963	19.3
S3 - extruded	Vp07	935	18.7
S3 - extruded	Vp08	853	17.1
S3 - extruded	Vp09	717	14.3
S3 - extruded	Vp10	830	16.6
	average	933	18.7
	standard deviation	200	
	coeff. of variation	21.5%	
S4 - facing	Vp01	1555	31.1
S4 - facing	Vp04	1280	25.6
S4 - facing	Vp05	1317	26.3
S4 - facing	Vp06	1795	35.9
S4 - facing	Vp11	1243	24.9
	average	1438	28.8
	standard deviation	234	
	coeff. of variation	16.3%	
S5 - extruded	Vp12	937	18.7

Table 6.5: Maximum and average peak load values for monotonic tests

Specimen	Brick type	P_u N	P_{avg} N
Vp01	S4 - facing	1555	1047
Vp05	S4 - facing	1317	792
Vp09	S3 - extruded	718	537
Vp12	S5 - extruded	938	669
Vp13	S2 - facing	912	551

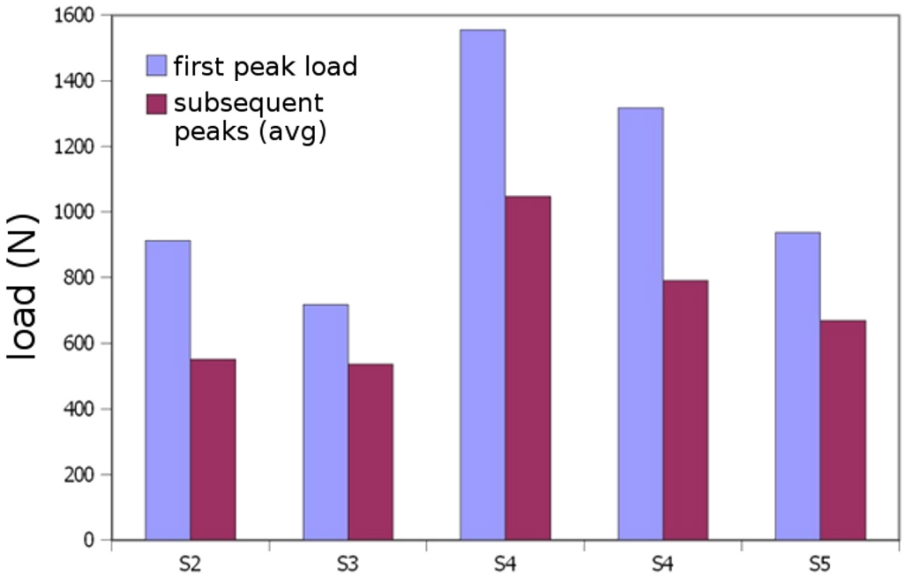

Figure 6.18: Comparison among peak load values for monotonic tests

implied an increasing unbonded length (Fig. 6.19 on the next page).

However, it could be concluded, since the load values do not manifest any evident decrease related to the progressive shortening of the bonded area, that the effective length involved by this mechanism is quite small, if compared to the effective length related to the longitudinal debonding: possibly around the 20-30 %, as previously observed by Panizza (2006), Panizza *et al.* (2008b), where a different test set-up was used to reproduce the same shear mechanism.

6.3.2 Peel angle

As shown in Figure 6.20 on the following page, the monitored displacements allowed to analytically evaluate (Eq. 6.4 on the next page, where α is the peel angle, l_{ub} is the distance between the bonded edge, δy the appropriate vertical displacement) the slope of the reinforcement during the detachment; although this estimation was slightly rough, it permitted to point out some characteristics of the phenomenon.

It can be observed (Fig. 6.21 on page 111) that facing bricks showed a more scattering evolution of the peel angle during the progressive detachment, if compared to extruded bricks; this fact could be justified by the different observed failure mode: it involved the brittle clay substrate of facing elements, whereas it evolved within the interface or the adhesive in the case of extruded ones.

The average values of peel angle α, which range from 4.5 to 7 degrees (lower than the 10 degrees observed by Wu *et al.* in the case of concrete substrate) are given in Table 6.6 on

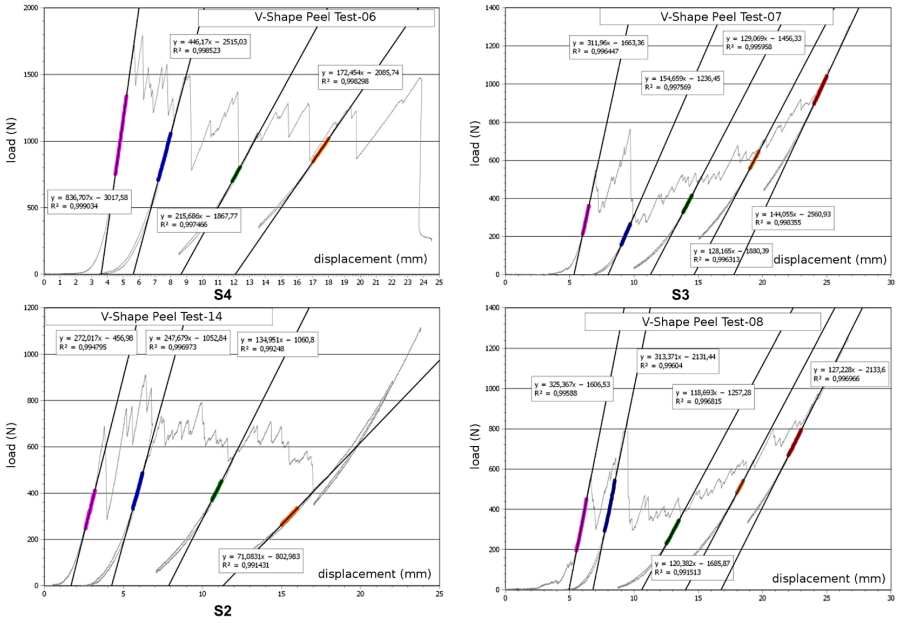

Figure 6.19: Tipical load-displacement functions for cyclic tests

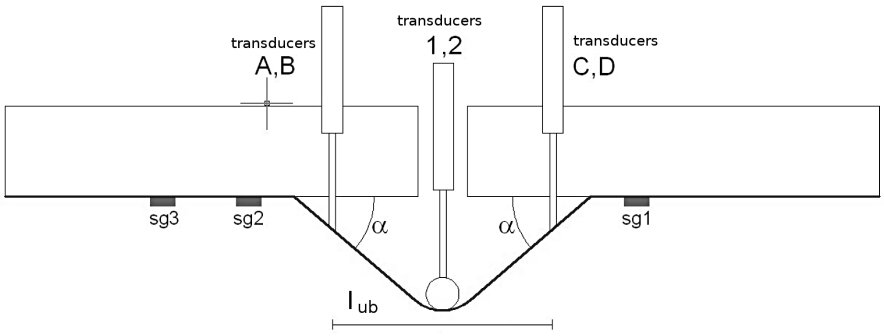

Figure 6.20: Evaluation of the peel angle during the test

the next page, for each specimen and each side, AB and CD, of the reinforcement strip.

$$\alpha = \text{atan}\,\frac{\delta y_{1,2} - \delta y_{\text{AB}\vee\text{CD}}}{0.5 l_{\text{ub}}} \tag{6.4}$$

6.3.3 Fracture energy evaluation

On the basis of the evaluated peel angles, and being known the corresponding vertical load, the mixed-mode fracture energy components mode I, G_{I}, and mode II, G_{II}, were evaluated following the analysis proposed by Thouless and Jensen (1992), reported also in De Lorenzis and Zavarise (2008), an the total mixed-mode fracture energy G was assumed to be the sum of its components (Karbhari and Engineer 1996, De Lorenzis and Zavarise 2008). Moreover, the simplified analysis proposed by Wu *et al.* (2005b), which allows to estimate the mixed-mode fracture energy, indicated by G_{W}, as a function of the vertical load P and the reinforcement axial stiffness per unit width, $E_{\text{f}}t_{\text{f}}$, was applied as well, and the results compared to the ones calculated through the first method.

Results are given in Tables 6.7 on page 112, 6.8 on page 113, 6.9 on page 114 and 6.10 on page 114, for the S2, S3, S4 and S5 sets of bricks, respectively, where α stands for the

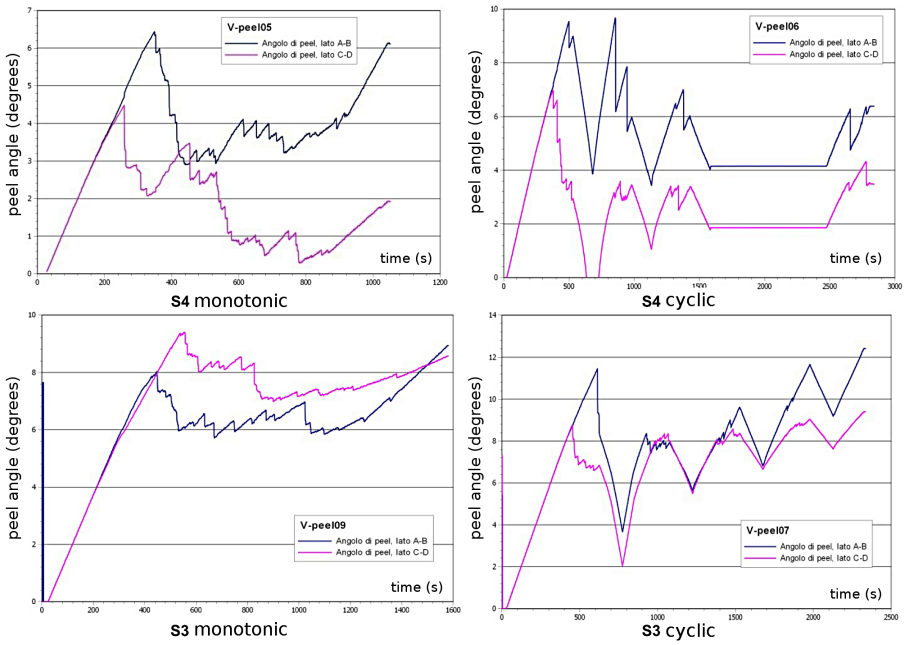

Figure 6.21: Peel angle evolution during monotonic and cyclic tests

Table 6.6: Average peel angles during the various tests phases

Specimen	Brick type	side AB $\alpha_{AB,1}$	side AB $\alpha_{AB,2}$ degrees	side AB $\alpha_{AB,3}$	side CD $\alpha_{CD,1}$	side CD $\alpha_{CD,2}$ degrees	side CD $\alpha_{CD,3}$
Vp13 (monot.)	S2 - facing	4.45	–	–	3.00	–	–
Vp14 (cyclic)	S2 - facing	5.62	5.16	3.76	5.03	4.53	5.21
	average	5.04	5.16	3.76	4.02	4.53	5.21
Vp02 (cyclic)	S3 - extruded	8.54	6.25	——	8.51	8.88	8.54
Vp03 (cyclic)	S3 - extruded	6.57	5.95		3.02	2.57	2.65
Vp07 (cyclic)	S3 - extruded	10.73	7.8	8.68	7.03	8.10	8.18
Vp08 (cyclic)	S3 - extruded	6.78	6.18	6.75	7.74	7.71	7.94
Vp09 (monot.)	S3 - extruded	6.42	–	–	7.76	–	–
Vp10 (cyclic)	S3 - extruded	2.79	3.67	5.49	3.90	2.4	1.94
	average	6.97	5.97	6.97	6.33	5.93	5.85
	st. dev.	2.63	1.48	1.61	2.29	3.18	3.26
	coeff. of var.	37.72%	24.79%	23.04%	36.14%	53.53%	55.76%
Vp01 (monot.)	S4 - facing	10.08	–	–	11.25	–	–
Vp04 (cyclic)	S4 - facing	7.25	6.32	5.74	7.30	–	–
Vp05 (monot.)	S4 - facing	3.74	–	–	1.69	–	–
Vp06 (cyclic)	S4 - facing	8.88	6.74	6.26	4.44	3.13	3.07
Vp11 (cyclic)	S4 - facing	5.06	4.35	3.41	7.78	6.38	6.39
	average	7	5.8	5.14	6.49	4.76	4.73
	st. dev.	2.62	1.28	1.52	3.61	2.3	2.35
	coeff. of var.	37.43%	21.99%	29.55%	55.66%	48.33%	49.63%
Vp12 (monot.)	S5 - extruded	5.56	–	–	4.51	–	–

Table 6.7: Phase angle and fracture energy for S2 bricks – facing

Side	peak	P N	α deg	G_{II} N/mm	G_I N/mm	ψ deg	G N/mm	G_W N/mm	ΔG %
Vp13 – monotonic									
AB	1	552	4.45	0.066	0.215	29.04	0.281	0.274	-2.5%
CD	1	552	3.00	0.146	0.145	45.11	0.291	0.274	-5.8%
Vp14 – cyclic									
AB	1	639	5.62	0.056	0.314	22.81	0.370	0.333	-9.8%
	2	720	5.16	0.084	0.325	26.91	0.409	0.391	-4.4%
	3	660	3.76	0.133	0.217	38.00	0.350	0.348	-0.6%
CD	1	632	5.03	0.068	0.278	26.30	0.346	0.329	-5.1%
	2	715	4.53	0.107	0.284	31.59	0.391	0.387	-0.9%
	3	590	5.21	0.055	0.269	24.34	0.324	0.300	-7.5%
	average	633	4.60	0.090	0.260	30.51	0.350	0.330	
	st. dev.	66	0.86	0.040	0.060	7.57	0.050	0.050	
coeff. of .var.		10.4%	18.8%	39.5%	23.4%	24.8%	13.1%	13.8%	

calculated peel angle and P for the corresponding vertical load, ψ is the phase angle and ΔG the percentage difference of the two fracture energy evaluations. Figure 6.22 on page 115 compares the fracture energy composition for the tested bricks, whereas the phase angle ψ is plotted versus the peel angle α in Figure 6.23 on page 115.

It can be noticed that facing bricks belonging to S4 set shown fracture energy values very high, around twice the other elements, while S3 and S5 sets gave similar results, being different sets of the same industrial product. Moreover, the total mixed-mode fracture energy values seem to be quite reasonable if compared to those adopted by De Lorenzis and Zavarise (2008) for their numerical models concerning FRP sheets externally bonded to masonry substrates, 0.5 N/mm, and measured by Wu *et al.* (2005b) in the case of concrete substrate, from 0.3 to 1.5 N/mm, being 0.2 N/mm the lower bound for practical design proposed by Dai *et al.* (2007).

6.4 Conclusive remarks

Fourteen V-shape Peel Tests, whose test set-up was adapted by similar tests carried out on concrete substrate (Wu *et al.* 2005b, Dai *et al.* 2007) were performed using CFRP reinforcement applied on solid clay bricks. This type of test has been found sufficiently feasible, requiring few mechanical devices, and easily adaptable to most universal test machines. Although these should be considered as pilot tests, the main characteristics of the investigated phenomenon were substantially identified, and the experimental observations do not differ much from what Wu *et al.* (2005b), Dai *et al.* (2007) reported:

- the peel load, during the detachment, oscillated within a limited range, though the scattering was in some cases very large;
- maximum loads of around 18 N/mm were observed, except for the S4 series that gave 28.8 N/mm;
- the first peak load was generally higher than the others, for monotonic tests;

Table 6.8: Phase angle and fracture energy for S3 bricks – extruded

Side	peak	P N	α deg	G_{II} N/mm	G_{I} N/mm	ψ deg	G N/mm	G_{W} N/mm	ΔG %
					Vp02 – cyclic				
	1	940	8.54	0.052	0.703	15.16	0.755	0.558	-26.1%
AB	2	684	6.25	0.051	0.374	20.34	0.425	0.365	-14.2%
	1	910	8.51	0.049	0.678	15.01	0.727	0.534	-26.5%
CD	2	690	8.88	0.026	0.536	12.35	0.562	0.369	-34.3%
	3	1038	8.54	0.063	0.776	15.89	0.839	0.637	-24.2%
					Vp03 – cyclic				
	1	550	6.57	0.030	0.316	17.12	0.346	0.273	-21.2%
AB	2	489	5.95	0.029	0.254	18.66	0.283	0.233	-17.7%
	1	498	3.02	0.117	0.132	43.30	0.249	0.239	-3.9%
CD	2	668	2.57	0.293	0.150	54.37	0.443	0.354	-20.1%
	3	864	2.65	0.459	0.201	56.54	0.660	0.499	-24.5%
					Vp07 – cyclic				
	1	614	10.73	0.014	0.577	8.80	0.591	0.316	-46.5%
AB	2	527	7.80	0.020	0.360	13.11	0.379	0.258	-32.0%
	3	588	8.68	0.020	0.447	11.81	0.466	0.298	-36.0%
	1	369	7.03	0.012	0.227	12.85	0.239	0.160	-32.8%
CD	2	460	8.10	0.014	0.326	11.61	0.340	0.215	-36.7%
	3	589	8.18	0.022	0.422	12.90	0.444	0.299	-32.6%
					Vp08 – cyclic				
	1	351	6.78	0.011	0.208	13.22	0.220	0.150	-31.7%
AB	2	387	6.18	0.017	0.209	15.84	0.226	0.171	-24.4%
	3	542	6.75	0.028	0.320	16.37	0.348	0.268	-23.0%
	1	341	7.74	0.008	0.231	10.73	0.239	0.144	-39.6%
CD	2	529	7.71	0.020	0.357	13.36	0.377	0.259	-31.3%
	3	870	7.94	0.051	0.605	16.23	0.656	0.503	-23.3%
					Vp09 – monotonic				
AB	1	538	6.42	0.030	0.302	17.51	0.332	0.265	-20.3%
CD	1	538	7.76	0.021	0.365	13.33	0.386	0.265	-31.3%
					Vp10 – cyclic				
	1	459	2.79	0.117	0.112	45.54	0.229	0.215	-6.2%
AB	2	460	3.67	0.068	0.148	34.11	0.215	0.215	-0.1%
	3	600	5.49	0.051	0.288	22.91	0.339	0.306	-9.7%
	4	760	3.43	0.212	0.228	43.98	0.440	0.420	-4.6%
	1	285	3.90	0.023	0.097	25.98	0.120	0.114	-5.4%
CD	2	305	2.40	0.070	0.064	46.23	0.134	0.124	-7.0%
	3	502	1.94	0.291	0.085	61.59	0.376	0.242	-35.7%
	average	579	6.22	0.070	0.330	23.77	0.400	0.300	
	st. dev.	192	2.39	0.100	0.190	15.63	0.180	0.130	
coeff. of .var.		33.2%	38.5%	139.6%	58.5%	65.8%	46.0%	44.5%	

Table 6.9: Phase angle and fracture energy for S4 bricks – facing

Side	peak	P N	α deg	G_{II} N/mm	G_I N/mm	ψ deg	G N/mm	G_W N/mm	ΔG %
Vp01 – monotonic									
AB	1	1047	10.80	0.040	0.991	11.32	1.031	0.644	-37.5%
CD	1	1047	11.25	0.037	1.033	10.65	1.069	0.644	-39.8%
Vp04 – cyclic									
AB	1	1160	7.25	0.110	0.737	21.09	0.846	0.738	-12.8%
	2	879	6.32	0.083	0.486	22.45	0.569	0.510	-10.4%
	3	872	5.74	0.099	0.438	25.44	0.537	0.505	-6.1%
	4	1131	5.82	0.162	0.577	27.94	0.739	0.714	-3.4%
CD	1	965	7.30	0.075	0.617	19.20	0.692	0.578	-16.5%
Vp05 – monotonic									
AB	1	792	3.74	0.194	0.259	40.82	0.453	0.444	-2.0%
CD	1	792	1.69	0.949	0.118	70.59	1.066	0.444	-58.4%
Vp06 – cyclic									
AB	1	1155	8.88	0.072	0.899	15.81	0.971	0.734	-24.4%
	2	1087	6.74	0.111	0.642	22.61	0.753	0.677	-10.1%
	3	1177	6.26	0.152	0.645	25.86	0.797	0.753	-5.6%
CD	1	1354	4.44	0.401	0.527	41.08	0.928	0.907	-2.2%
	2	784	3.13	0.271	0.215	48.34	0.486	0.438	-9.9%
	3	966	3.07	0.427	0.260	52.04	0.688	0.578	-15.9%
Vp11 – cyclic									
AB	1	1143	5.06	0.220	0.507	33.37	0.726	0.724	-0.3%
	2	812	4.35	0.150	0.310	34.83	0.459	0.459	-0.1%
	3	765	3.41	0.217	0.228	44.28	0.446	0.424	-4.9%
CD	1	887	7.78	0.055	0.604	16.86	0.660	0.516	-21.8%
	2	740	6.38	0.058	0.413	20.47	0.471	0.405	-13.9%
	3	884	6.89	0.071	0.533	19.99	0.604	0.514	-14.9%
	4	946	6.77	0.084	0.561	21.12	0.644	0.563	-12.7%
average		972	6.05	0.180	0.530	29.37	0.710	0.590	
st. dev.		168	2.40	0.200	0.250	14.89	0.200	0.140	
coeff. of .var.		17.3%	39.7%	109.9%	46.6%	50.7%	28.8%	23.1%	

Table 6.10: Phase angle and fracture energy for S5 bricks – extruded

Side	peak	P N	α deg	G_{II} N/mm	G_I N/mm	ψ deg	G N/mm	G_W N/mm	ΔG %
Vp12 – monotonic									
AB	1	669	5.56	0.062	0.326	23.59	0.388	0.354	-2.5%
CD	1	669	4.51	0.095	0.264	30.94	0.359	0.354	-5.8%
average		669	5.04	0.080	0.300	27.27	0.370	0.354	
st. dev.			0.74	0.020	0.040	5.20	0.020		
coeff. of .var.			14.8%	29.7%	14.9%	19.1%	5.5%		

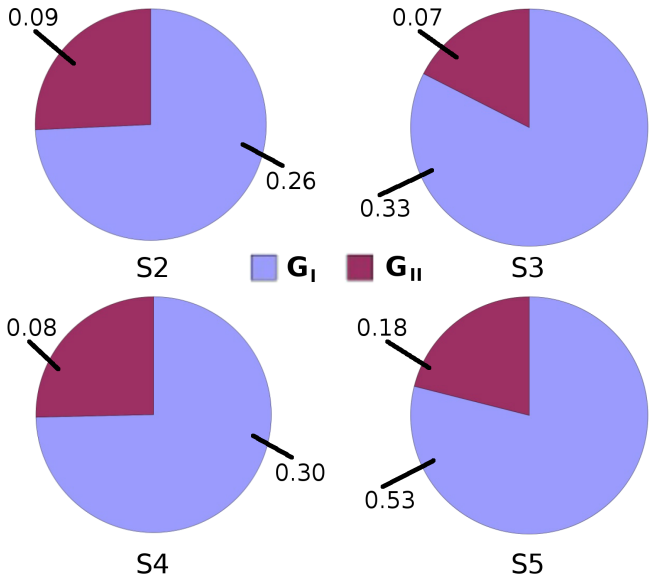

Figure 6.22: Evaluated components (N/mm) of the fracture energy for the tested bricks

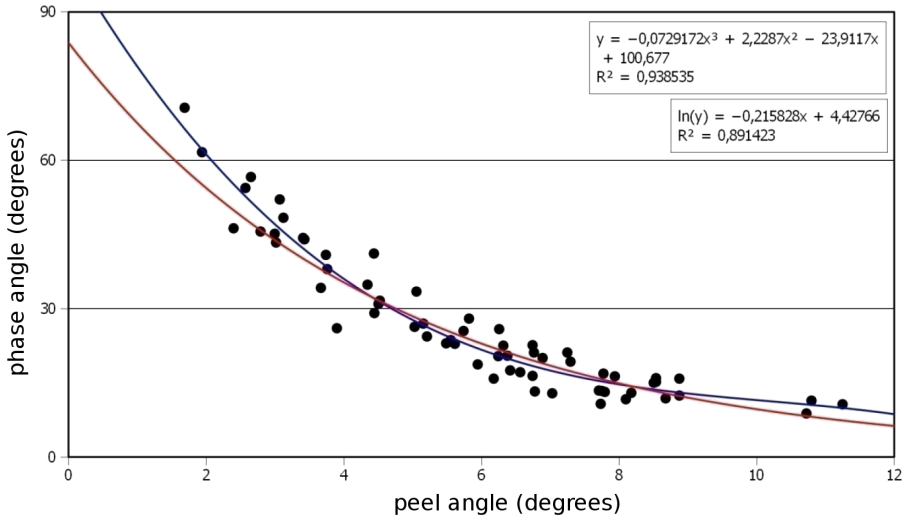

Figure 6.23: Experimentally evaluated phase plotted versus peel angles

- the peel angle, similarly to the peel load, oscillated around quasi-constant values, being high the scattering also in this case; the estimated average values ranged from 4.5 to 7 degrees;
- the calculated mixed-mode fracture energies ranged fom 0.3 to 0.7 N/mm, consistently with values proposed in literature for quasi-brittle substrates (Wu *et al.* 2005b, Dai *et al.* 2007, De Lorenzis and Zavarise 2008).

Chapter 7

Analisys of the global structural behaviour

This chapter presents the results of the application of available interpretative models to several experimental cases studies, masonry arches and barrel vaults strengthened to their extrados or intrados by means of FRP textiles, collected from literature.

First, a brief review of the experimental main results is reported, followed by a comparison of the experimental ultimate loads with the predicted failure loads, evaluated with regard to bending failure (crushing of masonry or fibres rupture), fibres debonding, shear failure at the springer (extrados only) and fibres detachment (intrados only).

7.1 Experimental case studies

The present collection of masonry arches experimentally tested was based on data reported by Valluzzi *et al.* (2001), who tested six arches having three different configurations that compared type of fibres, glass and carbon, and application at the extrados or the intrados; Briccoli Bati and Rovero (2008), who summarized the results of three reinforcement configurations at the extrados and three at the intrados, varying the width of carbon fibres; Basilio (2007), who dealt with four GFRP configuration, two for the extrados and two for the intrados; Castori (2006), whose work was mainly based on steel reinforced polymers and grouts (SRP/SRG), but tested one arch reinforced at the extrados and another at its intrados by carbon fibres; Badalà *et al.* (2008), who reported the results of one tested arch reinforced with carbon at the extrados.

Overall ten arch models (one or more specimens) for extrados reinforcement and six models for intrados reinforcement were gathered. In Tables 7.1 on the following page and 7.2 on the next page the main characteristics of the models, with extrados and intrados reinforcement, are summarized; "circular" or "catenary" refers to the axis shape, t and b are thickness and width of the masonry section, respectively, span and rise refer to the intrados surface, α, measured in degrees, is the slope of the starting section, W is the self-weight of the structure and, finally, FRP and b_f are fibres type and width.

In Figure 7.1 on page 120 a scaled comparison of the adopted shapes and dimensions shows differences among the analyzed models, while Figure 7.2 on page 120 reports some images from the experimental campaigns.

The main results are reported in Tables 7.3 on page 119 and 7.4 on page 119, concerning extrados and intrados reinforcement, respectively. For both extrados and intrados reinforcement the average failure loads per unit width of the arch, shown in Figure 7.3 on page 121 and 7.4 on page 121, were plotted versus the main geometric and mechanical

Table 7.1: Main properties of the experimental case studies – extrados reinforcement

Test	shape	t mm	b mm	span mm	rise mm	α deg	W N	FRP	b_f mm
Badalà	circular	70	550	1497	398	34°	1271	carbon	200
Basilio 2x50mm	circular	50	450	1413	562	13°	816	glass	100
Basilio 2x80mm	circular	50	450	1413	562	13°	816	glass	160
Briccoli Bati 12.5mm	circular	100	100	1502	434	30°	346	carbon	12.5
Briccoli Bati 25mm	circular	100	100	1502	434	30°	346	carbon	25
Briccoli Bati 50mm	circular	100	100	1502	434	30°	346	carbon	50
Castori	catenary	100	200	1980	480	–	1172	carbon	150
Valluzzi 2x200mm	catenary	55	1000	2000	730	–	2334	glass	400
Valluzzi 2x70mm	catenary	55	1000	2000	730	–	2334	carbon	140
Ricamato	circular	120	250	903	393	8°	798	carbon	100

Table 7.2: Main properties of the experimental case studies – intrados reinforcement

Test	shape	t mm	b mm	span mm	rise mm	α deg	W N	FRP	b_f mm
Basilio 2x50mm	circular	50	450	1413	562	13°	816	glass	100
Briccoli Bati 12.5mm	circular	100	100	1502	434	30°	346	carbon	12.5
Briccoli Bati 25mm	circular	100	100	1502	434	30°	346	carbon	25
Briccoli Bati 50mm	circular	100	100	1502	434	30°	346	carbon	50
Castori	catenary	100	200	1980	480	–	1172	carbon	150
Valluzzi 2x70mm	catenary	55	1000	2000	730	–	2334	carbon	140

parameters, namely the reinforcement percentage μ, given by the FRP and masonry section area ratio, the FRP normalized area fraction ω (see Triantafillou 1998a, Valluzzi *et al.* 2001), the rise/span ratio, the thickness/span and the span/thickness ratios (Fig 7.3 on page 121 and 7.4 on page 121). The corresponding data are reported in Table 7.5 on the facing page and 7.6 on the next page. As it can be noticed, no significative trend emerges from these data, except in the case of thickness/span ratio and its inverse, span/thickness ratio, whose tendencies resemble a linear or hyperbola branch progress, respectively.

Concerning the intrados reinforcement, no significant trend seems to emerge, considering that less data are available.

All the arches reinforced at their extrados failed due to shear sliding near the springer, except the Ricamato's one, which collapse mechanism is not clearly described and was probably due to crushing, and the arches reinforced at the intrados exhibited fibres detachment from the internal curved surface.

7.2 Analysis method

As well known, it is assumed that the combination of masonry and FRP works similarly to a reinforced masonry section, considering the FRP reinforcement corresponding to the steel one; moreover, the experimental testing on reinforced masonry arches demonstrated that, as reasonable, the presence of fibres avoids the formation of a hinge placed on the opposite surface of the structure but not on the same face; after a certain load value is reached, the mortar on the joints star to cracks, and the hinges not inhibited by the reinforcement begin to open (Triantafillou 1998a, Valluzzi *et al.* 2001, Foraboschi 2004, Basilio 2007, Castori 2006, Briccoli Bati and Rovero 2008, Focacci 2008).

Table 7.3: Results of the experimental case studies – extrados reinforcement

Test	load configuration	failure mechanism	Q_u kN	Q_u/b N/mm
Badalà	asymmetric	sliding	12.00	21.8
Basilio 2x50mm	asymmetric	sliding	3.17	7.0
Basilio 2x80mm	asymmetric	sliding	3.44	7.6
Briccoli Bati 12.5mm	symmetric	sliding	5.92	59.2
Briccoli Bati 25mm	symmetric	sliding	7.13	71.3
Briccoli Bati 50mm	symmetric	sliding	8.03	80.3
Castori	asymmetric	sliding	11.50	57.5
Valluzzi 2x200mm	asymmetric	sliding	19.98	20.0
Valluzzi 2x70mm	asymmetric	sliding	15.35	15.4
Ricamato	asymmetric	crushing	50.00	200.0

Table 7.4: Results of the experimental case studies – intrados reinforcement

Test	load configuration	failure mechanism	Q_u kN	Q_u/b N/mm
Basilio 2x50mm	asymmetric	detachment	4.45	9.9
Briccoli Bati 12.5mm	symmetric	detachment	3.56	35.6
Briccoli Bati 25mm	symmetric	detachment	5.18	51.8
Briccoli Bati 50mm	symmetric	detachment	6.58	65.8
Castori	asymmetric	detachment	12.30	61.5
Valluzzi 2x70mm	asymmetric	detachment	14.55	14.6

Table 7.5: Comparison of the experimental case studies – extrados reinforcement

Test	Q_{exp}/b N/mm	μ	ω	rise/span ratio	thickn./span ratio	span/thickn. ratio
Badalà	21.8	0.00086	0.3235	0.266	0.0468	21.39
Basilio 2x50mm	7.0	0.00066	0.0331	0.398	0.0354	28.26
Basilio 2x80mm	7.6	0.00106	0.0530	0.398	0.0354	28.26
Briccoli Bati 12.5mm	59.2	0.00021	0.0359	0.289	0.0666	15.02
Briccoli Bati 25mm	71.3	0.00041	0.0717	0.289	0.0666	15.02
Briccoli Bati 50mm	80.3	0.00083	0.1434	0.289	0.0666	15.02
Castori	57.5	0.00125	0.1447	0.242	0.0505	19.80
Valluzzi 2x200mm	20.0	0.00117	0.0888	0.365	0.0275	36.36
Valluzzi 2x70mm	15.4	0.00042	0.1127	0.365	0.0275	36.36
Ricamato	200.0	0.00057	0.0810	0.435	0.1329	7.53

Table 7.6: Comparison of the experimental case studies – intrados reinforcement

Test	Q_{exp}/b N/mm	μ	ω	rise/span ratio	thickn./span ratio	span/thickn. ratio
Basilio 2x50mm	9.89	0.00066	0.0331	0.398	0.0354	28.26
Briccoli Bati 12.5mm	35.60	0.00021	0.0359	0.289	0.0666	15.02
Briccoli Bati 25mm	51.80	0.00041	0.0717	0.289	0.0666	15.02
Briccoli Bati 50mm	65.80	0.00083	0.1434	0.289	0.0666	15.02
Castori	61.50	0.00125	0.1447	0.242	0.0505	19.80
Valluzzi 2x70mm	14.55	0.00042	0.1127	0.365	0.0275	36.36

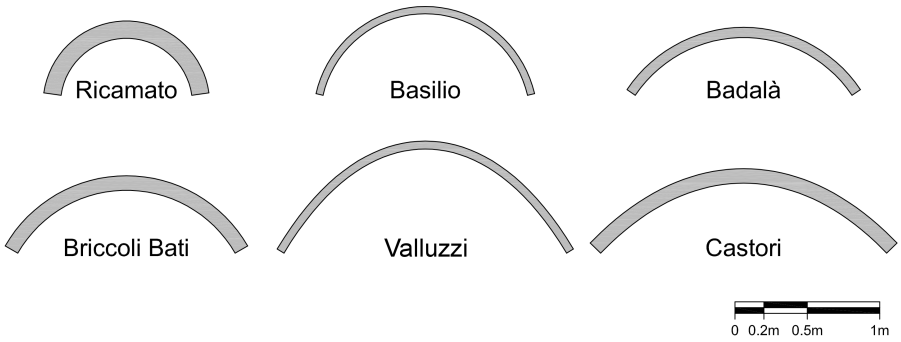

Figure 7.1: Comparison among the various shapes of the collected tests

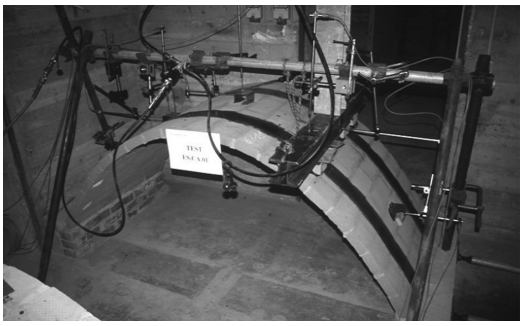

(a) Valluzzi (Valdemarca 1998)

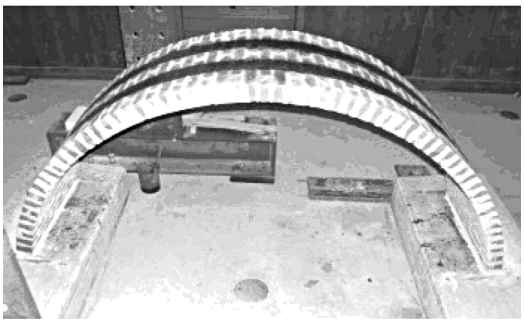

(b) Basilio (2007)

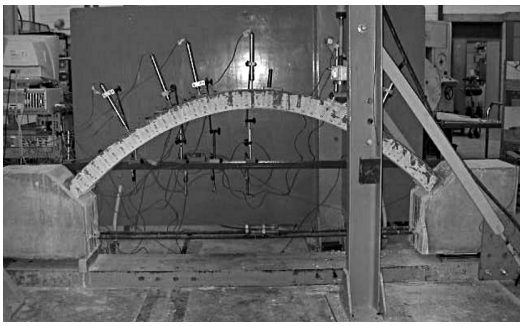

(c) Castori (2006)

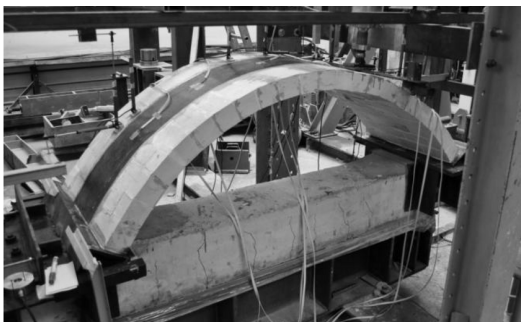

(d) Badalà *et al.* (2008)

Figure 7.2: Images of some tested arches

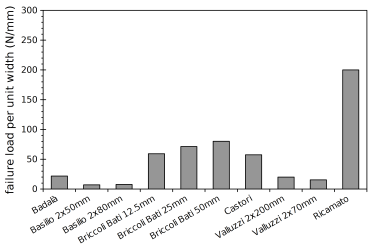

(a) Q_{exp} per unit width

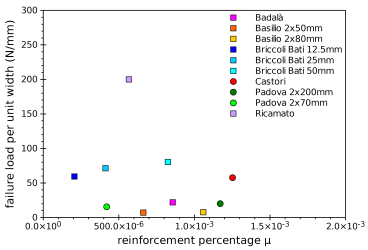

(b) Q_{exp} vs reinforcement percentage μ

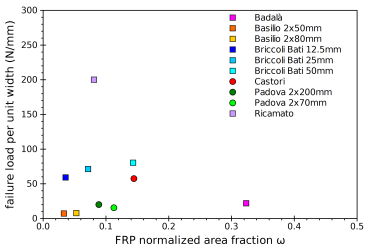

(c) Q_{exp} vs normalized area fraction ω

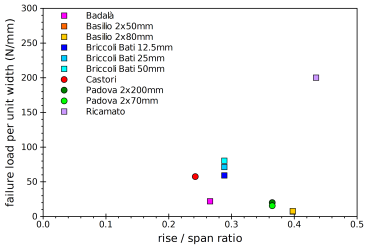

(d) Q_{exp} vs rise/span ratio

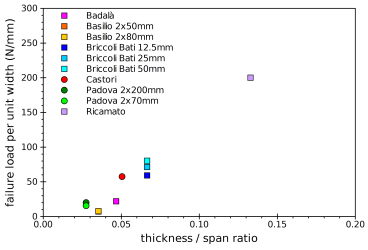

(e) Q_{exp} vs thickness/span ratio

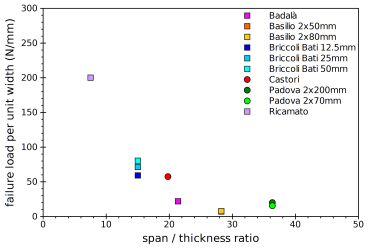

(f) Q_{exp} vs span/thickness ratio

Figure 7.3: Experimental failure loads Q_{exp} plotted versus the main mechanical and geometrical parameters – extrados reinforcement

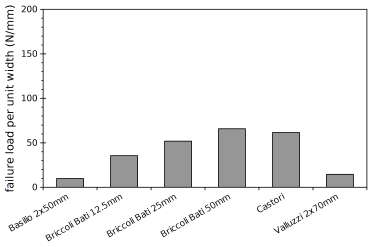

(a) Q_{exp} per unit width

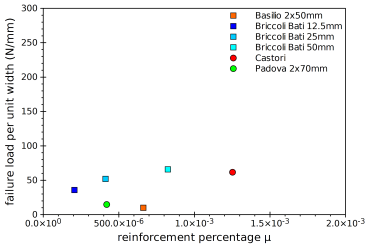

(b) Q_{exp} vs reinforcement percentage

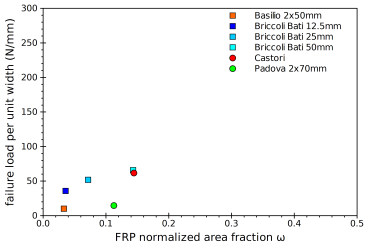

(c) Q_{exp} vs normalized area fraction

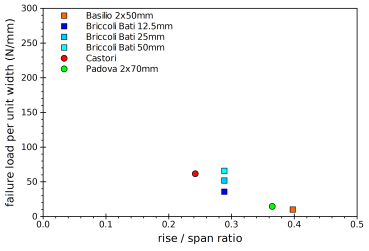

(d) Q_{exp} vs rise/span ratio

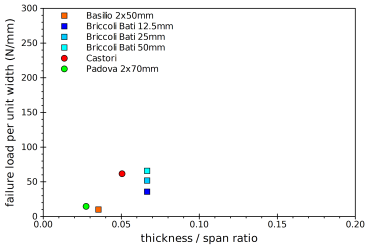

(e) Q_{exp} vs thickness/span ratio

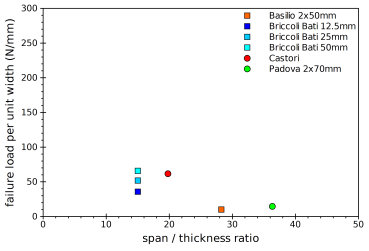

(f) Q_{exp} vs span/thickness ratio

Figure 7.4: Experimental failure loads Q_{exp} plotted versus the main mechanical and geometrical parameters – intrados reinforcement

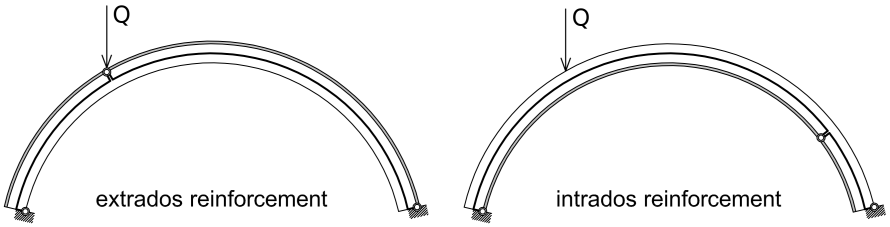

Figure 7.5: Static scheme to evaluate the internal forces - asymmetric concentrated load

Therefore, it is supposed that the arched element, after the formation of hinges on the same position pertinent to the unreinforced arch, where not prevented, could be described by an isostatic scheme, namely a three-hinge arch (Valluzzi *et al.* 2001, Briccoli Bati and Rovero 2008, Focacci 2008), in order to evaluate the reactions at the springer and the internal forces, compressive and shear one, and the bending moment (Fig. 7.5 and 7.6 on the next page, respectively related to loading at a quarter of span and at the keystone). To place the second hinge for intrados reinforcement, the approximated method proposed by Briccoli Bati and Rovero (2008) was adopted.

To carry out the analyses, each structure was divided into discrete elements, adopting as incrementing parameter the horizontal coordinate, for catenary arches, and the cross section angle, for semicircular arches.

Hence, once all the relevant quantities were calculated as function of the external load Q, it was possible to modify iteratively the load value until the appropriate acting parameter equalized the resisting one, with reference to each predictive model, obtaining in this manner the proper failure load Q_{u}.

Some examples of the analysis method are reported in Figure 7.7 on the facing page, which shows thrust line, bending moment, normal force and shear force, for three different load levels (being Q_{exp} the experimental mean failure load), related to the model tested by Basilio (2007) and strengthened at its extrados with two stripes of glass fibres 50 mm wide. The same parameters are given in Figure 7.8 on the next page, normalized with respect to the vertical load Q (for normal and shear forces) and to the product Qt (for bending moment), being t the thickness of the arch. It can be observed, as expected, that the normalized values show a slight variation with respect to the load level, since the adopted static scheme was isostatic.

Figure 7.9 on page 124 and 7.10 on page 124 show the above mentioned plots in the case of the model tested by Basilio (2007) and strengthened at its intrados with two stripes of glass fibres 50 mm wide. It can be observed that the thrust line shows a discontinuity under the concentrated load: as a matter of fact, under the load point the normal force decreases to low values and the jump on the shear profile provokes an inversion on the bending moment trend; therefore, to justify similar values of bending moment, which is given by the product Nu (being N the normal force and u its eccentricity), the eccentricity has to rise to higher values. If the load is applied on the keystone, as in the models tested by Briccoli Bati and Rovero (2008), the thrust line shows a cusp discontinuity, differently from the former one.

7.3 Application of predictive models

The application of available predictive models was based on the previously shown static schemes, used to evaluate the reaction at the springers and the internal forces, normal, N, and shear, V, ones, the bending moment M and, consequently, the eccentricity u that

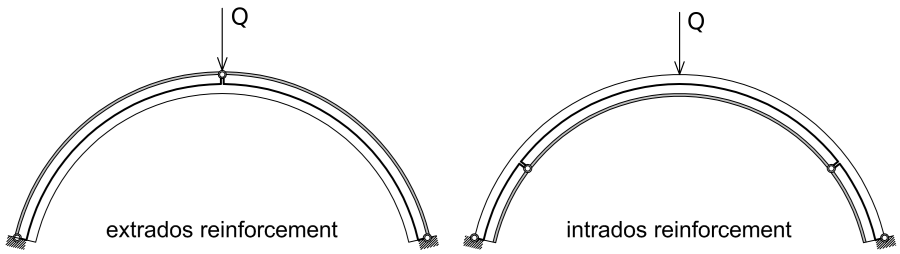

Figure 7.6: Static scheme to evaluate the internal forces - symmetric concentrated load

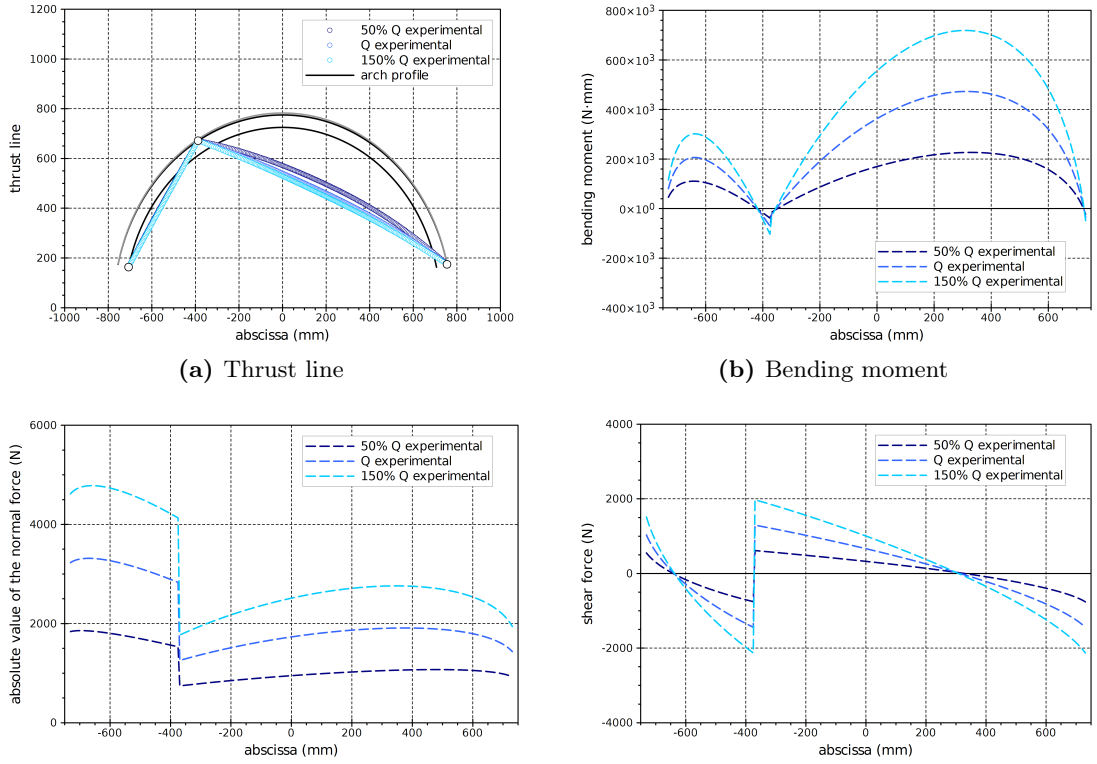

(a) Thrust line **(b)** Bending moment

(c) Normal force **(d)** Shear force

Figure 7.7: Thrust line and internal forces for extrados reinforcement at various load levels (Basilio 2007)

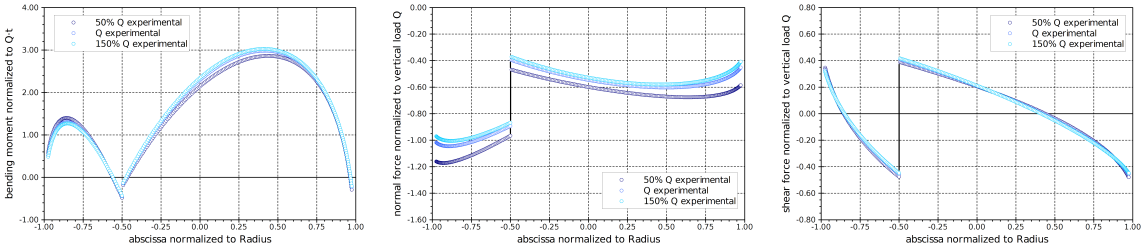

(a) Bending moment **(b)** Normal force **(c)** Shear force

Figure 7.8: Normalized internal forces for extrados reinforcement at various load levels (Basilio 2007)

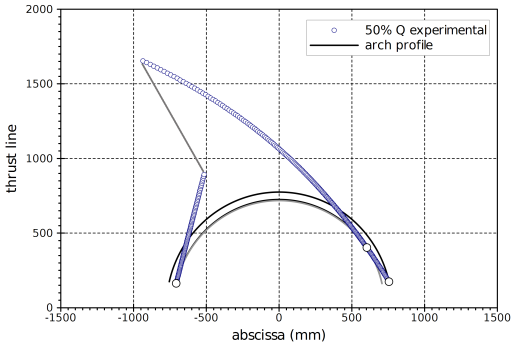

(a) Thrust line

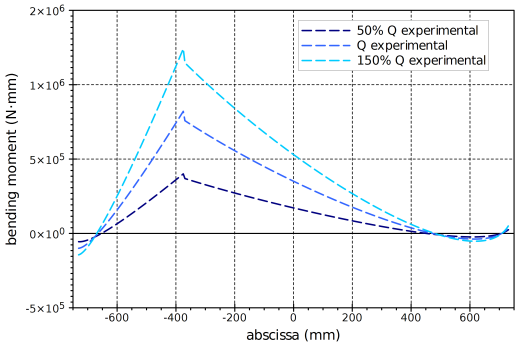

(b) Bending moment

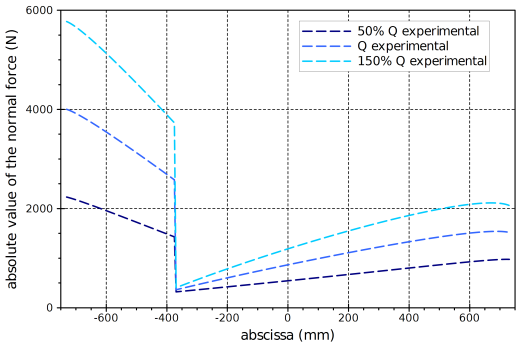

(c) Normal force

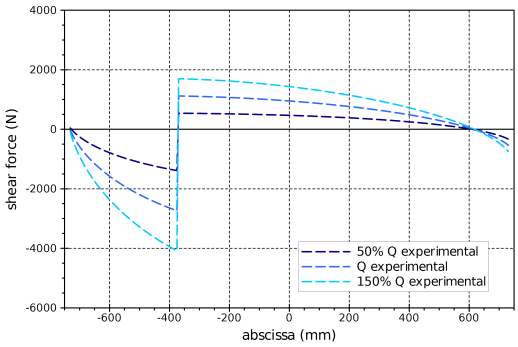

(d) Shear force

Figure 7.9: Thrust line and internal forces for intrados reinforcement at various load levels (Basilio 2007)

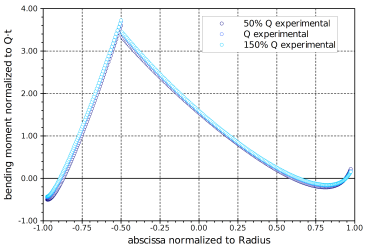

(a) Bending moment

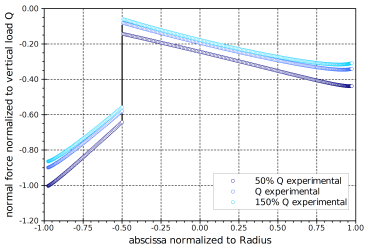

(b) Normal force

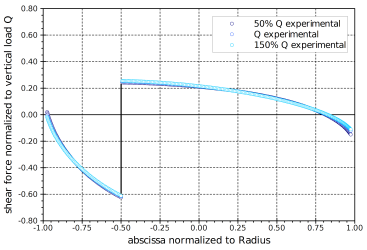

(c) Shear force

Figure 7.10: Normalized internal forces for intrados reinforcement at various load levels (Basilio 2007)

is given by the M/N ratio, related to an arbitrary value of external concentrated load Q. Where needed, the simplified approach proposed by Foraboschi (2004), which assumes a fixed stress block of one third of the masonry section for the compressive force, was adopted to estimate C and T, respectively the compressive force on the masonry and the tensile force on the reinforcement. Mechanical and geometric data reported by the available publications were used, assuming calculated values in place of missing experimentally measured ones, when needed.

7.3.1 Extrados reinforcements

Concerning the extrados reinforcement, the following mechanisms were considered:

- flexural failure: the corresponding failure load was evaluated by applying the sectional analysis developed by Triantafillou (1998a) and the other proposed by Foraboschi (2004); for the latter model, a further check was performed, related to the fibres rupture;
- intermediate debonding: the simplified approach, which consists in assuming a limit stress proportional to the one related to plate-end debonding, as proposed in CNR DT-200 (2004), was adopted, using the c_1 coefficient corresponding to the concrete substrate (0.03) instead of the halved one proposed for masonry, and the c_1 coefficient regressed by the above mentioned data analyses (0.124); the simplified hypotheses formalized by Foraboschi (2004) were assumed to estimate the compressive and tensile forces on the cross section;
- shear failure: the usual model based on a Coulomb-like law was adopted, without assigning any strength contribution to the reinforcement, conjectured by Valluzzi *et al.* (2001), Briccoli Bati and Rovero (2008), since the analyzed sections were placed at the final part of the arch and that resistance, if present, could not be activated.

Results in terms of absolute values and predicted versus experimental failure loads are given in Tables 7.7 on the following page and 7.8 on the next page, where TR stands for Triantafillou's model, FOR and FOR2 indicate Foraboschi's models, the latter calculated taking into account the fibres rupture (the maximum tensile force on the reinforcement was imposed), DB and DB2 stand for the intermediate debonding models evaluated assuming the c_1 values proposed by CNR DT-200 (2004) and the one calibrated in the present work, respectively, SF for shear failure, and shown in Figure 7.11 on page 127.

As it can be observed, Foraboschi's model for masonry crushing does not take into account the reinforcement amount, differently from Triantafillou's one. The intermediate debonding mechanism, although never observed, gives predictions generally lower than the experimental failure loads. The model for the shear resistance seems not to lead to reliable results (sometimes totally irrelevant, as for the arch models of Basilio, Briccoli Bati and Ricamato where the predictions are lower than a reasonable load value that provokes the hinges formation); this fact could be justified by taking into account the static scheme assumed to evaluate the internal forces: where the eccentricity of the internal normal force stands outside the masonry section, the reinforcement is assumed to work and the compressive force, given by the sum of the normal force and the tensile force on the reinforcement, assures high shear resistance, while the shear strength is proportional to the normal force only where it stands on the masonry section, situation that is supposed to be verified near the extrados hinge at the springer where the shear failure is generally observed, and causes a localized decrease of resistance (Fig. 7.12 on page 127), rather independent from the applied load and

Table 7.7: Predicted failure loads – extrados reinforcement

Test	EXP N	TR N	FOR N	FOR2 N	DB N	DB2 N	SF N
Badalà	12000	21900	18650	73300	15600	31150	3000
Basilio 2x50mm	3170	8900	16900	10100	3700	7250	750
Basilio 2x80mm	3440	10700	16900	16000	5750	11500	750
Briccoli Bati 12.5mm	5920	14400	18400	13100	5550	11050	350
Briccoli Bati 25mm	7130	17600	18400	25900	10850	21800	350
Briccoli Bati 50mm	8030	20900	18400	51500	21500	43500	350
Castori	11500	16600	17200	63200	17300	34400	3450
Valluzzi 2x200mm	19980	15900	20750	25150	9300	18250	21000
Valluzzi 2x70mm	15350	17200	20750	17300	6400	21000	21000
Ricamato	50000	82300	84500	51500	54700	111500	750

Table 7.8: Predicted versus experimental failure loads – extrados reinforcement

Test	TR	FOR	FOR2	DB	DB2	SF
Badalà	1.83	1.55	6.11	1.30	2.60	0.25
Basilio 2x50mm	2.81	5.33	3.19	1.17	2.29	0.24
Basilio 2x80mm	3.11	4.91	4.65	1.67	3.34	0.22
Briccoli Bati 12.5mm	2.43	3.11	2.21	0.94	1.87	0.06
Briccoli Bati 25mm	2.47	2.58	3.63	1.52	3.06	0.05
Briccoli Bati 50mm	2.60	2.29	6.41	2.68	5.42	0.04
Castori	1.44	1.50	5.50	1.50	2.99	0.30
Valluzzi 2x200mm	0.80	1.04	1.26	0.47	0.91	1.05
Valluzzi 2x70mm	1.12	1.35	1.13	0.42	1.37	1.37
Ricamato	1.65	1.69	1.03	1.09	2.23	0.01

strongly dependent on the assumed friction coefficient, which literature values could be very different, for example 0.5 (Heyman 1982), 0.64 (Foraboschi 2004), 0.73 (Valluzzi *et al.* 2001). Finally (Tab. 7.9 on the facing page,), the possible FRP contribution to shear resistance, obtained by multiplying minimum (18.2 N/mm) and maximum (28.8 N/mm) average peak load per unit width of V-shape Peel tests and reinforcement width of each arch model, has been related to the maximum shear stress calculated at the springer at failure, in order to provide a first estimation of this effect. It has to be noticed as this rough comparison does not take into account the likely influence of substrate, neither the actual possibility of effectively developing such a resistance mechanism, which is supposed not to affect the tested arches. A discussion on these issues can be found in Panizza *et al.* (2008b).

7.3.2 Intrados reinforcement

Concerning the intrados reinforcement, the following mechanisms were considered:

- flexural failure: the corresponding failure load was evaluated by applying the sectional analysis developed by Triantafillou (1998a), since the Foraboschi's model has been discussed in the previous section;
- intermediate debonding: the simplified approach, which consists in assuming a limit stress proportional to the one related to the plate-end debonding, exposed by CNR DT-200 (2004) was adopted, using the c_1 coefficient corresponding to the concrete substrate (0.03) instead of the halved one proposed for masonry, and the c_1 coefficient regressed

Table 7.9: FRP resistance compared to shear force at failure – extrados reinforcement

Test	Fail. load N	Max shear N	FRP1/max shear	FRP2/max shear
Badalà	12000	5835	62%	99%
Basilio 2x50mm	3170	1445	126%	199%
Basilio 2x80mm	3440	1562	186%	295%
Briccoli Bati 12.5mm	5920	2997	8%	12%
Briccoli Bati 25mm	7130	3602	13%	20%
Briccoli Bati 50mm	8030	4052	22%	36%
Castori	11500	4997	55%	86%
Valluzzi 2x200mm	19980	6030	121%	191%
Valluzzi 2x70mm	15350	7858	32%	51%
Ricamato	50000	19900	9%	14%

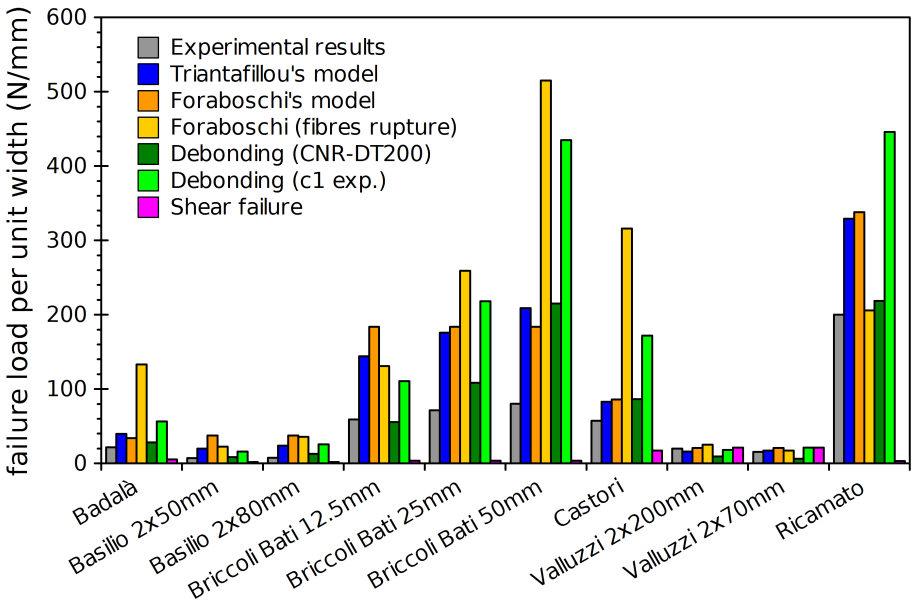

Figure 7.11: Comparison among experimental and predicted failure loads – extrados reinforcement

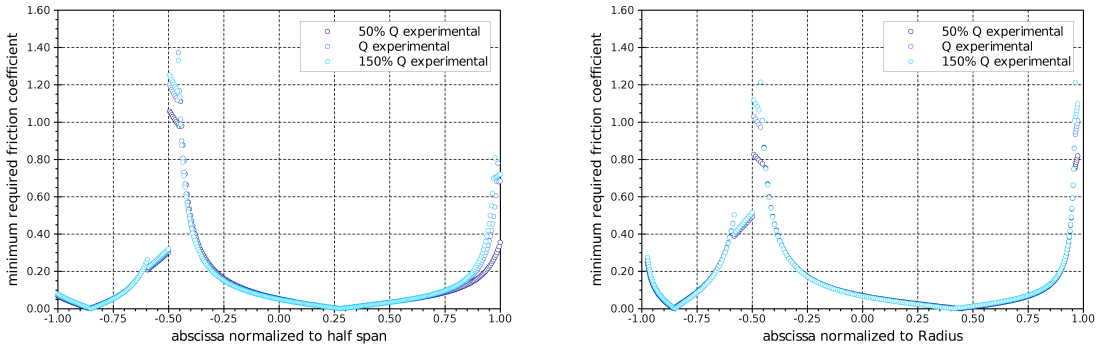

(a) Padova 2x70mm (Valluzzi *et al.* 2001)

(b) Basilio (2007) - 2x50mm

Figure 7.12: Minimum friction coefficient required to assure the shear resistance

by the above mentioned data analyses (0.124); the simplified hypotheses formalized by Foraboschi (2004) were assumed to estimate the compressive and tensile forces on the cross section;

- fibres detachment from the surface: the model usually reported in literature (Valluzzi *et al.* 2001, Briccoli Bati and Rovero 2008), which relates the normal tension on the masonry-FRP interface to the pull-off strength experimentally measured, was applied.

Results in terms of absolute values and predicted versus experimental failure load are given in Tables 7.10 on the next page and 7.11 on the facing page, where TR stands for Triantafillou's model, DB and DB2 stand for the intermediate debonding models evaluated assuming the c_1 values proposed by CNR DT-200 (2004) and the one calibrated in the present work, respectively, FD for fibres detachment, and shown in Figures 7.13 on the next page and 7.13 on the facing page.

Regarding the models related to flexural failure and intermediate debonding, considerations previously presented can apply also to the intrados reinforcement, being the same mechanisms; it can be observed as shear failure does not affect arches reinforced at their intrados, since the shear forces are generally lower (see Focacci 2008).

Concerning the fibres detachment model, the pull-off strength was evaluated by applying the third experimental relation (4.10), related to all data, which gives a strength of 1.1 N/mm^2 for a brick's compressive strength of 9 N/mm^2, that is the case of the models of Valluzzi and Basilio; pull-off tests on masonry prisms (with mortar joint within the cut area), carried out at the University of Minho on the same materials used for the arches (Basilio 2007), measured an average strength of 1.2 N/mm^2; tests made at the University of Perugia (Castori 2006) gave a strength of 1.6 N/mm^2 for concrete brick's compressive strength of 43.3, whereas the formula provides a pull-off strength of 3.1 N/mm^2. The minimum intrados curvature radii of the collected models, constant in the case of semicircular shape and variable for catenary arches (in these cases they were evaluated following Eq. 7.1, where $y(x)$ is the algebric expression of the arch profile on a Cartesian plane, κ and R stand for curvature and curvature radius, respectively), vary from 0.73 m (Basilio) to 1.08 m (Castori). As reported by Valluzzi *et al.* (2001), Briccoli Bati and Rovero (2008), the normal stress σ on the interface is proportional to the tensile force T on the reinforcement and inversely proportional to the product of FRP width b_f and curvature radius R; therefore, imposing the limit tensile strength of the masonry, it should be possible to calculate the maximum tensile force to be withstood by the reinforcement (Eq. 7.2. Imposing the minimum value of curvature radius, 0.73 m, and a tensile strength of 0.5 N/mm^2, a value of 730 N/mm arises, which is really high compared to usual strength per unit width of externally bonded reinforcement, as the MBrace® datasheets provide a range from 270 N/mm for very high modulus CFRP to 565 N/mm for high strength CFRP, being glass and aramid included between these two limits.

$$\kappa = \frac{y''(x)}{\sqrt{(1+(y'(x))^2)^3}}; \qquad R = \frac{1}{\kappa} \tag{7.1}$$

$$\sigma = \frac{T}{b_\mathrm{f} R} \qquad \Rightarrow \qquad \frac{T}{b_\mathrm{f}} = \sigma R \tag{7.2}$$

Table 7.10: Predicted failure loads – intrados reinforcement

Test	EXP N	TR N	DB N	DB2 N	FD N
Basilio 2x50mm	4450	7300	2950	5900	41500
Briccoli Bati 12.5mm	3560	11400	3900	7600	22600
Briccoli Bati 25mm	5180	15500	7500	14800	44900
Briccoli Bati 50mm	6580	19000	14600	29300	89500
Castori	12300	15700	14500	28900	270000
Valluzzi 2x70mm	14550	16700	5900	11500	33300

Table 7.11: Predicted versus experimental failure loads – intrados reinforcement

Test	TR	DB	DB2	FD
Basilio 2x50mm	1.64	0.66	1.33	9.33
Briccoli Bati 12.5mm	3.20	1.10	2.13	6.35
Briccoli Bati 25mm	2.99	1.45	2.86	8.67
Briccoli Bati 50mm	2.89	2.22	4.45	13.60
Castori	1.28	1.18	2.35	21.95
Valluzzi 2x70mm	1.15	0.41	0.79	2.29

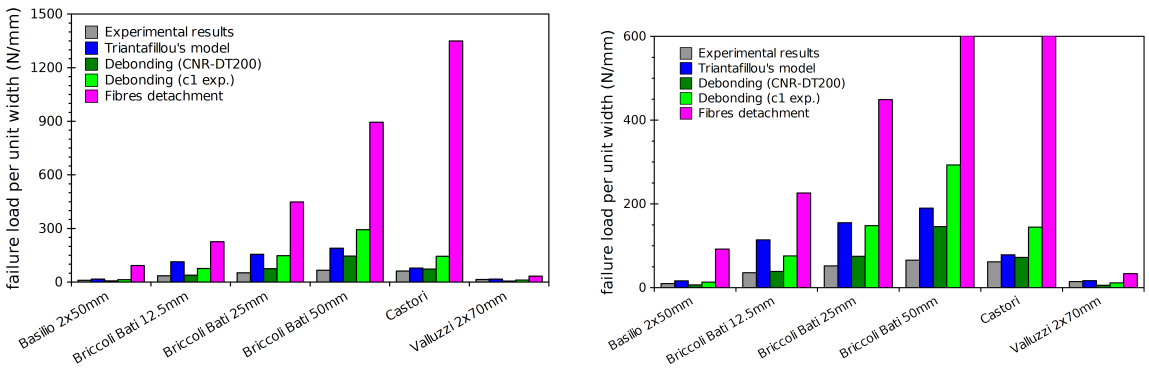

(a) **(b)**

Figure 7.13: Comparison among experimental and predicted failure loads – intrados reinforcement

7.4 Conclusive remarks

- Concerning the extrados reinforcement, models related to flexural crisis (masonry crushing or fibres rupture) lead to failure loads generally higher (from 150% to 300%) than the experimental ones, since the bending strength could not be reached before the shear crisis occurs at lower load levels. Only in the case of models tested at University of Padova (Valluzzi *et al.* 2001) these predictions were very close (80% and 112%) to the experimental failure loads, despite the different mechanisms, and it could be related to the peculiar thickness/span ratio of these arches, that could had emphasized the flexural behaviour.

- Models related to the intermediate FRP debonding, never observed during the reported campaigns, give to predictions that vary from 40% to 270% ($c_1 = 0.03$) or from 90% to 540% ($c_1 = 0.124$) of the experimental failure loads, strongly dependent on the chosen values of the experimental coefficient c_1. It has also to be noticed that the bond behaviour of FRP applied on masonry prisms with mortar joints, at present, is far from being investigated, as most tests have been carried out on single resisting elements: therefore, it is difficult to suppose if the presence of the joint has a negative or positive influence, since the irregular surface could generate a sort of dissipative mechanism similar to friction that could justified some experimental results reported by Basilio (2007), Casareto *et al.* (2003).

- The shear failure criterion does not seem to be sufficiently adequate to provide a reliable estimation of the failure load, since it is strongly dependent on the assumed friction coefficient, on the geometry of the structure and the adopted static schemes, including the position of hinges. Where the cross section is bended and the reinforcement is activated, the compressive force assures high strength against shear, as observed by Foraboschi (2004), but near the extrados hinge at the springer the eccentricity is lower than half the thickness of the arch, therefore the reinforcement is not active (and it could not be for the collected tests, since in that area the bonded length is lower than the effective one and there were no anchoring devices): hence, the minimum friction coefficient, required to assure the resistance of the joint, quickly increases along a very small area.

- Concerning the intrados reinforcement, models related to flexure and intermediate debonding give to considerations similar to the extrados reinforcement. The model describing fibres detachment due to normal stresses generated by the curved morphology of the intrados, while correctly interprets the phenomen, seems to overestimate the failure load (more than 230% the experimental one); this could be justified, for the collected cases, since assuming the minimum curvature radius pertinent to the colleted specimens, 0.76 m, the model gives a very high value (730 N/mm) of tensile force that activates the ultimate strength for 1 N/mm^2 of tensile strength of the substrate, approximately varying the commonly used FRP textiles tensile strength per ply from 270 N/mm to 565 N/mm (MBrace® datasheets). However, a deeper analysis could calibrate this model to assure higher adherence to experimental data.

- Finally, it has to be considered that the above presented inferences are related to the aim of predicting the experimental behaviour of structures that are significantly different to real structures, for absence of filling, the selected geometric proportion, the adopted materials and the load conditions.

Chapter 8

Conclusions

Starting from the previously exposed background related to strengthening and restoration of masonry arched structures by means of FRP materials, the present work has been devoted to the investigation of five main topics: the problem of collecting and sharing data concerning available activities based on applications on masonry structures; the analysis of possible correlations among pull-off strength and other more common mechanical properties of solid clay bricks; the investigation of bond behaviour in the case of tangential forces, targeted to the calibration of guidelines' provisions (available only for this mechanism); the investigation of a possible contribution of the reinforcement when subdued to mixed actions, as in the case of sliding of masonry on a mortar joint; finally, the validation of existing models, aimed at describing the collapse behaviour of reinforced masonry arches, through their application to several experimental case studies.

The first part of the work has led to the creation and the organization, among the activities of the RILEM Technical Committee 223-MSC, of a Database aimed to collect data concerning available experimental, analytical, numerical works, as well as interventions on real structures or other topics as durability or Non-Destructive Techniques. Latest releases present significant upgrades that modified the original Database into a Data-Warehouse, which allows to implement additional functions as data treatment and exportation, graphic tools, etc. This system, currently available on-line (details can be found on the RILEM site, at www.rilem.net), has been designed to guarantee access and contributions coming from external researchers, as well as to provide the possibility of being upgraded and improved during its service life, in order to be progressively adjusted to future progress of research and practice topics.

The first local mechanism, behaviour of the FRP-masonry interface in the case of normal actions, has been investigated through the execution of a large number tests on solid clay bricks (flexural, compressive, splitting and pull-off tests), combining three different tests on each element so as to obtain triplets of values mutually related. As expected, if the reinforcement is correctly applied, the type of fibres and the absence of primer should not have any influence on the strength measured by the pull-off test, since only the failure mode could be influenced; glass fibres caused some unwanted failures, which should however imputed to contingent factors related to that available portion of reinforcement, such as an incorrect conservation or cleaning. With reference to the available strength ranges, it has been found that pull-off tensile strength could be adequately correlated to flexural, splitting and compressive strength of the bricks by means of power-based regressions, different for extruded and facing bricks, although their trends were similar; only in the case of pull-off versus compressive strength, a single function seems to correctly depict the tendency for both

the brick types. A different behaviour of extruded and facing elements was observed also in the correlation between flexural and compressive strength, whereas a single power-based regression could be sufficient to describe the trend that relates flexural and splitting tensile strength. Finally, the correlations among average values of the bricks properties, where sufficiently evident, substantially confirmed the trends previously calculated on punctiform data.

The second local mechanism, bond behaviour in the case of tangential actions, has been investigated through the performance of ten Double-lap Shear Tests, five samples reinforced with carbon and five with glass fibres. The adopted symmetrical test set-up has revealed, despite its good feasibility related to the available universal test machine, some reliability problems, mainly related to the difficulty of control the actual load distribution on the two reinforcement strips, that could make more profitable the choice of an asymmetrical set-up for future activities, namely the Single-lap Shear Test.

The experimental strengths have been compared with twenty-one predictive models developed for concrete substrate. Most predictions underestimate the test results and, moreover, seem to work better for the carbon reinforcement. However, the analytical predictions vary into an wide range (between 44% and 154% of experimental mean failure load for CFRP, 43% and 85% for GFRP). Based on the measured failure loads, different fracture energy values have been derived, around 35% higher in the case of glass reinforcement than carbon one.

An exponential-based function, easy to integrate and derive, is proposed as bond-slip law to describe the interface behaviour; this function has been fitted twice, for carbon and glass reinforcement, as well as two bilinear functions, shape commonly proposed by guidelines (fib Bulletin 14 2001, CNR DT-200 2004). Results seem to show an interface local behaviour of CFRP slightly stiffer than GFRP, although it should be related only to the substrate properties.

Finite element analyses of the test specimens were carried out implementing the calibrated bond stress – slip laws. Several comparison of numerical results obtained from different models were performed: FRP modelled with the concentrated fibres approach versus FRP modelled with the distributed fibres, exponential-based versus bilinear bond stress–slip law, influence of the bond length. FE results were also compared with the results obtained from the analytical solution proposed by Yuan *et al.* (2001, 2004), which provides reasonable prediction of the maximum load and loaded end displacement. It has been pointed out that the concentrated fibres approach is practically equivalent to the distributed one, although the last one might entail a slightly lower computational burden. Moreover, the use of a simple bilinear bond stress–slip law could be sufficient to properly describe the bond phenomenon, without resorting to more sophisticated local laws. The combination of numerical modelling and analytical solution provided the minimum required bond length both for CFRP and GFRP applied on clay brick, which are of 70.13 mm and 59.41 mm, respectively.

Concerning the calibration of the c_1 coefficient, related to the evaluation of the fracture energy proposed in CNR DT-200 (2004), the obtained results, based on several data collected from literature, show a similar behaviour of stones and bricks, although a quite large scattering depending on the calibration method has been observed, whereas masonry prisms seem to offer higher performances. Reliability of these results, however, is strongly affected by the limited base of data currently available and by the lacking of some crucial data that are rarely given by common sources.

The third local mechanism, behaviour under mixed-mode load conditions, has been investigated through Fourteen V-shape Peel Tests, whose test set-up was adapted by similar

tests carried out on concrete substrate (Wu *et al.* 2005b, Dai *et al.* 2007), performed using CFRP reinforcement applied on solid clay bricks. Although these should be considered as pilot tests, the main characteristics of the investigated phenomenon were substantially identified, and the experimental observations do not differ much from what Wu *et al.* (2005b), Dai *et al.* (2007) reported in the case of concrete supports.

It has been highlighted that the peel load, during the detachment, oscillated within a limited range, though the scattering was in some cases very large. Maximum loads of around 18 N/mm were observed, except for the S4 series that gave 28.8 N/mm, being the strengths comparable for the other substrates. The peel angle, similarly to the peel load, oscillated around quasi-constant values, with high scattering also in this case; the estimated average values ranged from 4.5 to 7 degrees. Calculated mixed-mode fracture energies ranged from 0.3 to 0.7 N/mm.

In the final part of the work, available interpretative models, updated when possible with the results obtained at a local level, have been applied to the global behaviour of the collected experimental case studies.

Concerning the extrados reinforcement, models related to the flexural crisis (masonry crushing or fibres rupture) have led to failure loads generally higher (from 150% to 300%) than the experimental ones, since the bending strength could not be reached before the shear crisis occurs at lower load levels. Only in the case of arches tested at the University of Padova these predictions were very close (80% and 112%) to the experimental failure loads, despite the different mechanisms, and it could be related to the peculiar thickness/span ratio of these arches, that could had emphasized the flexural behaviour.

Models related to the intermediate FRP debonding, never observed during the reported campaigns, have given predictions that vary from 40% to 270% ($c_1 = 0.03$) or from 90% to 540% ($c_1 = 0.124$) of the experimental failure loads, strongly dependent on the chosen values of the experimental coefficient c_1. It has also to be noticed that the bond behaviour of FRP applied on masonry prisms with mortar joints, at present, is far from being investigated, as most tests have been carried out on single resisting elements: therefore, it is difficult to suppose if the presence of the joint has a negative or positive influence, since the irregular surface could generate a sort of dissipative mechanism similar to friction that could justified some experimental results reported by Basilio (2007), Casareto *et al.* (2003).

The shear failure criterion does not seem to be sufficiently adequate to provide a reliable estimation of the failure load, since it is strongly dependent on the assumed friction coefficient, on the geometry of the structure and the adopted static schemes, including the position of the hinges. Where the cross section is bended and the reinforcement is activated, the compressive force assures high strength against shear, as observed by Foraboschi (2004), but near the extrados hinge at the springer the eccentricity is lower than half the thickness of the arch, therefore the reinforcement is not active (and it could not be for the collected tests, since in that area the bonded length is lower than the effective one and there were no anchoring devices): hence, the minimum required friction coefficient, to assure the resistance of the joint, quickly increases along a very small area.

Concerning the intrados reinforcement, models related to flexure and intermediate debonding give to considerations similar to the extrados reinforcement. The model describing the fibres detachment due to normal stresses generated by the curved morphology of the intrados, while correctly interprets the phenomen, seems to overestimate the failure load (more than 230% the experimental one); this could be justified, for the collected cases, since assuming the minimum curvature radius pertinent to the colleted specimens, 0.76 m, the model gives a very high value (730 N/mm) of tensile force that activates the ultimate strength

for 1 N/mm^2 of tensile strength of the substrate, approximately varying the commonly used FRP textiles tensile strength per ply from 270 N/mm to 565 N/mm (MBrace® datasheets).

References

ACI 318-99 (2004). Building Code requirements for structural concrete. American Concrete Institute.

ACI 440.2R-02 (2002). Guide for the Design and Construction of Externally Bonded FRP Systems for Strengthening Concrete Structures. American Concrete Institute.

ACI 440.7R-10 (under development). Guide for the Design and Construction of Externally Bonded Fiber-Reinforced Polymer Systems for Strengthening Unreinforced Masonry Structures. American Concrete Institute.

ACI 440R-96 (1996). State-of-the-Art Report on Fiber Reinforced Plastic (FRP) Reinforcement for Concrete Structures. American Concrete Institute.

Aiello, M. A. and Sciolti, M. S. (2006). Bond analysis of masonry structures strengthened with CFRP sheets. *Construction and Building Materials*, **20**, 90–100.

ASTM C1583 (2004). Standard Test Method for Tensile Strength of Concrete Surfaces and the Bond Strength or Tensile Strength of Concrete Repair and Overlay Materials by Direct Tension (Pull-off Method). American Society for Testing and Materials.

Badalà, A., Cuomo, M. and D'Agata, G. (2008). Analisi limite di volte a botte rinforzate con CFRP. In *XVII Convegno Italiano di Meccanica Computazionale – GIMC2008*. Alghero (Italy). In Italian.

Barbieri, A., Borri, A., Corradi, M. and Di Tommaso, A. (2002). Dynamic Behaviour of Masonry Vaults Repaired with FRP: Experimental Analysis. In 6^{th} *Int. Masonry Conf. of the British Masonry Society.*

Barton, B., Wobbe, E., Dharani, L., Silva, P., Birman, A., V.and Nanni, Alkhrdaji, T., Thomas, J. and Tunis, G. (2005). Characterization of reinforced concrete beams strengthened by steel reinforced polymer and grout (SRP and SRG) composites. *Materials Science and Engineering: A*, **412**(1-2), 123–136.

Basilio, I. (2007). *Strengthening of arched masonry structures with composite materials.* Ph.D. thesis, University of Minho (Portugal).

Benvenuto, E. (1981). *La scienza delle costruzioni e il suo sviluppo storico.* Sansoni, Firenze (Italy). In Italian.

Bianculli, N. (2002). *Uso combinato di materiali innovativi e tradizionali per il consolidamento statico di murature storiche. Problemi di interazione meccanica locale.* Master's thesis, University of Padova (Italy). In Italian.

Bikerman, J. J. (1957). Theory of Peeling through a Hookean Solid. *Journal of Applied Physics*, **28**(12), 1484–1485.

Bizindavyi, L. and Neale, K. (1999). Transfer Lengths and Bond Strengths for Composites Bonded to Concrete. *ASCE Journal of Composites for Construction*, **3**(4), 153–160.

Borri, A., Castori, G., Grazini, A. and Giannantoni, A. (2006). Compositi SRP/SRG. Caratteristiche, sperimentazione e applicazioni per edifici esistenti in muratura. *L'Edilizia*, **144**, 38–43. In Italian.

Briccoli Bati, S. and Rovero, L. (2000). Consolidation of masonry arches with carbon-fiber reinforced plastics. In 12^{th} *Int. Brick and Block Masonry Conference*. Madrid (Spain).

Briccoli Bati, S. and Rovero, L. (2008). Towards a methodology for estimating strength and collapse mechanism in masonry arches strengthened with fibre reinforced polymer applied on external surfaces. *RILEM Materials and Structures*, **41**(7), 1291–1306.

Briccoli Bati, S. and Rovero, L. (2009). Bond strength between brick and CFRP strips. In *III Nat. Conf. on Mechanics of masonry structures strengthened with composite materials: modeling, testing, design, control – MuRiCo3*. Venice (Italy), pages 146–152.

Briccoli Bati, S., Rovero, L. and Tonietti, U. (2007). Adesione fra blocchi in laterizio e rinforzo in CFRP. In *Materiali ed Approcci Innovativi per il Progetto in Zona Sismica e la Mitigazione della Vulnerabilità delle Strutture – Nat. Workshop ReLUIS*. Salerno (Italy), pages 213–220. In Italian.

Caleca, L. (2000). *Architettura Tecnica*. Dario Flaccovio Ed., Palermo (Italy). In Italian.

Camli, U. and Binici, B. (2007). Strength of carbon fiber reinforced polymers bonded to concrete and masonry. *Construction and Building Materials*, **21**, 1431–1446.

Capozucca, R. (2010). Experimental FRP/SRP-historic masonry delamination. *Composite Structures*, **92**, 891–903.

Carbone, I., Fiore, A. and Pistone, G. (2001). *Le costruzioni in muratura. Interpretazione del comportamento statico e tecniche di intervento*. Hoepli, Milano (Italy). In Italian.

Cartolaro, A. (2004). *Volte in muratura di mattoni rinforzate con FRP. Studio sperimentale dei meccanismi resistenti alle interfacce*. Master's thesis, University of Padua (Italy). In Italian.

Casareto, M., Olivieri, A., Romelli, A. and Lagomarsino, S. (2003). Bond behaviour of FRP laminates adherent to masonry. In *Int. Conf. Advancing with Composites 2003*. Milan (Italy).

Castori, G. (2006). *Strengthening of masonry elements with innovative composite laminates*. Ph.D. thesis, University of Perugia (Italy).

Chajes, M., Finch, W. J., Januszka, T. and Thomson, T. (1996). Bond and Force Transfer of Composite Material Plates Bonded to Concrete. *ACI Structural Journal*, **93**(2), 295–303.

Chen, J. F. and Teng, J. G. (2001). Anchorage Strength Models for FRP and Steel Plates Bonded to Concrete. *Journal of Structural Engineering*, **127**(7), 784–791.

CNR DT-200 (2004). Guide for the Design and Construction of Externally Bonded FRP Systems for Strengthening Existing Structures. Italian National Research Council.

Collepardi, M., Ogoumah Olagot, J. J., Simonelli, F. and Troli, R. (2005). *Il calcestruzzo vulnerabile — Prevenzione, diagnosi del degrado e restauro*. Tintoretto, Treviso (Italy). In Italian.

Dai, J. and Ueda, T. (2003). Local Bond stress Slip relations for FRP Sheets-Concrete Interfaces. In 6^{th} *Int. Symp. on Fibre-Reinforced Polymer Reinforcement for Concrete Structures – FRPRCS-6*. Singapore (SGP), page 143–152.

Dai, J., Ueda, T. and Sato, Y. (2005). Development of the nonlinear bond stress-slip Model of Fiber Reinforced Plastics sheet-concrete Interfaces with a Simple Method. *ASCE Journal of Composites for Construction*, **9**(1), 52–62.

Dai, J., Ueda, T. and Sato, Y. (2007). Bonding Characteristics of Fiber-Reinforced Polymer Sheet-Concrete Interfaces under Dowel Load. *ASCE Journal of Composites for Construction*, **11**(2), 138–148.

De Lorenzis, L., Galati, N. and Ombres, L. (2004). In-plane shear strengthening of natural masonry walls with NSM CFRP strips and FRCM overlay. In *IV Int. Conf. on Structural Analysis of Historic Constructions*. Padova (Italy), pages 843–855.

De Lorenzis, L., Miller, B. and Nanni, A. (2001). Bond of FRP laminates to concrete. *ACI Materials Journal*, **98**(3), 256–264.

De Lorenzis, L. and Zavarise, G. (2008). Modeling of mixed-mode debonding in the peel test applied to superficial reinforcements. *Int. Journal of Solids and Structures*, **45**, 5419–5436.

Disarò, M. (2000). *Rinforzo di murature mediante ristilatura armata con FRP. Sperimentazione e modellazione*. Master's thesis, University of Padova (Italy). In Italian.

DM 09-01-96 (1996). Norme tecniche per il calcolo, l'esecuzione ed il collaudo delle strutture in cemento armato, normale e precompresso, e per le strutture metalliche. Decreto del Ministero dei Lavori Pubblici.

Faccio, P. and Foraboschi, P. (2000). Analisi agli stati limite ultimi di volte in muratura con rinforzi in FRP. *L'edilizia*, **5**(6), 48–56. In Italian.

Faella, C., Martinelli, E., Paciello, S. and Perri, F. (2009). Composite materials for masonry structures: the adhesion issue. In *III Nat. Conf. on Mechanics of masonry structures strengthened with composite materials: modeling, testing, design, control – MuRiCo3*. Venice (Italy), pages 266–273.

Ferracuti, B., Martinelli, E., Nigro, E. and Savoia, M. (2007a). Fracture energy and design rules against FRP - concrete debonding. In *Fibre-Reinforced Polymer Reinforcement for Concrete Structures – FRPRCS-6*. Patras (Greece).

Ferracuti, B., Savoia, M. and Mazzotti, C. (2007b). Interface law for FRP–concrete delamination. *Composite structures*, **80**(4), 523–531.

fib Bulletin 14 (2001). Externally bonded FRP reinforcement for RC structures - Technical Report on the design and use of externally bonded fibre reinforced polymer reinforcement for reinforced concrete structures. Fédération Internationale du Béton.

Focacci, F. (2008). *Rinforzo delle murature con materiali compositi*. Dario Flaccovio Ed., Palermo (Italy). In Italian.

Foraboschi, P. (2004). Strengthening of masonry Arches with Fiber-Reinforced Polymer Strips. *ASCE Int. Journal of Composites for Construction*, **8**(3), 191–202.

Garbin, E. (2008). *Characterization of bed joint reinforced brick masonry subjected to compression*. Ph.D. thesis, University of Padova (Italy).

Gaudini, G., Modena, C., Casarin, F., Bettio, C. and Lucchin, F. (2008). FRP-strengthening of masonry structures: effect of debonding phenomenon. In *VI Int. Conf. on Structural Analysis of Historic Constructions*. Bath (UK), pages 403–411. ISBN 978-0-415-46872-5.

Gent, A. N. and Hamed, G. R. (1975). Peel Mechanics. *Journal of Adhesion*, **7**, 91–95.

Giomo, F. (2008). *Rinforzo di strutture murarie con materiali compositi FRP: analisi sperimentale e modellazione del comportamento dell'interfaccia soggetta ad azioni composte nel caso di applicazione ad archi e volte*. Master's thesis, University of Padua (Italy). In Italian.

Giurgiutiu, V., Lyons, J., Petrou, M., Laub, D. and Whitley, S. (1999). Experimental fracture mechanics for the bond between composite overlays and concrete substrate. In *International Composites Expo – EXPO'99*. Cincinnati (USA).

Giurgiutiu, V., Lyons, J., Petrou, M., Laub, D. and Whitley, S. (2001). Fracture mechanics testing of the bond between composite overlays and a concrete substrate. *Journal of Adhesion Science Technology*, **15**(11), 1351–1371.

Grande, E., Imbimbo, M. and Sacco, E. (2008). FRP-strengthening of masonry structures: effect of debonding phenomenon. In *VI Int. Conf. on Structural Analysis of Historic Constructions*. Bath (UK), pages 1017–1023. ISBN 978-0-415-46872-5.

Guglielmi, E. (2002). *Storia dell'Architettura*. Newton & Compton, Roma (Italy). In Italian.

Hendry, A. W. (1986). *Statica delle strutture in muratura di mattoni*. Pàtron Editore, Bologna (Italy). Italian ed.

Heyman, J. (1982). *The masonry arch*. Ellis Horwood Limited, Chichester (GBA).

Huang, X., Birman, V., Nanni, A. and Tunis, G. (2005). Properties and potential for application of steel reinforced polymer and steel reinforced grout composites. *Composites Part B: Engineering*, **36**(1), 73–82.

Karbhari, V. M. and Engineer, M. (1996). Investigation of Bond between Concrete and Composites: Use of a Peel Test. *Journal of Reinforced Plastics and Composites*, **15**, 208–227.

Karbhari, V. M., Engineer, M. and Eckel II, D. A. (1997). On the durability of composite rehabilitation schemes for concrete: use of a peel test. *Journal of Materials Science*, **32**, 147–156.

Karbhari, V. M., Niu, H. and Sikorsky, C. (2006). Review and Comparison of Fracture Mechanics-based Bond Strength Models for FRP-strengthened Structures. *Journal of Reinforced Plastics and Composites*, **25**(17), 1757–1794.

Kimpara, I., Kageyama, K., Suzuki, T., Ohsawa, I. and Yamaguchi, K. (1998). Characterization on Peeling Strength of FRP Sheets Bonded on Mortar and Concrete. In *Eight Japan-U.S. Conf. on Composite Materials*. Baltimore (USA), pages 1010–1019.

Lam, C. C. (2009). *Finite element study of bond-slip behaviour of CFRP and GFRP laminates on brick masonry*. Master's thesis, University of Padua (Italy).

Lee, Y., Boothby, T., Bakis, C. and Nanni, A. (1999). Slip Modulus of FRP Sheets Bonded to Concrete. *ASCE Journal of Composites for Construction*, **3**(4), 161–167.

Lu, X. Z., Teng, J. G., Ye, L. P. and Jang, J. J. (2004). Bond-slip models for FRP sheet/plate-to-concrete interfaces. In 2^{nd} *Int. Conf. on Advanced Polymer Composites for Structural Applications in Construction – ACIC-2004*. Guildford, (UK), pages 152–161.

Lu, X. Z., Teng, J. G., Ye, L. P. and Jang, J. J. (2005). Bond-slip models for FRP sheets/plates bonded to concrete. *Engineering Structures*, **27**, 920–937.

Lucchin, F. (2003). *Uso combinato di materiali innovativi e tradizionali per il consolidamento statico di murature storiche. Indagini sperimentali*. Master's thesis, University of Padua (Italy). In Italian.

Marchetti, M. (1999). *Sperimentazione e modellazione del comportamento a taglio di pannelli murari rinforzati tramite FRP*. Master's thesis, University of Padova (Italy). In Italian.

Mazzotti, C., Savoia, M. and Ferracuti, B. (2009). A new single-shear set-up for stable debonding of FRP–concrete joints. *Construction and Building Materials*, **23**, 1529–1537.

Minguzzi, G. (1998). *Fiber Reinforced Plastics - Utilizzo dei materiali compositi a matrice polimerica in edilizia civile*. Alinea, Florence (Italy). In Italian.

Modena, C., Casarin, F., da Porto, F., Garbin, E., Mazzon, N., Munari, M., Panizza, M. and Valluzzi, M. R. (2009). Structural interventions on historical masonry buildings: review of Eurocode 8 provisions in the light of the Italian experience. In *Quali prospettive per l'Eurocodice 8 alla luce delle esperienze italiane – Workshop Reluis-UNI*. Naples (Italy).

Modena, C., Valluzzi, M. R., da Porto, F., Casarin, F. and Bettio, C. (2004). Structural upgrading of a brick masonry arch bridge at the Lido (Venice). In *4th Int. Conf. on Arch Bridges – ARCH'04*. Barcelona (Spain).

Nakaba, K., Kanakubo, T., Furuta, T. and Yoshizawa, H. (2001). Bond Behavior between fiber-reinforced Polymer Laminates ad Concrete. *ACI Structural Journal*, **98**(3), 359–367.

Nicholson, D. W. (1977). Peel mechanics with large bending. *Int. Journal of Fracture*, **13**(3), 279–287.

Panizza, M. (2006). *Analisi sperimentale di meccanismi di interazione locale di volte in muratura rinforzate con tessuti FRP*. Master's thesis, University of Padua (Italy). In Italian.

Panizza, M., Garbin, E., Valluzzi, M. R. and Modena, C. (2008a). Bond Behaviour of CFRP and GFRP Laminates on Brick Masonry. In *VI Int. Conf. on Structural Analysis of Historic Constructions*. Bath (UK), pages 763–770. ISBN 978-0-415-46872-5.

Panizza, M., Garbin, E., Valluzzi, M. R. and Modena, C. (2008b). Shear Mechanism of Brick Masonry Vaults. In *Structural Faults + Repair – SF&R2008*. Edinburgh (UK), pages 763–770. On CD-Rom.

Panizza, M., Garbin, E., Valluzzi, M. R. and Modena, C. (2009). Experimental study of the FRP-clay interface subject to normal stresses. In *III Nat. Conf. on Mechanics of masonry structures strengthened with composite materials: modeling, testing, design, control – MuRiCo3*. Venice (Italy), pages 391–398.

Papanicolaou, C. G., Triantafillou, T. C., Karlos, K. and Papathanasiou, M. (2008a). Textile reinforced mortar (TRM) versus FRP as strengthening material of URM walls: in-plane cyclic loading. *Materials and Structures*, **40**(10), 1081–1097.

Papanicolaou, C. G., Triantafillou, T. C., Papathanasiou, M. and Karlos, K. (2008b). Textile reinforced mortar (TRM) versus FRP as strengthening material of URM walls: out-of-plane cyclic loading. *Materials and Structures*, **41**(1), 143–157.

Preite, G. (1987). *Manuale delle costruzioni in muratura semplice e armata*. E.S.A.C., Roma (Italy). In Italian.

Prota, A., Marcari, G., Fabbrocino, G., Manfredi, G. and Aldea, C. (2006). Experimental In-Plane Behavior of Tuff Masonry Strengthened with Cementitious Matrix-Grid Composites. *ASCE Journal of Composites for Construction*, **10**(3), 223–233.

Savoia, M., Ferracuti, B. and Mazzotti, C. (2003a). Non linear bond-slip law for FRP-concrete interface. In 6^{th} *Int. Symp. on Fibre-Reinforced Polymer Reinforcement for Concrete Structures – FRPRCS-6*. Singapore (SGP), pages 1–10.

Savoia, M., Ferracuti, B. and Mazzotti, C. (2003b). Una legge di interfaccia non lineare per placcaggi con lamine in FRP. In 16^{th} *AIMETA Congress of Theoretical and Applied Mechanics*. Ferrara (Italy). In Italian.

Scarinci, G. (2002). *Proprietà meccaniche dei materiali polimerici e compositi*. Libreria Progetto, Padua (Italy). In Italian.

Shrive, N. G. (2006). The use of fibre reinforced polymers to improve seismic resistance of masonry. *Construction and Building Materials*, **20**, 269–277.

Subramanian, K., Focacci, F. and Carloni, C. (2009). An investigation on the interface fracture propagation between FRP and masonry. In *III Nat. Conf. on Mechanics of masonry structures strengthened with composite materials: modeling, testing, design, control – MuRiCo3*. Venice (Italy), pages 423–430.

Sun, Z., Wan, K. T. and Dillard, D. A. (2004). A theoretical and numerical study of thin film delamination using the pull-off test. *Int. Journal of Solids and Structures*, **41**, 717–730.

Täljsten, B. (1996). Strengthening of concrete prisms using the plate-bonding technique. *International Journal of Fracture*, **82**, 253–266.

Täljsten, B. (1997). Defining anchor lengths of steel and CFRP plates bonded to concrete. *Int. J. of Adhesion and Adhesives*, **19**, 319–327.

Tassios, T. P. (1988). *Meccanica delle murature*. Liguori Editore, Napoli (Italy). Italian ed.

Thouless, M. D. and Jensen, H. M. (1992). Elastic Fracture Mechanics of the Peel-Test Geometry. *Journal of Adhesion*, **38**, 185–197.

TNO Diana BV. (2008). DIANA Finite Element Analysis Release 9.3.

Triantafillou, T. (1998a). Strengthening of masonry structures using epoxy-bonded FRP laminates. *ASCE Int. Journal of Composites for Construction*, **2**(2), 96–104.

Triantafillou, T. (1998b). Strengthening of masonry structures using epoxy-bonded FRP laminates. Errata. *ASCE Int. Journal of Composites for Construction*, **2**(4), 203.

Ueda, T. and Dai, J. (2005). Interface bond between FRP sheets and concrete substrates: properties, numerical modelling and roles in member behaviour. *Progress in Structural Engineering Materials*, **7**, 27–43.

UNI-EN 1015-12 (2002). Determinazione dell'aderenza al supporto di malte da intonaco esterno ed interno. Ente Nazionale Italiano perl'Unificazione.

Valdemarca, M. (1998). *Analisi sperimentale del comportamento di volte murarie rinforzate con FRP.* Master's thesis, University of Padova (Italy). In Italian.

Valluzzi, M. R. (2008). Strengthening of masonry structures with Fibre Reinforced Plastics: from modern conception to historical building preservation. In *VI Int. Conf. on Structural Analysis of Historic Constructions*. Bath (UK), pages 33–45. ISBN 978-0-415-46872-5.

Valluzzi, M. R., Tinazzi, D., Garbin, E. and Modena, C. (2003). FEM modelling of CFRP strips bond behaviour for bed joints reinforcement techniques. In 6^{th} *Int. Conf. on Computer Methods in Structural Masonry*. Rome (Italy).

Valluzzi, M. R., Valdemarca, M. and Modena, C. (2001). Behaviour of brick masonry vaults strengthened by FRP laminates. *ASCE Int. Journal of Composites for Construction*, **5**(3), 163–169.

Wan, B., Petrou, M. F., Harries, K. A., Sutton, M. A. and Yang, B. (2002). Experimental investigation of bond between FRP and concrete. In 3^{th} *Int. Conf. on Composites in Infrastructure – ICCI-02*. San Francisco (USA).

Wan, B., Sutton, M. A., Petrou, M. F., Harries, K. A. and Li, N. (2004). Investigation of Bond between Fiber Reinforced Polymer and Concrete Undergoing Global Mixed Mode I/II Loading. *ASCE Int. Journal of Engineering Mechanics*, **130**(12), 1467–1475.

Watkin, D. (1990). *Storia dell'architettura occidentale (Italian ed.).* Zanichelli, Bologna (Italy). Italian ed.

Wu, Z., Yuan, H., Asakura, T., Yoshizawa, H., Kobayashi, A., Kojima, Y. and Ahmed, E. (2005a). Peeling Behavior and Spalling Resistance of Bonded Bidirectional Fiber Reinforced Polymer Sheets. *Int. Journal of Composites for Construction*, **9**(3), 214–226.

Wu, Z., Yuan, H., Kojima, Y. and Ahmed, E. (2005b). Experimental and analytical studies on peeling and spalling resistance of unidirectional FRP sheets binded to concrete. *Composites Science and Technology*, **65**, 1088–1097.

Wu, Z., Yuan, H. and Niu, H. (2002). Stress Transfer and Fracture Propagation in Different Kinds of Adhesive Joints. *ASCE Journal of Engineering Mechanics*, **128**(5), 562–573.

Yao, J., Teng, J. and Chen, J. (2005). Experimental study on FRP-to-concrete bonded joints. *Composites: Part B*, **36**, 99–113.

Yuan, H., Chen, J. F. and Teng, J. G. (2003). Interfacial stresses between FRP plate and concrete in a peel test: an analytical solution. In 10^{th} *Int. Conf. on Structural Faults + Repair*. London (UK).

Yuan, H., Teng, J., Seracino, R., Wu, Z. and Yao, J. (2004). Full-range behavior of FRP-to-concrete bonded joints. *Engineering Structures*, **26**, 553–565.

Yuan, H., Wu, Z. and Yoshizawa, H. (2001). Theoretical solutions on interfacial stress transfer of externally bonded steel/composite plates. *Journal of Structural Mechanics and Earthquake Engineering*, **18**(1), 27–39.